

Investigating Proton Spin Structure: A Measurement of g_2^p at Low Q^2

Melissa A. Cummings

Palmyra, NY

Master of Science, The College of William and Mary, 2011

Bachelor of Arts, SUNY Geneseo, 2009

A Dissertation presented to the Graduate Faculty
of the College of William and Mary in Candidacy for the Degree of
Doctor of Philosophy

Department of Physics

The College of William and Mary
May 2016

© by Melissa A. Cummings 2016

APPROVAL PAGE

This Dissertation is submitted in partial fulfillment of
the requirements for the degree of

Doctor of Philosophy

Melissa A. Cummings
Melissa A. Cummings

Approved by the Committee, December, 2015

Todd Averett
Committee Chair
Professor Todd Averett
The College of William and Mary

David Armstrong
Chancellor Professor David Armstrong, Physics
The College of William and Mary

Carl E. Carlson
Class of 1962 Professor Carl Carlson, Physics
The College of William and Mary

Wouter Deconinck
Assistant Professor Wouter Deconinck, Physics
The College of William and Mary

Jian-Ping Chen C
Dr. Jian-Ping Chen, Hall A Staff Scientist
Thomas Jefferson National Accelerator Facility

ABSTRACT PAGE

The g_2^p collaboration performed the first measurement of the reaction $\vec{p}(\vec{e}, e')X$ in the kinematic range $0.02 < Q^2 < 0.2 \text{ GeV}^2$ in the resonance region. Experiment E08-027 took place in Hall A at the Thomas Jefferson National Accelerator Facility from March-May of 2012. Data was taken with a longitudinally polarized electron beam, using an NH_3 target polarized in both parallel and perpendicular configurations. Very preliminary results for g_1^p and g_2^p are shown in this thesis. To extract the spin structure functions, asymmetries are calculated from data taken with a 2.2 GeV electron beam and a 5 T target field, and combined with the Bosted model proton cross section. Preliminary dilution factors and preliminary radiative corrections are included in the asymmetry analysis. Sum rules and χPT allow us to test the Burkhardt-Cottingham (BC) sum rule and obtain the spin polarizability quantities γ_0 and δ_{LT} . The BC sum rule, valid for all values of Q^2 , says that the integral of g_2 over all Bjorken x vanishes. The very preliminary result presented here shows the contribution to the integral from the measured kinematic region. Although the contribution from the resonance region is not consistent with the expected result of zero, an extrapolation to high and low x must be included to test whether the BC sum rule is satisfied. The difficulty in χPT calculations of γ_0 and δ_{LT} is how to include the resonance contributions, particularly the Δ -resonance, which dominates. Recent developments have found better agreement with neutron experimental results, however this is little proton data to compare with the calculations, particularly at low Q^2 . The very preliminary results shown here do not show agreement with any of the current χPT predictions. However, as this is only the contribution from the measured kinematic region, it is necessary to include the extrapolation outside the resonance region to draw a stronger conclusion. Further analysis is ongoing, and preliminary results, including a cross section extracted from data instead of a model prediction, are expected within the next year.

TABLE OF CONTENTS

Acknowledgments	vi
Dedication	viii
List of Tables	ix
List of Figures	xi
CHAPTER	
1 Introduction	2
2 Inclusive Electron Scattering	6
2.1 Kinematic Variables	6
2.2 Differential Cross Section	8
2.2.1 Electron-Muon Scattering $e^- \mu^- \rightarrow e^- \mu^-$	8
2.2.2 Electron-Proton Scattering	12
2.3 Types of Inclusive Electron Scattering	16
2.3.1 Elastic Scattering	16
2.3.2 Quasi-Elastic Scattering	17
2.3.3 Resonance Region	18
2.3.4 Deep Inelastic Scattering	19
3 Theoretical Tools and Motivation	20
3.1 Virtual Photoabsorption Cross Sections	20
3.2 The Quark-Parton Model	23
3.3 The g_2 Structure Function	24
3.4 Operator Product Expansion	26
3.5 Chiral Perturbation Theory	27

3.6	Model Predictions	29
3.6.1	Phenomenological MAID Model	29
3.6.2	Bosted-Christy Model	29
3.7	Sum Rules	30
3.7.1	Burkhardt-Cottingham Sum Rule	30
3.7.2	Spin Polarizabilities	34
3.8	Additional Motivation	37
3.8.1	Proton Hyperfine Splitting	38
3.8.2	Proton Charge Radius	40
4	The Experiment	43
4.1	Overview	43
4.2	The Electron Accelerator	45
4.2.1	Polarized Electron Beam	46
4.3	Hall A Beamline	47
4.3.1	Beam Position	48
4.3.2	Beam Current	48
4.3.3	Rasters	49
4.3.4	Chicane Magnets	50
4.3.5	Beam Energy Measurement	50
4.3.6	Beam Polarization	52
4.4	The Polarized NH ₃ Target	54
4.4.1	Dynamic Nuclear Polarization	54
4.4.2	Target Setup	56
4.5	High Resolution Spectrometers	60
4.6	Detector Stack	60
4.6.1	Vertical Drift Chambers	61

4.6.2	Scintillator Planes	63
4.6.3	Gas Cherenkov	64
4.6.4	Electromagnetic Calorimeters	66
4.7	Third Arm Detector	68
5	Analysis	70
5.1	Asymmetries and Cross Sections	70
5.2	Detector Calibrations and Efficiency Studies	73
5.2.1	Gas Cherenkov	73
5.2.2	Lead Glass Calorimeters	74
5.2.3	Efficiency Studies	79
5.2.4	Scintillator Trigger Efficiencies	82
5.2.5	VDC Multitrack Efficiency	84
5.3	Particle Identification Cuts	88
5.4	Charge Asymmetry	92
5.5	Livetime Asymmetry	92
5.6	Optics and Acceptance Studies	94
5.6.1	Coordinate Systems	94
5.6.2	Central Scattering Angle Measurement	96
5.6.3	HRS Optics	99
5.7	Target Polarization	100
5.7.1	Determination of Calibration Constants	100
5.7.2	Polarization Uncertainty	103
5.8	Beam Position Reconstruction	104
5.8.1	Equipment	104
5.8.2	Calibration	107
5.9	Dilution Analysis	112

5.9.1	Method	112
5.9.2	Preliminary Dilution Factor	114
5.10	Packing Fraction Analysis	115
5.10.1	Method	116
5.10.2	Yield Spectra and Fitting Routine	118
5.10.3	Dummy Run	119
5.10.4	Ammonia Run	120
5.10.5	Cross Section Model Input	124
5.10.6	Variation in Yields	125
5.10.7	Uncertainty	139
5.10.8	Results	140
5.10.9	Summary	150
5.10.10	Preliminary p_f Values used for this Analysis	151
6	Results and Conclusions	152
6.1	Asymmetry Results	152
6.1.1	Pion Asymmetry	155
6.2	Radiative Corrections	163
6.2.1	Unpolarized Radiative Corrections	163
6.2.2	Preliminary Radiative Corrections	167
6.2.3	Contribution to Systematic Uncertainty	171
6.3	Kinematics	175
6.4	Polarized Cross Section Differences	177
6.5	Systematic Uncertainties	178
6.6	Spin Structure Functions g_1^p and g_2^p	183
6.7	Contribution to Burkhardt-Cottingham Sum Rule	185
6.8	Spin Polarizabilities γ_0 and δ_{LT}	188

6.9 Conclusions and Future Work	193
APPENDIX A	
Particle ID Cuts	195
A.0.1 Right HRS Results	196
A.0.2 Left HRS Results	200
Bibliography	204
Vita	211

ACKNOWLEDGMENTS

It isn't possible to thank everyone who played a role in this journey, but know that I am grateful for your support and encouragement along the way.

First, thank you to my advisor, Todd Averett, for being my mentor and advocate. Our weekly discussions were always enjoyable, whether they were about physics, or an unrelated, but equally interesting topic. Thank you for always sandwiching the bad news in between the good, and for being a constant source of encouragement as I finished this thesis.

Many thanks to my JLab supervisor, Jian-Ping Chen, who enthusiastically answered my many questions to better understand the theory of the g_2^p experiment. His rigorous constructive criticism helped me improve the quality of my analysis. Thank you also to the rest of my committee, David Armstrong, Carl Carlson, and Wouter Deconinck, for their careful reading of this document.

I must thank my undergraduate advisor, Stephen Padalino, for sparking my interest in experimental nuclear physics by inviting me to work in the accelerator lab at SUNY Geneseo, and for first planting the idea of graduate school in my head.

Every experiment has its problems, the g_2^p experiment seemed to experience all of them. We were lucky to have Alexandre Camsonne, Don Crabb, J.-P. Chen and Karl Slifer as our spokespeople, who pushed past the multitude of difficulties during our run period. Without the efforts of the Hall A collaboration and the JLab target group, the experiment would not have been a success. Thank you also to J-P and Karl for continuing to guide us through the analysis. Thanks to my fellow g_2^p grad students, Toby Badman, Chao Gu, Min Huang, Jie Liu, Pengjia Zhu, and Ryan Zielinski; I feel fortunate to have worked with such a talented group of students. We had several postdocs whose hard work was crucial to the success of g_2^p ; many thanks to Kalyan Allada, Ellie Long, James Maxwell, Vince Sulkosky, and Jixie Zhang. Thanks to Vince for teaching me the hardware and DAQ aspects of the HRS, for numerous valuable analysis discussions, and many cups of tea. Thank you to Kalyan for reminding me to think of the big picture when I became frustrated, and for the pep talks when I was convinced I would never finish.

I will always be grateful for the friendships I formed at William and Mary. Thanks to my cohort for making our two years of coursework not only bearable, but

enjoyable, despite the absurd amounts of time we spent doing homework in the basement of Millington. Thanks to Jess Lehman for helping me cover our mirror with equations while we studied for the qual. Thanks to Leo Aliaga and Juan Carlos Cornejo for our weekly “work parties” as we all tried to graduate; it was easier to stomach working on the weekends when there was good company. Thanks to Gleb Romanov for “drinks!” and to Anne Norrick for spontaneous dance parties. Thanks to Meredith and Chris Nusbaum for countless taco nights and margaritas. Thanks to Ellie Radue and Charlie Fancher for berry picking adventures and family dinners. You all make leaving Williamsburg a bittersweet event.

I could never have reached this point without the support of my family. Thanks to Shawn and Lindsay (and Ainsley!) for being my cheerleaders. Thanks to Lauren and Kristen for reminding me that it’s just “simple physics”. And most of all, thank you to my parents, Don and Melanie. The words “thank you” don’t seem like enough, but know that your constant support and endless encouragement is what made all of this possible.

To my parents, Don and Melanie Cummings, who made all of this possible.

LIST OF TABLES

3.1	Data sets included in Bosted-Christy Model	31
3.2	Measurements of the proton charge radius	41
4.1	Beam energy and target configurations	43
4.2	Deflection angles	51
4.3	HRS Characteristics	62
5.1	Survey measurement uncertainties	96
5.2	Central scattering angle from survey	97
5.3	Normalization values for setting 1	126
5.4	Normalization values for setting 2	129
5.5	Normalization values for setting 3	132
5.6	Normalization values for setting 4	134
5.7	Normalization values for setting 5	137
5.8	Packing fraction uncertainty	140
5.9	Packing fraction fit uncertainty	140
5.10	p_f results for setting 1	142
5.11	p_f results for setting 2	144
5.12	p_f results for setting 3	145

5.13	p_f results for setting 3 (short cell)	146
5.14	p_f results for setting 4	148
5.15	p_f results for setting 5	149
5.16	Preliminary p_f values	151
6.1	Systematic uncertainties for A_{\parallel}	182
6.2	Systematic uncertainties for A_{\perp}	182
6.3	Systematic uncertainties for $\Delta\sigma_{\parallel,\perp}$ (Kinematic Setting L)	183
6.4	Systematic uncertainties for $\Delta\sigma_{\parallel,\perp}$ (Kinematic Setting T)	183

LIST OF FIGURES

1.1	Zeeman effect	3
1.2	Theoretical tools for different ranges of Q^2	4
2.1	First order Feynman diagram for inclusive electron scattering	7
2.2	Lepton-muon scattering digaram	9
2.3	Electron-muon scattering diagram	11
2.4	Electron-proton scattering diagram	12
2.5	Electron-proton scattering in the lab frame	14
2.6	Beam and target polarization configurations	15
2.7	Inclusive scattering cross section	16
3.1	Helicity projections for virtual photoabsorption cross sections	22
3.2	Twist-2 and twist-3 diagrams	25
3.3	Burkhardt-Cottingham Sum Rule	34
3.4	Neutron generalized spin polarizabilities	37
3.5	Integrand of Δ_2	40
3.6	Results for g_2^p from E94-010	42
4.1	Kinematic coverage for the g_2^p experiment	44

4.2	The Jefferson Lab electron accelerator setup	45
4.3	Structure of GaAs crystal	47
4.4	Hall A beamline	47
4.5	Raster Patterns	50
4.6	Chicane Magnets	51
4.7	Møller polarimeter	53
4.8	Target Polarization	55
4.9	Dynamic Nuclear Polarization	56
4.10	Polarized target setup	58
4.11	g_2^p target stick	60
4.12	High Resolution Spectrometer	61
4.13	Vertical Drift Chambers	63
4.14	s1 and s2m scintillator planes	64
4.15	Diagram of Cherenkov radiation	66
4.16	Gas Cherenkov detector	67
4.17	Electromagnetic calorimeters	68
4.18	Third arm detector	69
5.1	HRS Detector Stack	74
5.2	Cherenkov single photoelectron peak	75
5.3	Lead glass calorimeter layout	75
5.4	Acceptance cuts for PID analysis	77
5.5	E_{tot}/p distribution	79

5.6	Method of calculating detection efficiency	80
5.7	Leadglass calorimeter detector efficiencies	81
5.8	Gas Cherenkov detector efficiencies	82
5.9	Trigger efficiencies	85
5.10	VDC single track probability	86
5.11	Total VDC efficiency	88
5.12	Gas Cherenkov cut efficiencies	89
5.13	Leadglass calorimeter cut efficiencies	89
5.14	Example of particle ID cuts	90
5.15	Pion contamination (LHRS)	91
5.16	Pion Contamination (RHRs)	91
5.17	Residual pion contamination	91
5.18	Charge asymmetries	92
5.19	Livetime asymmetries	93
5.20	Target coordinate system	95
5.21	Sieve slit diagram	95
5.22	Central scattering angle measurement	98
5.23	HRS magnets	99
5.24	Raw and baseline NMR signals	101
5.25	Baseline subtracted NMR signal	102
5.26	2.5T Polarization results	102
5.27	5T Polarization results	103
5.28	Beam position reconstruction equipment	105

5.29 Beam position monitor	106
5.30 Harp design	106
5.31 Method of images for determining beam position	108
5.32 Comparison of harp scan and BPM data	109
5.33 Preliminary dilution factors (materials 17 and 18)	115
5.34 Preliminary dilution factors (materials 19 and 20)	115
5.35 Target cell diagram	117
5.36 Yield spectra for production and dummy run	119
5.37 Fit to dummy run	120
5.38 Comparison of dummy run with simulation	122
5.39 Comparison of carbon run with simulation	123
5.40 Fit to production run	123
5.41 Elastic cross sections from simulation	124
5.42 Elastic yields for setting 1	125
5.42 Yield stability checks for setting 1	127
5.43 Elastic yields for setting 2	128
5.44 Yield stability checks for setting 2	130
5.45 Elastic yields for setting 3	131
5.45 Yield stability checks for setting 3	133
5.46 Elastic yields for setting 4	135
5.47 Yield stability checks for setting 4	136
5.48 Elastic yields for setting 5	137
5.48 Yield stability checks for setting 5	139

5.49	Fit examples for setting 1	142
5.50	Ratio of p_f and yield for setting 1	143
5.51	Fit examples for setting 2	143
5.52	Ratio of p_f and yield for setting 2	144
5.53	Fit examples for setting 2	145
5.54	Ratio of p_f and yield for setting 3	146
5.55	Ratio of p_f and yield for setting 3 (short cell)	147
5.56	Fit example for setting 4	147
5.57	Ratio of p_f and yield for setting 4	148
5.58	Fit examples for setting 5	149
5.59	Ratio of p_f and yield for setting 5	150
6.1	Physics asymmetries	156
6.2	Event selection for pion asymmetry	157
6.3	Event section for pion and electron yields	158
6.4	Electron and pion asymmetries (longitudinal configuration)	159
6.5	Electron and pion asymmetries (transverse configuration)	160
6.6	Electron yields	161
6.7	Pion yields	162
6.8	Residual pion contamination	164
6.9	Leading order diagram for electron-proton scattering	165
6.10	Higher order corrections to electron proton scattering	166
6.11	Bremsstrahlung radiation	167

6.12	Model predictions for longitudinal asymmetry	169
6.13	Model predictions for transverse asymmetry	170
6.14	Preliminary radiative corrections	172
6.15	Effect of varying θ , longitudinal setting	173
6.16	Effect of varying θ , transverse setting	174
6.17	Estimate of uncertainty on MAID model	176
6.18	Variation in scattering angle	177
6.19	Bosted model prediction for unpolarized cross section	178
6.20	Cross section difference, longitudinal setting	179
6.21	Cross section difference, longitudinal setting	180
6.22	g_1^p and g_2^p results for kinematic setting L	184
6.23	g_1^p and g_2^p results for kinematic setting T	184
6.24	g_2^p vs. x	185
6.25	Contribution to BC Sum Rule	186
6.26	RSS results for g_2^p	187
6.27	RSS results for g_2^p	188
6.28	Value of γ_0 integrand, vs. x	189
6.29	Value of δ_{LT} integrand, vs. x	190
6.30	Contribution to generalized spin polarizabilities	192
6.31	RSS results for g_2^p	193

INVESTIGATING PROTON SPIN STRUCTURE: A MEASUREMENT OF g_2^p
AT LOW Q^2

CHAPTER 1

Introduction

Hints of spin physics can be traced back to Pieter Zeeman's work in 1896. Although Michael Faraday had already shown the first evidence of a connection between light and magnetic forces by demonstrating that the angle of polarization of light could be modified when passed through certain materials in a magnetic field, Faraday was not able to find a demonstrable effect that described the direct influence of a magnetic field on light. With significant developments in technology at his advantage, Zeeman was able to expand on Faraday's work and observe the broadening of D-lines in the spectrum of sodium (see Fig. 1.1) when a sodium flame was exposed to an electromagnet [1]. Despite this milestone, it would take three more decades until the “anomalous Zeeman Effect” was understood to be a consequence of spin.

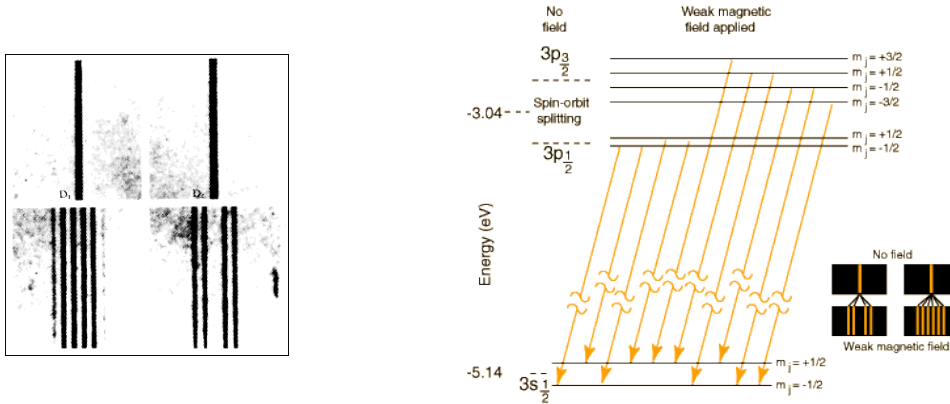


FIG. 1.1: Broadening of sodium D-lines when sodium flame is placed in an electromagnet, as demonstrated by P. Zeeman. On the left is a photo of Zeeman's work [2], on the right is a detailed diagram of the energy level transitions that lead to the broadening of the spectral lines [3].

The Stern-Gerlach experiment in 1922 gave the first measurement of the electron magnetic moment [4, 5]. A beam of silver particles was passed through an inhomogeneous magnetic field and detected at two highly-localized points, a result that could not be understood in the classical picture of the electron. Scientists were still struggling to understand the shell structure of the atom. It was thought that the Zeeman effect was a consequence of the interaction between the angular momentum of the “core” electron and the “radiant” electron in the outermost unclosed shell. But, this did not explain why, in an atom in its ground state, the electrons were not bound to the innermost shell. Wolfgang Pauli proposed a new quantum degree of freedom with 2 possible values and formulated the Pauli Exclusion Principle, which said that no two electrons could exist in the same quantum state [6, 7]. This two valued-ness was later identified as spin. In 1928 Paul Dirac published his famous relativistic wave equation, governing the behavior of fundamental point-like particles. Described in Eqn. 1.1, the Dirac equation expresses the spin of a particle in terms of its magnetic moment, μ , where eQ and M are the charge and mass of the particle, respectively,

$$\vec{\mu} = \frac{eQ}{M} \vec{S}. \quad (1.1)$$

This result agreed well with the experimental results of Stern and Gerlach for the electron magnetic moment. However, by 1933, Stern had improved his experimental apparatus sufficiently to measure the proton magnetic moment. The result disagreed with Dirac's prediction by $\sim 150\%$. This was the first indication that protons were not solid lumps of positive charge. Decades later, extensive studies were performed at SLAC to confirm that nucleons had composite structure. In the tradition of the Rutherford gold foil experiment, scattering experiments are used to investigate the structure of the nucleon. High resolution lepton or hadron beams, such as the facilities at Jefferson Lab, SLAC, CERN or DESY, are used as the probe. Nuclear targets can include protons, deuterons, NH_3 , ND_3 and ${}^3\text{He}$.

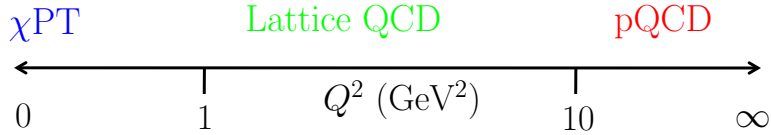


FIG. 1.2: Theoretical tools for different ranges of Q^2 .

Spin physics has since become a laboratory for testing the theory of the strong interaction, one of the four fundamental forces. Quantum Chromodynamics (QCD) describes the interactions of quarks and gluons inside the nucleon. In the high energy region, perturbative QCD (pQCD) calculations agree well with experimental results. However, as we move to lower energy and momentum transfer, these calculations become more difficult. Low energy effective field theories, such as Chiral Perturbation Theory (χPT) are used to make these calculations easier. In the intermediate energy range, lattice QCD is used to bridge the gap in the region where

both pQCD and χPT predictions begin to fail.

The purpose of the g_2^p experiment is to study the spin structure of the proton in the low momentum transfer region, which is relatively unknown. This dissertation will describe the theoretical formalism of spin physics and the motivation for the g_2^p experiment. The details of the experimental setup will be described. Finally, details of the analysis and *very preliminary* results will be discussed.

CHAPTER 2

Inclusive Electron Scattering

The process of lepton scattering is well understood in the framework of Quantum Electrodynamics (QED), making it a powerful probe for studying the internal structure of the nucleon. This chapter will present the formalism of this process, along with the relevant kinematic variables. The different types of inclusive electron-nucleon scattering will also be discussed.

2.1 Kinematic Variables

The process of lepton-nucleon scattering is described by:

$$l(k) + N(P) \rightarrow l(k') + X(P') \quad (2.1)$$

where l represents a charged lepton with 4-momentum k scattering from a nucleon N with 4-momentum P . The right side of Eqn. 2.1 gives the scattered lepton with

4-momentum k' and the final hadronic state of the nucleon X with 4-momentum P' . According to the Born Approximation, the scattering occurs by exchange of a virtual photon. The lowest order Feynman diagram for inclusive electron scattering is shown in Fig. 2.1.

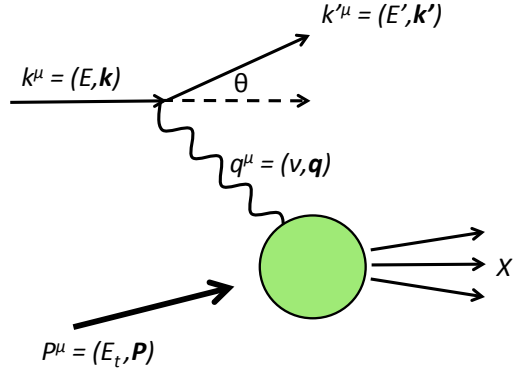


FIG. 2.1: First order Feynman diagram for inclusive electron scattering.

For an incoming electron with 4-momentum $k^\mu = (E, \vec{k})$ interacting with a target nucleon with 4-momentum $P^\mu = (E_t, \vec{P})$, a single virtual photon will be exchanged, scattering from the electron at an angle θ . The final state of the scattered electron is given by $k'^\mu = (E', \vec{k}')$. The 4-momentum of the virtual photon is given by $q^\mu = (\nu, \vec{q})$, where ν is the energy loss of the electron and, for a space-like virtual photon, has $q^2 < 0$. In inclusive scattering, the final hadronic state (X) goes undetected, but it is useful to define the invariant mass of the final state $W = \sqrt{(P + q)^2}$. In the laboratory frame, where $P^\mu = (M, \vec{0})$, it is useful to define the following kinematic relations:

$$\begin{aligned}\nu &= E - E' \\ Q^2 &= -q^2 = 4EE' \sin^2 \frac{\theta}{2} \\ W^2 &= M^2 + 2M\nu - Q^2\end{aligned}\tag{2.2}$$

2.2 Differential Cross Section

The differential cross section $d\sigma/d\Omega$ is proportional to the probability that an incident particle will interact with a target particle and scatter through a solid angle Ω . The cross section can first be written in the form

$$\frac{d\sigma}{d\Omega} \propto |T_{fi}|^2 = |\mathcal{M}|^2 \Phi, \quad (2.3)$$

where \mathcal{M} is the matrix element for the process, Φ is a phase-space factor (which is purely kinematic information), and T_{fi} represents the probability of a particle in initial state ϕ_i to scatter into final state ϕ_f , such that:

$$T_{fi} = -i \int d^4x \phi_f^*(x) V(x) \phi_i(x), \quad (2.4)$$

where $V(x)$ is the interaction potential. We will start with the simpler case of electron-muon scattering to illustrate the complexity of obtaining the unpolarized cross section.

2.2.1 Electron-Muon Scattering $e^- \mu^- \rightarrow e^- \mu^-$

The first order Feynman diagram for this process is shown in Fig. 2.2; we can now build the matrix element using the Feynman calculus.

For each external line, we include a term such as $u(k)$ or $\bar{u}(k')$, which represent solutions to the momentum space Dirac equation $(\gamma^\mu p_\mu - mc)u = 0$, where γ^μ are the gamma matrices and m is the mass of the particle. The internal line propagator, in this case a photon, adds a factor of $-ig_{\mu\nu}/q^2$. Finally, each vertex adds a factor

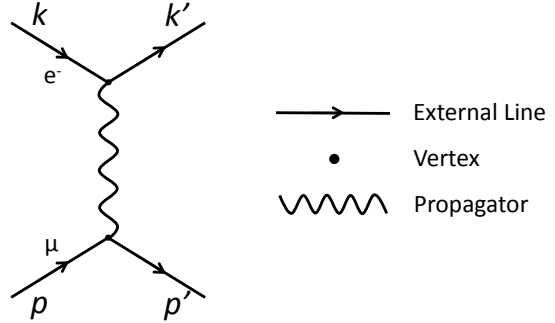


FIG. 2.2: Feynman diagram for electron-muon scattering.

of $i g_e \gamma^\mu$, where g_e is the strength of the vertex, which in this case is the charge of the electron e . In this way we can write down \mathcal{M} as

$$\mathcal{M} = -\frac{e^2}{q^2} [\bar{u}(k') \gamma^\mu u(k)] [\bar{u}(p') \gamma_\mu u(p)]. \quad (2.5)$$

The unpolarized cross section is obtained by taking the square of the matrix element \mathcal{M} and summing over the spin states. But first, it is useful to separate the sums over the electron and muon spins;

$$|\mathcal{M}|^2 = \frac{e^4}{q^4} L_e^{\mu\nu} L_{\mu\nu}^{muon}, \quad (2.6)$$

where $L_e^{\mu\nu}$ ($L_{\mu\nu}^{muon}$) is the tensor associated with the electron (muon) vertex and is written as:

$$L_e^{\mu\nu} = \frac{1}{2} \sum_{e \text{ spins}} [\bar{u}(k') \gamma^\mu u(k)] [\bar{u}(k') \gamma^\nu u(k)]^*, \quad (2.7)$$

$$L_{\mu\nu}^{muon} = \frac{1}{2} \sum_{\mu \text{ spins}} [\bar{u}(p') \gamma^\mu u(p)] [\bar{u}(p') \gamma^\nu u(p)]^*. \quad (2.8)$$

The process of summing over spin states is made simpler by applying well-

established trace techniques. Recalling that $\sum_{s=1,2} u^{(s)} \bar{u}^{(s)} = \not{k} + m$, with the Feynman slash notation defined as $\not{k} = \gamma^\mu k_\mu$, the electron tensor can be re-written in the form

$$L_e^{\mu\nu} = \frac{1}{2} Tr [(\not{k}' + m)\gamma^\mu (\not{k} + m)\gamma^\nu], \quad (2.9)$$

and when evaluated can be written as

$$L_e^{\mu\nu} = 2 \left(k'^\mu k^\nu + k'^\nu k^\mu - \left(\vec{k}' \cdot \vec{k} - m^2 \right) g^{\mu\nu} \right). \quad (2.10)$$

Similarly, the muon tensor can be evaluated as

$$L_{\mu\nu}^{muon} = 2 \left(p'_\mu p_\nu + p'_\nu p_\mu - \left(\vec{p}' \cdot \vec{p} - M^2 \right) g_{\mu\nu} \right). \quad (2.11)$$

Here, m and M are the electron and muon masses, respectively. Putting these two expressions back into (2.6) gives us the exact expression for electron-muon scattering amplitude:

$$|\mathcal{M}|^2 = \frac{8e^4}{q^4} \left[(k' \cdot p')(k \cdot p) + (k' \cdot p)(k \cdot p') - (p' \cdot p)m^2 - (k' \cdot k)M^2 + 2m^2M^2 \right], \quad (2.12)$$

where the quantities $(k' \cdot p')$ etc. represent the vector dot product.

We can further evaluate this expression in the lab frame, where the initial μ is at rest (Fig. 2.3). By neglecting the mass of the electron, and using the kinematic relations $q^2 \simeq -2k \cdot k' \simeq -4EE' \sin^2 \frac{\theta}{2}$, and $q^2 = -2p \cdot q = -2\nu M$ so that $\nu \equiv$

$E - E' = -\frac{q^2}{2M}$, we can re-write the matrix element as:

$$|\mathcal{M}|^2 = \frac{8e^4}{q^4} 2M^2 EE' \left[\cos^2 \frac{\theta}{2} - \frac{q^2}{2M^2} \sin^2 \frac{\theta}{2} \right]. \quad (2.13)$$

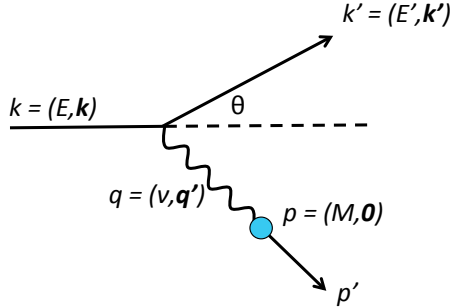


FIG. 2.3: Feynman diagram for electron-muon scattering in the lab frame.

We can now start to build the differential cross section, while still neglecting the mass of the electron:

$$d\sigma = \frac{1}{4ME} \frac{|\mathcal{M}|^2}{4\pi^2} \frac{1}{2} E' dE' d\Omega \frac{d^3 p'}{2p'_0} \delta^{(4)}(p + q - p'). \quad (2.14)$$

After integrating over dE' , this gives us the exact formula for electron-muon scattering in the lab frame,

$$\left. \frac{d\sigma}{d\Omega} \right|_{lab} = \left(\frac{\alpha^2}{4E^2 \sin^4 \frac{\theta}{2}} \right) \frac{E'}{E} \left[\cos^2 \frac{\theta}{2} - \frac{q^2}{2M^2} \sin^2 \frac{\theta}{2} \right], \quad (2.15)$$

where the factor $E'/E = 1 + (2E/M) \sin^2 \theta$ arises from the recoil of the target and the factor $\alpha = e^2/4\pi \approx 1/137$. Furthermore, if we consider the case where the mass of the target particle is much larger than the scattering energy ($M \gg q^2$), the cross section simplifies to the well known Mott scattering result, which includes the

target recoil factor $\frac{E'}{E}$,

$$\sigma_{Mott} = \frac{d^2\sigma}{d\Omega dE'} = \frac{\alpha^2}{4E^2} \frac{E'}{E} \left(\frac{\cos^2 \frac{\theta}{2}}{\sin^4 \frac{\theta}{2}} \right). \quad (2.16)$$

2.2.2 Electron-Proton Scattering

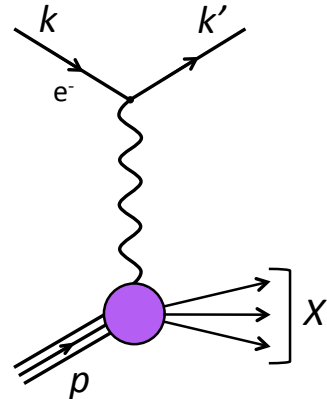


FIG. 2.4: Feynman diagram for electron-proton scattering.

Unfortunately, due to the complex structure of the nucleon, electron-nucleon scattering is not as simple as the case described above. We can generalize the cross section in a similar method as Eqn. 2.6,

$$\frac{d^2\sigma}{d\Omega dE'} = \frac{\alpha^2}{Q^4} \frac{E'}{E} L_e^{\mu\nu} W_{\mu\nu}, \quad (2.17)$$

where $L_e^{\mu\nu}$ is the same leptonic tensor used in the above example, and the hadronic tensor, $W_{\mu\nu}$, parameterizes the unknown form of the nucleon target. In order to include the possibility of a polarized electron and target, we must write down the

lepton tensor while summing explicitly over the spin,

$$\begin{aligned} L_e^{\mu\nu} &= \frac{1}{2} \sum_{e \text{ spins}} \bar{u}(k, s) \gamma^\mu u(k', s') \bar{u}(k', s) \gamma_\nu u(k, s) \\ &= k^\mu k'^\nu + k^\nu k'^\mu - k \cdot k' g^{\mu\nu} + [i\epsilon^{\mu\nu\alpha\beta} q_\alpha s_\beta], \end{aligned} \quad (2.18)$$

where $s_\beta = \bar{u}\gamma_\beta\gamma_5 u$ is the lepton spin vector, $\epsilon_{\mu\nu\alpha\beta}$ is the Levi-Civita tensor, and $m_e \approx 0$. The term in square brackets represents the antisymmetric piece of this tensor.

Due to the complex structure of the nucleon, the hadronic tensor is more complicated to calculate directly. It is generally parameterized in terms of structure functions. This tensor can be broken into symmetric and antisymmetric pieces, $W_{\mu\nu} = W_{\mu\nu}^S + W_{\mu\nu}^A$. Using Lorentz and gauge invariance and taking into account parity conservation, we can write down the most general form of these two terms,

$$W_{\mu\nu}^S = W_1 \left(-g_{\mu\nu} + \frac{q^\mu q^\nu}{q^2} \right) + \frac{W_2}{M^2} \left(p^\mu - \frac{p \cdot q}{q^2} q^\mu \right) \left(p^\nu - \frac{p \cdot q}{q^2} q^\nu \right) \quad (2.19)$$

and

$$W_{\mu\nu}^A = i\epsilon_{\mu\nu\alpha\beta} q^\alpha \left[G_1(\nu, q^2) S^\beta + \frac{G_2(\nu, Q^2)}{M^2} (S^\beta p \cdot q - p^\beta S \cdot q) \right] \quad (2.20)$$

where $S^\beta = \bar{u}(p)\gamma^\beta\gamma_5 u(p)/2M$ is the hadronic spin vector and the structure functions $W_{1,2}$ and $G_{1,2}$ describe the internal structure of the proton. Typically, the structure functions are rewritten as dimensionless functions which depend on the kinematic

variables Q^2 and x :

$$\begin{aligned}
 MW_1(\nu, Q^2) &= F_1(x, Q^2) \\
 \nu W_2(\nu, Q^2) &= F_2(x, Q^2) \\
 M\nu G_1(\nu, Q^2) &= g_1(x, Q^2) \\
 \nu^2 G_2(\nu, Q^2) &= g_2(x, Q^2)
 \end{aligned} \tag{2.21}$$

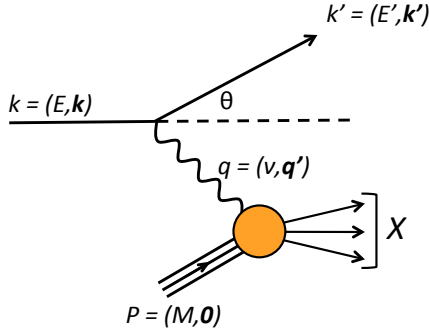


FIG. 2.5: Electron-proton scattering in the lab frame.

By summing over the incident electron and target spins, we can write down the differential cross section for unpolarized electron-nucleon scattering, in the laboratory frame, as

$$\frac{d^2\sigma}{d\Omega dE'} = \frac{\alpha^2 \cos^2 \frac{\theta}{2}}{4E^2 \sin^4 \frac{\theta}{2}} \left(\frac{2}{M} F_1(x, Q^2) \tan^2 \frac{\theta}{2} + \frac{1}{\nu} F_2(x, Q^2) \right). \tag{2.22}$$

The structure functions F_1 and F_2 parameterize the internal structure of the nucleon for the case of an unpolarized electron and unpolarized nucleon.

Moving to the more complicated case with a polarized electron beam and polarized nucleon target, two additional structure functions, g_1 and g_2 , are necessary to

parameterize the internal structure of the nucleon. These so-called “spin structure functions” can be accessed by using different combinations of the beam and target spin polarization; either longitudinal or perpendicular to the scattering plane of the electron (shown in Fig. 2.6). In the notation below, a single arrow represents the electron polarization, which can be either aligned (\uparrow) or anti-aligned (\downarrow) with the direction of the beam. A double arrow signifies the proton polarization, which is either parallel ($\uparrow\uparrow$ or $\downarrow\downarrow$) or perpendicular ($\leftarrow\leftarrow$ or $\Rightarrow\Rightarrow$) to the beam polarization. For the longitudinal case, the differential cross section is given as

$$\Delta\sigma_{\parallel} = \frac{d^2\sigma}{dE'd\Omega} (\downarrow\uparrow - \uparrow\downarrow) = \frac{4\alpha^2}{MQ^2} \frac{E'}{\nu E} \left[(E + E' \cos\theta) g_1(x, Q^2) - \frac{Q^2}{\nu} g_2(x, Q^2) \right], \quad (2.23)$$

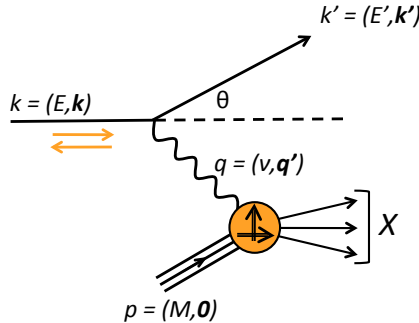


FIG. 2.6: Different combinations of the beam and target polarization.

and for the transverse case, the differential cross section is given as

$$\Delta\sigma_{\perp} = \frac{d^2\sigma}{dE'd\Omega} (\downarrow\Rightarrow - \uparrow\Rightarrow) = \frac{4\alpha^2 \sin\theta}{MQ^2} \frac{E'^2}{\nu^2 E} [\nu g_1(x, Q^2) + 2E g_2(x, Q^2)]. \quad (2.24)$$

For the longitudinal case, the cross section is dominated by the g_1 term at low Q^2 , but for the transverse configuration, the contributions from g_1 and g_2 are more balanced.

2.3 Types of Inclusive Electron Scattering

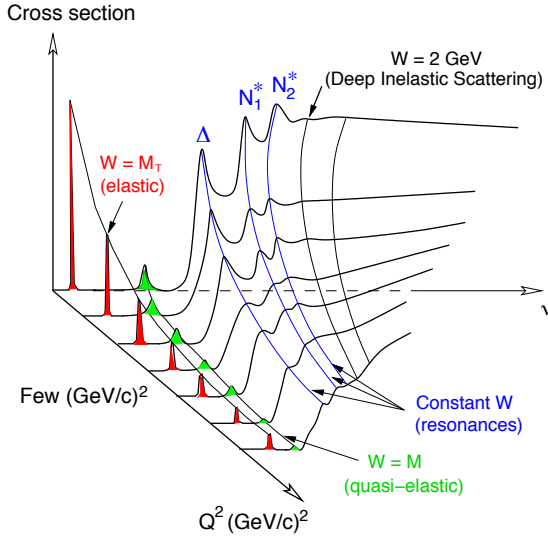


FIG. 2.7: Generic representation of the cross section for inclusive scattering, plotted as a function of ν and Q^2 . Reproduced from [8].

The previous section gave us a representation of the cross section in general terms. However, as seen in Fig. 2.7, the cross section clearly has a dependence on the momentum and energy transferred from the electron to the target, so breaking it into different kinematic regions is useful. This section will discuss the elastic, quasi-elastic and inelastic scattering kinematic regions.

2.3.1 Elastic Scattering

Elastic scattering is characterized by the nucleus remaining in the ground state after the scattering process. The energy/momentum transfer is absorbed by the recoil nucleon, meaning the invariant mass W is equal to the mass of the nucleon: $\nu = \frac{Q^2}{2M}$. Through conservation of energy and momentum, $P'^2 = (k + P - k')^2$, the

energy of the scattered electron can be constrained as such:

$$E' = \frac{E}{1 + \frac{2E}{M} \sin^2 \frac{\theta}{2}}. \quad (2.25)$$

In elastic scattering we can use Sachs form factors to describe the electric and magnetic distributions of the nucleon, G_E and G_M [9],

$$\begin{aligned} F_1 &= \frac{Q^2}{4M} G_M^2 \\ F_2 &= \frac{\nu \left(G_E^2 + \frac{Q^2}{4M^2} G_M^2 \right)}{1 + \frac{Q^2}{4M^2}}, \end{aligned} \quad (2.26)$$

meaning the differential cross section now takes the form

$$\frac{d\sigma}{d\theta} = \sigma_{Mott} \left[\frac{2}{M} \tau G_M^2 \tan^2 \frac{\theta}{2} + \frac{(G_E^2 + \tau G_M^2)}{1 + \tau} \right], \quad (2.27)$$

where $\tau = Q^2/4M^2$. These form factors carry information on the charge and current distributions of the nucleon.

2.3.2 Quasi-Elastic Scattering

When the energy transfer ν becomes much larger than the binding energy, the nucleus will no longer remain intact. In quasi-elastic scattering, the incident electron elastically scatters from one of the nucleons in the nucleus, resulting in the nucleon being ejected from the nucleus, however the nucleon is left in its ground state. The quasi-elastic peak gets smeared about $\nu = \frac{Q^2}{2M}$ due to Fermi motion, meaning

the distribution is much broader in comparison to the elastic peak. Quasi-elastic scattering implies that the incident electron is scattering from a nucleon within the nucleus, thus there is no quasi-elastic peak if the target is a nucleon.

2.3.3 Resonance Region

As we continue to increase the energy transfer, we begin to move from the elastic to the inelastic region. The first region to be considered inelastic is characterized by a number of resonances. As energy/momentum transfer increases, quarks within the nucleon begin to absorb the virtual photon, causing an excitation of the nucleon to a higher resonant state. The existence of the resonances is further proof that the nucleon is a composite system.

The resonance region is typically defined in the invariant mass region $1.0 < W < 2.0$ GeV, in between pion production threshold ($W_\pi = M_p + m_\pi$) and the onset of deep inelastic scattering at 2 GeV. Three significant resonance features are typically seen. The first peak contains the $\Delta(1232)$ resonance, which is the dominant spin-3/2 resonance in $\pi - N$ scattering and only overlaps a small amount with other resonance states. The second peak contains two resonance, the $N^*(1520)$ and $N^*(1535)$, and the third peak contains many resonances, but the strongest at low- Q^2 is the $N^*(1680)$. The $N^*(1440)$ resonance also exists between the Δ and the second peak. There are numerous other resonances that contribute to the cross section, but these resonances cannot be isolated using inclusive electron scattering.

2.3.4 Deep Inelastic Scattering

By increasing the energy transfer even further we reach the deep inelastic scattering (DIS) region, which is typically defined as $W > 2 \text{ GeV}$ and $Q^2 > 1 \text{ GeV}^2$. At this level the resonance peaks are no longer distinguishable and the scattering process becomes an incoherent sum over the nucleon's constituents. In DIS, the energy of the scattered electron is measured, but the final hadronic state (X) goes undetected.

Recall that the invariant mass of the final state is $W^2 = M^2 + 2M\nu - Q^2$. For elastic scattering, $W = M$, so $2M\nu - Q^2 = 0$. For inelastic scattering, $W > M$, and $2M\nu - Q^2 > 0$, which suggests the existence of a dimensionless parameter $x = Q^2/2M\nu$, known as the Bjorken scaling variable. Instead of being dependent on both ν and Q^2 , the structure functions now become dependent only on x . The phenomenon known as scaling was predicted by Bjorken [10], and is in clear contrast with the behavior in the elastic and resonance regions. Feynman's quark-parton model [11] offers a clearer explanation; the fact that structure functions are not dependent (or, only weakly dependent) on momentum transfer implies that the nucleon contains point-like objects, which Feynman called partons. These partons would later be identified as the quarks and gluons of Quantum Chromodynamics.

CHAPTER 3

Theoretical Tools and Motivation

Now that the basics of inclusive electron scattering have been covered in the previous chapter, the formalism of spin physics can be discussed.

3.1 Virtual Photoabsorption Cross Sections

We saw in the previous chapter that the inclusive electron scattering cross section can be described in terms of the four structure functions, F_1 , F_2 , g_1 and g_2 . An equivalent method to parameterize the inclusive cross section is to use four virtual photoabsorption cross sections $(\sigma_L, \sigma_T, \sigma_{LT}, \sigma_{TT})$ [12, 13]:

$$\frac{d^2\sigma}{d\Omega dE'} = \Gamma \left[\sigma_T + \epsilon\sigma_L - hP_x\sqrt{2\epsilon(1-\epsilon)}\sigma_{LT} - hP_z\sqrt{1-\epsilon^2}\sigma_{TT} \right], \quad (3.1)$$

where $h = \pm 1$ is the helicity of the incoming longitudinally polarized electron, and the longitudinal (transverse) polarization of the target with respect to the virtual

photon momentum \vec{q} , is given by P_z (P_x). The ratio of longitudinal to transverse polarization is given by

$$\epsilon = \left[1 + 2 \left(1 + \frac{\nu^2}{Q^2} \right) \tan^2 \frac{\theta}{2} \right]^{-1}, \quad (3.2)$$

and the virtual photon flux factor Γ is given by

$$\Gamma = \frac{\alpha}{2\pi^2 Q^2} \frac{E'}{E} \frac{K}{1 - \epsilon}. \quad (3.3)$$

The virtual photon flux factor is dependent on the choice of virtual photon flux K , which is convention dependent. The three most common conventions are listed below, defined in terms of the kinematic quantities ν and Q^2 .

$$\begin{aligned} K_A &= \nu \\ K_G &= |\vec{q}| = \sqrt{\nu^2 + Q^2} \\ K_H &= \frac{W^2 - M^2}{2M} = \nu(1 - x) \end{aligned} \quad (3.4)$$

The first convention, K_A , equates the virtual photon flux factor to the photon energy ν [14]. The second convention, known as Gilman's convention [15], associates K with the momentum of the photon in the lab frame. The final convention, K_H , is known as Hand's convention [16] and describes the flux as the equivalent photon energy, or the energy required for the same reaction from a real photon. It is worth noting that at $Q^2 = 0$, all three conventions reduce to the real photon scattering energy ν . In the DIS region, all three conventions give similar results, but at intermediate Q^2 , K is strongly dependent on the chosen convention.

The four partial cross sections in Eqn. 3.1 are functions of ν and Q^2 . They

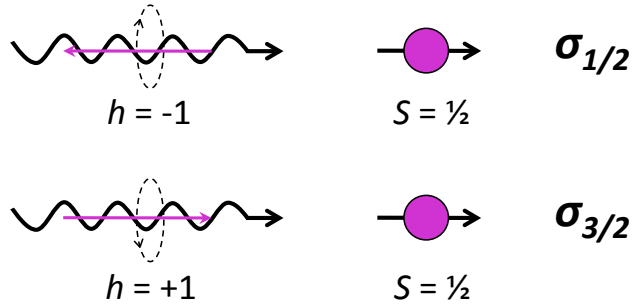


FIG. 3.1: Helicity projections for the virtual photoabsorption cross sections $\sigma_{\frac{1}{2}}$ and $\sigma_{\frac{3}{2}}$. The quantities h and S represent the virtual photon helicity and target spin projections, respectively.

consist of the absorption cross section for longitudinal (σ_L) and transverse (σ_T) virtual photons as well as two interference terms, the longitudinal-transverse (σ_{LT}) and transverse-transverse (σ_{TT}) cross sections. For the unpolarized case at $Q^2 = 0$, σ_L vanishes and the total photoabsorption cross section is given by σ_T . The other two cross sections, σ_{LT} and σ_{TT} can be measured using double-polarization experiments.

We can introduce two additional helicity-dependent photoabsorption cross sections, $\sigma_{\frac{1}{2}}$ and $\sigma_{\frac{3}{2}}$, that can be written as functions of the transverse spin-averaged and transverse-transverse spin-dependent partial cross sections,

$$\begin{aligned}\sigma_T &= \frac{1}{2} \left(\sigma_{\frac{1}{2}} + \sigma_{\frac{3}{2}} \right) \\ \sigma_{TT} &= \frac{1}{2} \left(\sigma_{\frac{1}{2}} - \sigma_{\frac{3}{2}} \right).\end{aligned}\tag{3.5}$$

The helicity projections for a spin 1/2 particle are illustrated in Fig. 3.1. The

standard structure functions are also related to the virtual photon cross sections,

$$\begin{aligned}
\sigma_L &= \frac{4\pi^2\alpha}{K} \left[\frac{F_2}{\nu} (1 + \gamma^2) - \frac{F_1}{M} \right] \\
\sigma_T &= \frac{4\pi^2\alpha}{MK} F_1 \\
\sigma_{LT} &= \frac{4\pi^2\alpha}{K} \gamma [g_1 + g_2] \\
\sigma_{TT} &= \frac{4\pi^2\alpha}{MK} [g_1 - \gamma^2 g_2],
\end{aligned} \tag{3.6}$$

where $\gamma = \frac{Q}{\nu}$.

3.2 The Quark-Parton Model

Discussed briefly in Sec. 2.3.4, the Quark-Parton model, which was put forth by Feynman in 1969 [11] represents one way to interpret the structure functions. This model describes the nucleon as being composed of point-like particles, called partons, which were later identified as quarks and gluons. We can define the Bjorken limit as

$$\begin{aligned}
Q^2 &\rightarrow \infty \\
\nu &\rightarrow \infty \\
x &= \frac{Q^2}{2M\nu} \text{(finite).}
\end{aligned} \tag{3.7}$$

In this limit, the partons are considered to be semi-free and point-like; an interaction of the electron with one parton does not affect the other partons in the nucleon. In this limit, the structure functions can be written in terms of quark

distribution functions [17],

$$\begin{aligned}
F_1(x) &= \frac{1}{2} \sum_f z_f^2 [q_f(x) + \bar{q}_f(x)] \\
F_2(x) &= 2x F_1(x) \\
g_1(x) &= \frac{1}{2} \sum_f z_f^2 [q_f(x) - \bar{q}_f(x)] \\
g_2(x) &= 0,
\end{aligned} \tag{3.8}$$

where $q_f(x)$ ($\bar{q}_f(x)$) are the quark (anti-quark) distributions (with quark flavor f) and z_f is the quark charge. The second line of Eqn. 3.8 is known as the Callan-Gross relation [18]. In the context of this model, $g_2(x)$ does not contribute to the nucleon structure. This is where we begin to see the cracks in this so-called “naïve” quark model. In order for $g_2(x)$ to be non-zero, transverse momentum of the partons must be considered, which is neglected in the preceding discussion.

3.3 The g_2 Structure Function

After learning in the previous section that there is no simple interpretation for g_2 in the quark-parton model, the question must be asked: what *is* g_2 ? This structure function can be written in terms of its twist expansion as [19]

$$g_2(x, Q^2) = g_2^{WW}(x, Q^2) + \bar{g}_2(x, Q^2), \tag{3.9}$$

where “twist” is related to the number of quarks and gluons involved in the interaction. The term g_2^{WW} , also known as the Wandzura-Wilczek relation [20], describes

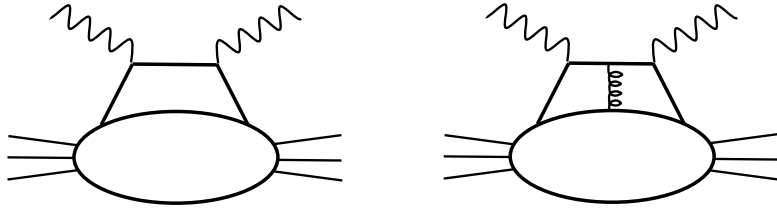


FIG. 3.2: Feynman diagram describing twist-2 effects (on the left) and twist-3 effects (on the right).

the leading twist behavior of g_2 (Fig. 3.2).

$$g_2^{WW}(x, Q^2) = -g_1(x, Q^2) + \int_x^1 \frac{dy}{y} g_1(y, Q^2) \quad (3.10)$$

Since g_2^{WW} is written entirely in terms of g_1 , it also allows us to interpret g_2 in the context of the quark-parton model. The *interesting* part of g_2 is the second term, \bar{g}_2 :

$$\bar{g}_2 = \int_x^1 \frac{\partial}{\partial y} \left[\frac{m_q}{M} h_T(y, Q^2) + \zeta(y, Q^2) \right] \frac{dy}{y}. \quad (3.11)$$

The transversity term, h_T , arises from the quark transverse polarization distribution, but is usually suppressed due to the smallness of the constituent quark mass (m_q). The term ζ is twist-3 and arises from quark-gluon correlations (Fig. 3.2). These higher twist terms are usually suppressed kinematically, but at typical JLab kinematics, we are sensitive to these effects. Higher twist terms can be thought of as involving more than one parton of the nucleon in the scattering process. Instead of probing a single quark, we are beginning to see how quarks and gluons interact in the context of the nucleon. The function g_2 offers a unique sensitivity to these effects, so it becomes an attractive quantity to measure [19].

3.4 Operator Product Expansion

To apply QCD to deep-inelastic scattering and to evaluate calculations outside the perturbative region, we use the Operator Product Expansion (OPE). Introduced by K. Wilson in 1969 [21], the OPE uses describes the moments of g_2 in the context of QCD via sum rules.

To interpret the spin structure functions in terms of the OPE, we first write the hadronic tensor $W_{\mu\nu}$ in terms of the commutator of EM currents, J_μ, J_ν :

$$W_{\mu\nu}(q; p, s) = \frac{1}{2\pi} \int d^4z e^{iq\cdot z} \langle p, s | [J_\mu(z), J_\nu(0)] | p, s \rangle. \quad (3.12)$$

If we take the Fourier transform of Eqn. 3.12 we get the momentum space version of the OPE, as the spatial 4-vector z goes to zero:

$$\lim_{z \rightarrow 0} \int d^4z e^{iq\cdot z} \sigma_a(z) \sigma_b(0) = \sum_k C_{abk}(q) \sigma_k(0), \quad (3.13)$$

and the product of EM currents can now be expanded as a sum of local operators (σ) multiplied by Wilson coefficients (C_{abk}) which are functions of q . The contribution of any operator to the cross section is of the order:

$$X^{-n} \left(\frac{M}{Q} \right)^{\tau-2}. \quad (3.14)$$

Here, $Q = \sqrt{Q^2}$ and $\tau \equiv D - n$, with D , n , and τ the dimensionality, spin, and twist of the operator, respectively. As higher twist terms are suppressed by increasing powers of $\frac{M}{Q}$, the leading twist terms (twist-2) dominate at large values of Q^2 . For small values of Q^2 , higher twist terms become more important.

Furthermore, by using dispersion relations, the OPE can be applied to Eqn. 3.12 to determine an expression for the odd moments of g_1 and g_2 .

$$\int_0^1 x^{n-1} g_1(x, Q^2) dx = \frac{1}{2} a_{n-1}; \text{ for } n = 1, 3, 5, \dots \quad (3.15)$$

$$\int_0^1 x^{n-1} g_2(x, Q^2) dx = \frac{n-1}{2n} (d_{n-1} - a_{n-1}); \text{ for } n = 3, 5, \dots, \quad (3.16)$$

where a_{n-1} and d_{n-1} are matrix elements of quark and gluon operators for twist-2 and twist-3, respectively.

3.5 Chiral Perturbation Theory

QCD is the non-abelian gauge theory of the strong interaction. The matter fields of QCD are the quarks and gluons. Since quarks have not been observed in free, asymptotic states, the value and meaning of the quark masses are dependent on the method by which they are extracted [22]. The complete QCD Lagrangian, for one quark flavor, is [23]:

$$\mathcal{L}_{QCD} = -\frac{1}{4g^2} G_{\mu\nu}^\alpha G_\alpha^{\mu\nu} + \bar{q} i \gamma^\mu D_\mu q - \bar{q} \mathcal{M} q, \quad (3.17)$$

where $G_{\mu\nu}$ represents the gluon field, q is the quark field, g is the coupling constant, and \mathcal{M} is the diagonal quark mass matrix. In the low energy region, it becomes impractical to deal with quarks and gluons directly in QCD. Instead, the relevant degrees of freedom become the composite hadrons. At a scale of 1 GeV, the running

quark masses of the up and down quark are [9]:

$$\begin{aligned}\overline{m}_u &= (4 \pm 2) \text{MeV} \\ \overline{m}_d &= (8 \pm 4) \text{MeV.}\end{aligned}\tag{3.18}$$

These masses are small compared to the hadron mass scale. If we consider the limit where the quark masses vanish, the light quark masses (u, d, s) can then be treated as a perturbation. It should be noted that the heavy quark masses (c, t, b) can be treated as infinitely heavy in this approximation. For massive quarks (or massive fermions in general), the state of the particle is determined by the helicity h , which is defined as the projection of the particle's spin onto its momentum:

$$h = \vec{S} \cdot \vec{p}. \tag{3.19}$$

For a massless fermion, the chirality (or, handedness) is identical to the particle's helicity. The consequence of this is an extra symmetry of the QCD Lagrangian:

$$q_{L,R} = \frac{1}{2}(1 \mp \gamma_5)q. \tag{3.20}$$

The left (q_L) and right (q_R) handed quark fields do not interact with each other. So, in the limit of massless quarks, the theory admits a $SU(3)_L \times SU(3)_R$ symmetry. The existence of a small, but non-zero, quark mass breaks this symmetry, and can be treated as a perturbation.

We can now construct an effective Lagrangian to replace Eqn. 3.17:

$$\mathcal{L}_{QCD} = \mathcal{L}_{QCD}^0 + \mathcal{L}'_{QCD}, \tag{3.21}$$

where \mathcal{L}_{QCD}^0 is the chiral symmetric part of the Lagrangian and $\mathcal{L}'_{QCD} = -\bar{q}\mathcal{M}q$ can be treated as a perturbation. This approach is only valid when the quark mass is small compared to the composite system being considered. At high energies, Chiral Perturbation Theory (χPT) will begin to fail and must be replaced with a different approach.

3.6 Model Predictions

3.6.1 Phenomenological MAID Model

The Unitary Isobar Model (MAID) contains phenomenological fits to world pion photo- and electroproduction data [24]. Resonance contributions are assumed to be of the form of Breit-Wigner functions:

$$\sigma_{\frac{1}{2}(\frac{3}{2})} = \frac{4M}{W_{res}\Gamma_{res}} A_{\frac{1}{2}(\frac{3}{2})} B(\nu, Q^2), \quad (3.22)$$

where $B(\nu, Q^2)$ is the generalization to electroproduction of the Breit-Wigner form, $A_{\frac{1}{2}(\frac{3}{2})}$ are the helicity-dependent amplitudes, M is the nucleon mass, and W_{res} and Γ_{res} are the mass and the width of the resonance, respectively. Non-resonant background contributions and vector meson exchange are also included in the model.

3.6.2 Bosted-Christy Model

The model developed by P. Bosted and M.-E. Christy represents an empirical fit to describe inclusive measurements of inelastic electron-deuteron scattering [25].

This model covers the resonance region in the kinematic range $0 \leq Q^2 \leq 10$ GeV 2 and $1.1 \leq W \leq 3.2$ GeV. The data sets included in the fit are summarized in Table 3.1. The structure of the fit can be described as:

$$\sigma_D^T(W, Q^2) = \sigma_{dip}(W, Q^2) + \int \sigma_N^T(W', (Q^2)') \Phi^2(\vec{k}) d^3\vec{k}, \quad (3.23)$$

where $\sigma_D^T(W, Q^2)$ describes the transverse cross section for the deuteron and the quantity $\sigma_{dip}(W, Q^2)$ represents the parameterization for the dip region between the quasi-elastic peak and the $\Delta(1232)$ resonance. The average nucleon transverse cross section is given by $\sigma_N^T(W, Q^2)$, which is integrated over the Fermi momentum \vec{k} . The agreement between the fit and data is good at the 3-5% level. There are two noticeable deviations at low W and Q^2 , which may indicate that additional parameters are necessary at low Q^2 to adequately describe the photoproduction data. The underlying fit is to an average nucleon. As such, the results can be used in combination with a proton fit to determine predictions for electron-nucleon scattering in the resonance region.

3.7 Sum Rules

3.7.1 Burkhardt-Cottingham Sum Rule

The OPE does not include the $n = 1$ term of the g_2 expression in Eqn. 3.16. In 1970, Burkhardt and Cottingham proposed a sum rule [37]:

$$\Gamma_2(Q^2) = \Gamma_2 = \int_0^1 g_2(x, Q^2) dx = 0, \quad (3.24)$$

Data Set	Q^2_{Min} (GeV 2)	Q^2_{Max} (GeV 2)	# Data Points
Photoproduction (1972) [26–28]	0	0	242
Photoproduction (DAPHNE) [29]	0	0	57
CLAS [30]	0.35	5.9	11725
Early JLab [31]	0.5	4.2	600
JLab E00-116 [32]	3.6	7.5	288
SLAC E133 [33]	2.5	10.0	488
JLab E02-109 [34]	0.02	2.0	1435
JLab E00-002 [35]	0.05	1.5	1445
SLAC E140 [36]	2.5	10.0	48

TABLE 3.1: Summary of the data sets used in the Bosted-Christy fit, with the Q^2 range and number of data points listed. Reproduced from [25].

or, written in terms of the Compton amplitude, $A_2(q^2, \nu)$:

$$\int_{-q^2/2}^{\infty} d\nu \text{Im} [A_2(q^2, \nu)] = 0. \quad (3.25)$$

The lower limit of the integral comes from the definition of the kinematic relations:

$$q^2 \equiv -Q^2 < 0, \quad q \cdot P \equiv \nu \geq \frac{Q^2}{2}. \quad (3.26)$$

The derivation of this sum rule is, as described by R. L. Jaffe, “deceptively simple” [38]. First we must assume that the behavior of the Compton amplitudes, $A_2(q^2, \nu)$, at large ν and fixed (non-zero) q^2 is governed by Regge Theory, which allows for values of angular momentum to be any complex value, instead of being constrained to integer values. One can then argue that all known Regge singularities contributing to this amplitude have an intercept less than zero. Starting with a dispersion relation:

$$A_2(q^2, \nu) = \frac{2}{\pi} \nu \int_{-q^2/2}^{\infty} \frac{d\nu'}{\nu'^2 - \nu^2} \text{Im} [A_2(q^2, \nu')], \quad (3.27)$$

and looking at the convergence at fixed q^2 ,

$$A_2(q^2, \nu) \sim \frac{\beta_c(q^2)}{(\ln \nu)^5} + \sum_i \beta_i^2(q^2) \frac{\nu^{\alpha_i(0)-1}}{\ln \nu}, \quad (3.28)$$

with $\alpha_i(0)$ and $\beta_i(q^2)$ representing the intercept and residue of the Regge pole contribution [39]. If we ignore the $1/(\ln \nu)^5$ term, as $\nu \rightarrow \infty$, this gives us,

$$A_2(q^2, \nu) \sim \nu^{-1-\epsilon}, \quad (3.29)$$

for some $\epsilon < 0$. Now, if we take a look at the large ν behavior of A_2 , taking Eqn. 3.27 at the limit $\nu \rightarrow \infty$ under the ν' integral,

$$A_2(q^2, \nu) \sim \frac{-2}{\pi\nu} \int_{q^2/2}^{\infty} d\nu' \text{Im} [A_2(Q^2, \nu')] , \quad (3.30)$$

which contradicts the assumed behavior in Eqn. 3.25, unless the integral vanishes. Hence, the sum rule must exist! The BC sum rule, which is valid for all values of Q^2 , could be violated due to one of the following two circumstances [19],

1. g_2 is singular enough that the integral $\int_0^1 g_2(x, Q^2) dx$ does not exist.
2. g_2 has a delta function singularity at $x = 0$.

The existing data for the BC sum rule is shown in Fig. 3.3. The bottom plot shows results for the neutron, while the top plot shows the, far fewer, proton results. The open circles represent the value of the sum rule over the measured region of x , and the solid squares include the extrapolation to high and low x . For the neutron, the BC sum rule has been tested over a large range of Q^2 and shows consistency with the expected result of zero, within small uncertainties. The lack of data from the proton leaves this sum rule largely untested. The results from SLAC E155x suggest an inconsistency on the level of 2.75σ , which arises from both a large experimental uncertainty as well as uncertainty associated with the low x extrapolation that is difficult to quantify. In addition, the SLAC point represents data taken over a large range of Q^2 . The results from the RSS experiment show better agreement; the integral over the measured region is negative, but is consistent with zero once the low x extrapolation is included. Precision data from JLab is consistent with the BC sum rule in all cases, which suggests that g_2 is a well behaved function with good convergence. The data from the g_2^p experiment will provide an additional test for

the proton at low Q^2 .

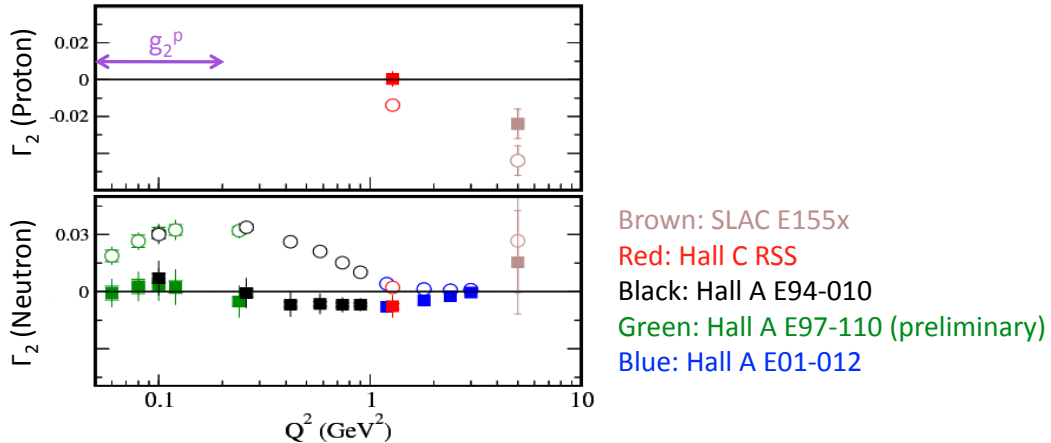


FIG. 3.3: Tests of the BC sum rule. The top plot shows results for the proton while the bottom plot shows results for the neutron. Experiments E97-010 [40], E94-010 [41, 42], E01-012 [43] and RSS [42, 44] are from Jefferson Lab, E155x is from SLAC [45]. The open circles represent the value of the integral over the measured region, while the solid squares include the extrapolation to high and low x . The purple arrow shows the range of Q^2 covered by the g_2^p experiment. Reproduced from [46].

3.7.2 Spin Polarizabilities

The spin-dependent structure functions can be used as a test of QCD using sum rules. The spin polarizability quantities, γ_0 and δ_{LT} , describe a relation between the nucleon structure functions and real or virtual Compton amplitudes [47]. A spin polarizability is analogous to a magnetic polarizability, except it characterizes the nucleon's response to a virtual photon, as opposed to a magnetic field. The Compton amplitudes can be calculated theoretically. If we first consider forward Compton scattering with two virtual, space-like photons, known as doubly-virtual Compton Scattering (VVCS), the absorption of the virtual photon can be related to inclusive electron scattering. The cross section for inclusive scattering contains

four partial cross sections, $\sigma_L, \sigma_T, \sigma_{LT}$ and σ_{TT} , which can be related to the four nucleon structure functions, F_1, F_2, g_1 and g_2 . For the purposes of this document, we are interested in the spin-dependent partial cross sections σ_{LT} and σ_{TT} .

The spin polarizability sum rules can be determined using dispersion relations and the optical theorem [48]. First considering the spin-flip VVCS amplitude, g_{TT} , applying an unsubtracted dispersion relation gives us

$$Re \left[g_{TT}(\nu, Q^2) - g_{TT}^{pole}(\nu, Q^2) \right] = \frac{\nu}{2\pi^2} \mathcal{P} \int_{\nu_0}^{\infty} \frac{K(\nu', Q^2) \sigma_{TT}(\nu', Q^2)}{\nu'^2 - \nu^2} d\nu', \quad (3.31)$$

where g_{TT}^{pole} is the elastic (nucleon pole) contribution, K is a factor that describes the virtual photon flux, and \mathcal{P} denotes the principal value integral. The lower limit of the integral, ν_0 , is the nucleon threshold for pion-production. The definition of the generalized spin polarizability γ_0 comes from the low-energy expansion of Eqn. 3.31:

$$Re \left[g_{TT}(\nu, Q^2) - g_{TT}^{pole}(\nu, Q^2) \right] = \frac{2\alpha}{M^2} I_{TT}(Q^2) \nu + \gamma_0(Q^2) \nu^3 + \mathcal{O}(\nu^5), \quad (3.32)$$

where I_{TT} is the coefficient of the $\mathcal{O}(\nu)$ term of the Compton amplitude. By looking closer at the $\mathcal{O}(\nu^3)$ term, we obtain a sum for the generalized forward spin polarizability in terms of the spin-dependent structure functions:

$$\begin{aligned} \gamma_0(Q^2) &= \frac{1}{2\pi^2} \int_{\nu_0}^{\infty} \frac{K(\nu, Q^2)}{\nu} \frac{\sigma_{TT}(\nu, Q^2)}{\nu^3} d\nu \\ &= \frac{16\alpha M^2}{Q^6} \int_0^{x_0} x^2 \left[g_1(x, Q^2) + \frac{4M^2}{Q^2} x^2 g_2(x, Q^2) \right] dx \end{aligned} \quad (3.33)$$

Now, if we consider the longitudinal-transverse interference amplitude, g_{LT} ,

again using dispersion relations, gives

$$\text{Re} \left[g_{LT}(\nu, Q^2) - g_{LT}^{pole}(\nu, Q^2) \right] = \frac{2\alpha}{M^2} Q I_{LT}(Q^2) + Q \delta_{LT}(Q^2) \nu^2 + \mathcal{O}(\nu^4), \quad (3.34)$$

where g_{LT}^{pole} is the elastic contribution. Looking closer at the $\mathcal{O}(\nu^2)$ term gives us an expression for the generalized longitudinal-transverse spin polarizability in terms of g_1 and g_2 ,

$$\begin{aligned} \delta_{LT}(Q^2) &= \frac{1}{2\pi^2} \int_{\nu_0}^{\infty} \frac{K(\nu, Q^2)}{\nu} \frac{\sigma_{LT}(\nu, Q^2)}{Q\nu^2} d\nu \\ &= \frac{16\alpha M^2}{Q^6} \int_0^{x_0} x^2 [g_1(x, Q^2) + g_2(x, Q^2)] dx. \end{aligned} \quad (3.35)$$

As these polarizabilities are calculable using χPT , the spin polarizabilities represent a benchmark test of this theory. Since there is little data available for the proton, the neutron results for these quantities will be discussed here. The difficulty in χPT calculations is how to include the resonance contributions, particularly the Delta resonance. Fig. 3.4 shows the χPT prediction for the neutron compared with available data. The plot on the left side shows the results for γ_0 . The red and blue data points are the results from JLab experiments E97-110 and E94-010 [42]. The blue dotted line shows the χPT prediction, and the light blue band shows the same prediction, but explicitly including the Delta-resonance and vector meson contributions. Including these contributions changes the shape of the prediction considerably, indicating that the resonance contribution is significant. At low Q^2 , the prediction (with explicit resonance contributions) shows agreement with the experimental results, but the discrepancy seems larger as we move to higher Q^2 .

The plot on the right shows the neutron results for the longitudinal-transverse spin polarizability, δ_{LT} . This quantity is seen as a better testing ground for χPT

predictions as it is insensitive to the Delta resonance. As in the previous plot, the red and blue data points are results from JLab experiments. The blue dotted line shows the χPT prediction and the solid blue band shows the same prediction with explicit Δ -resonance and vector meson contributions. As expected, including the Δ -resonance has no effect on the shape of the distribution, but it does shift the central value, due to spreading in the Δ form-factor. However, the current prediction does not accurately represent the experimental results.

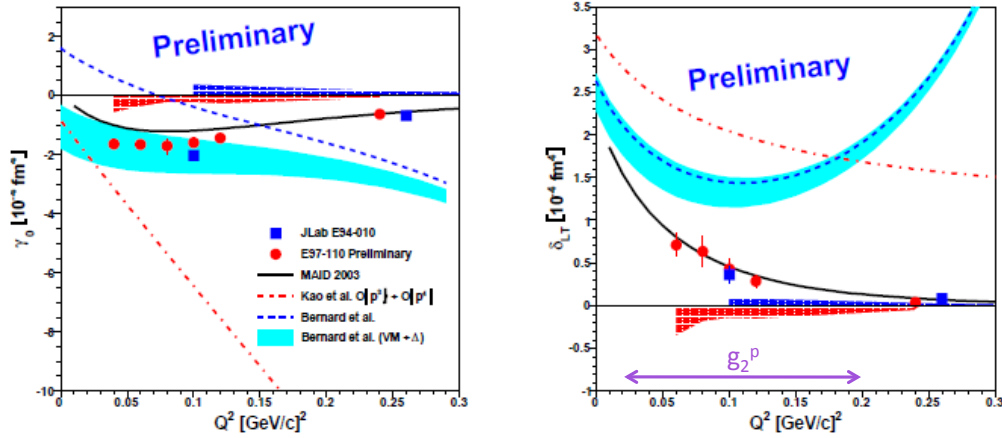


FIG. 3.4: On the left are the current neutron results for the generalized spin polarizability γ_0 , and on the right are neutron results for δ_{LT} . The blue squares represent published data from E94-010 [41], while the red circles are preliminary data from E97-110. The blue dotted line is the $RB\chi PT$ prediction [49], and the light blue band is the same prediction, but explicitly including Δ -resonance and vector meson contributions. The red dotted line is the $HB\chi PT$ prediction [50]. The black curve is the MAID model [24]. The purple arrow shows the range of Q^2 covered by the g_2^p experiment. Reproduced from [51].

3.8 Additional Motivation

These data will provide additional insight to the theoretical understanding of hyperfine splitting of the hydrogen atom, specifically by constraining the correction

due to proton structure. Furthermore, a precision measurement of g_2^p will provide insight to discrepancies of measurements of the proton charge radius.

3.8.1 Proton Hyperfine Splitting

The hyperfine splitting of hydrogen has been measured experimentally to very high accuracy [52]:

$$E_{hfs} = 1420.4057517667(9)\text{MHz}, \quad (3.36)$$

however calculations of this quantity are only accurate to a few parts per million [53]. The splitting is defined in terms of the Fermi energy E_f

$$\Delta E = (1 + \delta) E_f, \quad (3.37)$$

with

$$\delta = 1 + (\delta_{QED} + \delta_R + \delta_{small}) + \Delta_S. \quad (3.38)$$

The term δ_R accounts for recoil effects, δ_{QED} is known to high accuracy and represents the QED radiative correction, and δ_{small} corrects for hadronic and muonic vacuum polarizations. The final term, Δ_S , has the largest uncertainty and represents a correction for proton structure:

$$\Delta_S = \Delta_Z + \Delta_{pol}. \quad (3.39)$$

The term Δ_Z is given as:

$$\Delta_Z = -2\alpha m_e r_z (1 + \delta_z^{rad}), \quad (3.40)$$

where δ_z^{rad} represents radiative corrections and r_z is the Zemach radius, which is dependent on both electric (G_E) and magnetic (G_M) form factors [54]:

$$r_z = -\frac{4}{\pi} \int_0^\infty \frac{dQ}{Q^2} \left[G_E(Q^2) \frac{G_M(Q^2)}{1 + \kappa_p} - 1 \right]. \quad (3.41)$$

The second term in Eqn. 3.39, Δ_{pol} contains contributions from the spin structure functions,

$$\Delta_{pol} = \frac{\alpha m_e}{\pi g_p m_p} (\Delta_1 + \Delta_2), \quad (3.42)$$

where Δ_1 involves contributions where the proton is excited and can be written in terms of the Pauli form factor and g_1 . The correction Δ_2 is defined in terms of the g_2 structure function:

$$\Delta_2 = -24m_p^2 \int_0^\infty \frac{dQ^2}{Q^4} B_2(Q^2), \quad (3.43)$$

where,

$$B_2(Q^2) = \int_0^{x_{th}} dx \beta_2(\tau) g_2(x, Q^2), \quad (3.44)$$

and,

$$\beta_2(\tau) = 1 + 2\tau - 2\sqrt{\tau(\tau + 1)}, \quad (3.45)$$

with $\tau = \nu^2/Q^2$, and the upper integration limit x_{th} represents pion production threshold.

The correction Δ_2 is dominated by the low- Q^2 region as shown in Fig. 3.5. To calculate the size of this correction, theorists must currently rely heavily on models, as there is little data available for the proton in this region. The Wandzura-Wilczek relation [20] in Eqn. 3.10 may be a reasonable prediction at high- Q^2 , but other measurements suggest that this approximation may be insufficient at low- Q^2 . Results from E94-010 [55] are shown in Fig. 3.6, and demonstrate the deviation of g_2 from the leading-twist contribution g_2^{WW} . The g_2^p experiment will provide additional data for the proton in the low- Q^2 region. As the total uncertainty for this experiment is projected to be less than 10%, the published error on Δ_2 can be expected to improve by an order of magnitude [56].

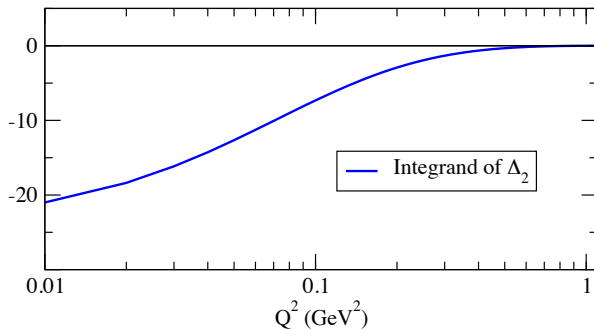


FIG. 3.5: The integrand of Δ_2 (Eqn. 3.43), which is dominated by the low Q^2 region. Reproduced from [56].

3.8.2 Proton Charge Radius

The RMS charge radius of the proton, r_p , has been determined from electron-proton scattering results with an accuracy of $\sim 2\%$ [57, 58]. The most accurate measurement of r_p comes from a compilation of CODATA results [59]. This result, accurate to 1%, is based on atomic hydrogen spectroscopy [60–63] and bound-state QED calculations [64, 65]. An alternate method to improve the accuracy of this mea-

r_p (fm)	Method
0.84184 ± 0.00067	Lamb Shift in Muonic Hydrogen
0.897 ± 0.018	World Analysis of eP Scattering
0.8768 ± 0.0069	CODATA World Average

TABLE 3.2: Current measurements of the proton charge radius.

surement is through pulsed laser spectroscopy on muonic hydrogen, which consists of a proton orbited by a negative muon. Compared to ordinary atomic hydrogen, the radius is much smaller than the Bohr radius. As a consequence, the difference between the $2S_{\frac{1}{2}}$ and $2P_{\frac{1}{2}}$ states, known as the Lamb shift [66], is affected by as much as 2%.

The current results for r_p are summarized in Table 3.2. The value of r_p from CODATA differs from the muonic hydrogen results by $\sim 5\sigma$. This discrepancy suggests that either the Rydberg constant must be shifted by as much as $-110 \text{ kHz}/c$, a 4.9σ deviation, or the calculated QED effects in atomic or muonic hydrogen are not satisfactory [67].

The main theoretical uncertainties in spectroscopy measurements of r_p arise from the proton polarizability and differences in the Zemach radius. As discussed above, the polarizabilities represent integrals of g_1 and g_2 , weighted by $1/Q^4$. The Zemach radius is defined as an integral of the form factors G_E and G_M , weighted by $1/Q^2$. These quantities are dominated by the low- Q^2 kinematic region of the g_2^p experiment. While these results will contribute to constraining the uncertainty in eP measurements of r_p , the proton structure correction to hyperfine splitting will only have a slight effect on the extracted proton radius, as it is small compared to the proton structure correction of the $2S$ energy level [68].

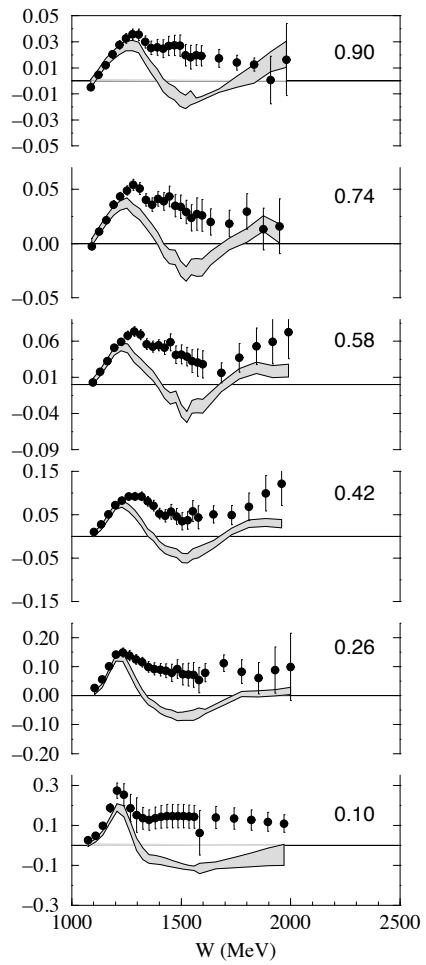


FIG. 3.6: Results from E94-010 for ${}^3\text{He}$ g_2 . The circles represent the total value of g_2 compared to the band, which is the leading-twist contribution, g_2^{WW} . The constant Q^2 value is given in each panel in GeV^2 . Reproduced from [56].

CHAPTER 4

The Experiment

4.1 Overview

Experiment E08-027, the g_2^p Experiment, took place in Hall A from March to May of 2012. Data were taken with a longitudinally polarized electron beam with energies of 1.2, 1.7, 2.2, and 3.3 GeV, using an average beam current of \sim 50-100 nA. An NH_3 target was polarized in 2.5 and 5 T magnetic fields, in both longitudinal and transverse configurations. Scattered electrons with $\theta = 5.7^\circ$ were detected in singles mode in the High Resolution Spectrometers (HRS).

E_{beam} (GeV)	B_{target} (T)	B_{target} Config.
2.2	2.5	Transverse
1.7	2.5	Transverse
1.2	2.5	Transverse
2.2	5.0	Longitudinal
2.2	5.0	Transverse
3.3	5.0	Transverse

TABLE 4.1: Beam energy and target configurations.

Table 4.1 gives a summary of the beam energy and target configurations used throughout the experiment. The kinematic range covers $0.02 \leq Q^2 \leq 0.2$ GeV 2 , in the resonance region ($W < 2$), shown in Fig. 4.1.

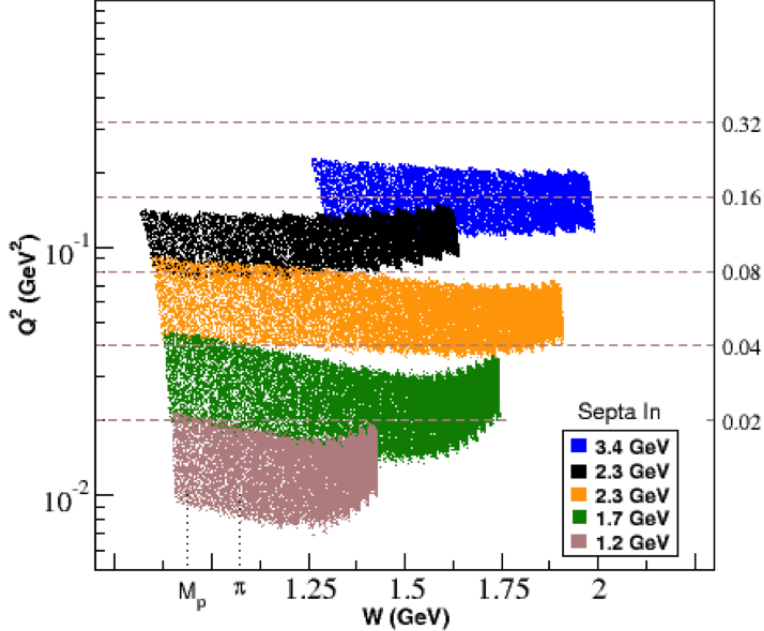


FIG. 4.1: Kinematic coverage for the g_2^p experiment.

For this analysis, the data at $E_{beam} = 2.2$ GeV, $B_{target} = 5$ T, both the longitudinal and transverse configurations were included. During the run period, there were problems with the RHRS septum magnet, which made optics studies more complicated. As the RHRS optics analysis is still being finalized, only LHRs runs were included in this analysis. This chapter will describe details of the experimental setup in Hall A.

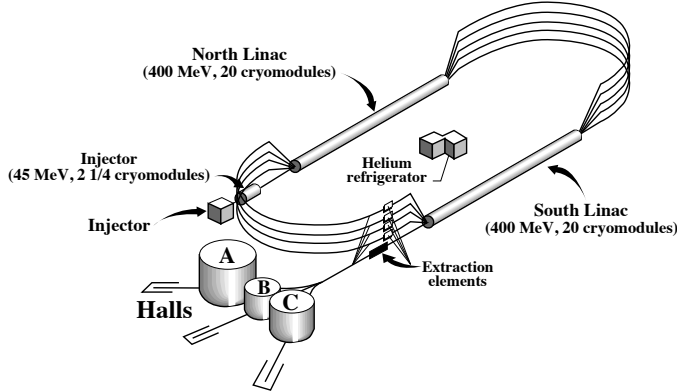


FIG. 4.2: The Jefferson Lab electron accelerator setup.

4.2 The Electron Accelerator

The Continuous Electron Beam Accelerator Facility (CEBAF) at Jefferson Lab was designed to deliver a highly polarized beam simultaneously to the 3 experimental halls, A, B and C [69]. The recent upgrade, an additional experimental hall (D) was added and the maximum beam energy was increased from 6 GeV to 12 GeV. The accelerator is made up of a polarized source, an injector, two linacs, two re-circulation arcs, and elements to extract the beam and send it into the experimental halls. After the polarized electrons are produced, they are extracted by applying a voltage of -100 kV to the photo-cathode. Once the electrons enter the injector they are accelerated up to 45 MeV before reaching the North Linac. Each Linac is comprised of 20 superconducting cryomodules with an accelerating gradient of ~ 7 MeV/m. When the electrons reach the end of the North Linac, a series of bending magnets are used to deflect the beam 180° towards the South Linac. The beam can be re-circulated up to five times to achieve a maximum beam energy of ~ 6 GeV. After each pass an RF separator can be utilized to extract the beam into any of the 3 experimental halls. The maximum achievable beam current is $200 \mu\text{A}$ CW, which

can be arbitrarily split between 3 interleaved 499 MHz bunch trains, one for each hall. Each hall can also receive different beam currents; Halls A and C typically run at currents of $\sim 100 \mu\text{A}$, while CLAS can require currents as low as $\sim 1 \text{nA}$ in Hall B. For this experiment, lower currents (50-100 nA) were used in Hall A to minimize depolarization effects on the target, which will be discussed later.

4.2.1 Polarized Electron Beam

Polarized electrons are produced by circularly polarized photons incident on a gallium arsenide (GaAs) photocathode [70]. Electrons in the GaAs are excited from the valence band to the conduction band by the photons.

The structure of the GaAs cathode crystal consists of a $\text{P}_{3/2}$ valence band and a $\text{S}_{1/2}$ conduction band. The crystal is constructed using several layers of GaAs doped with varying levels of phosphorus. The phosphorus doping creates a “strain” in the GaAs, which subsequently breaks the degeneracy of the valence band. Electrons are excited from the $m = \pm 3/2$ band to the $m = \pm 1/2$ band, where they can escape. Right-handed circularly polarized light excites electrons into the $m = +1/2$ state of the conduction band, while left-handed circularly polarized light excites electrons into the $m = -1/2$ state, as seen in Fig. 4.3. The electrons are pulled from the conduction band and into the accelerator with a bias voltage of -100kV. The polarization angle of the electrons can be set with a Wien filter. The sign of the beam polarization can be flipped with the insertable half-wave plate (IHW), which flips the sign of the circularly polarized light incident on the photocathode.

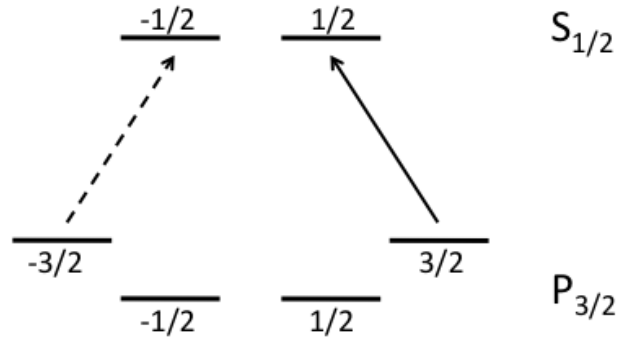


FIG. 4.3: Structure of GaAs crystal. Electrons are excited by circularly polarized light from the $m = \pm 3/2$ state in the valence band to the $m = \pm 1/2$ state in the conduction band.

4.3 Hall A Beamlne

The g_2^p experiment required a large-scale installation in Hall A. A top view of the beamline can be seen in Fig. 4.4. Details of each subsystem will be discussed in the following sections.

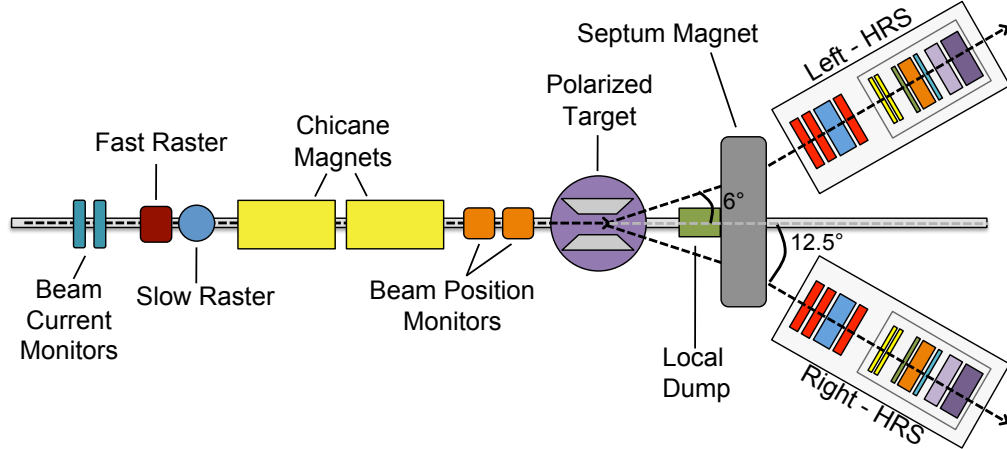


FIG. 4.4: Diagram of the beamline in Hall A

4.3.1 Beam Position

Beam position monitors (BPMs) are located at 7.524 m and 1.286 m upstream of the target and are used to provide a non-invasive measurement of the position and direction of the beam at the location of the target [69]. Comprised of four antennae situated at 90 degrees to one another, they are positioned perpendicular to the beam to provide a high resolution measurement of the beam position. The signal produced by the beam passing through the BPM is inversely proportional to the distance from the beam. Calibration of the BPMs is done using two wire scanners called harps, located adjacent to the BPMs. The harp consists of 3 wires, oriented vertically, and at $\pm 45^\circ$. Harp measurements are invasive; the wires are scanned through the beam and the current in the wires is measured.

4.3.2 Beam Current

Two beam current monitors (BCMs) are used to get an accurate measurement of the beam current. Located 25m upstream from the target, the BCMs are stainless-steel cylindrical high-Q (~ 3000) resonant cavities tuned to the frequency of the beam (1.497 GHz) [69]. The output voltage levels are proportional to the beam current. Standard BCMs have a linearity good to 0.2% up to $180 \mu\text{A}$ and down to $1 \mu\text{A}$. For this experiment, low beam currents (50-100 nA) were used to minimize radiation damage and depolarization of the target. New BCM readout systems were installed that were designed to work with these low currents. A tungsten calorimeter [71] was used to calibrate the BCM for currents less than $3 \mu\text{A}$. The calorimeter is used to determine the average beam current by measuring the temperature change over time in a metal slug that has been exposed to the electron beam.

4.3.3 Rasters

In addition to using low beam currents, a raster system is used to minimize heating of the target. The existing Hall A fast raster was used in combination with a newly installed slow raster, located upstream of the target. Located 23 m upstream of the target, the fast raster is made up of two dipole magnets; one vertical and one horizontal. The beam position is moved with a time-varying magnetic field with a triangular waveform, allowing for a uniform intensity distribution of beam on the target.

The electronic design of the fast raster [8] utilizes an “H-bridge”; a pair of switches that open and close at a rapid rate of 25 kHz. When one switch is closed, the current is driven by HV supplies and rises exponentially:

$$I(t) = \frac{\varepsilon}{R} \left(1 - e^{-\frac{t}{\tau}}\right) \quad (4.1)$$

where the time and voltage are t and ε , respectively and $\tau = \frac{L}{R}$ is the time constant with inductance L and resistance R .

The slow raster is necessary to evenly distribute the heating and ionizing effect on the target. By linearly scanning the beam, increases in the target temperature are minimized [72]. The fast raster generates a 4 mm x 4 mm square pattern while the slow raster can increase this size up to 2.5 cm x 2.5 cm. With this size, variations in the density due to heating are limited to a few percent at a beam current of 100 nA [56]. In Fig. 4.5 sample raster patterns can be seen. A larger beam pipe is needed after the slow raster to account for the large beam size.

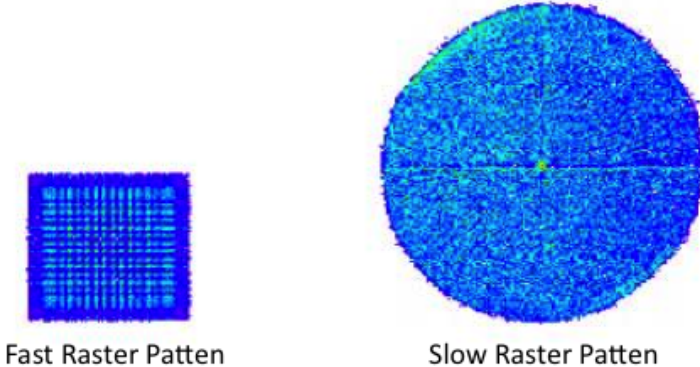


FIG. 4.5: An example of the raster patterns from the fast and slow raster. The fast raster pattern is 4 mm x 4 mm, while the slow raster pattern can be as large as 2.5 cm in diameter.

4.3.4 Chicane Magnets

The target polarization for the majority of the experiment was perpendicular to the beam axis, resulting in a significant deflection of the beam for low energy electrons. To combat this, a pair of chicane magnets (dipole magnets) was utilized [56]. The first chicane, located 10 m upstream of the target, gives the beam a kick out of the horizontal plane. The second chicane, located 4 m upstream of the target, bends the beam back onto the target with the necessary angle to compensate for the 5 T target magnetic field, as seen in Table 4.2. BPMs were placed before and after the chicane to ensure proper beam transport. A diagram of the beamline setup with the chicanes is shown in Fig. 4.6.

4.3.5 Beam Energy Measurement

The beam energy is measured by the Arc method [69], which measures the deflection of the beam in the arc section of the beamline while the beam is tuned in

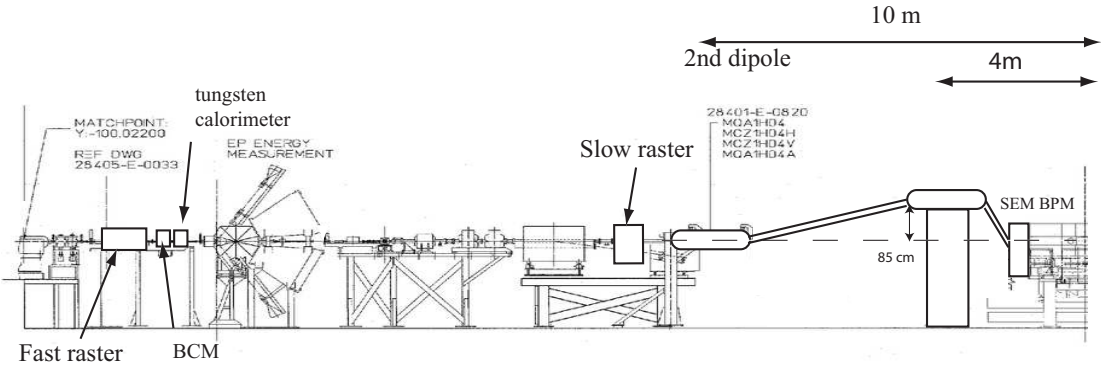


FIG. 4.6: A schematic of the beamline including the location of the chicane magnets. The second chicane is mounted on a hydraulic stand to accommodate the range of deflection angles (Table 4.2). Reproduced from [56].

Beam Energy (GeV)	Deflection Angle (deg)
1.1	11.7
1.7	7.6
2.2	5.9
3.3	3.9

TABLE 4.2: Deflection angles due to the 5 T target magnetic field for each energy setting used in the experiment.

dispersive mode. The momentum of the beam, p , can then be related to the integral of the magnetic field \vec{B} of the eight dipoles and the net bend angle through the arc section, θ , as:

$$p = k \frac{\int \vec{B} \cdot d\vec{l}}{\theta} \quad (4.2)$$

where $k = 0.299792 \text{ GeV rad T}^{-1} \text{ m}^{-1}/c$. This method relies on two simultaneous measurements; the bend of the arc, which is based on a series of wire scanners, and the magnetic field integral of the eight dipoles in the arc.

4.3.6 Beam Polarization

Knowledge of the beam polarization is important in determining the physics asymmetry. Although Hall A has two independent methods for measuring beam polarimetry, for this experiment we used only the Møller polarimeter [69]. The principle of Møller scattering is the scattering of polarized electrons from a magnetized foil via the reaction $\vec{e}^- + \vec{e}^- \rightarrow e^- + e^-$. In Hall A, the target for the Møller polarimeter is a ferromagnetic foil, magnetized in a field of about 24 mT along its plane. The cross section of this reaction is dependent on the polarization of the beam and the foil target:

$$\sigma \propto \left[1 + \sum_{i=X,Y,Z} (A_{ii} P_i^{target} P_i^{beam}) \right] \quad (4.3)$$

where X, Y and Z define the projections of the polarizations. Here we will say the beam travels in the Z direction and the electron scattering occurs in the ZX plane. The analyzing power (A) is dependent on the scattering angle in the center-of-mass frame (θ_{CM}):

$$A_{ZZ} = -\frac{\sin^2 \theta_{CM} (7 + \cos^2 \theta_{CM})}{(3 + \cos^2 \theta_{CM})^2} \quad (4.4)$$

$$A_{XX} = -A_{YY} = -\frac{\sin^4 \theta_{CM}}{(3 + \cos^2 \theta_{CM})^2} \quad (4.5)$$

The purpose of the polarimeter is to measure the longitudinal component of the beam polarization, which can be extracted from A_{ZZ} . The maximum value of this quantity, $A_{ZZ} = 7/9$, occurs at $\theta_{CM} = 90^\circ$.

The asymmetry is measured at two different target angles, $\pm \sim 20^\circ$, with the results being averaged. An asymmetry is measured in order to avoid many of

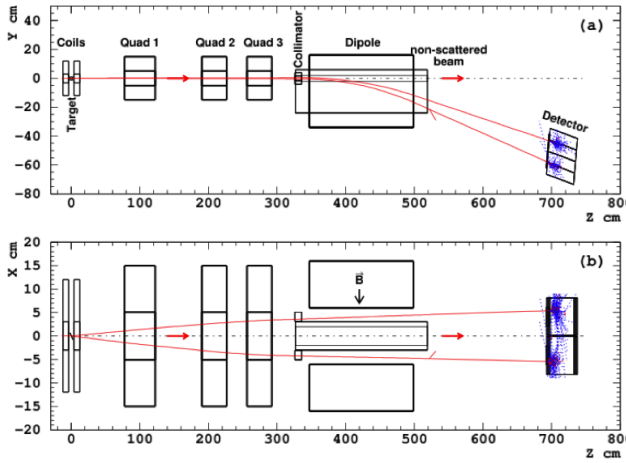


FIG. 4.7: Components of the Møller polarimeter system [69]. The top diagram shows a side view of the system while the bottom diagram give a top view.

the systematic uncertainties that arise in a cross section measurement. The target polarization can have both longitudinal and transverse components, but since the transverse component has opposite signs for these target angles, the transverse components cancel out when the average is taken. It is also possible to minimize the contribution from false asymmetries by taking subsequent measurements with the target polarized in the opposite direction. The scattered electron events are selected by a magnetic spectrometer comprised of 3 quadrupoles and 1 dipole, as can be seen in Fig. 4.7. The non-scattered electron beam passes through a 4 cm hole into a 6 cm thick steel plate. The detector itself is made up of two lead glass calorimeters modules, split into two arms in order to allow for scattered electrons to be detected in coincidence. The beam polarization measurements provided by the Møller polarimeter have a typical statistical uncertainty of about 0.2%. This measurement is invasive and takes a couple hours to complete, so Møller measurements were only taken once per beam energy setting.

4.4 The Polarized NH₃ Target

A polarized ammonia target (NH₃) was used for this experiment. This solid target had been used previously in Hall C, but this experiment marked the first time it had been installed in Hall A. This section will discuss the target setup and the Dynamic Nuclear Polarization process used to polarize the ammonia material.

4.4.1 Dynamic Nuclear Polarization

To start the polarization process, the ammonia material is cooled to a low temperature and placed in a strong magnetic field. The material is polarized according to Boltzmann statistics,

$$P_{TE} = \frac{e^{\frac{\mu B}{kT}} - e^{-\frac{\mu B}{kT}}}{e^{\frac{\mu B}{kT}} + e^{-\frac{\mu B}{kT}}} = \tanh\left(\frac{\mu B}{kT}\right) \quad (4.6)$$

where T is the temperature, B is the magnetic field, k is the Boltzmann constant and μ is the magnetic moment of the particle. (Eqn. 4.6). In the case of an electron/proton, this would result in two states, spin up or spin down, as shown in Fig. 4.8.

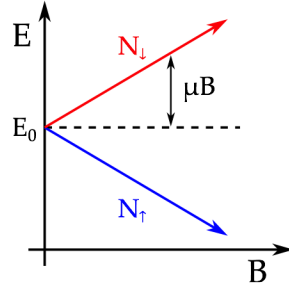


FIG. 4.8: When placed in a strong magnetic field and cooled to a low temperature, particles will align according to Boltzmann statistics. The particles will split into two states; spin up and spin down.

For a temperature of 1 K and a magnetic field of 2.5 T, a configuration used during the experiment, the electron polarization is above 90%, but the proton polarization is only 0.25%. This is a good starting point, but clearly not practical for experimental purposes. To enhance this polarization a technique called Dynamic Nuclear Polarization (DNP) [73–75] is used, which takes advantage of electron-proton spin coupling. The Hamiltonian of this system (Eqn. 4.7) contains the Zeeman energy for the electron and proton as well as a spin-spin interaction term, H_{ss} , which creates mixing, allowing access to previously “forbidden” transitions.

$$H = \vec{\mu}_e \cdot \vec{B} + \vec{\mu}_p \cdot \vec{B} + H_{ss} \quad (4.7)$$

By carefully tuning microwaves to the energy of the band gap between the two states, we can align the spin of the electron and proton.

For example, by tuning the microwaves to a frequency equal to the difference between the electron paramagnetic resonance (EPR) and the proton nuclear magnetic resonance (NMR), the electron and proton will be aligned in the spin up state. Using

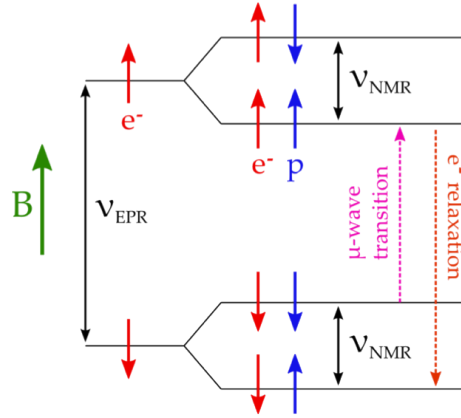


FIG. 4.9: By carefully tuning microwaves to the proper frequency, it is possible to align (or anti-align) the spin of the electron and proton.

a similar method, the proton and electron spins can also be anti-aligned (Eqn. 4.8).

$$\begin{aligned}
 e_{\downarrow}p_{\downarrow} &\rightarrow e_{\uparrow}p_{\uparrow} & \nu_{\mu} = \nu_{EPR} - \nu_{NMR} \\
 e_{\downarrow}p_{\uparrow} &\rightarrow e_{\uparrow}p_{\downarrow} & \nu_{\mu} = \nu_{EPR} + \nu_{NMR}
 \end{aligned} \tag{4.8}$$

The alignment of the electron and proton spin is not permanent; the electron will relax back into the lowest energy state very quickly, on the order of milliseconds. The proton, however, will take on the order of tens of minutes to relax. Since the electron relaxation time is so much quicker, the electrons can be re-used to polarize additional protons. As long as the rate of proton polarization is greater than the rate of proton relaxation, the polarization will grow and can be maintained with microwaves.

4.4.2 Target Setup

An extensive setup [76] is necessary to maintain the low temperature and high magnetic field required by the DNP process (Fig. 4.10). Several months before the

original start date of the experiment, a test was being performed on the target magnet prior to its installation in Hall A when it shorted during a large quench and was damaged beyond repair. Fortunately, an alternate magnet from Hall B was identified as a suitable replacement, and the target group was able to modify it quite successfully. The magnet is a niobium-titanium split-pair magnet. In order for the DNP process to be efficient, the magnetic field must not only be strong, but also very uniform over the volume of the material. The open geometry of the magnet allows the beam to pass through in both the parallel and perpendicular configurations. In addition, the method to rotate between target configurations was also improved. The previous method took several hours, multiple sets of hands, a crane, and required the refrigerator to be isolated and the diffusion pumps powered down. The new design features a custom designed large bore diffusion pump rotary seal, and the transition between configurations can be performed by a single person in approximately 10 minutes. A reservoir of liquid helium maintained at 4 K is used to cool the magnet and maintain its superconductivity. For this experiment, several modifications were made to the design and construction of the refrigerator; improved techniques were used to make the system more leak tight and overall more reliable. This reduced the fridge temperature to 1.1 K with 3 W microwave power.

The target stick can be seen in Fig. 4.11. It was re-designed prior to this experiment to make it more rigid and less cumbersome, making it easier to insert at a repeatable orientation. The stick contains two ammonia samples, a polyethylene disk (used for optics studies) and a carbon disk, empty hole and “dummy” cell used for dilution runs. The dummy cell was identical to the ammonia cells in that it included aluminum foils and an NMR coil, but did not contain any ammonia beads.

The choice of NH_3 as a proton target material was made for several reasons. It is capable of reaching high polarizations: above 90% at the 5 T magnetic field setting.

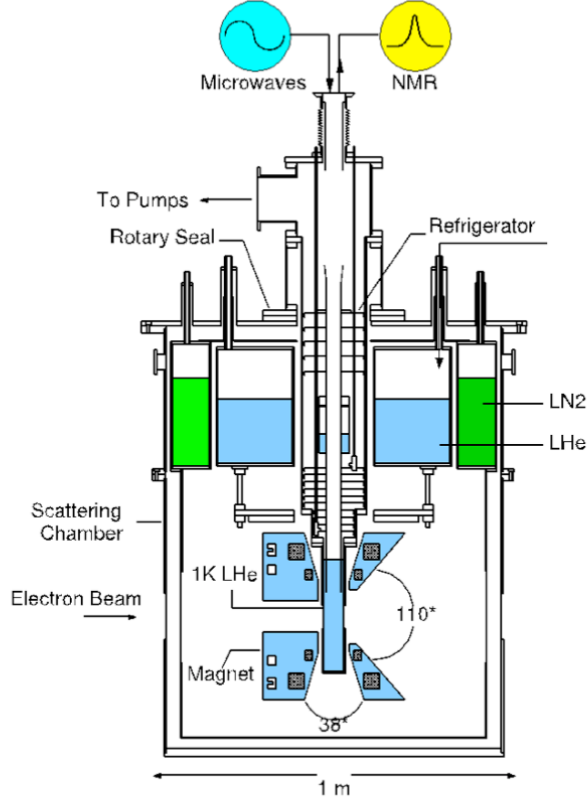


FIG. 4.10: A cross section of the polarized target setup which shows the location of the magnet, NMR coil, and liquid helium and nitrogen reservoirs used to cool the setup.

In addition, it polarizes very quickly, on the order of 30 minutes or less, compared to other materials, such as lithium hydride, which can take on the order of hours. The solid ammonia also holds up very well to radiation damage, which was important to minimize down time during the run period. Prior to bringing the target material to JLab, the ammonia was irradiated at the NIST 10 MeV linear accelerator in order to produce additional radicals in the material. Considered a “warm dose”, meaning above 77 K, this process provides NH₂ radicals, which allow the material to polarize faster when placed in the beam. Later on, when the material is cooled below 4 K and irradiated by the electron beam in Hall A, atomic hydrogen radicals

are produced. The irradiation is what causes the solid ammonia beads to turn a deep purple color, as seen in Fig. 4.11. The number of radicals in the material must be carefully balanced; they are necessary for the DNP process, but they also offer a short cut for proton de-polarization. As the target accumulates radiation, there will be an excess of these radicals, and the DNP process will become inefficient. To counteract this effect, the target is annealed by heating the material. This forces the radicals to recombine, thus allowing the material to again reach high levels of polarization. There is a limit to how many times the material can be annealed, and the maximum achievable polarization will decrease with each anneal. At some point, the build up of radicals will be too large and the material will have to be replaced.

Microwaves are necessary to drive the spin transitions. They are provided via an Extended Interaction Oscillator (EIO) tube and carried via waveguides to a horn positioned near the ammonia cup. As radiation damage accumulates, the optimal frequency for the microwaves will change, so the frequency must be constantly tweaked throughout the run period. To measure the proton polarization, an nuclear magnetic resonance (NMR) system is used. An LCR circuit is constructed with the capacitance chosen such that the resonance frequency of the circuit is equal to the Larmor frequency of the proton. The power lost or gained in the circuit can be observed versus frequency using a Q-meter, which measures the quality factor of a given circuit. The inductor of the circuit is imbedded in the target material, and an RF generator sweeps through a range of frequencies which includes the resonance of the circuit. More details of the NMR signal analysis will be discussed in Sec. 5.7.



FIG. 4.11: The end of target insert containing, from left to right, a carbon disk, a “dummy” cell, and two ammonia cells, which have aluminum foil caps. The full insert is roughly 1.5 m long, and the ammonia cells have a diameter of 2.5 cm.

4.5 High Resolution Spectrometers

Hall A contains two identical High Resolution Spectrometers (HRS), one on each side of the beam line. From here on, they will be referred to as the Left HRS (LHRS) and Right HRS (RHRS). The purpose of the HRS is to select scattered electrons in a small range of momentum and scattering angle and transport them to the detector stack. Each spectrometer contains 3 quadrupole and 1 dipole magnet in a QQDQ configuration (Fig. 4.12). The 3 superconducting quadrupoles (Q1, Q2 and Q3) provide focusing; Q1 focuses in the vertical plane while Q2 and Q3 focus in the transverse plane. The superconducting dipole magnet has a vertical bend of 45° , resulting in a momentum resolution on the 10^{-4} level. A summary of the other characteristics of the left and right HRS can be seen in Table 4.3.

4.6 Detector Stack

The detector packages for each of the HRSs contain a series of detectors to provide tracking and particle identification information. A pair of vertical drift chambers provide the particle trajectory for use in target reconstruction. When coupled with the dipole, they also provide the momentum resolution. Two planes of

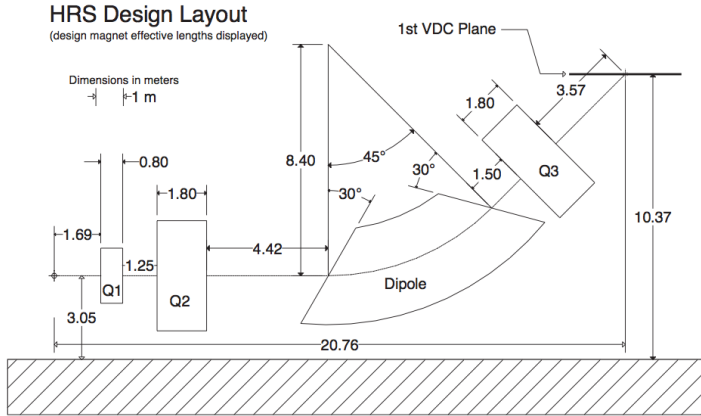


FIG. 4.12: HRS diagram. Reproduced from [69].

scintillator paddles, located ~ 2 m apart make up the trigger for the data acquisition system. Sandwiched in between the scintillator planes is a Cherenkov threshold detector used for particle identification. Finally, there are two layers of lead glass that also provide particle identification information, particularly pion rejection. The details of these detectors will be discussed in this section.

4.6.1 Vertical Drift Chambers

The vertical drift chambers (VDC) are comprised of 4 total wire chambers in a UV configuration [77]. The U and V planes are oriented orthogonal to one another and lie in the horizontal plane of the laboratory, at a 45° angle to the dispersive and non-dispersive directions. Each plane contains 368 sense wires with a spacing of 4.24 mm, and the spacing between the upper and lower UV planes is 335 mm.

The VDCs are filled with a 62/38 gas mixture of argon and ethane. The argon functions as the ionizing medium while the ethane absorbs the photons produced from ionization. Charged particles which enter the VDCs collide with the

Bending angle	45°
Optical length	23.4 m
Momentum range	0.3-4.0 GeV/c
Momentum acceptance	$-4.5\% < \delta p/p < +4.5\%$
Momentum resolution	1×10^{-4}
Dispersion at the focus (D)	12.4 m
Radial linear magnification (M)	-2.5
D/M	5.0
Angular range LHRs	12.5° – 150°
Angular range RHRs	12.5° – 130°
Angular acceptance horizontal	±30 mrad
Angular acceptance vertical	±60 mrad
Angular resolution horizontal	0.5 mrad
Angular resolution vertical	1.0 mrad
Solid angle at $\delta p/p = 0, y_0 = 0$	6 msr
Transverse length acceptance	±5 cm
Transverse position resolution	1 mm

TABLE 4.3: Characteristics of the HRS. Reproduced from [69].

gas molecules creating electron-ion pairs. The VDC electric field is shaped by gold-plated Mylar planes, held at -4 kV. Ionized electrons drift along the radial electric field lines, rapidly accelerating towards the wires when close. This acceleration can cause many secondary electrons to be produced. The resulting avalanche of electrons produces a detectable signal on the wire. Electrons that travel across the wires at a angle of 45° will normally produce a cluster of four to six wires per plane. This provides accurate reconstruction of the particle's trajectory. The tracks can be reconstructed using the timing information provided by time-to-digital converters (TDC) which can be used to determine the drift distance between each wire and the track. Using a linear fit of drift distances versus wire position, the cross-over point of the trajectory can be determined.

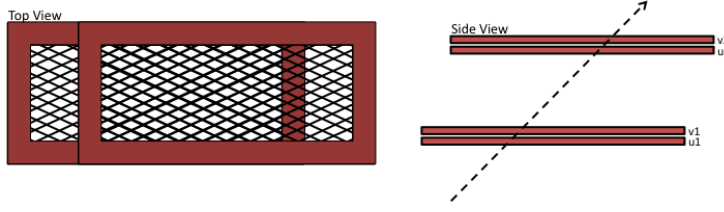


FIG. 4.13: A diagram of the vertical drift chambers.

4.6.2 Scintillator Planes

Two planes of scintillators are used to form the trigger for the data acquisition system (DAQ). The two planes, S1 and S2m, as seen in Fig. 4.14, are separated by a distance of about 2 m and are made up of overlapping paddles of scintillator plastic (5 mm and 50 mm BC408, respectively) [69]. The S1 plane is made up of 6 overlapping paddles, while the S2m plane is comprised of 12 paddles; all paddles are monitored by a pair of photomultiplier tubes (PMTs). The timing resolution for each plane is about 0.3 ns. The singles trigger (T_1 on the RHRs and T_3 on the LHRs) is formed by the following requirements:

- The left and right PMT both fire on a paddle in S1
- The left and right PMT both fire on a paddle in S2m
- The S1 and S2m paddles both fire within a specified timing window

A secondary trigger (T_2 and T_4 on the right and left HRS, respectively) is used to monitor the efficiency of the main trigger. The efficiency trigger is exclusive of $T_1(T_3)$ and requires that either S1 or S2m fire (but not both), and that a signal was seen in the gas Cherenkov. These represent “good” electrons events when one of the scintillator planes failed to detect a particle. After a trigger is formed, the signal is

sent to the trigger supervisor (TS). During periods of high rates, the DAQ cannot record every event; the trigger supervisor decides which events should be recorded. The fraction of events which the DAQ records is represented by the deadtime (DT) or livetime ($LT = 1 - DT$). The deadtime comes from two sources; computer deadtime and detector deadtime. The computer deadtime is related to the speed of the data processing power, and can be decreased by scaling the incoming events with a prescale value (ps) at the TS. That is, only 1 of every ps events will be recorded by the DAQ. Electronic deadtime can also arise due to the response of the detectors, but this is negligible compared to the computer deadtime. A discussion of the LT analysis will be seen in Sec. 5.2.4.

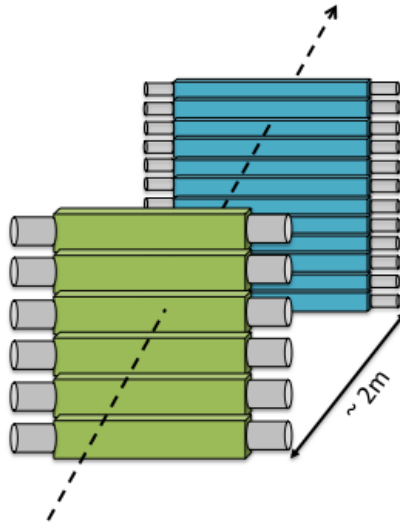


FIG. 4.14: A diagram of the S1 and S2m scintillator planes.

4.6.3 Gas Cherenkov

A gas Cherenkov detector [78] is sandwiched between the two scintillator planes. When light travels through a transparent medium, such as a gas or a liquid, the

velocity of light is decreased according to the index of refraction (n) of that medium. While the velocity of a particle is limited to the speed of light in a vacuum, c , a high energy particle with velocity βc may exceed the velocity of light within the medium ($\frac{c}{n}$). Analogous to a sonic boom created by a supersonic aircraft, an electromagnetic shockwave is produced, known as Cherenkov radiation [79]. The wave is emitted in a conical pattern, as seen in Fig. 4.15. The threshold for the production of Cherenkov radiation is given by

$$\beta c \geq \frac{c}{n} \Rightarrow \beta \geq \frac{1}{n}. \quad (4.9)$$

This velocity-dependent threshold makes the detection of Cherenkov light a very effective method to discriminate between particles of differing mass. In this case, the detector is filled with CO₂, which has an index of refraction of $n = 1.00041$. The momentum threshold is dependent on the mass of the particle and is given by

$$p = \frac{mc}{\sqrt{n^2 - 1}}. \quad (4.10)$$

For this material, the momentum threshold for electrons is ~ 0.017 GeV, whereas the threshold for pions is ~ 4.8 GeV, above the acceptance for the spectrometers. In this way, the detector allows for good particle detection, since only electrons will produce a trigger in the detector.

The detector has a path length of 1.5 m. Once the Cherenkov light is produced, it is focused onto 10 PMTs by 10 spherical mirrors which partially overlap to avoid “dark zones” between adjacent mirrors. The signal from the PMTs passes through an analog-to-digital converter (ADC) and is summed together, representing the total

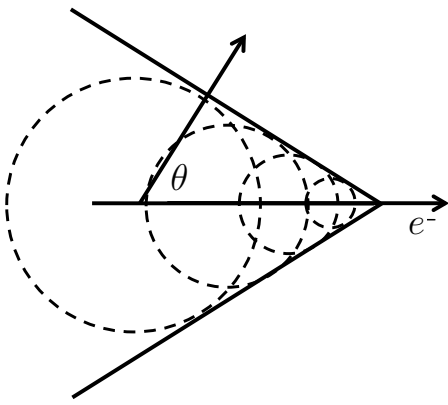


FIG. 4.15: Cherenkov radiation is emitted in a cone. The angle θ is given by $\cos \theta = \frac{1}{n\beta}$.

light output from that electron event. A background signal is present and comes mainly from δ -electrons produced by interactions of pions with materials inside the detector. The Cherenkov detector analysis will be discussed more thoroughly in Sec. 5.2.1.

4.6.4 Electromagnetic Calorimeters

The gas Cherenkov detector provides the first stage of pion rejection, but the electromagnetic calorimeters provide further particle identification. The calorimeters take advantage of pair-production and bremsstrahlung radiation, which is the electromagnetic radiation produced by the deceleration of a charged particle when deflected by another charged particle. When a charged particle passes through the dense lead glass bricks which make up the calorimeters, a shower of photons and electron-positron pairs is produced. The light produced by the cascade is linearly proportional to the energy deposited, and is collected by PMTs mounted to the lead glass blocks.

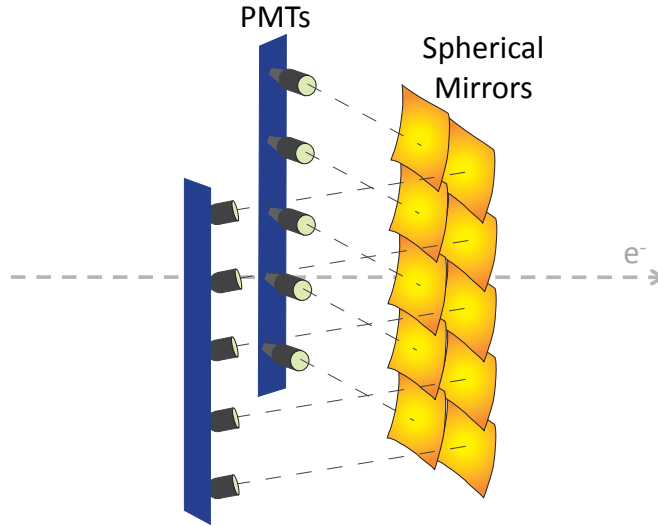


FIG. 4.16: A diagram of the gas Cherenkov counter showing the spherical mirrors focusing Cherenkov light onto the PMTs.

The left and right HRS calorimeters are slightly different in construction [69]. The RHR_S calorimeter is a total energy absorber, meaning the full energy of the scattered electron will be deposited in the calorimeter. The first layer, called the preshower, is comprised of forty-eight lead glass blocks, oriented perpendicular to the particle track. Each block is 10 cm x 10 cm x 35 cm. The second layer, the shower, is composed of eighty blocks, oriented parallel to the particle track. Each block in the shower is 15 cm x 15 cm x 35 cm. On the LHR_S, the two layers are each made of thirty-four blocks, oriented perpendicular to the particle trajectory. The blocks in the first layer are 15 cm x 15 cm x 30 cm while the blocks in the second layer are 15 cm x 15 cm x 35 cm. The LHR_S calorimeter differs from that of the RHR_S because it is not a full energy absorber. Analysis of the lead glass calorimeters will be discussed later in Sec. 5.2.2.

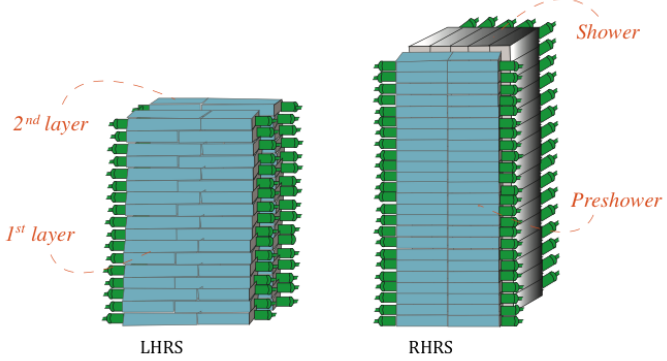


FIG. 4.17: The lead glass calorimeters on the left and right HRS.

4.7 Third Arm Detector

The third arm detector was designed for the g_2^p experiment to measure the elastic asymmetry of the recoil proton [80]. Using this asymmetry, it would be possible to get a relative measurement of the product of the beam and target polarization. The detector is comprised of a dE and E scintillator plane, as shown in Fig. 4.18. The dE plane was 1.2 cm thick and the E plane was \sim 5 cm thick. The detector was mounted to the left of the scattering chamber at 74° . In addition to its intended use, the third arm detector was useful as a beam position monitor. The beam pipe was in the acceptance of the third arm, so if the beam was scraping the beam pipe or the target frame, hot spots could be seen in the third arm data.

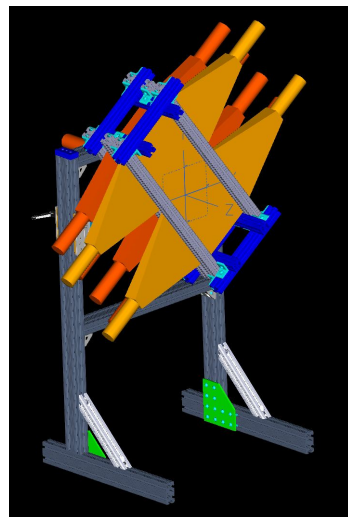


FIG. 4.18: Diagram of the third arm detector.

CHAPTER 5

Analysis

To extract the polarized spin structure functions, two physics quantities are needed, the asymmetry and the unpolarized cross section. These quantities were measured using a polarized electron beam and a polarized NH₃ target. This chapter will give an overview of the analysis method and discuss details of the inputs necessary for extracting the asymmetry and cross section.

5.1 Asymmetries and Cross Sections

The physics asymmetry is defined as the difference in polarized cross sections over the sum. The longitudinal (A_{\parallel}) and transverse (A_{\perp}) asymmetries can be written as

$$A_{\parallel} = \frac{\frac{d^2\sigma^{\downarrow\uparrow}}{dE'd\Omega} - \frac{d^2\sigma^{\uparrow\uparrow}}{dE'd\Omega}}{\frac{d^2\sigma^{\downarrow\uparrow}}{dE'd\Omega} + \frac{d^2\sigma^{\uparrow\uparrow}}{dE'd\Omega}}, \quad (5.1)$$

and

$$A_{\perp} = \frac{\frac{d^2\sigma^{\downarrow\rightarrow}}{dE'd\Omega} - \frac{d^2\sigma^{\uparrow\rightarrow}}{dE'd\Omega}}{\frac{d^2\sigma^{\downarrow\rightarrow}}{dE'd\Omega} + \frac{d^2\sigma^{\uparrow\rightarrow}}{dE'd\Omega}}. \quad (5.2)$$

The electron spin is polarized either parallel or anti-parallel to the direction of the beam and is denoted by $\downarrow\uparrow$. The target spin is given by \uparrow if polarized along the direction of the electron beam, or \Rightarrow if polarized in the transverse configuration.

The raw asymmetry is calculated using the number of events in the \pm helicity state,

$$A_{raw} = \frac{\frac{N^+}{LT^+Q^+} - \frac{N^-}{LT^-Q^-}}{\frac{N^+}{LT^+Q^+} + \frac{N^-}{LT^-Q^-}}, \quad (5.3)$$

where N^\pm , LT^\pm and Q^\pm are the number of accepted events, livetime and charge, respectively. The physics asymmetry can then be calculated using,

$$A_{\parallel,\perp}^{phys} = \pm \frac{1}{fP_bP_t} A_{\parallel,\perp}^{raw}, \quad (5.4)$$

where P_b is the beam polarization, P_t is the target polarization, and f represents the dilution factor that accounts for events that scatter from unpolarized material in the target. The sign of the asymmetry is dependent on the target spin direction, the status of the IHWP, and which spectrometer the data was taken with.

The Born asymmetries are calculated by applying radiative corrections:

$$A_{\parallel,\perp}^{Born} = A_{\parallel,\perp}^{phys} + \Delta A_{RC}^{ext} + \Delta A_{RC}^{int}, \quad (5.5)$$

where ΔA_{RC}^{ext} and ΔA_{RC}^{int} represent the corrections for external and internal radiative effects, respectively.

The unpolarized cross section can be calculated using

$$\sigma_0^{raw} = \frac{d^2\sigma^{raw}}{d\Omega dE'} = \frac{psN}{N_{in}\rho LT\epsilon_{det}} \frac{1}{\Delta\Omega\Delta E'\Delta Z}, \quad (5.6)$$

where the variables are defined as:

- N : the number of detected electrons that survive the particle identification and acceptance cuts
- ps : the prescale factor for the singles trigger
- $N_{in} = Q/e$: the number of electrons incident on the target, determined from the total charge accumulated
- ρ : the target density
- LT : livetime correction for computer and electronic deadtime
- ϵ_{det} : the product of hardware and software detector efficiencies (including gas Cherenkov and lead glass calorimeter detector efficiencies, trigger efficiencies, and VDC multitrack efficiencies)
- $\Delta\Omega$: solid angle acceptance, as seen by the spectrometer
- $\Delta E'$: momentum acceptance, as seen by the spectrometer
- ΔZ : target length, as seen by the spectrometer

To calculate the experimental cross section, the contribution from materials other than hydrogen in the target must be subtracted from the raw cross section:

$$\sigma_0^{phys} = \sigma_0^{raw} - \frac{\rho_N}{\rho_H + \rho_N + \dots} \sigma_N \quad (5.7)$$

Finally, the Born cross section can be determined after applying internal and external radiative corrections:

$$\sigma^{Born} = \sigma_0^{exp} + \Delta\sigma_{RC}^{ext} + \Delta\sigma_{RC}^{int}. \quad (5.8)$$

The cross section difference used is then given as the product of these two quantities:

$$\Delta\sigma_{||,\perp}^{phys} = 2A_{||,\perp}^{phys}\sigma_0^{phys} \quad (5.9)$$

5.2 Detector Calibrations and Efficiency Studies

A diagram of the HRS detector stack is shown in Fig. 5.1. The details of the HRS detectors were discussed in Sec. 4.6. The detector stacks in the left and right HRSs are nearly identical, with the exception of the lead glass calorimeters. This section will describe the details of the calibration and efficiency studies of each component.

5.2.1 Gas Cherenkov

For analysis purposes, the signals from the 10 ADC channels of the gas Cherenkov are summed and a cut is placed on the final distribution to distinguish between electrons and pions. Before the 10 PMT channels can be combined, a software gain is adjusted to align the single photoelectron peak of each channel. A good electron event will produce multiple photoelectrons in the gas Cherenkov, so events that fall in the single photoelectron peak will be removed for the final analysis. Single photoelectron events could result from secondary scattering within the detector, or

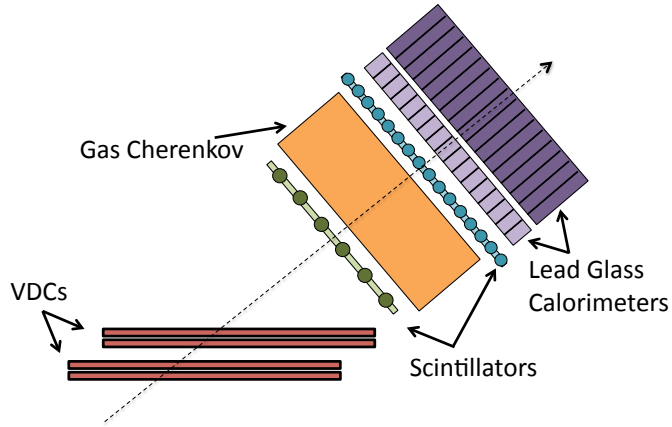


FIG. 5.1: Components of the detector stack on the RHRs including vertical drift chambers (VDCs), two planes of scintillators, a gas Cherenkov and two layers of lead glass bricks that form an electromagnetic calorimeter.

from noise in the photomultiplier tube.

It can be difficult to isolate the single photoelectron peak, as the number of events is much smaller than in the main Cherenkov peak. Several runs within a kinematic setting were combined to achieve a significant number of events. To isolate the peak, tight cuts were made on the Cherenkov TDC. Each peak was fit with a Landau-Gaussian convolution function; the shape of the peak is Gaussian, but the addition of a Landau function accounts for the residual background tail leftover after cuts are applied. Once the center of the peak is determined from the fit, a calibration constant is determined to shift that peak to channel 100. An example of the single photoelectron peak with the described fit is shown in Fig. 5.2.

5.2.2 Lead Glass Calorimeters

Electromagnetic Calorimeter:

Energetic particles passing through a dense medium will produce a cascade of

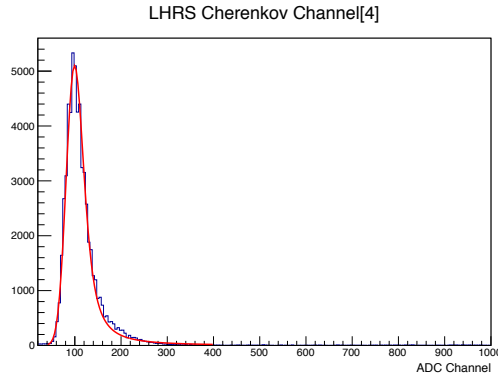


FIG. 5.2: Isolated single photoelectron peak, with Landau-Gaussian fit.

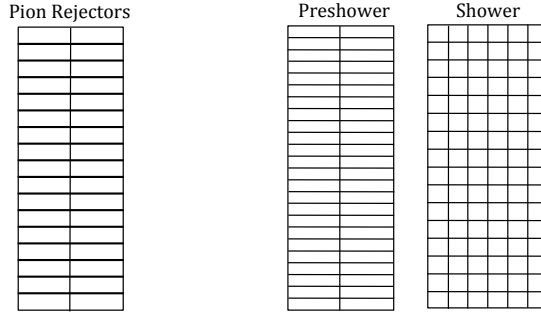


FIG. 5.3: Front view of the lead glass calorimeter layout. On the left is the layout of the pion rejectors in the LHRS; both layers are identical. On the right is the layout of the preshower and shower layers in the RHRS.

secondary particles (γ, e^+, e^-). This shower of particles will continue to propagate through the medium, converting the energy of the original particle to heat and light. An electromagnetic calorimeter relies on the collection of this light to determine the energy of the incident particle. In this section, the layers of the LHRS calorimeter will be referred to as the first and second layer of the *pion rejector* and the RHRS calorimeter will be referred to as the *preshower* and *shower*. In both systems, the calorimeters are composed of lead glass bricks, with each segment monitored by a photomultiplier tube. The layout of these detectors is shown in Fig. 5.3.

Calorimeter Calibration Technique:

To calibrate the detector, the raw ADC signal from each PMT must be converted to the energy deposited by the particle. The cascade of secondary particles is typically spread over several adjacent blocks. The output of these segments must be integrated over the total detectable signal to determine the original energy. As described in Sec. 4.6.4, the lead glass calorimeters are slightly different in the left and right HRSs. The LHS layers are identical, while the shower layer on the RHS is much thicker than the preshower layer.

First, we discuss the RHS case; a set of calibration coefficients must be determined to transform the ADC amplitude of each block into a corresponding energy deposition. Since the total energy of the electron is deposited in the preshower/shower combination, the calibration constants can be determined by minimizing the following function [81]:

$$\chi^2 = \sum_i^n \left[\sum_j C_j \cdot (A_j^i - P_j) + \sum_k C_k \cdot (A_k^i - P_k) - P_{kin}^i \right]^2 \quad (5.10)$$

where:

- i = # of the selected calibration event
- j (k) = # of the preshower (shower) block included in cluster
- A_j^i (A_k^i) = amplitude value in the j^{th} preshower (k^{th} shower) block
- P_j (P_k) = mean value of the pedestal of the j^{th} preshower (k^{th} shower) channel
- P_{kin}^i = momentum of the particle
- C_j (C_k) = calibration constants to be determined for the preshower (shower).

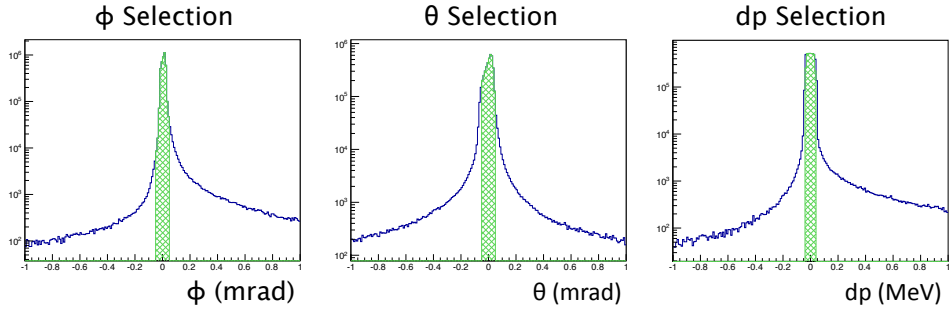


FIG. 5.4: An example of the cuts applied to the golden variables θ , ϕ and dp to get rid of events on the edge of the acceptance. The blue line represents the raw variable, while the green shaded in regions show the selected events.

In total, there are 128 calibration constants; 48 for the preshower layer and 80 for the shower layer.

To optimize the calibration, events were first selected to ensure a pure electron sample. Loose software cuts were made on the golden track variables, θ , ϕ and dp to get rid of events on the edge of the acceptance (see Fig. 5.4), as well as a cut to require only single track events. The golden track variables represent the best track in the transport coordinate system. The transport coordinate system represents the coordinate system at the VDCs, rotated clockwise by 45° around the y -axis, so that z of the transport system coincides with the central ray of the spectrometer. Additionally, a cut was placed on the gas Cherenkov sum, well above the single photoelectron peak, to ensure only good electron events were selected.

The code used to perform the χ^2 minimization was based on code written by H.-J. Lu *et. al.* [81]. Once the calibration constants are produced and added to the run database, the calibration can be checked by looking at the E_{tot}/p distribution, where E_{tot} is the total energy deposited in the detector and p is the momentum of the particle. The total energy deposited in the preshower/shower can be written as

a sum over the blocks (M) in each layer,

$$E_{tot} = E_{ps} + E_{sh} = \sum_{j \in M_{ps}^i} C_j \cdot (A_j^i - P_j) + \sum_{k \in M_{sh}^i} C_k (A_k^i - P_k). \quad (5.11)$$

For electrons, this distribution should be centered around 1, with the width of the peak representing the resolution. An example is shown in Fig. 5.5. For this experiment, we took data over a large range of momentum settings. The same calibration coefficients were not suitable for every setting. In total, 11 different calibration constant configurations were used for the RHRs calorimeters.

Now we can consider the case of the LHRs. The lead glass calorimeters on the LHRs were constructed in a slightly different design. Since the overall thickness of the combined layers is not as thick as in the RHRs, the total energy of the electron is not deposited in the detector. The calibration procedure described for the RHRs is not valid here, as it assumes total absorption of the electron energy. For the LHRs calibration, it is assumed that the longitudinal shower will obey a gamma distribution:

$$\frac{dE}{dt} = E_0 \beta (\beta t)^{\alpha-1} \frac{e^{-\beta t}}{\Gamma(\alpha)} \quad (5.12)$$

where

$$\frac{\alpha-1}{\beta} = \ln \left(\frac{E_0}{E_c} \right) - 1, \quad (5.13)$$

where E_0 is the electron momentum, $E_c = 15.8$ MeV is the critical energy, and t is the radiation thickness. Along the y -direction width, the full energy is deposited, but along the x -direction it is assumed that only 95% of the energy is deposited. The calibration constants can be determined using Eqn. 5.14, where μ , ρ and β are

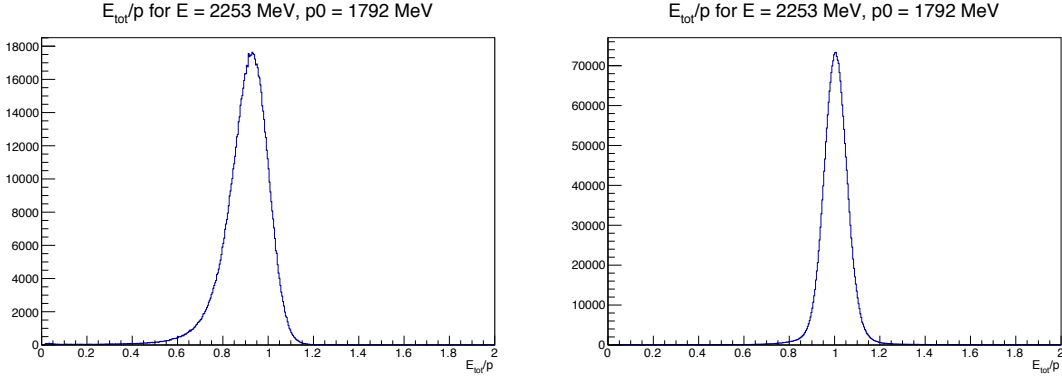


FIG. 5.5: An example of the E_{tot}/p distribution for the LHR and RHR calorimeters (left and right respectively). Since the LHR calorimeter is not an total energy absorber, the distribution is not centered around 1.

free parameters:

$$\rho E_{prl1} + \mu E_{prl2} = \int \frac{dE}{dt}. \quad (5.14)$$

The quantity $\frac{dE}{dt}$ is defined in Eqn. 5.12, and E_{prl1} and E_{prl2} are the energy deposited in the first and second layer of the pion rejector, respectively.

Similar to the RHR, the calibration can be tested by looking at the E_{tot}/p_0 distribution. In contrast to the RHR, the distribution will not be centered around 1, since the total energy is not absorbed by the calorimeter. An example of this distribution is seen in Fig. 5.5, again, the width of the distribution gives the resolution of the calibration. A total of 3 different sets of calibration constants were used for the LHR calorimeters.

5.2.3 Efficiency Studies

To ensure a good electron sample, cuts were applied to the data to select a pure electron sample. The cuts applied are the same as those used for the preshower/shower calibration described in the previous section.

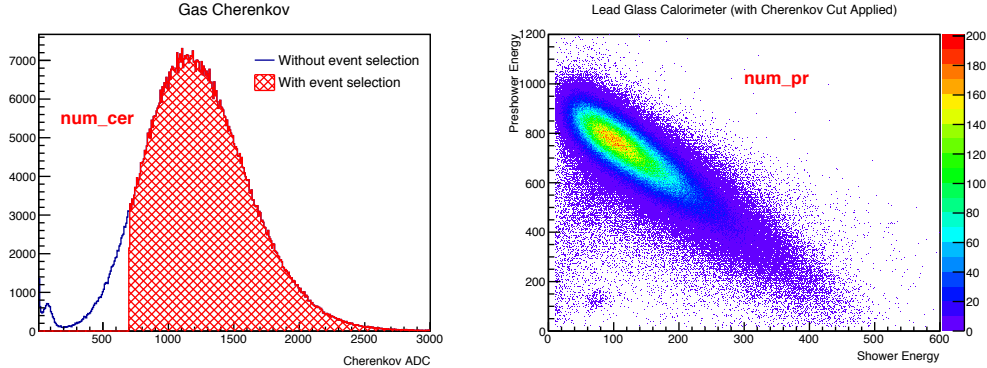


FIG. 5.6: An example of the method to determine the detection efficiency for the lead glass calorimeters. On the left, the shaded region represents a selection of events that triggered the gas Cherenkov. On the right are the events from this selection that *also* triggered the lead glass calorimeter.

The detection efficiency is an indicator of the performance of the detector throughout the run period. To determine the detector efficiency for the lead glass calorimeters on the RHRs, a selection of electrons was made that triggered the gas Cherenkov and fell well above the single-photoelectron peak threshold. The number of these events that also trigger the preshower and shower were then counted. An example of these cuts can be seen in Fig. 5.6. The efficiency can then be calculated as such:

$$num_{cer} = \# \text{ of events selected in gas Cherenkov}$$

$$num_{pr} = \# \text{ of events also detected in the calorimeter}$$

$$\text{efficiency} = \frac{num_{pr}}{num_{cer}}.$$

Since the LHRs is not a total energy absorber, it was necessary to alter this procedure slightly. It was found that the detection efficiency dropped considerably for momentum settings lower than 0.9 GeV. The problem, however, appears not to be an actual inefficiency of the system, but rather a consequence of the design of

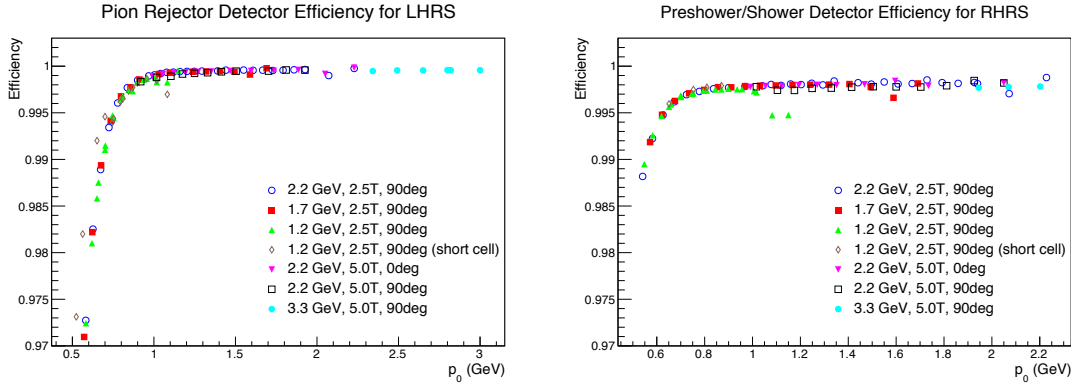


FIG. 5.7: Detector efficiencies for the electromagnetic calorimeter in the left and right HRS. The data points include one representative run for each kinematic setting.

the detector. For low momentum settings, some electrons deposit the majority of their energy in the first layer of lead-glass, therefore not firing the second layer. To account for this, a separate condition was created for these low momentum settings. An event would still be counted even if it had no hit in the second layer, as long as the majority, that is, $E \geq E_{tot} - 30$ MeV, of the total energy has been deposited in the first layer. The detector efficiencies for the electromagnetic calorimeters for the left and right HRS can be seen in Fig. 5.7. The detection efficiency for the preshower/shower is above 98.8% for all kinematic settings, and the efficiency for the pion rejectors is above 98% with the described condition included.

To determine the detection efficiency of the gas Cherenkov, a similar procedure is followed. A sample of events is selected in the lead-glass calorimeter, and the number of these events which also fired the gas Cherenkov are counted. The detection efficiency for the gas Cherenkov was found to be very high, above 99.8% across the entire range of kinematics for both the left and right HRS (see Fig. 5.8). These results, combined with those for the electromagnetic calorimeter, indicate good detector performance throughout the run period.

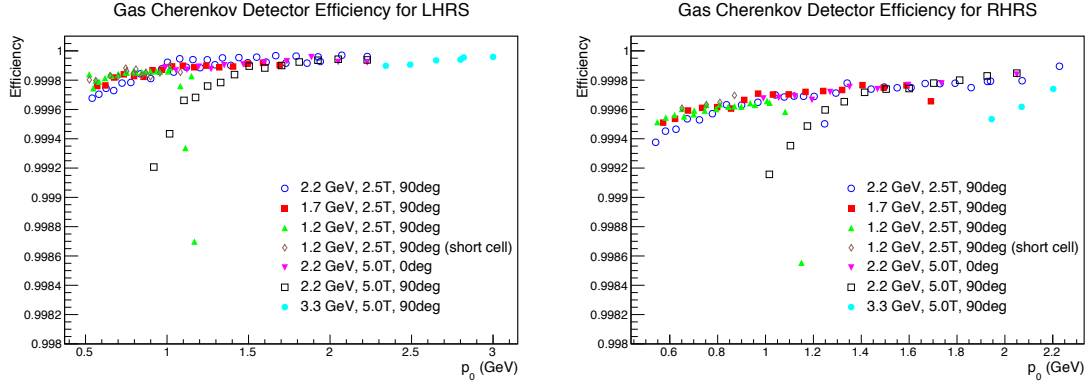


FIG. 5.8: Detector efficiencies for the gas Cherenkov on the left and right HRS. The data points include one representative run for each kinematic setting.

5.2.4 Scintillator Trigger Efficiencies

Overview of the Trigger: As described in Sec. 4.6.2, this experiment used the S1 and S2m scintillator planes along with the gas Cherenkov counter to produce two separate singles trigger. The main trigger, used for data acquisition, is defined by a particle passing through both scintillator planes. It is referred to as T_1 on the RHRs, and T_3 on the LHRs. Physically, it is defined as the logical AND of the following conditions:

- Both the left and right PMTs of 1 segment of S1 fire.
- Both the left and right PMTs of 1 segment of S2m fire.
- The event causes both S1 and S2m to fire.

There was no restriction made on which segments fired in the scintillator planes S1 and S2m. A secondary trigger, called T_2 (T_4) on the RHRs (LHRs) is used to measure the efficiency of the main trigger. The efficiency trigger is formed exclusive to the main trigger, and requires the following conditions:

- Either the S1 or S2m planes fire (but not both).
- The event caused the gas Cherenkov to fire.

After the trigger is formed, it is sent to the trigger supervisor, which decides whether or not the DAQ will record the event. The event rate will determine the trigger supervisor's ability to accept events. The DAQ deadtime is a correction for the number of events that are not recorded by the DAQ. The deadtime can be decreased by prescaling the events. In this way, the trigger supervisor only accepts one of every ps events, where ps is defined as the integer prescale value.

Trigger Efficiencies and Livetime Correction:

The trigger efficiency is defined as:

$$Eff = \frac{T_{main}}{T_{main} + T_{eff}}, \quad (5.15)$$

T_{main} and T_{eff} are the total number of counts of the main and efficiency triggers described above. There are two ways to determine the number of counts; either from the trigger scalers or the trigger latch pattern. The trigger latch pattern shows the pattern of triggers that co-exist for an event in the data stream. Since the trigger latch pattern is correlated directly with correlated events, it is easier to apply event selection cuts, but it is also susceptible to deadtime effects. It is necessary to correct for the deadtime as follows:

$$T_{cor} = \frac{T_i \cdot ps_i}{1 - DT_i}, \quad (5.16)$$

where i is the trigger type (1-4), T_i is the number of accepted triggers, ps_i is the corresponding prescale factor, and DT_i is the deadtime associated with that trigger. The livetime (LT) is the ratio of accepted triggers to total triggers, adjusted by the prescale factor:

$$LT = \frac{ps_i T_i^{acc}}{T_i^{tot}}. \quad (5.17)$$

The number of accepted triggers (T_i^{acc}) is determined from the trigger latch pattern while the total trigger count (T_i^{tot}) is determined from the trigger scalers. The deadtime is then simply defined as $DT = 1 - LT$.

For this analysis, cuts were placed on the data to ensure that only good electron events were used in the efficiency calculations. These cuts are described in reference [82], along with additional details of this analysis. The results can be seen in Fig. 5.9. Overall, the efficiencies are greater than 99.1%. There is some substructure seen in the data; at lower momenta the trigger efficiency tends to drop off. However, the correction to the cross-section measurement for the trigger inefficiency is less than 1%. There are a few RHRS dilution runs where the efficiency falls below 99%. To try to improve the efficiency for these runs, a cut was placed on the lead glass. However, it had no effect. For RHRS runs taken during the 2.2 GeV, 2.5 T target field setting, the efficiency trigger (T_2) was not working properly, so the trigger efficiency was not calculated for these runs.

5.2.5 VDC Multitrack Efficiency

VDC Track Reconstruction:

To determine the momentum, it is necessary to have good position and angle

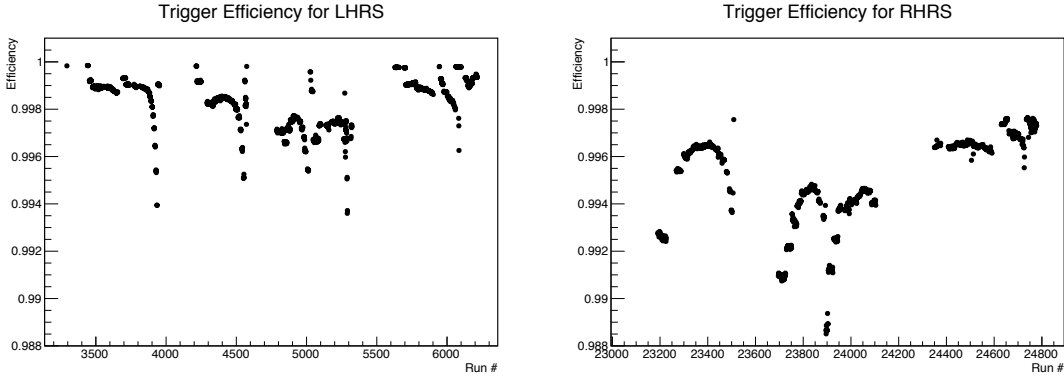


FIG. 5.9: Trigger efficiencies; on the left (right) are results for the LHRs (RHRs). Details of analysis can be found in [82].

reconstruction of the particle trajectories. The Vertical Drift Chambers (VDCs), which were described in detail in Sec. 4.6.1, provide tracking information for this purpose. While each detected event should have only one associated track in the VDC, multiple events can be seen due to noisy wires, or, in the case of high rates, several particles passing through the system simultaneously. For some kinematic settings, the number of multitrack events can be as high as 30%, which, if left uncorrected, will contribute a large uncertainty to the final cross section.

The VDC timing signal is produced by an avalanche of electrons hitting the sense wire. This signal provides the “start” for the TDC, while the “stop” is provided by the trigger supervisor. Using the TDC signal in conjunction with the drift velocity, the drift distance for each wire in a cluster can be determined. A linear fit of the drift distance is then used to determine cross-over point at the sense wire plane. In this way, the particle trajectory can be reconstructed with a position reconstruction of $\sigma_{x(y)} \sim 100 \mu\text{m}$ and angle reconstruction of $\sigma_{\theta(\phi)} \sim 0.5 \text{ mrad}$ [83].

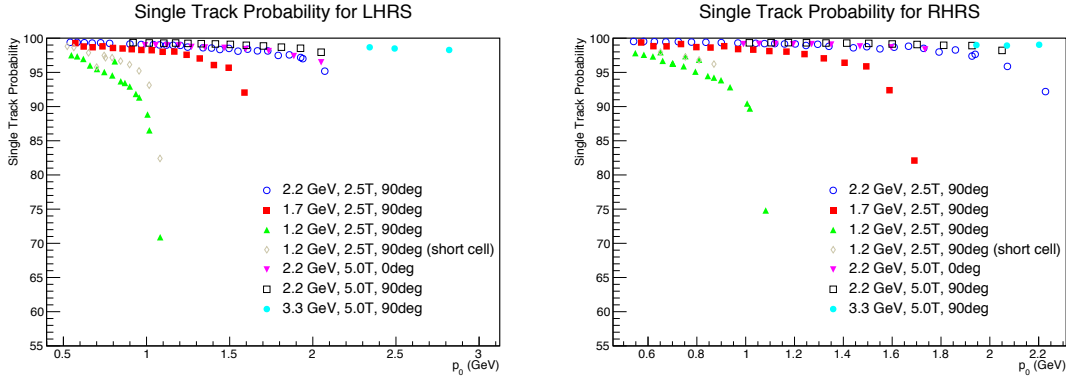


FIG. 5.10: Probability of an event having only one track in the VDC. For kinematic settings with a high rate, the number of multitrack events can be as high as 30%. Full analysis details can be seen in [83].

Multitrack Efficiency:

The efficiency of the VDC is defined as:

$$efficiency = \frac{N_{good}}{N_{total}}, \quad (5.18)$$

where N_{good} is the number events with a successful track reconstruction and N_{total} is the total number of events that survive the acceptance and PID cuts. For kinematic settings with a low event rate the fraction of multitrack events is small. For settings with higher event rates, the multitrack events must be examined more carefully to determine whether or not the event has at least one good track reconstruction in the VDC [83].

To get more information about multitrack events, we can look at the energy deposited in the calorimeters for each track. For example, let's consider events with 2 tracks. Using E_1 as the energy deposited in the calorimeter by the first track, E_2 as the energy deposited by the second track, and p_0 as central momentum of the spectrometer. If $E_1 \ll p_0$ and $E_2 \ll p_0$, the events would not survive the PID cuts,

so we would not expect to see a good track in the VDC. If $E_1 \approx p_0$ and $E_2 \ll p_0$, or $E_1 \ll p_0$ and $E_2 \approx p_0$, or $E_1 \approx 2p_0$, or $E_2 \approx 2p_0$, although the energy deposited for one track will not survive the PID cuts, the related track will, so we will expect to see at least one good track. If $E_1 \approx p_0$ and $E_2 \approx p_0$, it is more difficult to discern whether or not there is one good track.

For the third case, we can further examine the distance between the tracks. If the distance between the 2 tracks is more than the width of a lead glass block, the energy cluster associated with each event can be separated, so this event is counted to have at least one good track. If the 2 tracks pass through the calorimeter with a distance less than the width of one block, the associated clusters will overlap, so it is difficult to know the energy contribution from each individual track. If the energy deposited in one cluster is equal to twice the energy deposited in the directly pointed blocks of another track, therefore satisfying the PID and acceptance cuts, we can also expect this event to have at least one good track. This case arises due to knock-out δ electrons or misre-constructed tracks in the VDC. The inefficiency caused by multiple tracks gives the upper limit of the systematic, while the unresolved tracks determines the lower limit of the uncertainty.

The single track probability for the left and right HRS is shown in Fig. 5.10 and the total efficiency is shown in Fig. 5.11. After careful examination of multitrack events, the uncertainty has been reduced to $< 1\%$ for most kinematic settings. More details of this analysis is given in [83].

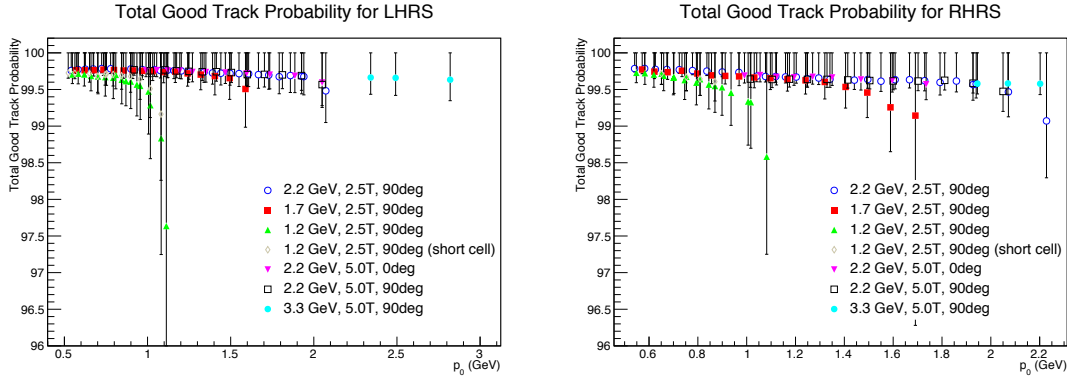


FIG. 5.11: Total VDC efficiency, after careful examination of multitrack events. More details of the analysis can be found in [83].

5.3 Particle Identification Cuts

The purpose of the gas Cherenkov and calorimeter detectors is to identify good electron events to be used in the final analysis by cutting out other events that were detected, such as pions. There are three cuts used for particle identification; a gas Cherenkov threshold cut, a cut on the first layer of lead glass, and a cut on the total energy deposited in the calorimeter. These cuts are chosen to maximize pion suppression while minimizing the inefficiency caused by cutting out good electron events. On the RHRs, the gas Cherenkov cut was placed at channel 150, while on the LHRs the cut was placed at channel 200. In both cases, a high detection efficiency is maintained, as seen in Fig. 5.12.

The lead glass cuts are chosen such that the overall electron detection efficiency does not fall below 99%. For the RHRs, a conservative cut is placed on the preshower, and a separate cut is placed on the summed energy in both layers. The cuts on the calorimeter are momentum dependent, unlike the gas Cherenkov, which has a constant cut for every kinematic setting. For the LHRs, the cut on the first layer of lead glass does not need to be as conservative, since more energy is deposited in layer 1 of the pion rejector than the (thinner) preshower layer. The cut

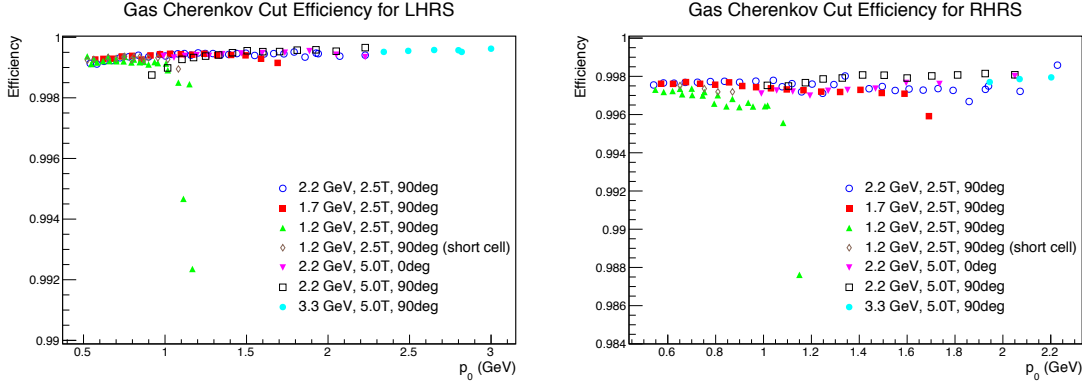


FIG. 5.12: Cut efficiencies for the gas Cherenkov on the left and right HRS. The data points include one representative run for each kinematic setting.

efficiencies are shown for the left and right HRS in Fig. 5.13. For some kinematic settings in the 1.2 GeV energy setting, a short ammonia cell was used; separate cuts were determined for these runs.

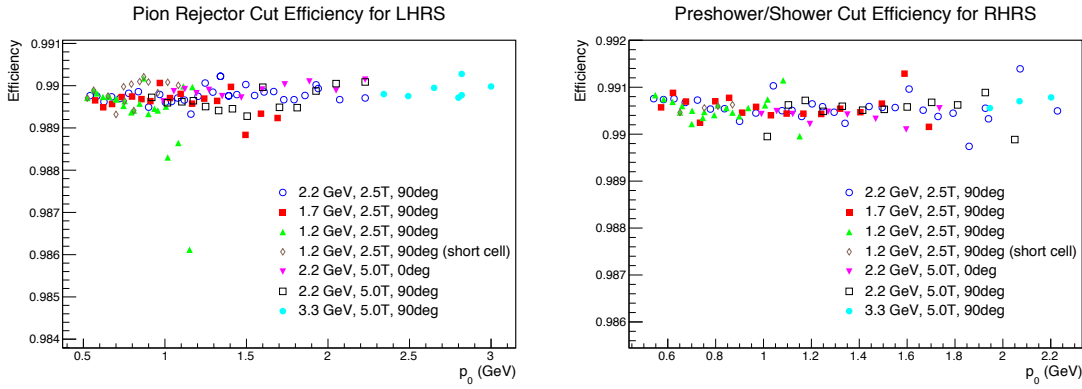


FIG. 5.13: Cut efficiencies for the leadglass calorimeters on the left and right HRS. The data points include one representative run for each kinematic setting.

The overall pion suppression can be examined by applying the 3 cuts described above and looking at the number of pion events that remain. The effect of the gas Cherenkov and lead glass cuts on the overall pion suppression can be seen in Fig. 5.14. The cut on the Cherenkov removes most of the contamination, while the cut on the first layer of lead glass removes low energy events.

In plot (C) of Fig. 5.14, the black line separates the “good” electron events from

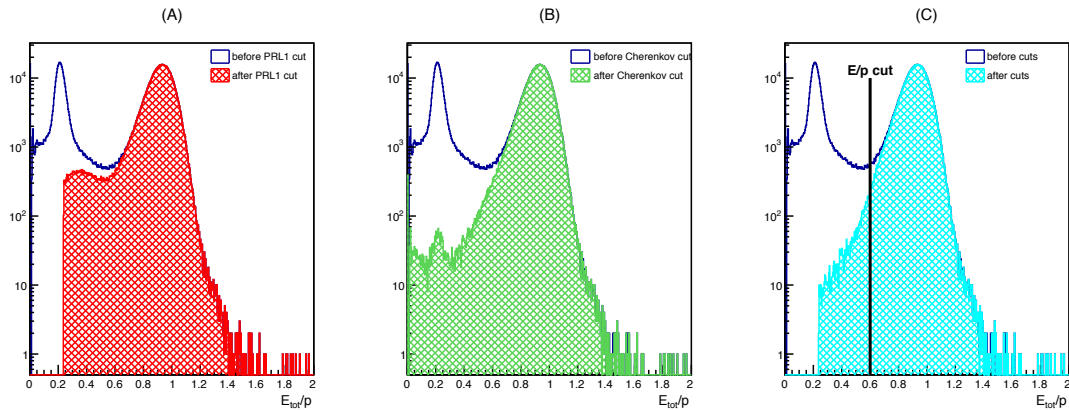


FIG. 5.14: An example of the particle ID cuts for a sample run with a large pion contamination. The blue line in all three plots is the same; the total energy deposited in the calorimeter divided by the particle's momentum. (A) shows the effect of a cut on the preshower layer, and (B) shows the effect of the gas Cherenkov cut. (C) shows the result of applying both cuts, with the black line indicating the location of the E_{tot}/p cut.

what we will call the residual pion contamination. This represents the maximum value of the contamination, as these events will actually be cut out in the final analysis. The level of pion contamination, before any cuts are applied, can be seen in Fig. 5.15 and 5.16. After PID cuts are applied, the level of residual pion contamination is very low, with $\pi/e < 0.0052$ for all kinematic settings for both the left and right HRS, as shown in Fig. 5.17. The PID cuts used for data analysis are detailed in Appendix A.

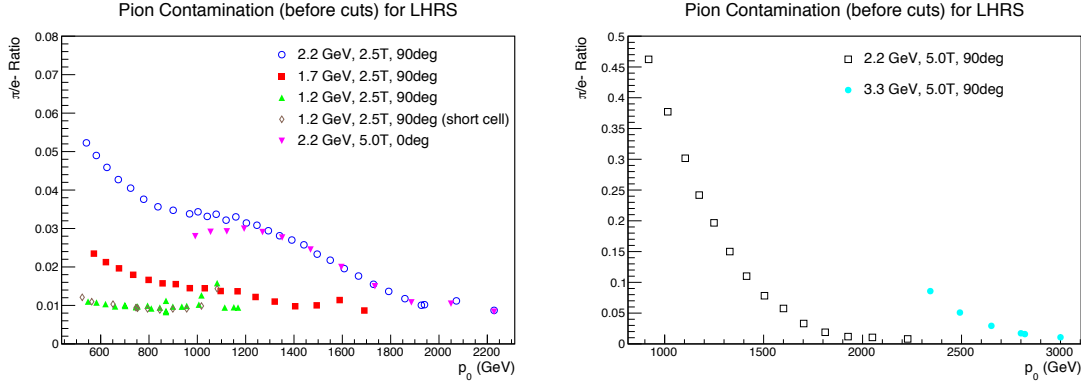


FIG. 5.15: Pion contamination before PID cuts are applied for the LHRs.

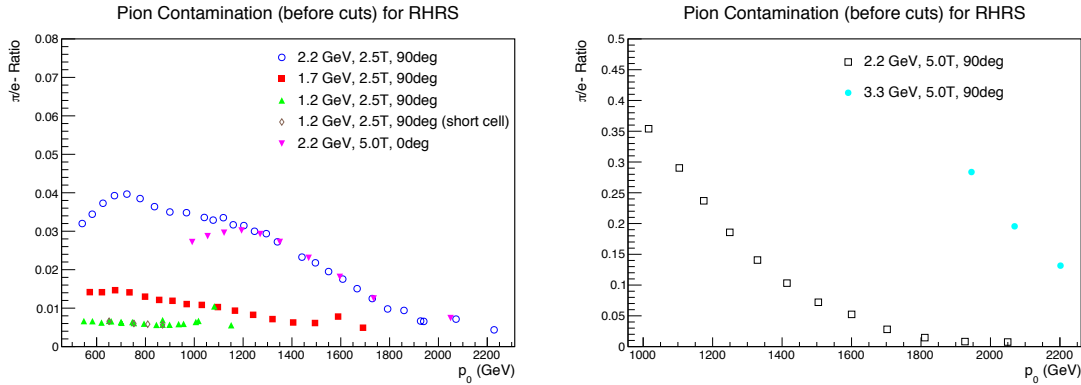


FIG. 5.16: Pion contamination before PID cuts are applied for the RHRs.

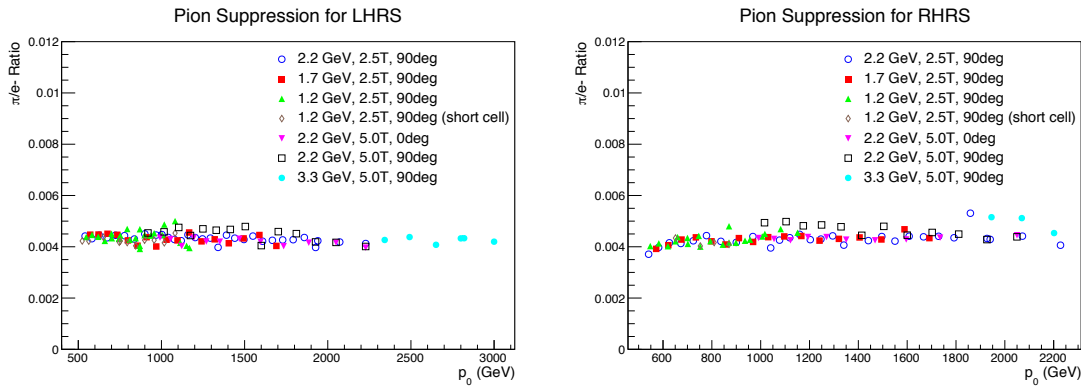


FIG. 5.17: Residual pion contamination after PID cuts are applied.

5.4 Charge Asymmetry

Different amounts of beam charge can accumulate for each helicity state, which results in a charge asymmetry:

$$A_Q = \frac{Q^+ - Q^-}{Q^+ + Q^-}, \quad (5.19)$$

where Q^\pm is the total accumulated charge for the \pm helicity state, which is measured by the BCM. The charge asymmetry could arise from imperfections in the Pockels cell or half-wave plate in the accelerator injector. The charge asymmetry for production runs is shown in Fig. 5.18; the measured charge asymmetry was small throughout the run period.

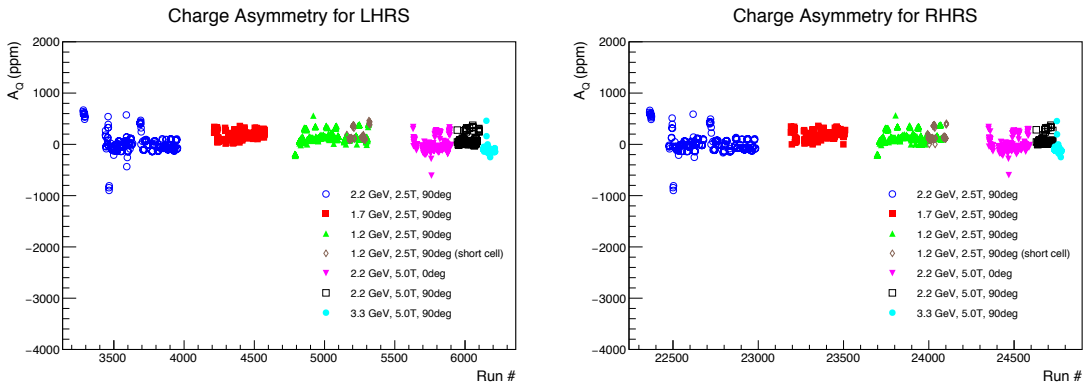


FIG. 5.18: Charge asymmetries for production runs on the left and right HRS for the entire run period.

5.5 Livetime Asymmetry

Similarly to the charge asymmetry correction, while the livetime should be helicity independent, circumstances can arise where there is a significant livetime asymmetry [84]:

- If the physics asymmetry is large and the deadtime increases quickly with DAQ rate.
- If the event size is significantly different for \pm helicity events.
- If the deadtime is unstable during the run, and therefore the average deadtime effect will not cancel out.

The livetime asymmetry is calculated as:

$$A_{LT} = \frac{LT^+ - LT^-}{LT^+ + LT^-}, \quad (5.20)$$

where LT^\pm is the helicity gated livetime for each run. As seen in Fig. 5.19, the livetime asymmetry is small throughout the run period.

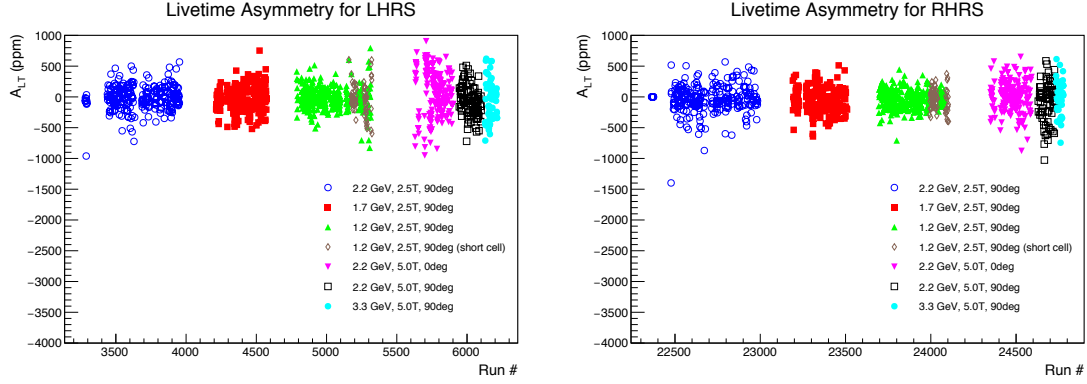


FIG. 5.19: Livetime asymmetries for production runs on the left and right HRS for the entire run period.

5.6 Optics and Acceptance Studies

5.6.1 Coordinate Systems

After an event is detected by the VDCs, two spatial and two angular coordinates can be extracted to represent the focal plane (fp) coordinate system. The quantities x_{fp} and θ_{fp} are given by the particle's position and tangent of the angle made by its trajectory projected onto the dispersive axis, and after being corrected for detector offsets from the ideal central ray of the spectrometer. By projecting onto the non-dispersive axis, two more quantities, y_{fp} and ϕ_{fp} , can be extracted. From there, we can determine the relative momentum (δ) and target coordinates $(x_{tg}, y_{tg}, \theta_{tg}$ and ϕ_{tg} , which are defined in Fig. 5.20) of the system by using the optics matrix elements. The quantity δ is defined as:

$$\delta = \frac{p - p_0}{p_0}, \quad (5.21)$$

where p is the measured momentum of the particle and p_0 is the central momentum setting of the spectrometer.

The target coordinate system is shown in Fig. 5.20. The sieve slit is a tungsten sheet with a thickness of 5mm that is used to calibrate the optics matrix (see Fig. 5.21). The z -axis points towards the sieve slit and is perpendicular to its surface. Furthermore, the z -axis can be defined as a line passing through the midpoint of the central sieve slit hole. If the spectrometer and sieve slit offsets are zero, the z -axis will pass through hall center, representing the origin of the target coordinate system. In this case, the quantity L represents the distance from hall center to the midpoint of the central hole of the sieve slit, and D is the horizontal offset of

the spectrometer from the hall center. The x_{tg} axis points vertically down into the dispersive plane, while the y_{tg} axis is parallel to the sieve surface in the transverse plane. The quantity Θ_0 represents the central angle of the spectrometer. With respect to the central trajectory, θ_{tg} represents the tangent of the out-of-plane angle and ϕ_{tg} represents the tangent of the in-plane angle.

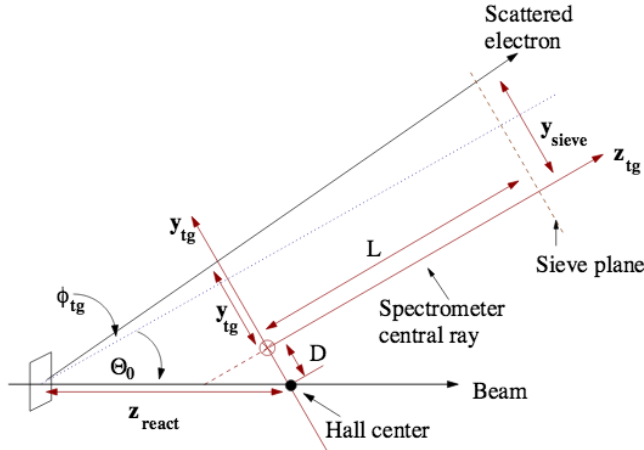


FIG. 5.20: A schematic of the target coordinate system for electron scattering from a foil target for the LHRS. Note that the x_{tg} coordinate points into the page, and is not shown here. Reproduced from [8].

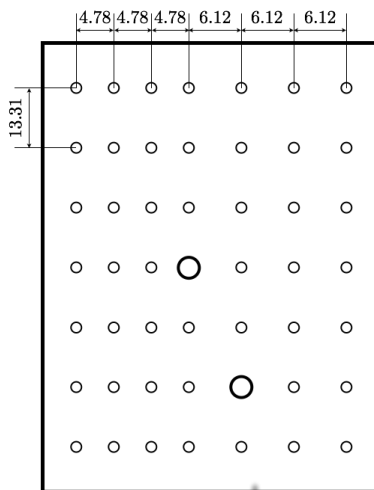


FIG. 5.21: Diagram of the sieve slit. The larger sized holes are used to determine the orientation of the hole pattern seen at the focal plane. Reproduced from [85].

5.6.2 Central Scattering Angle Measurement

Important to the overall optics study is the measurement of the scattering angle, θ , or the angle between the direction of the electron beam and the scattered electron. Measuring the scattering angle can be broken into two parts; determination of the central scattering angle θ_0 and spectrometer optics reconstruction of the target angles θ_{tg} and ϕ_{tg} [86]. The scattering angle can be expressed in terms of the central scattering angle and the target angles as:

$$\cos \theta = \frac{\cos \theta_0 - \phi_{tg} \sin \theta_0}{\sqrt{1 + \theta_{tg}^2 + \phi_{tg}^2}}. \quad (5.22)$$

The spectrometer angle θ_0 is the angle between the ideal beam line and an imaginary line drawn between the sieve slit and target center. There are two available methods to measure this angle; using the results from the beamline survey, or from a pointing measurement. The survey results give the location of the sieve slit and target center; the uncertainties of these measurements are shown in Table 5.1.

Object	Uncertainty (mm)
sieve slit x, y	0.5
sieve slit z	1.0
target z	1.5

TABLE 5.1: Uncertainties from survey measurements, reproduced from [87].

The central scattering angle calculated from survey measurement are shown in Table 5.2 for the left and right HRS. These measurements have an uncertainty of 0.7 mrad.

HRS Arm	θ_0 (rad)
LHRS	0.1007 ± 0.0007
RHRS	0.1009 ± 0.0007

TABLE 5.2: Value of the central scattering angle determined from survey results.

The second method to determine the central scattering angle is a pointing study, which takes advantage of elastic scattering from a target of mass M :

$$E' = \frac{E - E_{loss}}{1 + \frac{E - E_{loss}}{M} (1 - \cos \theta)} - E'_{loss}, \quad (5.23)$$

where E is the beam energy, E' is the energy of the scattered electron, θ is the scattering angle, and E_{loss} is the energy loss. Since the target mass is well known, an accurate measurement of the energy of the beam and scattered electron allows θ to be extracted. To improve the accuracy of this calculation, the difference in scattered electron energy of two different nuclei was used, as shown in Eqn. 5.24,

$$\Delta E' = E'_1 - E'_2 = \frac{E - E_{1,loss}}{1 + \frac{E - E_{1,loss}}{M_1} (1 - \cos \theta)} - \frac{E - E_{2,loss}}{1 + \frac{E - E_{2,loss}}{M_2} (1 - \cos \theta)} - (E'_{1,loss} - E'_{2,loss}). \quad (5.24)$$

If the two nuclei are in the same target, the E'_{loss} terms will cancel.

For this study, pointing data was taken with a 2.254 GeV electron beam for two cases, a carbon foil (in liquid helium), and a CH_2 foil target. Fig. 5.22 shows the method for measuring the scattering angle using the CH_2 foil. The electron beam hits the target foil at a distance x_b away from the nominal target center, at an angle of θ_b . For this experiment setup, the uncertainty of this offset from the nominal center is 1.5mm.

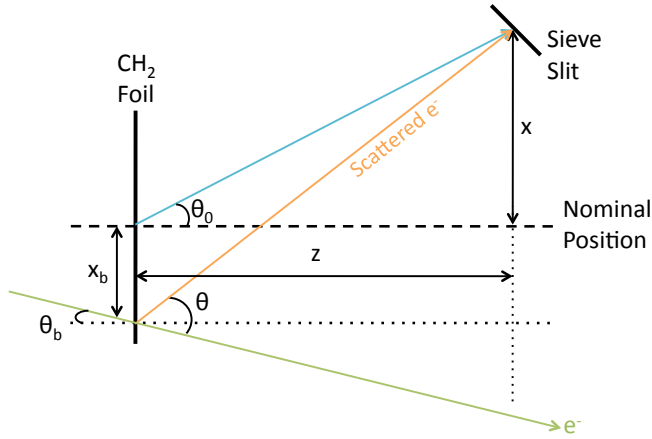


FIG. 5.22: Schematic of the setup to measure the central scattering angle using a CH₂ foil. The beam hits the foil at an offset of x_b from the nominal position, at angle θ_b . Reproduced from [86].

Before θ_b can be extracted, the relationship between θ and θ_b must be understood. A Monte-Carlo simulation was developed to determine the uncertainty of this relation, the details of which can be found in [86]. Additionally, the uncertainty of the incoming beam angle, which has a value of ~ 1.5 mrad, contributes directly to the uncertainty of θ .

For the second nucleus in the pointing study, runs were taken on a carbon foil in liquid helium. However, since the thickness of liquid helium in this setup is ~ 4.2 cm, the measurement results in a much larger uncertainty than in the case of the CH₂ foil. Due to these restrictions, the pointing method is not useful here. Given the level of uncertainty in the beam position and incoming angle measurements, the uncertainty in using the pointing study is larger than the uncertainty resulting from the method using survey results to calculate the central scattering angle.

5.6.3 HRS Optics

The spectrometer itself is a series of 4 magnets, (3 quadrupoles and 1 dipole), and the g_2^p experiment used an additional septum and target magnet (Fig. 5.23).

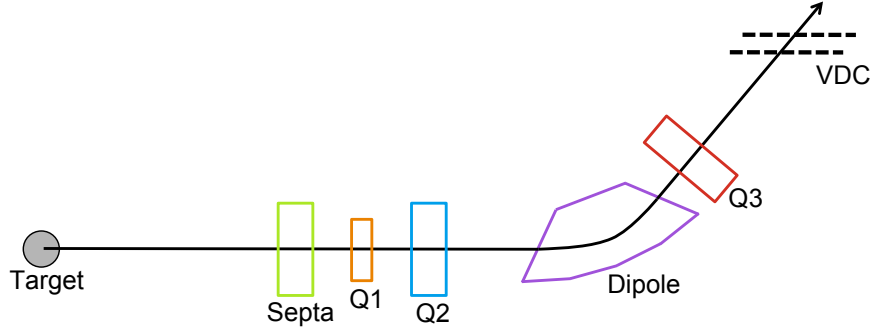


FIG. 5.23: The HRS is composed of 4 magnets in a QQQDQ configuration. The g_2^p experiment used an additional septum and target magnet.

The purpose of the optics study is to provide a matrix to transform kinematic variables at the focal plane, where the particle is detected, to the target plane, where the scattering occurs. To first-order, the optics matrix is given as:

$$\begin{pmatrix} \delta \\ \theta \\ y \\ \phi \end{pmatrix}_{tg} = \begin{pmatrix} \langle \delta | x \rangle & \langle \delta | x \rangle & 0 & 0 \\ \langle \theta | x \rangle & \langle \theta | \theta \rangle & 0 & 0 \\ 0 & 0 & \langle y | y \rangle & \langle y | \phi \rangle \\ 0 & 0 & \langle \phi | y \rangle & \langle \phi | \phi \rangle \end{pmatrix} \begin{pmatrix} x \\ \theta \\ y \\ \phi \end{pmatrix}_{fp}. \quad (5.25)$$

The angular matrix elements are calibrated using the sieve slit described above to obtain the real scattering angle from geometry. Once the scattering angle is known, it can be used in conjunction with elastic scattering data taken on a carbon foil target with point beam to calibrate the momentum matrix elements.

This method works well for the case with no target field. However, once the target magnetic field is included, the sieve slit method is no longer useful. Instead, the calibration is split into two different parts; from the focal plane to the sieve slit, and then from the sieve slit to the target. To go from the focal plane to the sieve slit, the transform matrix described above is the starting point, and a simulation is used to determine the effective θ and ϕ angle. A map of the target field was then used to calculate the trajectory of the scattered electron from the sieve slit to the target. The target field map was created prior to the start of the experiment and is discussed in Ref. [88–90].

5.7 Target Polarization

The polarized target setup was described in Sec. 4.4. Here we will discuss the determination of the target polarization calibration constants. Full details of the analysis are discussed in Ref. [91].

5.7.1 Determination of Calibration Constants

Nuclear Magnetic Resonance (NMR) is used to measure the proton polarization, which was recorded every 30 seconds. The resulting “Q-curve” created by the LCR circuit represents the impedance as a function of the frequency of the RF generator. For an unpolarized target, this curve would be a parabola. However, when the material is polarized, a dip or a peak can be seen in the curve. For example, a loss of energy in the circuit near the resonance frequency would indicate the *absorption* of energy by the proton as its spin is flipped. In Fig. 5.24, the raw signal is seen in red with the blue baseline signal in the background. The baseline signal represents

the non-polarized NMR signal. Baseline measurements were taken often during the run period, particularly after anneals were performed. The baseline is subtracted from the raw signal, revealing the dip or peak resulting from proton polarization, as seen in Fig. 5.25. A 3rd order polynomial is used to fit the wings of the resulting baseline-subtracted data in order to remove any residual background. The area of the resulting curve is proportional to the polarization:

$$\frac{P_{Enh}}{P_{TE}} = \frac{(AG)_{Enh}}{(AG)_{TE}}, \quad (5.26)$$

which includes the polarization (P), area of the NMR curve (A), and amplifier gain used during the measurement (G). The subscript TE refers to measurements taken when the target was at thermal equilibrium. The polarization can be predicted for these conditions, as described in Sec. 4.4.1. The subscript Enh refers to the *enhanced* polarization, that is, when microwaves are used to drive the spin transitions to enhance the polarization resulting from thermal equilibrium.

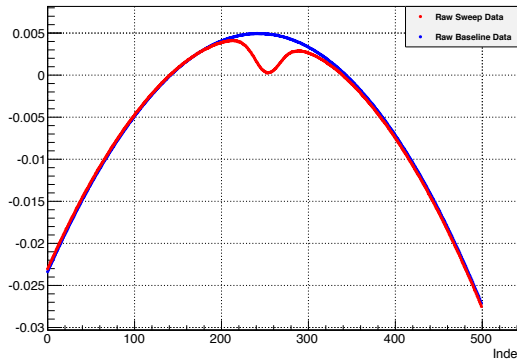


FIG. 5.24: An example of a raw signal (red) and baseline signal (blue). The x -axis index is proportional to the frequency of the RF generator.

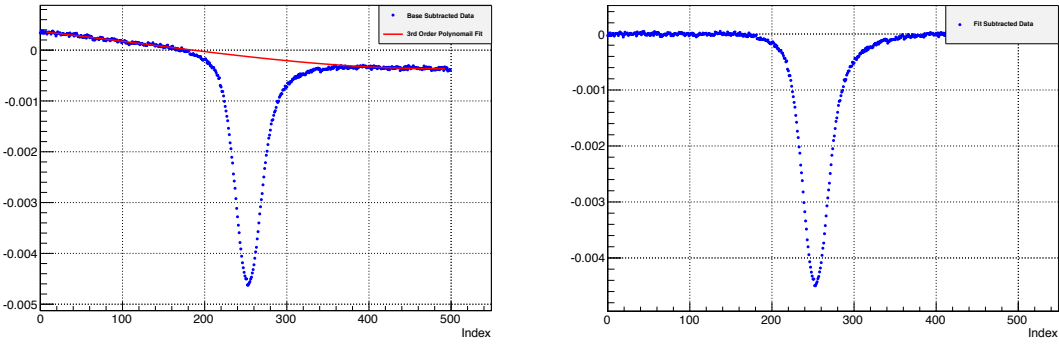


FIG. 5.25: On the left is a baseline-subtracted signal with a 3^{rd} order polynomial fit to the wings. The plot on the right includes the subtraction of the 3^{rd} order fit.

Calibrations were determined using Eqn. 5.26, where P_{TE} is the thermalized polarization and A_{TE} is the thermalized NMR area. A different calibration constant was calculated each time a TE measurement was performed, and averaged for each different ammonia sample. The number of TE measurements taken on a material varied from 1 to 8 measurements, depending on the time available. The calibration constant was then used to determine the average polarization on a run-by-run basis. The final polarization results can be seen in Fig. 5.26 and 5.27. An average polarization of 70% and 15% was seen for the 5 T and 2.5 T setting, respectively.

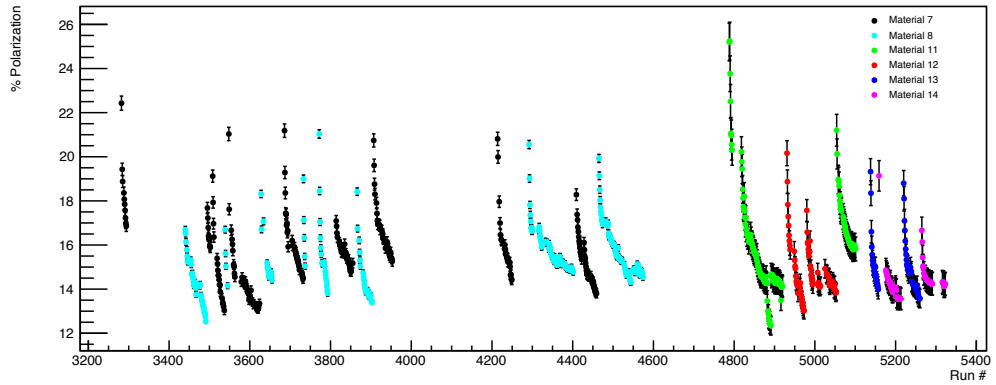


FIG. 5.26: LHRs run-by-run polarization results for a magnetic field setting of 2.5 T.

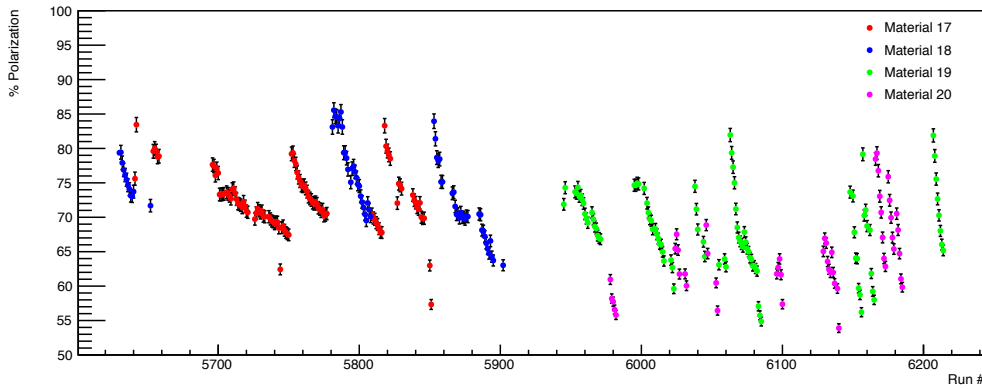


FIG. 5.27: LHRs run-by-run polarization results for a magnetic field setting of 5 T.

5.7.2 Polarization Uncertainty

There are two main factors that contribute to the uncertainty for each calibration constant. First is the uncertainty in the fit of the raw NMR signal, and the second is the uncertainty in the magnetic field and temperature readings, which contribute to the TE polarization calculation. To determine the uncertainty in the NMR fit (δ_A), a Gaussian curve of known area was generated, and the variance in the area between the integrated NMR signal and the Gaussian area was determined as the uncertainty. Depending on the quality of the NMR signal, this uncertainty varied largely, but was never greater than 3%.

The uncertainty in the target field reading, δ_B , is dictated by the stability of the magnet power supply, and was given as 2%. The target temperature was monitored by both a ^3He , and a ^4He , manometer that converted a pressure reading in the target nose to a temperature. The variance in the two measurements was considered to be the uncertainty, δ_T . The total uncertainty in the TE polarization calculation can

then be given as:

$$\delta_{TE_{pol}} = \frac{\mu B}{kT} \sqrt{\left[\left(1 - \tanh^2 \frac{\mu B}{kT} \right) \frac{\delta_B}{B} \right]^2 + \left[\left(1 - \tanh^2 \frac{\mu B}{kT} \right) \frac{\delta_T}{T} \right]^2}. \quad (5.27)$$

Combining $\delta_{TE_{pol}}$ with the uncertainty from the area of the NMR fit ($\delta_{TE_{area}}$), the final uncertainty in the calibration constant, δ_{CC} , is calculated by Eqn. 5.28:

$$\delta_{CC} = \frac{P_{TE}}{A_{TE}} \sqrt{\left(\frac{\delta_{TE_{pol}}}{P_{TE}} \right)^2 + \left(\frac{\delta_{TE_{area}}}{A_{TE}} \right)^2}. \quad (5.28)$$

5.8 Beam Position Reconstruction

An accurate reconstruction of the beam position is necessary for optics calibrations and production data. This section will discuss the equipment and analysis involved in the determination of the beam position. The full details of this analysis can be found in Ref. [92].

5.8.1 Equipment

The requirements of the g_2^p experiment were a challenge for the design of the beamline diagnostics. Specifically, in order to minimize depolarization and radiation damage to the target, production runs were taken at low currents of 50-100 nA. Due to these low current limits, some of the equipment used previously in Hall A needed to be replaced. A close up of the beamline components is shown in Fig. 5.28.

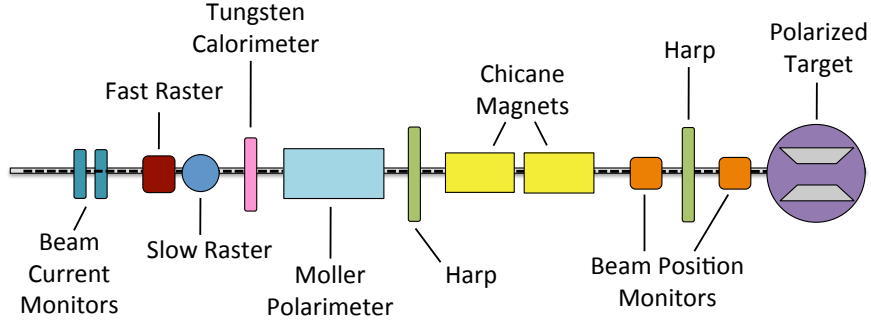


FIG. 5.28: Beam position reconstruction equipment.

Two beam position monitors (BPMs), used to measure the position and angle of the beam, were installed upstream of the target and downstream of the chicane magnets. Each BPM is composed of four antennae (x_+, x_-, y_+, y_-), placed on the interior wall of the BPM pipe at an angle of 90° to one another (Fig. 5.29). The BPM chamber is part of the beam pipe, and performs a non-invasive measurement. The output signal from the antenna was connected to two systems in the DAQ setup, in order to prevent redundancy in the measurement. The first system is a 13-bit ADC with an integration time of 50 ns that is triggered by electron events. The second system is an 18-bit ADC with an integration time of 875 μs , that is triggered by a 1 kHz helicity signal. The relation between the signal recorded in the ADC and the signal received in the antenna is given by Eqn. 5.29, where A is the signal recorded in the ADC, ϕ is the signal received in the antenna, and g represents the BPM receiver gain.

$$A \propto \phi \cdot 10^{\frac{g}{20}}. \quad (5.29)$$

The harps provide a measurement of the absolute beam position, which is used to calibrate the BPMs. Harp measurements are not reliable at low beam currents,

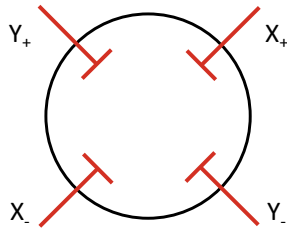


FIG. 5.29: Diagram of a beam position monitor (BPM).

such as the 50-100 nA range required by this experiment. Instead, it is possible to use high current, pulsed beam. The harps used previously in Hall A were not suitable in either low current continuous wave or high current pulsed beam conditions, so two new harps were installed for the g_2^p experiment. The new harps have 50 μm thick wires and an updated fork and controller chassis that were designed to work in high current pulsed beam. Due to space limitations, one harp (1H05A) was installed between the two BPMs, and the other (1H04) was placed upstream of the first chicane magnet. Harp H105A was rotated 45° with respect to the beam pipe, for convenience. Each harp is made up of 3 wires, (as shown in Fig. 5.30), arranged in a fork that can be moved in and out of the beam with a motor.

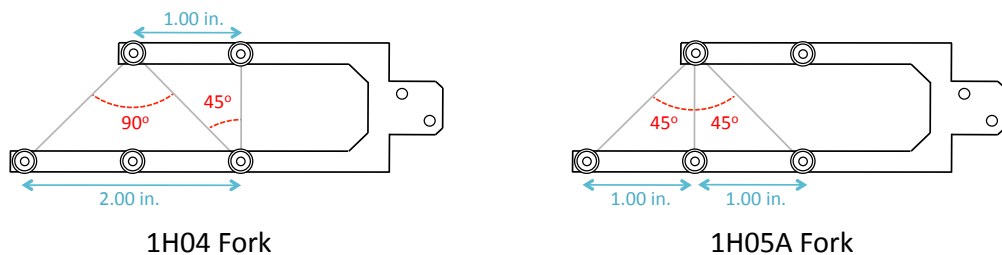


FIG. 5.30: Diagram of the fork design in the two harps; the wire configuration is slightly different between the two.

A fast and slow raster system is employed to minimize radiation damage and

depolarization of the target material. Located 17 m upstream of the target, each raster contains 2 dipole magnets and scans the beam in the x and y direction. The fast raster is used to spread the beam into a 2 mm by 2 mm square pattern. The slow raster further spreads the beam into a circular pattern with a diameter of ~ 2 cm. The combination of the fast and slow raster yields a beam with a diameter of ~ 2.2 cm, which is spread evenly over the face of the target, the diameter of which is 2.5 cm.

5.8.2 Calibration

The two harps described above were used to provide an absolute measurement of the beam position. The vertical wire was used to determine the x -position of the beam, while the angled wires were used to determine the y -position. The original position of the wires was measured during survey to a level of 0.1 mm. The data recorded from the wire signals (“peak”) is combined with survey data to determine the absolute beam position, using Eqn. 5.30. The x -position can be determined from the vertical wire (denoted by |), and the y -position is determined from the angled wires (\ and /).

$$\begin{aligned} pos_x &= survey_{|} - peak_{|} \\ pos_y &= peak_{/} - survey_{/} = survey_{\backslash} - peak_{\backslash} \\ &= \frac{1}{2} [(survey_{\backslash} - survey_{/}) - (peak_{\backslash} - peak_{/})] \end{aligned} \quad (5.30)$$

To determine the beam position from the BPMs, the traditional “diff/sum”

method is used. Eqn. 5.31 shows the method to calculate the X and Y position:

$$\begin{aligned} X = kx_b &= k \frac{\phi_{x,+} - \phi_{x,-}}{\phi_{x,+} + \phi_{x,-}}, \\ Y = ky_b &= k \frac{\phi_{y,+} - \phi_{y,-}}{\phi_{y,+} + \phi_{y,-}}, \end{aligned} \quad (5.31)$$

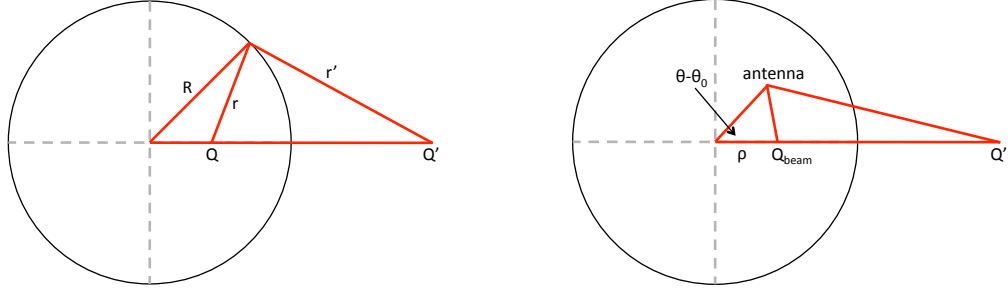


FIG. 5.31: On the left is a diagram of the method of images used to determine the beam position. On the right is an example of the signal on the BPM antenna.

where $\phi_{x,\pm}$ ($\phi_{y,\pm}$) is the signal from BPM antenna x_\pm , (y_\pm), and k is the amplitude factor. The method of images [93], depicted in Fig. 5.31 is used to express the signal ϕ seen from the beam:

$$\phi = \phi_0 I \frac{R^2 - \rho^2}{R^2 + \rho^2 - 2R\rho \cos(\theta - \theta_0)} \quad (5.32)$$

where ϕ_0 is a constant related to the BPM geometry and output resistance, R is the radius of the BPM vacuum chamber, and I is the beam current. The angle θ is the angle of each BPM antenna with the x -axis (in the Hall A coordinate system), given by $\frac{\pi}{4}$, $\frac{3\pi}{4}$, $-\frac{\pi}{4}$ and $-\frac{3\pi}{4}$, and θ_0 is the angle of the beam with the x -axis. Rewriting

Eqn. 5.31 using Eqn. 5.32 gives us an expression for the x and y beam position:

$$\begin{aligned} x &= \frac{Rx_b}{x_b^2 + y_b^2} \left(1 - \sqrt{1 - (x_b^2 + y_b^2)} \right) \\ y &= \frac{Ry_b}{x_b^2 + y_b^2} \left(1 - \sqrt{1 - (x_b^2 + y_b^2)} \right). \end{aligned} \quad (5.33)$$

The receiver on the BPM was designed to have a linear response to the beam current:

$$\phi = a(A - A_{ped} + b), \quad (5.34)$$

where A is the ADC signal, and A_{ped} is the pedestal value, which is determined when the beam is off. The variable a is related to the gain of the antenna and b is a calibration constant determined for each antenna. The data from harp scans is then used to calibrate the BPM signals. Fig. 5.32 shows a comparison of the harp scan data and BPM data, after calibration.

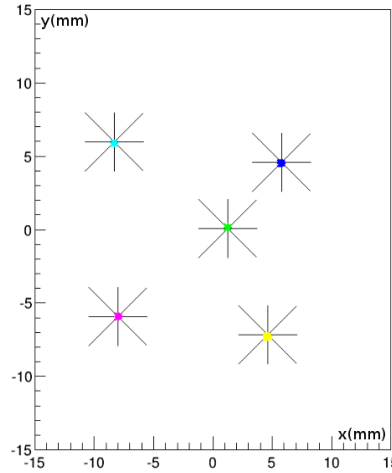


FIG. 5.32: Comparison of harp scan and BPM data

Data from harp scans (asterisk) compared with calibration BPM data (colored points). Reproduced from [92].

The linear method is appropriate for the case with no target field, but when the transverse target field, and therefore the chicane magnets, are included, the reconstruction of the beam position at the target becomes more complicated. For these settings, a simulation is used to transport a series of beam positions to the target, using the known target field map [88–90]. However, it should be noted that the transportation method is only useful for transporting the *average* beam position to the target; in order to obtain the beam position event-by-event additional information is needed from the raster.

As mentioned above, the fast and slow raster spread the beam out to a 2 x 2 mm square and \sim 2 cm circular pattern, respectively. An example of the raster patterns are shown in Fig. 4.5. The square pattern of the fast raster is produced using a triangle function, while the circular shape of the slow raster is constructed using a sinusoidal function modulated by a $t^{\frac{1}{2}}$ function. The calibration of the slow raster was done in two different ways. The first method was to use the raster shape produced by the calibrated BPM. Data were taken at several different raster sizes, using the same beam current, to understand the relationship between the raster magnet current and the corresponding beam position offset at the location of the beam. This result must then be transported to give the value of the offset at the target. The alternate method used to calibrate the slow raster is to take advantage of the two small holes located between the ammonia cells on the target stick. This hole was used for a CH₂ foil for optics data, but was left empty during most of the run period. The aluminum material of the target stick is significantly more dense than the liquid helium surrounding the stick, so it is possible to image the hole using the rastered beam. Since the hole is known to have a diameter of 10 ± 0.2 mm, it can be used to calibrate the size of the raster pattern.

The calibration of the fast raster uses a similar procedure, but is made more

difficult by the faster frequency used by the system and the need for a higher frequency, low-pass filter setting for the BPM [92]. The use of the high frequency filter means that a larger beam current is necessary to produce a clear picture of the beam, without using such a large current that it causes damage to the target material.

Using the information from the raster system in combination with the BPM data, we can construct the beam position event by event as:

$$x = x_{BPM} + x_{raster,fast} + x_{raster,slow} \quad (5.35)$$

$$y = y_{BPM} + y_{raster,fast} + y_{raster,slow}.$$

Contributions to the beam position uncertainty take the following forms:

- Early on in the run period, the auto-gain function on the BPMs was used to modify the BPM gain with fluctuating beam currents. It was found that for low currents used during g_2^p , the signal-to-noise ratio so low that the auto-gain mode did not function properly. The BPMs were then changed to a fixed gain setting for all CW beam, with an alternate gain setting for beam tuning.
- The fluctuating gain setting also caused the pedestal value to change during data taking. In general, the pedestal values were determined in two ways; during beam trips, and using dedicated pedestal runs taken when the beam was off. It was found there was little difference between these two methods. For each run, the pedestal value was assigned using pedestal data taken at the closest gain setting.
- There is some uncertainty associated with the locations of the BPMs from survey.
- The uncertainty from the target field, which is on the level of $\sim 1\%$.

5.9 Dilution Analysis

Since the g_2^p target is not a pure proton target, we must consider the events which scatter from unpolarized material, such as nitrogen, liquid helium, and the aluminum foil end caps on the ammonia target cups. This correction, known as the *dilution factor*, is denoted by f and scales the asymmetry, as shown in Eqn. 5.4. This section will summarize the general method used to obtain preliminary results for the dilution factor. Full details of the analysis can be found in Ref. [94]

5.9.1 Method

The measured asymmetry is diluted by events that scatter from unpolarized material in the target, which we will call background material. The asymmetry can be re-written in terms of N_{bg} , which represents the number of detected events which result from scattering from background material:

$$A_{measured} = \frac{(N_+ + \frac{1}{2}N_{bg}) - (N_- + \frac{1}{2}N_{bg})}{(N_+ + \frac{1}{2}N_{bg}) + (N_- + \frac{1}{2}N_{bg})} = \frac{N_+ - N_-}{N_+ + N_- + N_{bg}}. \quad (5.36)$$

The quantity N_{bg} represents the sum of the number of counts from each of the various unpolarized materials: $N_{bg} = N_N + H_{He} + N_{Al}$. The number of counts from a given material can be written, in general, as

$$N_x = \frac{N_0 \rho_x L_x}{e M_x} \sigma_x, \quad (5.37)$$

N_0 is Avogadro's number, A is the experimental acceptance, ρ_x is the density of the material, M_x is the atomic mass, L_x is the thickness of the material, and σ_x is the

cross section for material x with radiative effects included. The number of counts resulting from background material can now be expressed as

$$N_{bg} = \frac{AN_0}{e} \left(\frac{\rho_{NH_3} L_{tg} p_f}{M_{NH_3}} \sigma_N + \frac{\rho_{He} L_{tg} (1 - p_f)}{M_{He}} \sigma_{He} + \frac{\rho_{Al} L_{Al}}{M_{Al}} \sigma_{Al} \right), \quad (5.38)$$

where p_f is the relative length of ammonia material compared to the liquid helium in which it is submersed. The extraction of this quantity, known as the *packing fraction*, is discussed in the next section. To determine the background contribution, data were taken on various target materials, including a pure carbon target, which can be scaled using simulation results to approximate the nitrogen contribution, a dummy cell, which is identical to the ammonia cell, but without ammonia material, and empty runs, where the target stick was moved out of the way and data was taken on only liquid helium. Each of these runs can be written in terms of its composite materials:

$$\begin{aligned} N_{empty} &= \frac{AN_0}{e} \frac{\rho_{He} L_{tg}}{M_{He}} \sigma_{He} \\ N_{dummy} &= \frac{AN_0}{e} \left(\frac{\rho_{He} L_{tg}}{M_{He}} \sigma_{He} + \frac{\rho_{Al} L_{foil}}{M_{Al}} \sigma_{Al} \right) \\ N_{carbon} &= \frac{AN_0}{e} \left(\frac{\rho_C L_C}{M_C} \sigma_C + \frac{\rho_{He} (L_{tg} - L_C)}{M_{He}} \sigma_{He} \right) \end{aligned} \quad (5.39)$$

Rewriting Eqn. 5.38 in terms of Eqn. 5.39 gives us an expression for the background contribution in terms of available data:

$$N_{bg} = a \frac{M_C \rho_{NH_3} L_{tg} p_f}{M_{NH_3} \rho_C L_C} \left(N_{carbon} - \left(\frac{L_{tg} - L_C}{L_{tg}} \right) N_{empty} \right) + N_{dummy} - p_f N_{empty}, \quad (5.40)$$

where a represents the factor used to scale σ_C to σ_N .

An approximation for the scaling factor a is to take the ratio of the number of constituent nucleons in each material, i.e.:

$$\sigma_C = 6\sigma_H, \quad \sigma_N = 7\sigma_H \quad \rightarrow \quad \sigma_N = \frac{7}{6}\sigma_C. \quad (5.41)$$

While this may be sufficient in the DIS region, this approximation breaks down in the resonance region. Instead of using a constant scaling factor, Eqn. 5.41 is re-written as $\sigma_N = a\sigma_C$. The scaling factor a is determined by producing a cross section model, including radiative corrections, which is tuned to match the g_2^p data. The deviation of the model from the data is included in the final systematic uncertainty.

5.9.2 Preliminary Dilution Factor

For the purpose of this analysis, a preliminary dilution factor was extracted using Bosted model predictions [25] for the various target materials. The results are combined as follows:

$$f = \frac{3^{\frac{\rho_{NH_3} L_{tg} p_f}{M_{NH_3}}} \sigma_H}{\frac{\rho_{NH_3} L_{tg} p_f}{M_{NH_3}} (\sigma_N + 3\sigma_H) + \frac{\rho_{He} L_{tg} (1-p_f)}{M_{He}} \sigma_{He} + \frac{\rho_{Al} L_{Al}}{M_{Al}} \sigma_{Al}}. \quad (5.42)$$

The results using this method are shown in Fig. 5.33 and 5.34. For this thesis, only the settings with $E_{beam} = 2.2$ GeV and a 5 T magnetic field (both longitudinal and transverse settings) were analyzed. Materials 17 and 18 are associated with the longitudinal setting, and materials 19 and 20 were used during the transverse setting. The p_f values used in this analysis will be described in the next section.

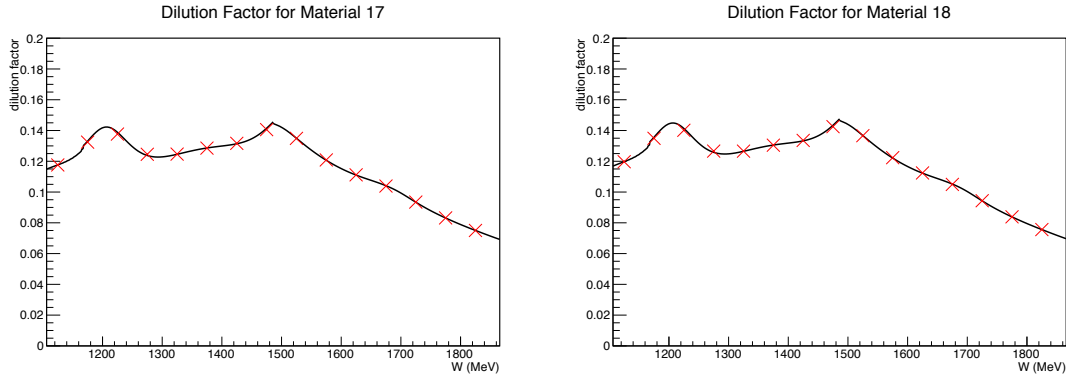


FIG. 5.33: Preliminary dilution factors for materials 17 and 18, which were used for the $E_{beam} = 2.2$ GeV, $B_{target} = 5$ T, longitudinal setting. The black line shows the model prediction, and the red markers give the average value for each 50 MeV bin in W .

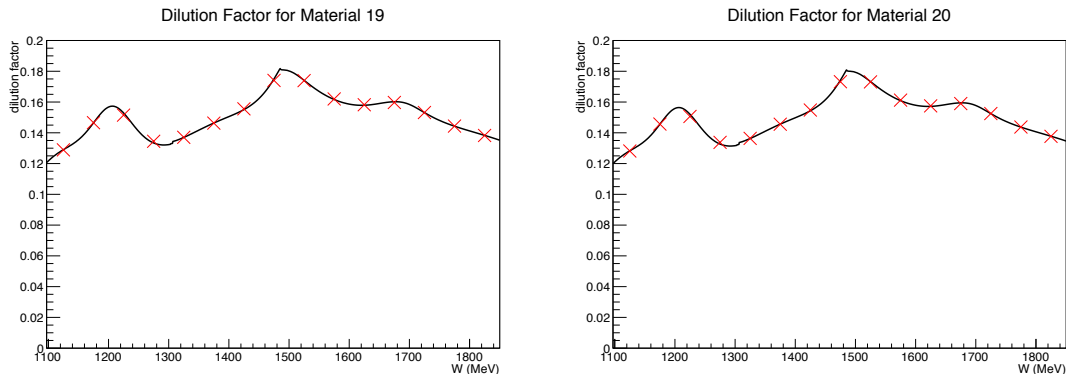


FIG. 5.34: Preliminary dilution factors for materials 19 and 20, which were used for the $E_{beam} = 2.2$ GeV, $B_{target} = 5$ T, transverse setting. The black line shows the model prediction, and the red markers give the average value for each 50 MeV bin in W .

5.10 Packing Fraction Analysis

In order to determine the dilution factor described in the previous section, the packing fraction (p_f), or the proportion of ammonia target material to the liquid helium in which it is immersed must be extracted. Ideally, each target cell would be completely full of ammonia, but due to the size and shape of the ammonia beads

along with different load sizes, the packing fraction can change for each material sample. A total of 10 different ammonia samples were used throughout the experiment. This section will discuss the procedure and challenges involved in the extraction of this quantity. This analysis is also detailed in Ref. [95].

5.10.1 Method

This analysis will utilize data taken at the elastic setting. For the $E_{beam} = 2.2$ GeV, $B_{target} = 2.5$ T setting, there is good separation between the nitrogen and hydrogen elastic peaks, so it will be used as an example for this section. Similar to the dilution analysis, this method will take advantage of the dilution runs taken throughout the run period. To extract the packing fraction, two types of runs are needed, an ammonia run and a dummy run. The normalized yield for each run is calculated as:

$$Y = \frac{N \cdot ps}{Q \cdot LT \cdot \epsilon} \quad (5.43)$$

where:

- N = number of events
- ps = prescale factor
- Q = total charge for the run
- LT = livetime correction to account for computer deadtime in the system
- ϵ = product of detector efficiencies, including scintillator trigger efficiency [82], Cherenkov and lead glass calorimeter detector efficiencies [96], and multitrack efficiencies [83].

The yield from a production run can be broken into its constituent parts, as shown in Eqn. 5.44:

$$Y_{prod} = Y_{He}^{out} + (1 - p_f)Y_{He}^{full} + p_f Y_{NH_3}^{full}, \quad (5.44)$$

where Y_x refers to the yield from ammonia (NH_3), and helium (He). The superscript “*full*” refers to the yield resulting from a target cell full of that material. The superscript “*out*” refers to the yield from liquid helium inside the target nose, but outside the target cell. The contributions from helium can be obtained using the yield from a dummy run, Y_{dummy} , given in Eqns. 5.45 and 5.46. A simple diagram of the target cell is shown in Fig. 5.35, which shows the length of the target cell (l_{tg}) and the total length of the target nose (l_{tot}).

$$Y_{He}^{out} = \left(\frac{l_{tot} - l_{tg}}{l_{tot}} \right) Y_{dummy}, \quad (5.45)$$

$$Y_{He}^{full} = \left(\frac{l_{tg}}{l_{tot}} \right) Y_{dummy}. \quad (5.46)$$

Eqn. 5.44 can be manipulated to solve for p_f :

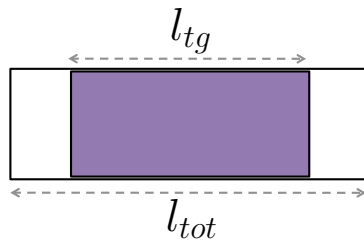


FIG. 5.35: Diagram of the target cell inside the target nose. The length of the target cell is given by $l_{tg} = 28.2$ mm, while the full length of the target nose is given by $l_{tot} = 37$ mm.

$$p_f = \left(\frac{l_{tot}}{l_{tg}} \right) \left(\frac{Y_{prod}}{Y_{dummy}} - 1 \right) \left(\frac{Y_{NH_3}^{full}}{Y_{He}^{full}} - 1 \right)^{-1}. \quad (5.47)$$

From the data, it is not possible to obtain the quantity $Y_{NH_3}^{full}$, which represents the yield if the entire cell were to be filled with ammonia. Although it is possible to extract the quantity Y_{He}^{full} , as shown in Eqn. 5.46, it is advantageous to leave Eqn. 5.47 in this form so that absolute cross sections are not necessary; the acceptance factors will cancel out in the cross section ratio. In terms of the cross section, the yield can be expressed as

$$Y_x \sim \sigma_x \rho_x. \quad (5.48)$$

The cross section input σ_x will be discussed later in this section. The target number density, ρ_x , is expressed by

$$\rho_x = \frac{\rho_{mass} l_x N_0}{M_{molar}}, \quad (5.49)$$

where σ_{mass} , l_x , and M_{molar} are the mass density, length, and molar mass of the material, respectively. Substituting Eqn. 5.48 in Eqn. 5.47 gives the following expression for the packing fraction:

$$p_f = \left(\frac{l_{tot}}{l_{tg}} \right) \left(\frac{Y_{prod}}{Y_{dummy}} - 1 \right) \left(\frac{\sigma_N \frac{\rho_{mass,N}}{M_N} + \sigma_H \frac{\rho_{mass,H}}{M_H}}{\sigma_{He} \frac{\rho_{mass,He}}{M_{He}}} - 1 \right)^{-1} \quad (5.50)$$

5.10.2 Yield Spectra and Fitting Routine

In Eqn. 5.50, the quantities Y_{prod} and Y_{dummy} are obtained from data; an example of the yield from a production and a dummy run is shown in Fig. 5.36. The yield is binned in 1 MeV bins in ν , where $\nu = E - E'$, the difference between the incident and scattered electron energy. For this energy setting, the region of interest is from $\nu = 0$ to $\nu = 13$ MeV. For an ammonia run, this region includes the nitrogen and helium elastic peaks, which cannot be resolved individually, and a small percentage of “contamination” from the second peak. For a dummy run, this region includes the

elastic peak and the contamination from the helium quasi-elastic peak. Since only elastic events are of interest, it is necessary to quantify the level of contamination from the second peak in the production and dummy yield spectra.

To fit the entire spectra, the fit is broken down into two parts; the first and second peaks. The components of the fit differ between the dummy and production run, as described below.

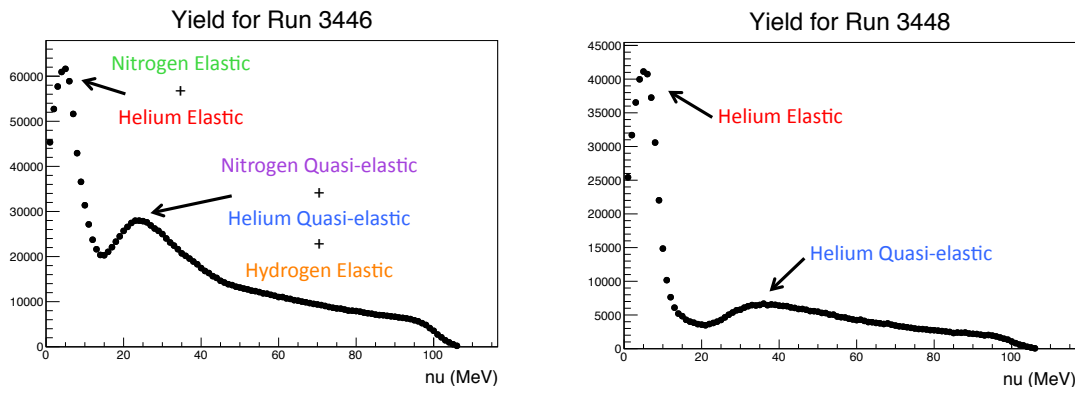


FIG. 5.36: Yield vs. ν for a production run (left) and a dummy run (right).

5.10.3 Dummy Run

The yield spectrum for a dummy run is comprised predominantly of one material, helium. In reality, this data also contains contributions from the aluminum target cell cap, but the contribution from Al (that is, the difference between a helium and dummy run) is negligible. For this case, there are only two features to fit, the elastic peak and the quasi-elastic peak. The elastic peak is not a true Gaussian, as it has some radiative tail, so a Landau-Gaussian convolution function is used to fit this peak. As it is only necessary to fit the left side of the quasi-elastic peak, a simple

Gaussian function can be used. An example of this fit can be seen in Fig. 5.37. The level of contamination is small, less than 5% of the total area of the elastic peak.

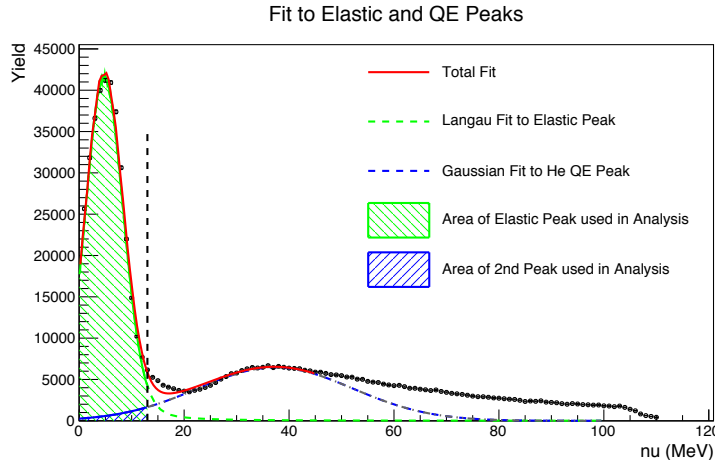


FIG. 5.37: Dummy run 3448 with fit. The vertical dotted line represents the cut-off point for the region of interest for this analysis.

5.10.4 Ammonia Run

The yield spectrum for an ammonia run is more complicated, as it has contributions from ammonia (nitrogen and hydrogen) and helium. The fit is, therefore, also more complicated. The elastic peak, which contains contributions from both nitrogen and helium elastic events, is again fit with a Landau-Gaussian (Langau) convolution fit. The second peak is comprised of nitrogen and helium quasi-elastic events as well as hydrogen elastic events. This peak is fit with the sum of three functions; the nitrogen and helium peaks are each fit with a Gaussian, and the hydrogen peak is fit with a Landau function. To understand the relative contributions from each material, the Quasi-Free-Scattering (QFS) model was used within the g2psim package, a Monte Carlo simulation package based on Geant4 and built to match the experimental settings of the g_2^p experiment.

Quasi-Free Scattering Model:

The QFS model, developed by Lightbody and O'Connell [97], is used to predict cross sections for electron scattering. The cross section is accurate to within 20% for an incident electron energy between 0.5-5 GeV. The Fortran code parameterizes electron scattering using five reaction channels in the impulse approximation:

- Quasielastic scattering
- Two nucleon process in the dip region
- Δ resonance production
- Higher nucleon resonance electron production (two resonances, centered at $W = 1500$ MeV and 1700 MeV)
- Deep inelastic scattering

This model will be used to understand the relative contributions from nitrogen, helium, and hydrogen in the quasi-elastic region for an ammonia run.

Matching QFS Model Parameters to Data:

Within the model, there are 3 parameters that can be adjusted by the user:

- P_f : the Fermi momentum of the target nucleon
- Eps: the nucleon separation energy
- Epsd: the delta separation energy

For this analysis, the separation energies were chosen to best match the data, while the Fermi momentum values are reasonable for that material. The delta separation parameter does not contribute to this study, so it will not be discussed here.

Before fitting the production run, the data can be compared to the QFS model predictions to parameterize the different contributions. The dummy run is the simplest scenario to start with. Fig. 5.38 shows the simulation result compared to the data, with the associated QFS parameters. Similarly, the carbon dilution run can be used to understand the QFS parameters for carbon, which in turn can be used to estimate the nitrogen parameters. The comparison between the QFS prediction and data for a carbon run is shown in Fig. 5.39. From these results it is possible to constrain the fit of the helium and nitrogen contributions to the overall fit. The hydrogen elastic peak contribution can be predicted using elastic form factors, which allows for additional constraints on the location and width of the hydrogen elastic peak.

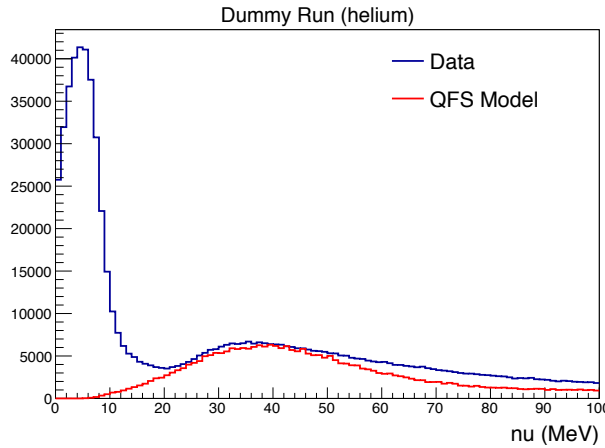


FIG. 5.38: Dummy run compared to simulation output using the QFS model.

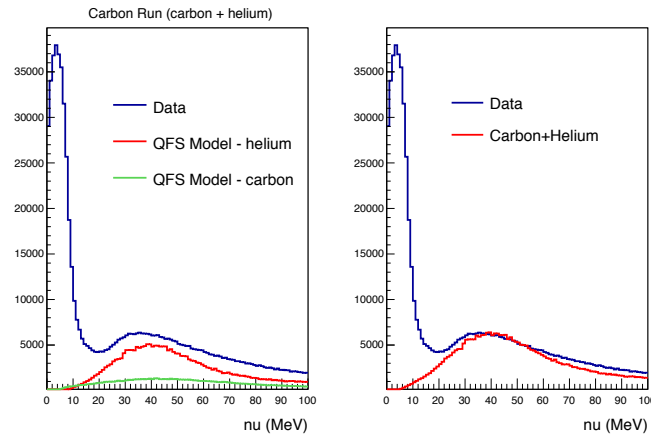


FIG. 5.39: Carbon run compared to simulation output using the QFS model.

In the overall fit to the second peak, the nitrogen and helium contributions are fit with a Gaussian function. The remaining hydrogen elastic peak is fit with a Landau-Gaussian convolution function. An example of the total fit is seen in Fig. 5.40. The fits shown in Figs. 5.37 and 5.40 give the level of contamination from the second peak to the elastic peak, which is $\sim 5.7\%$ for this example.

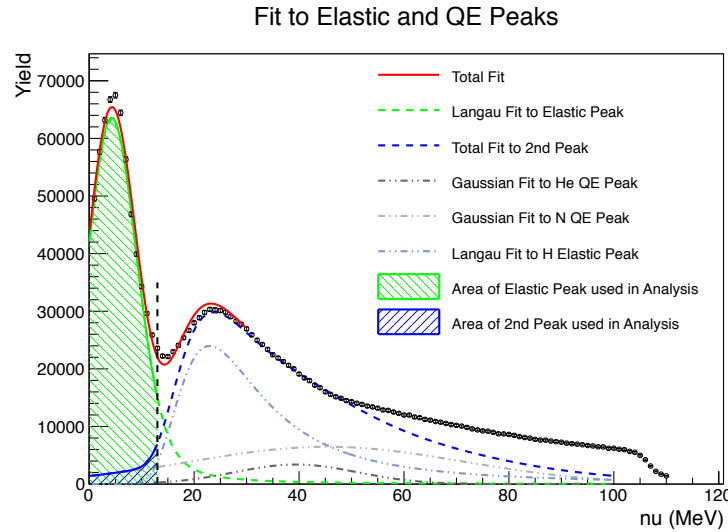


FIG. 5.40: Production run 3446 with fit. The vertical dotted line represents the cut-off point for the region of interest for this analysis.

5.10.5 Cross Section Model Input

The final piece of input required to extract the packing fraction are the cross section ratios σ_N/σ_{He} and σ_H/σ_{He} . The cross sections are determined using elastic form factors [98, 99]. Since the cross section ratios are being combined with data, which already includes radiative effects, it is necessary to first radiate the cross sections. This is accomplished using the g2psim package, which has been constructed to mirror the experimental conditions. An example of the simulation results is shown in Fig. 5.41. The cross section ratios were determined for each run individually, using the beam position values for that run.

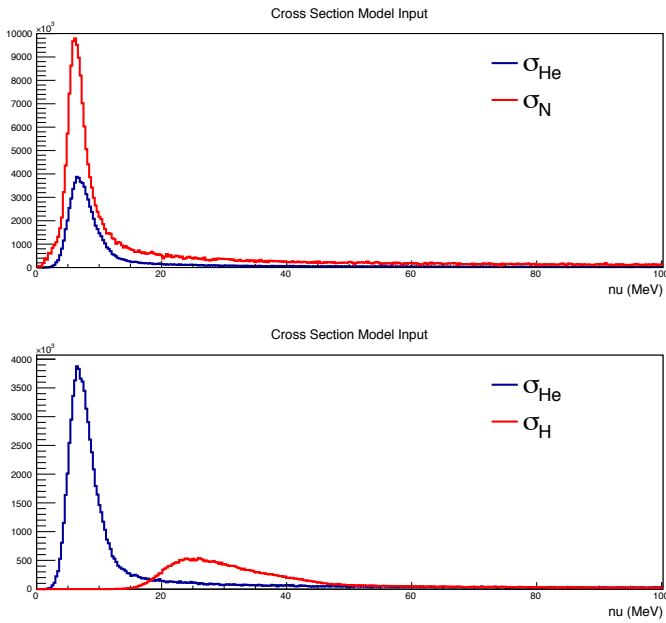


FIG. 5.41: Elastic cross section results from g2psim for the $E_{beam} = 2.2$ GeV, $B_{target} = 2.5$ T, transverse setting.

5.10.6 Variation in Yields

For several settings, there was a significant variation seen in the yields for different runs taken at the elastic setting. In an effort to flesh out the cause for this variation, many parameters were checked to test the effect on the yield for each run. These checks will be described for each configuration in this section.

$E_{beam} = 2.2 \text{ GeV}$, $B_{target} = 2.5 \text{ T}$, Transverse (setting 1):

The normalized yields (calculated using Eqn. 5.43) are shown in Fig. 5.42.

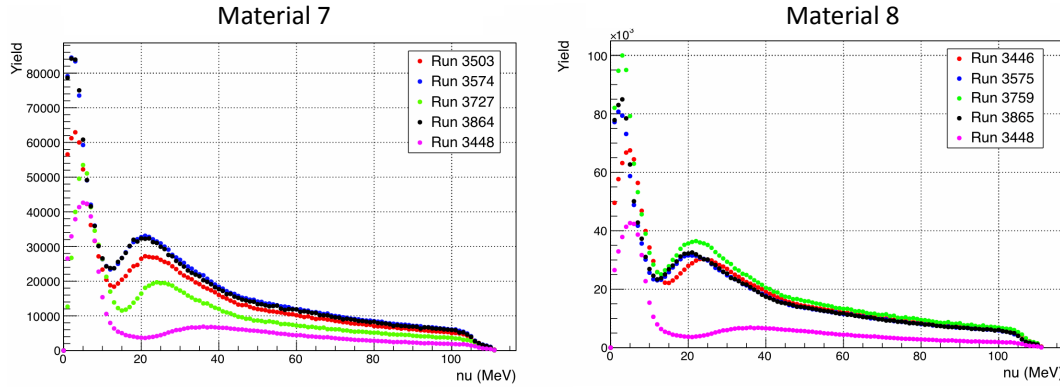


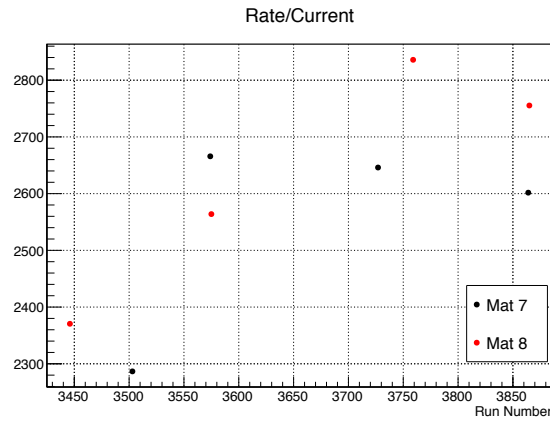
FIG. 5.42: Yields for elastic runs (production and dummy) in setting 1 (materials 7 and 8) Run 3448 is a dummy run, so the yield is expected to be different for this run.

Normalization values for $E_{beam} = 2.2$ GeV, $B_{target} = 2.5$ T, Transverse, $p_0 = 2.228$ GeV

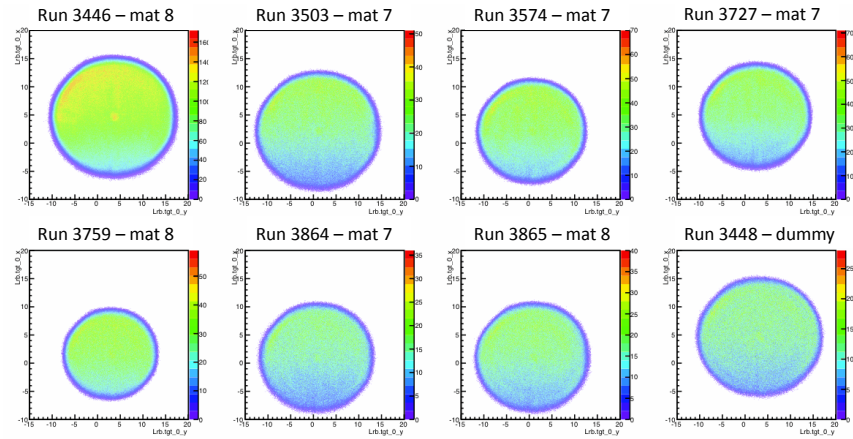
Run #	Material	Charge (μ C)	Livetime	Cer. Det.	PR. Det.	Multi Track	Trigger	Prescale
				Eff.	Eff.	Eff.	Eff.	Factor
3446	8	66.6	0.895	0.99996	0.99980	0.916	0.99984	15
3503	7	14.5	0.915	0.99995	0.99984	0.920	0.99984	15
3574	7	18.9	0.944	0.99997	0.99988	0.904	0.99985	20
3575	8	17.9	0.949	0.94949	0.99995	0.908	0.99986	20
3727	7	16.6	0.941	0.94114	0.99995	0.915	0.99986	18
3759	8	11.4	0.925	0.92468	0.99993	0.908	0.99987	19
3864	7	8.9	0.857	0.99995	0.99980	0.905	0.99986	20
3865	8	9.6	0.944	0.94431	0.99991	0.907	0.99986	20
3448	dummy	8.6	0.948	0.99995	0.99986	0.967	0.99984	7

TABLE 5.3: Normalization values for setting 1.

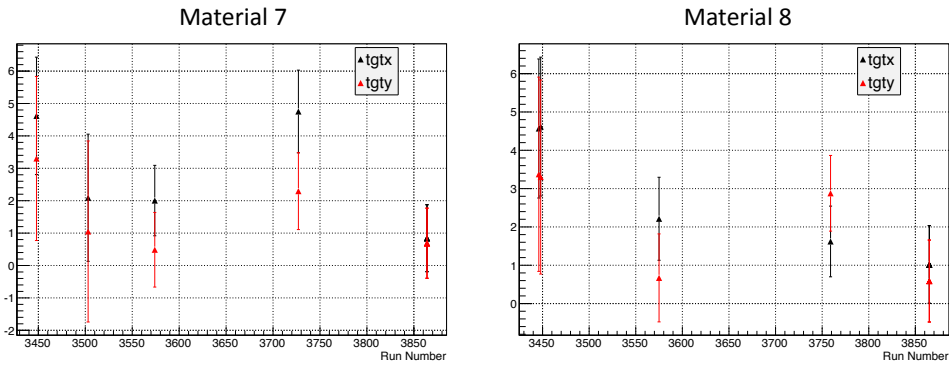
For the same kinematic settings, the ratio of the raw singles trigger rate (T3 on the LHRS) divided by the beam current for each run should be stable; for this setting variation is seen in this quantity (see Fig. 5.42). The likely reason for this discrepancy is that the raster size was changed following a Moller measurement on March 30th. After the measurement, higher rates were seen in the third arm detector, suggesting that the beam was scraping something. Reducing the raster size from 2 cm to 1.8 cm caused the rates to return to normal. For this set of runs, the change in raster size occurred after run 3503, but before run 3574. It is also apparent from these plots that the beam position was also shifting throughout this series of runs. The ratio of rate/current, change in raster size, and central beam position with uncertainty for each run is plotted in Fig. 5.42.



(a) The ratio of T3 rate to current for setting 1.



(b) Raster patterns for setting 1 (target x vs. target y).



(c) Beam position at the target for elastic runs in setting 1. The y-axis shows the x/y beam position in mm.

FIG. 5.42: Yield stability checks for setting 1.

Since the only dummy run in this setting was taken with the large raster, it may not be appropriate to compare the yield to production runs taken without first applying a beam size correction to account for this difference.

$E_{beam} = 1.7 \text{ GeV}$, $B_{target} = 2.5 \text{ T}$, Transverse (setting 2):

The normalized yields and associated normalization constants are shown in Fig. 5.43 and Table 5.4, and the yield stability checks are shown in Fig 5.44. The yields are considerably more stable for this set of runs, but there does appear to be some drifting.

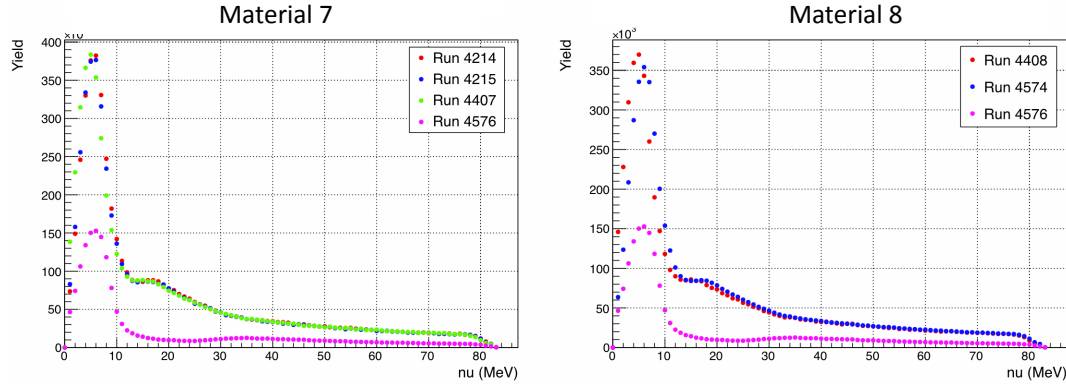
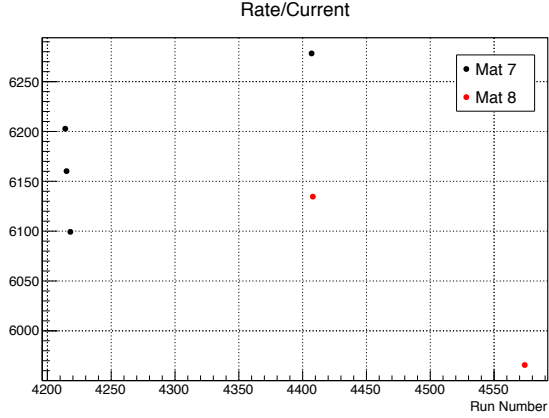


FIG. 5.43: Yields for elastic runs (production and dummy) in setting 2 (materials 7 and 8). Run 4576 is a dummy run, so the yield is expected to be different for this run.

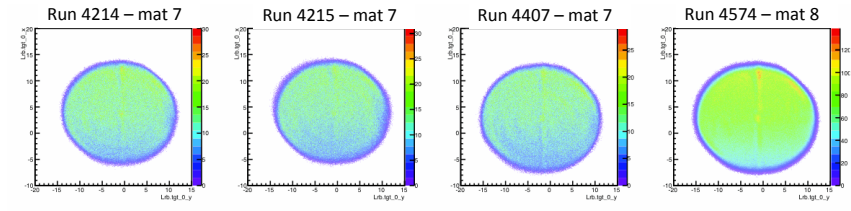
Normalization values for $E_{beam} = 1.7$ GeV, $B_{target} = 2.5$ T, Transverse, $p_0 = 1.691$ GeV

Run #	Material	Charge (μ C)	Livetime	Cer.	Det.	PR.	Det.	Multi Track	Trigger	Prescale
				Eff.	Eff.	Eff.	Eff.	Eff.	Eff.	Factor
4214	7	7.5	0.951	0.99994	0.99976	0.819	0.99982	44		
4215	7	6.9	0.934	0.99991	0.99976	0.826	0.99983	40		
4407	7	5.9	0.830	0.99991	0.99979	0.818	0.99980	30		
4408	8	5.9	0.845	0.99995	0.99980	0.822	0.99980	30		
4574	8	45.1	0.874	0.99991	0.99979	0.818	0.99981	34		
4576	dummy	6.6	0.870	0.99993	0.99987	0.937	0.99978	11		

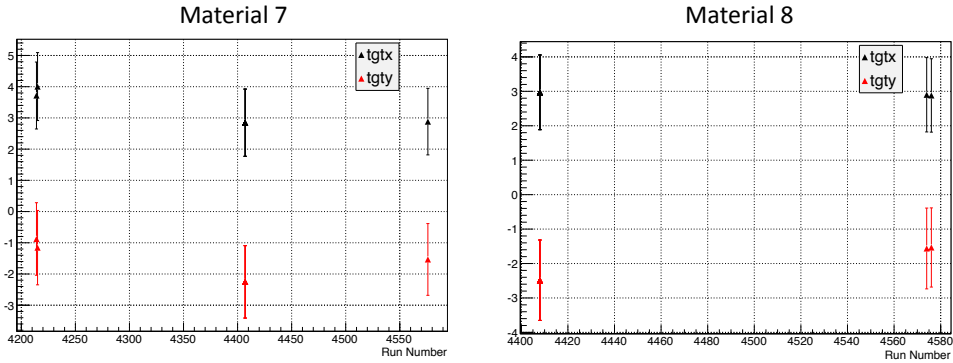
TABLE 5.4: Normalization values for setting 2.



(a) The ratio of T3 rate to current for setting 2.



(b) Raster patterns for setting 2 (target x vs. target y).



(c) Beam position at the target for elastic runs in setting 2. The y-axis shows the x/y beam position in mm.

FIG. 5.44: Yield stability checks for setting 2.

$E_{beam} = 1.2 \text{ GeV}$, $B_{target} = 2.5 \text{ T}$, Transverse (setting 3):

The normalized yields and associated normalization constants are shown in

Fig. 5.45 and Table 5.5. A number of runs were also taken in this setting with a short ammonia cell (material 14), which was 1.295 cm in length. For some runs, beam position information was not available due to the low current limitations of the BPMs. In these cases, neighboring runs were included in the raster and beam position plots shown below in Fig. 5.45. It should be noted, however, that the neighboring runs may not give an accurate estimate of the missing beam position information, since significant changes in the current can cause a shift in the beam position.

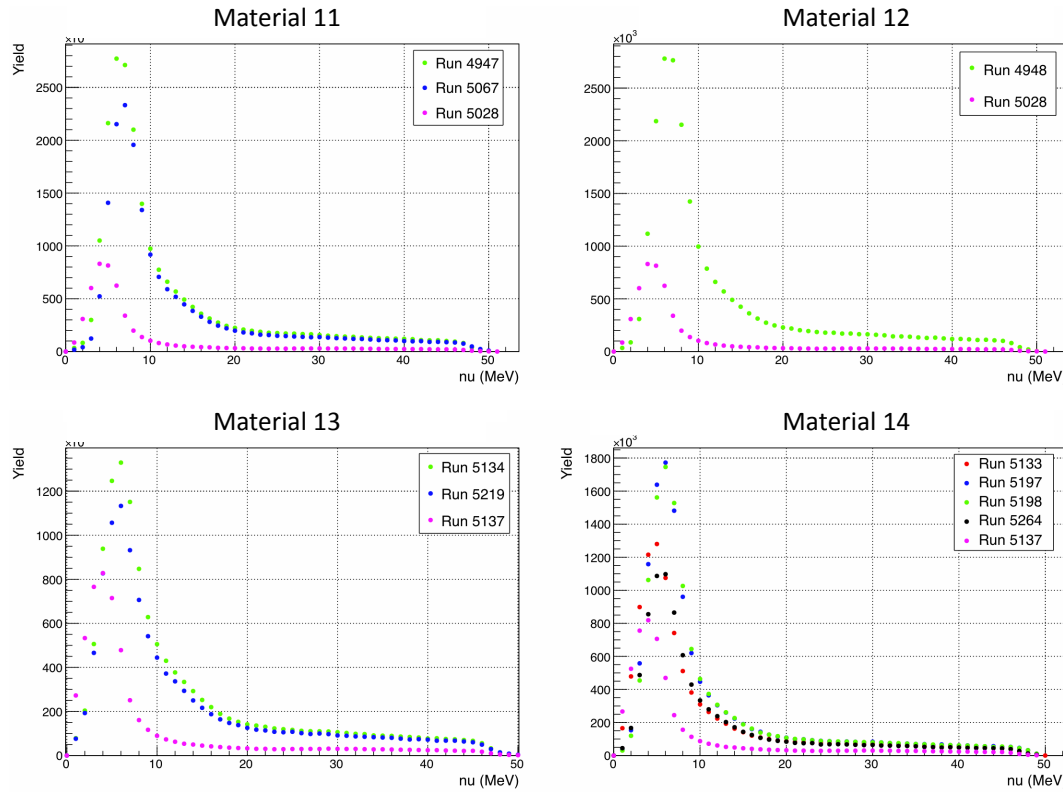
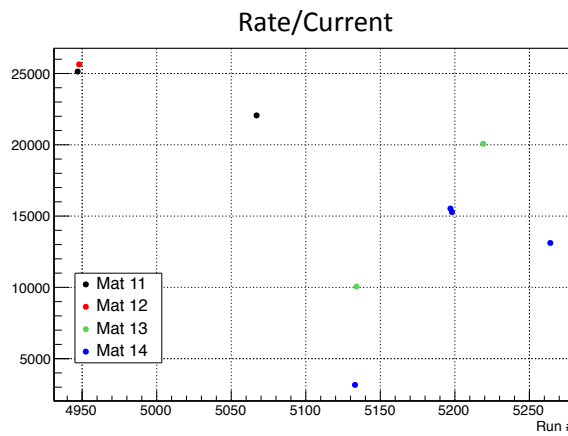


FIG. 5.45: Yields for elastic runs (production and dummy) in setting 3 (materials 11, 12, 13 and 14). Material 14 is a short cell. Runs 5028 and 5137 were dummy runs, so the yield is expected to be different for these runs.

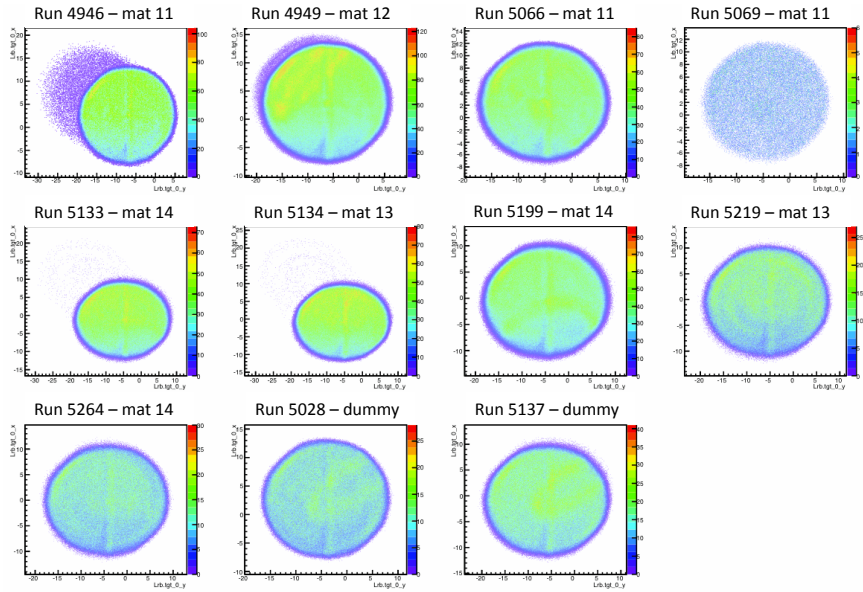
Normalization values for $E_{beam} = 1.2$ GeV, $B_{target} = 2.5$ T, Transverse, $p_0 = 1.151$ GeV

Run #	Material	Charge (μ C)	Livetime	Cer. Det.	PR. Det.	Multi Track	Trigger	Prescale
				Eff.	Eff.	Eff.	Eff.	Factor
4947	11	1.6	0.926	0.99976	0.99954	0.850	0.99976	34
4948	12	2.0	0.922	0.99974	0.99957	0.848	0.99975	34
5067	11	3.7	0.928	0.99955	0.99936	0.737	0.99973	65
5133	14	21.3	0.983	0.99896	0.99845	0.610	0.99968	150
5134	13	18.3	0.917	0.99710	0.99771	0.495	0.99960	150
5197	14	3.3	0.894	0.99972	0.99939	0.793	0.99972	45
5198	14	3.4	0.889	0.99972	0.99945	0.791	0.99971	45
5219	13	8.1	0.880	0.99639	0.99806	0.485	0.99959	137
5264	14	9.1	0.922	0.99881	0.99885	0.594	0.99965	109
5028	dummy	7.3	0.885	0.99984	0.99942	0.812	0.99966	40
5137	dummy	14.4	0.921	0.99925	0.99881	0.822	0.99968	100

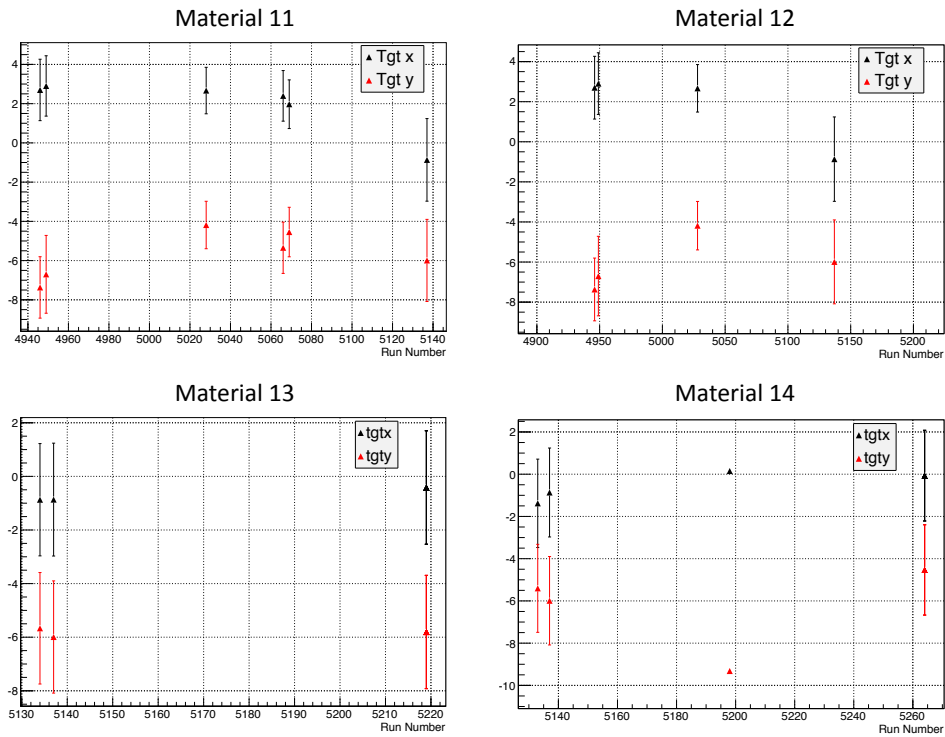
TABLE 5.5: Normalization values for setting 3.



(a) The ratio of T3 rate to current for setting 3.



(b) Raster patterns for setting 3 (target x vs. target y). The structure in run 4946 suggests that the beam position was not stable during this run.



(c) Beam position at the target for elastic runs in setting 3. The y-axis shows the x/y beam position in mm. No beam position uncertainty information was available for run 5198.

FIG. 5.45: Yield stability checks for setting 3.

$E_{beam} = 2.2 \text{ GeV}$, $B_{target} = 5 \text{ T}$, Longitudinal (setting 4):

The normalized yields and associated normalization constants are shown in Fig. 5.46 and Table 5.6.

Normalization values for $E_{beam} = 2.2 \text{ GeV}$, $B_{target} = 5 \text{ T}$, Longitudinal, $p_0 = 2.228 \text{ GeV}$

Run #	Material	Charge (μC)	Livetime	Cer. Det.	PR. Det.	Multi Track	Trigger	Prescale
				Eff.	Eff.	Eff.	Eff.	Factor
5626	17	6.9	0.912	0.99991	0.99987	0.919	0.99977	15
5628	18	7.2	0.875	0.99989	0.99985	0.917	0.99977	14
5631	18	33.5	0.878	0.99993	0.99986	0.916	0.99977	14
5635	18	44.2	0.884	0.99993	0.99986	0.917	0.99976	14
5639	18	44.8	0.876	0.99994	0.99986	0.915	0.99976	14
5641	17	47.5	0.866	0.99992	0.99987	0.912	0.99977	14
5652	18	29.9	0.898	0.99993	0.99977	0.911	0.99977	16
5654	17	48.8	0.921	0.99993	0.99986	0.916	0.99977	16
5655	17	35.7	0.926	0.99994	0.99985	0.918	0.99977	16
5656	17	48.0	0.937	0.99993	0.99987	0.918	0.99976	16
5704	17	42.9	0.852	0.99994	0.99988	0.915	0.99976	13
5651	dummy	7.5	0.916	0.99998	0.99989	0.963	0.99965	7

TABLE 5.6: Normalization values for setting 4.

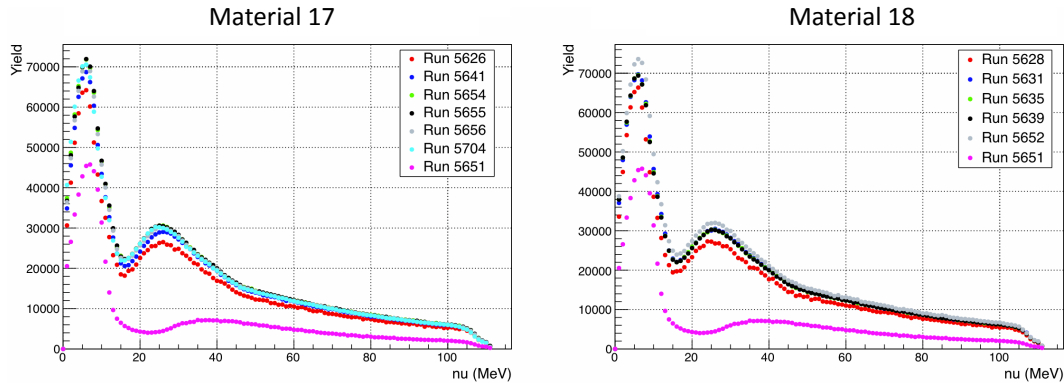
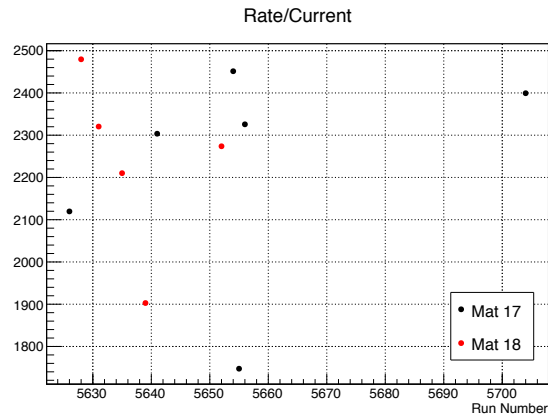
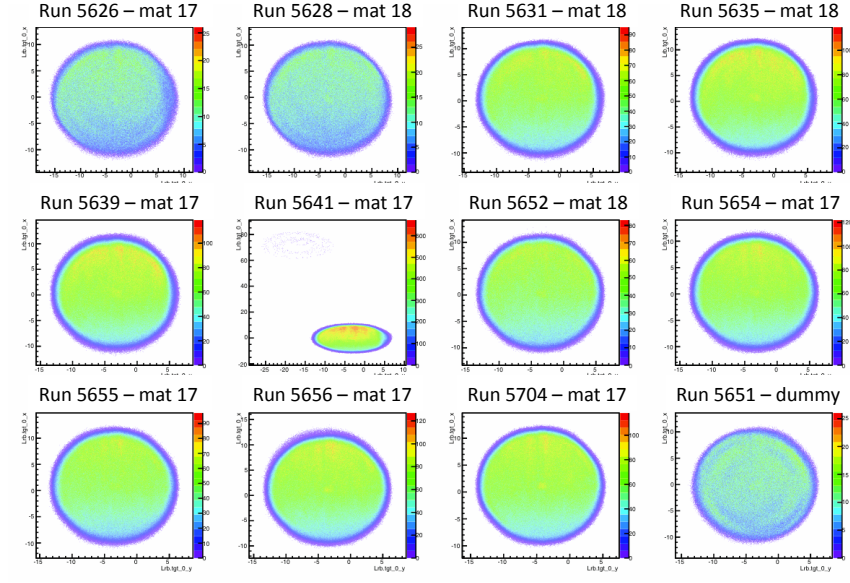


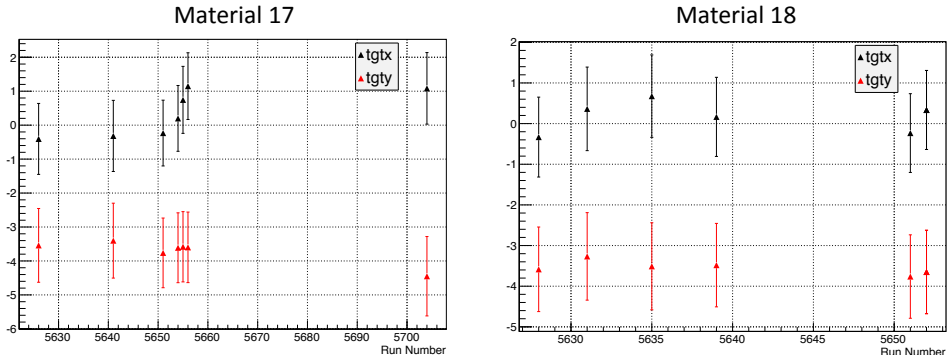
FIG. 5.46: Yields for elastic runs (production and dummy) in setting 4 (materials 17 and 18).



(a) The ratio of T3 rate to current for setting 4.



(b) Raster patterns for setting 4 (target x vs. target y). The structure in the top left portion of the raster pattern for run 5641 suggests that the beam position was not stable during this run.



(c) Beam position at the target for elastic runs in setting 4. The y-axis shows the x/y beam position in mm.

FIG. 5.47: Yield stability checks for setting 4.

$E_{beam} = 2.2 \text{ GeV}$, $B_{target} = 5 \text{ T}$, Transverse (setting 5):

The normalized yields and associated normalization constants are shown in Fig. 5.48 and Table 5.7. There is some drifting seen in the yields for this set of runs.

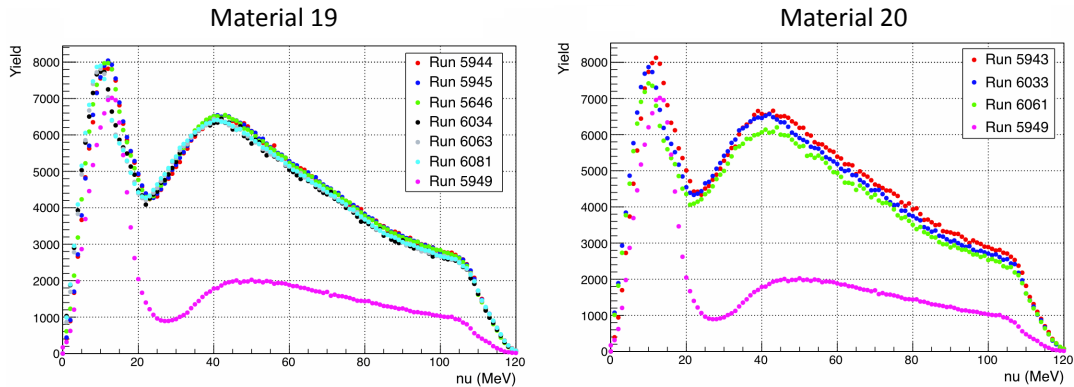
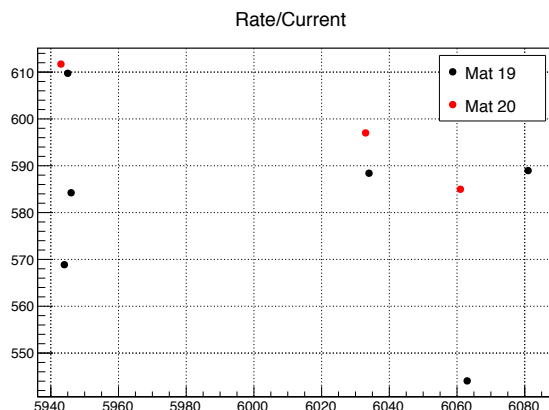


FIG. 5.48: Yields for elastic runs (production and dummy) in setting 5 (materials 19 and 20).

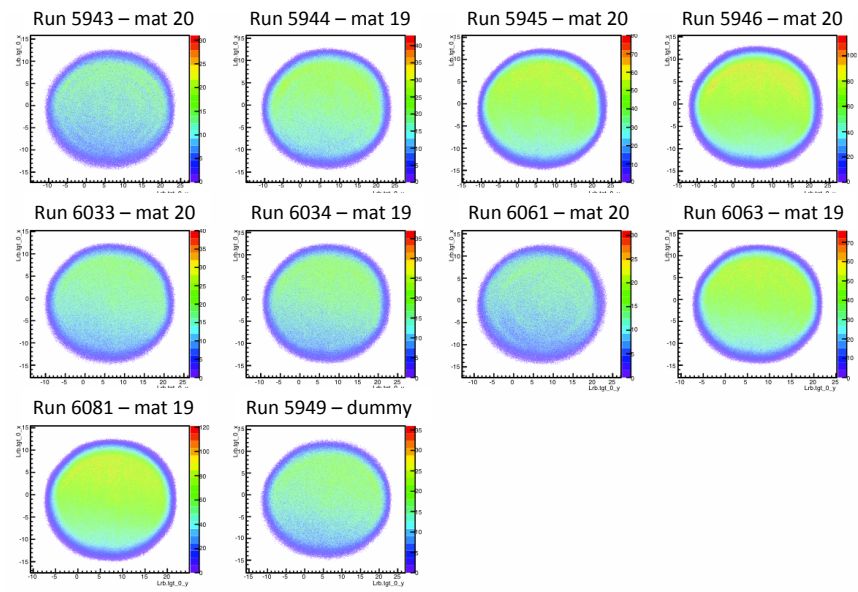
Normalization values for $E_{beam} = 2.2$ GeV, $B_{target} = 5$ T, Transverse, $p_0 = 2.228$ GeV

Run #	Material	Charge (μ C)	Livetime	Cer. Det.	PR. Det.	Multi Track	Trigger	Prescale
				Eff.	Eff.	Eff.	Eff.	Factor
5943	20	7.9	0.907	0.99993	0.99988	0.977	0.99980	4
5944	19	14.6	0.907	0.99995	0.99987	0.977	0.99979	4
5945	19	31.7	0.901	0.99995	0.99986	0.976	0.99980	4
5946	19	50.5	0.916	0.99995	0.99987	0.977	0.99980	4
6033	20	13.6	0.933	0.99992	0.99988	0.973	0.99981	5
6034	19	13.4	0.934	0.99993	0.99986	0.974	0.99980	5
6061	20	9.8	0.909	0.99993	0.99990	0.971	0.99980	5
6063	19	38.2	0.878	0.99994	0.99988	0.969	0.99980	5
6081	19	65.9	0.885	0.99994	0.99988	0.969	0.99980	5
5949	dummy	13.0	0.904	0.99994	0.99990	0.989	0.99982	2

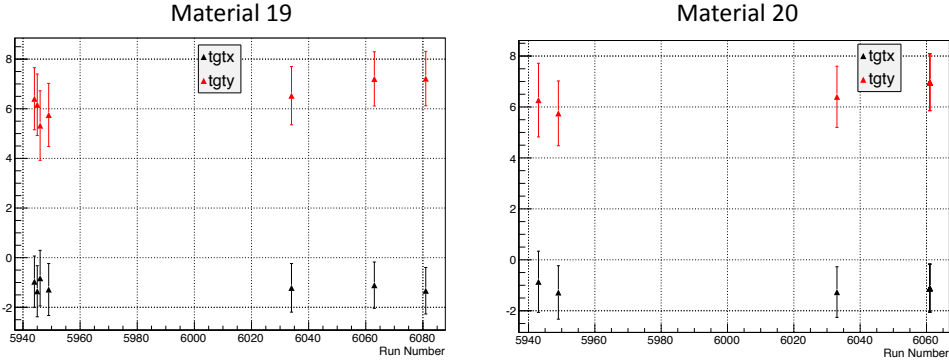
TABLE 5.7: Normalization values for setting 5.



(a) The ratio of T3 rate to current for setting 5.



(b) Raster patterns for setting 5 (target x vs target y).



(c) Beam position at the target for elastic runs in setting 5. The y-axis shows the x/y beam position in mm.

FIG. 5.48: Yield stability checks for setting 5.

5.10.7 Uncertainty

There are several contributions to the overall uncertainty for the packing fraction. Setting 1 (runs 3448 and 3446) will be used as an example.

- Standard propagation of uncertainty; the contributing factors are listed in Table 5.8. The uncertainty of σ_N and σ_{He} was determined to be 3% and the uncertainty of σ_H was determined to be 1%.
- To calculate the packing fraction, the quantity Y_{prod} and Y_{dummy} are determined by summing over the elastic peak, while the level of contamination is determined using the fitting routine described above. $Y_{prod} = Y_{elastic} - Y_{contam} + Y_H$, where $Y_{elastic}$ is the sum over the elastic peak, Y_{contam} is the contamination determined from the fit, and Y_H is the hydrogen contribution, which is also determined from the fit. $Y_{dummy} = Y'_{elastic} - Y'_{contam}$, where $Y'_{elastic}$ is the sum over the elastic peak of the dummy run, and Y'_{contam} is the contamination determined from the fit. The difference between the fit and the sum is also included in the overall

uncertainty, the area from the fit is calculated by adding the area of the elastic and contamination fits (Table 5.9).

Contributions to Uncertainty		
Quantity	Value	Uncertainty
l_{tg}	28.2 mm	0.1 mm
l_{tot}	37 mm	0.1 mm
Y_{prod}	618866.1	1534.8
Y_{dummy}	356016.1	641.2
σ_N/σ_{He}	2.9149	4.24%
σ_H/σ_{He}	0.0042	3.16%

TABLE 5.8: Contributions to the packing fraction uncertainty. The yield (Y) has arbitrary units. Values for setting 1 are shown here as an example.

Contributions to Uncertainty from Fit			
Run	Sum ($\nu = 0\text{-}13$)	Area from Fit ($\nu = 0\text{-}13$)	% Difference
Production	647701.9	636250.2	1.78
Dummy	362430.8	358233.7	1.16

TABLE 5.9: Contribution to the packing fraction uncertainty from the fitting routine. Values for setting 1 are shown here as an example.

5.10.8 Results

An example of the fit to the dummy and production run is shown for each setting, followed by a table of the packing fraction results for each elastic run. The table also includes the quantity Y_{prod}/Y_{dummy} , which is the ratio of the sum over the elastic peak of the production and dummy runs, and the quantity σ_N/σ_{He} , which

is the cross section (from model) ratio determined using the beam position for that run.

Setting 1:

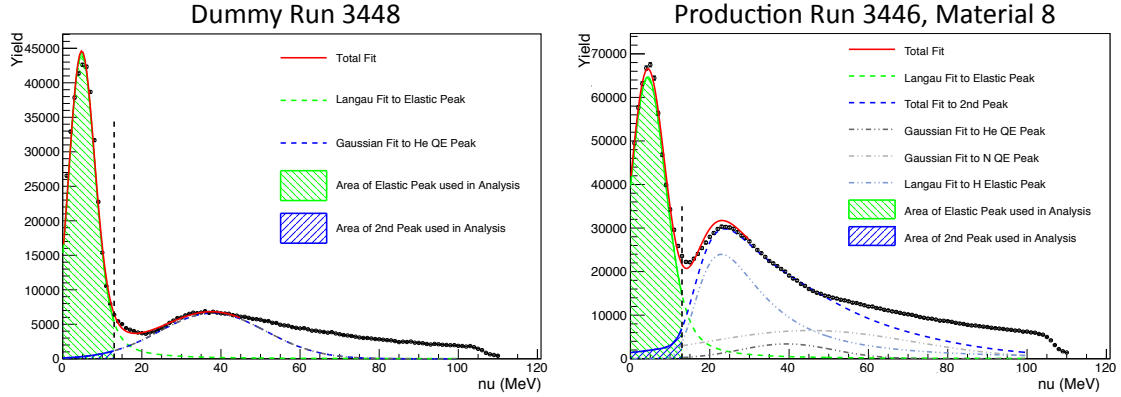


FIG. 5.49: Fit examples for setting 1. The dummy run (3448) is on the left and the ammonia run (3446) is on the right.

$E_{beam} = 2.2 \text{ GeV}$, $B_{target} = 2.5 \text{ T}$, Transverse

Run #	Material	Y_{prod}/Y_{dummy}	σ_N/σ_{He}	$p_f \pm \text{Uncertainty}$
3446	8	1.787	2.201	0.505 ± 0.013
3503	7	1.464	1.860	0.327 ± 0.007
3574	7	1.821	1.833	0.648 ± 0.018
3575	8	1.780	1.884	0.606 ± 0.015
3727	7	1.188	2.212	0.074 ± 0.003
3759	8	2.180	1.929	0.894 ± 0.031
3864	7	1.830	1.652	0.795 ± 0.031
3865	8	1.854	1.661	0.810 ± 0.031

TABLE 5.10: Results for setting 1.

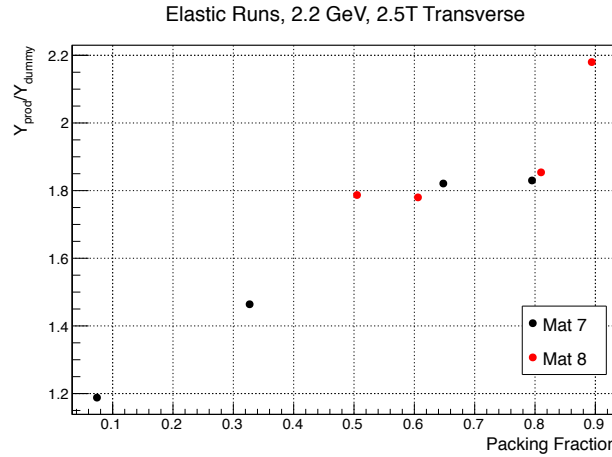


FIG. 5.50: Relation between the packing fraction and the ratio of the production yield over the dummy yield, setting 1.

Setting 2:

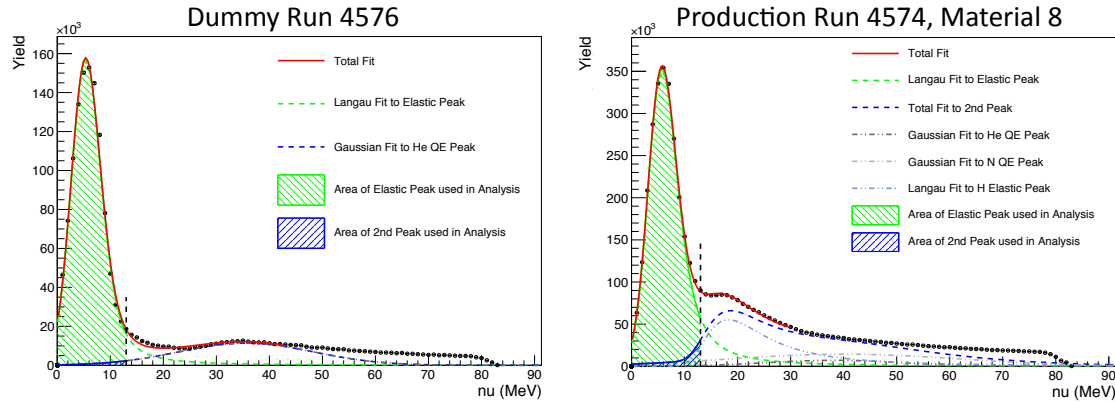


FIG. 5.51: Fit examples for setting 2. The dummy run (4576) is on the left and the ammonia run (4574) is on the right.

$E_{beam} = 1.7$ GeV, $B_{target} = 2.5$ T, Transverse

Run #	Material	Y_{prod}/Y_{dummy}	σ_N/σ_{He}	$p_f \pm \text{Uncertainty}$
4214	7	2.497	3.829	0.467 ± 0.012
4215	7	2.472	3.822	0.460 ± 0.010
4407	7	2.551	3.705	0.503 ± 0.007
4408	8	2.482	3.677	0.484 ± 0.007
4574	8	2.395	3.732	0.452 ± 0.015

TABLE 5.11: Results for setting 2.

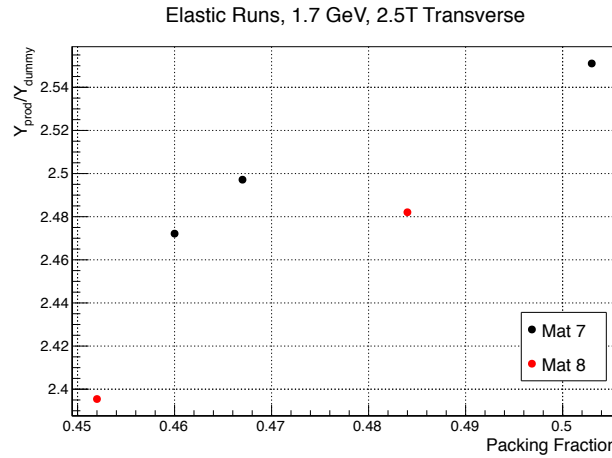


FIG. 5.52: Relation between the packing fraction and the ratio of the production yield over the dummy yield, setting 2.

Setting 3:

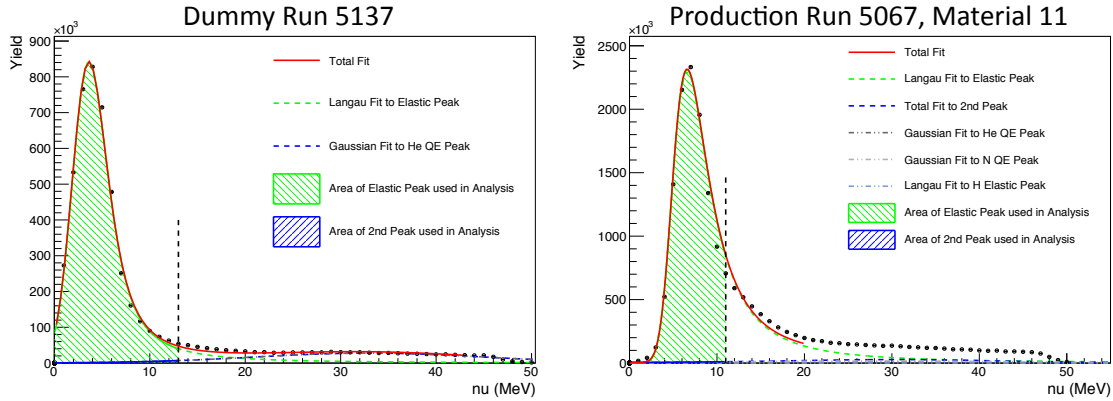


FIG. 5.53: Fit examples for setting 3. The dummy run (5137) is on the left and the ammonia run (5067) is on the right.

$E_{beam} = 1.1 \text{ GeV}$, $B_{target} = 2.5\text{T}$, Transverse

Run #	Material	Y_{prod}/Y_{dummy}	σ_N/σ_{He}	$p_f \pm \text{Uncertainty}$
4947	11	3.585	6.235	0.444 ± 0.029
4948	12	3.651	6.235	0.456 ± 0.030
5067	11	2.937	5.994	0.350 ± 0.012
5134	13	1.896	5.774	0.171 ± 0.011
5219	13	1.630	5.937	0.116 ± 0.006

TABLE 5.12: Results for setting 3.

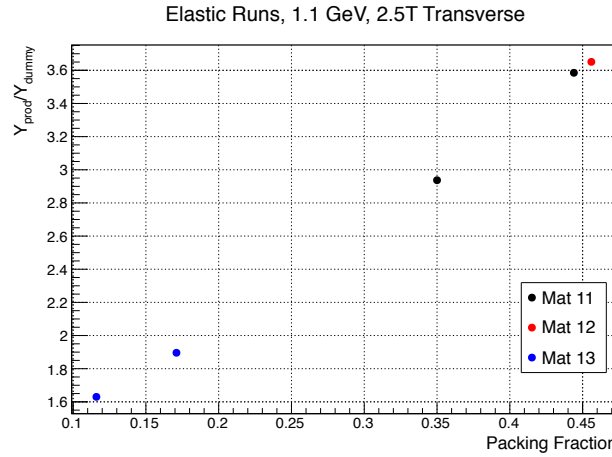


FIG. 5.54: Relation between the packing fraction and the ratio of the production yield over the dummy yield, setting 3.

$E_{beam} = 1.1 \text{ GeV}, B_{target} = 2.5\text{T}$, Transverse (short cell)

Run #	Material	Y_{prod}/Y_{dummy}	σ_N/σ_{He}	$p_f \pm \text{Uncertainty}$
5133	14	1.735	7.076	0.229 ± 0.0086
5197	14	2.184	7.499	0.347 ± 0.0153
5198	14	2.143	7.499	0.335 ± 0.0155
5264	14	1.493	7.440	0.143 ± 0.0073

TABLE 5.13: Results for setting 3 (short cell).

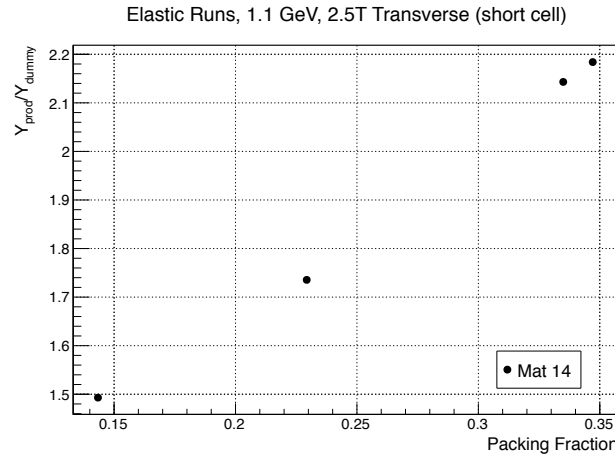


FIG. 5.55: Relation between the packing fraction and the ratio of the production yield over the dummy yield, setting 3, short cell.

Setting 4:

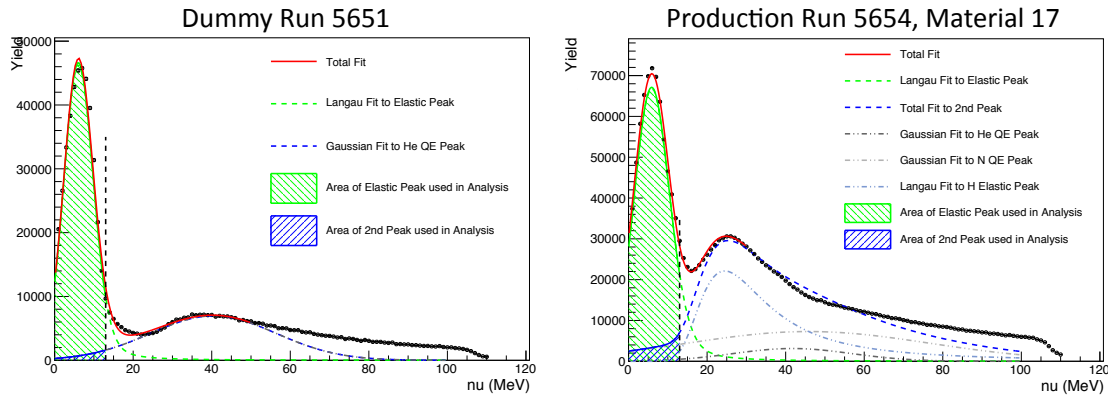


FIG. 5.56: Fit examples for setting 4. The dummy run (5651) is on the left and the ammonia run (5654) is on the right.

$E_{beam} = 2.2$ GeV, $B_{target} = 5$ T, Longitudinal

Run #	Material	Y_{prod}/Y_{dummy}	σ_N/σ_{He}	$p_f \pm \text{Uncertainty}$
5626	17	1.439	1.772	0.366 ± 0.015
5628	18	1.499	1.773	0.446 ± 0.018
5631	18	1.670	1.936	0.531 ± 0.022
5635	18	1.663	1.937	0.525 ± 0.021
5639	18	1.660	1.886	0.546 ± 0.023
5641	17	1.607	1.810	0.515 ± 0.022
5652	18	1.782	1.898	0.619 ± 0.027
5654	17	1.702	1.859	0.579 ± 0.025
5655	17	1.704	1.942	0.537 ± 0.023
5656	17	1.672	1.974	0.492 ± 0.021
5704	17	1.660	1.841	0.551 ± 0.022

TABLE 5.14: Results for setting 4.

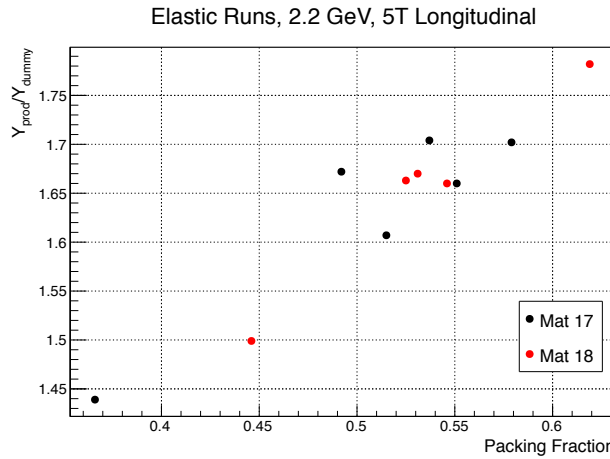


FIG. 5.57: Relation between the packing fraction and the ratio of the production yield over the dummy yield, setting 4.

Setting 5:

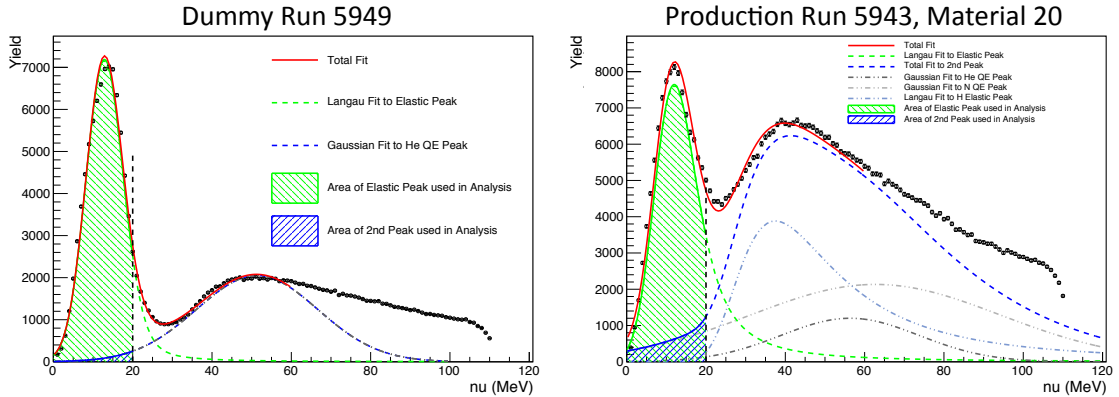


FIG. 5.58: Fit examples for setting 5. The dummy run (5949) is on the left and the ammonia run (5943) is on the right.

$E_{beam} = 2.2 \text{ GeV}$, $B_{target} = 5 \text{ nT}$, Transverse

Run #	Material	Y_{prod}/Y_{dummy}	σ_N/σ_{He}	$p_f \pm \text{Uncertainty}$
5943	20	1.336	1.144	0.552 ± 0.052
5944	19	1.317	1.118	0.565 ± 0.056
5945	19	1.333	1.083	0.660 ± 0.072
5946	19	1.353	1.111	0.684 ± 0.074
6033	20	1.351	1.090	0.633 ± 0.064
6034	19	1.345	1.105	0.655 ± 0.071
6061	20	1.351	1.118	0.600 ± 0.049
6063	19	1.325	1.134	0.479 ± 0.040
6081	19	1.342	1.112	0.587 ± 0.055

TABLE 5.15: Results for setting 5.

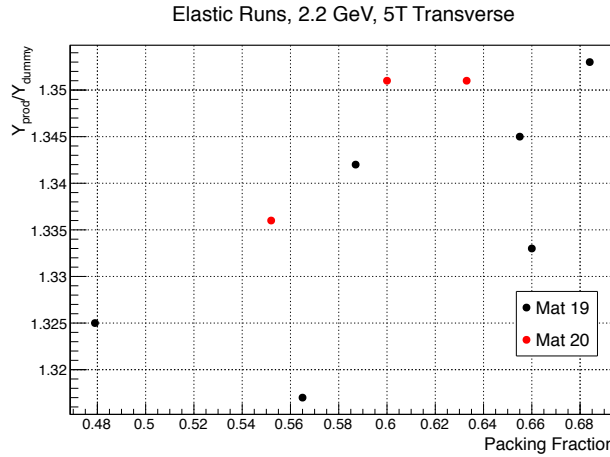


FIG. 5.59: Relation between the packing fraction and the ratio of the production yield over the dummy yield.

5.10.9 Summary

The packing fraction, p_f , represents the proportion of ammonia target material compared to the liquid helium in which it is immersed, and is necessary for the dilution analysis described previously. The packing fraction was extracted for each of the 10 material samples used in the g_2^p experiment. Variation was seen in the elastic yields from run to run, which resulted in a variation in the packing fraction. It is unclear what is causing the variation in the yield for some settings, but a possibility is a drift in the beam position from run to run, resulting in variation in the scattering angle. Since the scattering angle is only $\sim 6^\circ$, small changes can lead to significant variation in the cross section, particularly at the elastic setting. A study is currently underway to understand the effect of the fluctuating beam position on the cross section and acceptance. Once this study is complete, the packing fraction values can be updated to include this correction.

5.10.10 Preliminary p_f Values used for this Analysis

As described above, the p_f values are not finalized due to variations in the yields. For the kinematic settings used in this analysis, a value for p_f was determined by taking the average of all runs within a material. The uncertainty for each value is calculated from the average uncertainty for all runs within that material, and the standard deviation of the distribution of p_f values for that material. The results used for this analysis are summarized in Table 5.16.

Preliminary p_f Values					
Material	Avg.	Avg. Relative	Standard	Total	%
ID	p_f	Uncertainty	Deviation	Uncertainty	
17	0.507	0.042	0.075	0.154	
18	0.533	0.042	0.062	0.123	
19	0.605	0.101	0.101	0.163	
20	0.595	0.092	0.041	0.115	

TABLE 5.16: Preliminary p_f values used for this analysis.

CHAPTER 6

Results and Conclusions

In this chapter, preliminary results are presented for proton asymmetries. Preliminary results for the polarized cross section differences and spin structure functions, g_1^p and g_2^p , were extracted using an unpolarized cross section model. In addition, their contribution to the Burkhardt-Cottingham sum rule and the generalized polarizabilities from the resonance region are presented and discussed.

6.1 Asymmetry Results

The method for extracting the asymmetry was discussed in Sec. 5.1. For this thesis, data at two settings were analyzed: $E_{beam} = 2.2$ GeV, $B_{target} = 5$ T, in both the longitudinal and transverse target magnetic field configurations. Only runs taken with the LHRs were included here. The dilution factor and target polarization analyses were discussed in Secs. 5.9.2 and 5.7, respectively, and the beam polarization values were obtained from [100].

Since the data is taken in small pieces (referred to as “runs”), it must be combined to form the final asymmetry using a statistically weighted average. Eqn. 6.1 gives the expression for calculating the final asymmetry, where A_i is the asymmetry calculated for each run, and δA_i is the statistical uncertainty (Eqn. 6.2).

$$A = \frac{\sum_i A_i / \delta A_i^2}{\sum_i 1 / \delta A_i^2} \quad (6.1)$$

$$\delta A = \sqrt{\sum_i \frac{1}{1/\delta A_i^2}} \quad (6.2)$$

The statistical uncertainty is, in general, related to the square root of the number of events. However, when the raw trigger rate is high enough that it requires a prescale factor, the statistical uncertainty must be altered [101]. If we define the number of useful events, C , as:

$$C = \frac{N \text{ } LT \text{ } f}{ps}, \quad (6.3)$$

where N is the total number of events, LT is the livetime correction, f is the acceptance for useful events ($f = \frac{N_{accepted}}{N_{recorded}}$) and ps is the prescale factor, the statistical fluctuation of events can originate from two sources:

- Fluctuation of the total number of events, N
- Fluctuation due to the acceptance, $(LT \text{ } f)$.

In the first case, the fluctuation can be defined as $\sigma_N = \sqrt{N}$. In the second case, the fluctuation is derived using a binomial distribution, and gives the fluctuation

due to the acceptance as $\sigma_C = \sqrt{C(1 - LT f)}$. Combining these two expressions together gives us the correction to the statistical uncertainty:

$$S = \sqrt{1 - LT f \left(1 - \frac{1}{p_s}\right)}. \quad (6.4)$$

The scaling factor S goes directly into the uncertainty for Y_{\pm} as $\sigma_{N_{\pm}} = S_{\pm} \sqrt{N_{\pm}}$. The statistical uncertainty can then be written as:

$$\delta A = \frac{2Y_+ Y_-}{(Y_+^2 + Y_-^2)^2} \sqrt{\frac{S_+^2}{N_+} + \frac{S_-^2}{N_-}}. \quad (6.5)$$

The sign of the asymmetry is dependent on the status of the IHWP and the target spin configuration. For each run, if the IHWP is “OUT” (“IN”), the asymmetry is multiplied by a factor of $+1$ (-1). For this experiment, the target polarization is always in the plane of the electron polarization. The following sign conventions contribute to the overall sign of the asymmetry:

- Longitudinal configuration, target field points towards the Hall A beam dump (0°): $+1$
- Longitudinal configuration, target field points towards the Møller polarimeter (180°): -1
- Transverse configuration, target field points towards the RHRS (90°): $+1$
- Transverse configuration, target field points towards the LHRS (270°): -1

Since acceptance studies have not yet been completed, only loose cuts were placed on the target variables x and y to avoid significant loss of statistics:

- $-0.5 < x < 0.5$
- $-0.05 < y < 0.05$

The physics asymmetries, before any radiative corrections have been applied, and using the preliminary acceptance cuts and dilution factor described in Sec. 5.9.2, are shown in Fig. 6.1.

6.1.1 Pion Asymmetry

The goal of the particle identification cuts described in Sec. 5.3 is to obtain a pure electron sample from which to extract physics quantities, such as asymmetries. However, if there is some residual pion contamination left behind, it can dilute the asymmetry. The goal of this analysis is to understand the effect of this contamination and the size of the correction to the asymmetry.

The measured asymmetry, which has been corrected for dilution factor, and beam and target polarizations is denoted here by A_m , and can be written in terms of the electron and pion asymmetries:

$$A_m = f_{e^-} A_{e^-} + f_\pi A_\pi, \quad (6.6)$$

where f_{e^-} and f_π are the fraction of electron and pion events in the sample, respectively. Rearranging this equation gives us an expression for the desired electron asymmetry:

$$A_{e^-} = \frac{1}{f_{e^-}} A_m - \frac{f_\pi}{f_{e^-}} A_\pi. \quad (6.7)$$

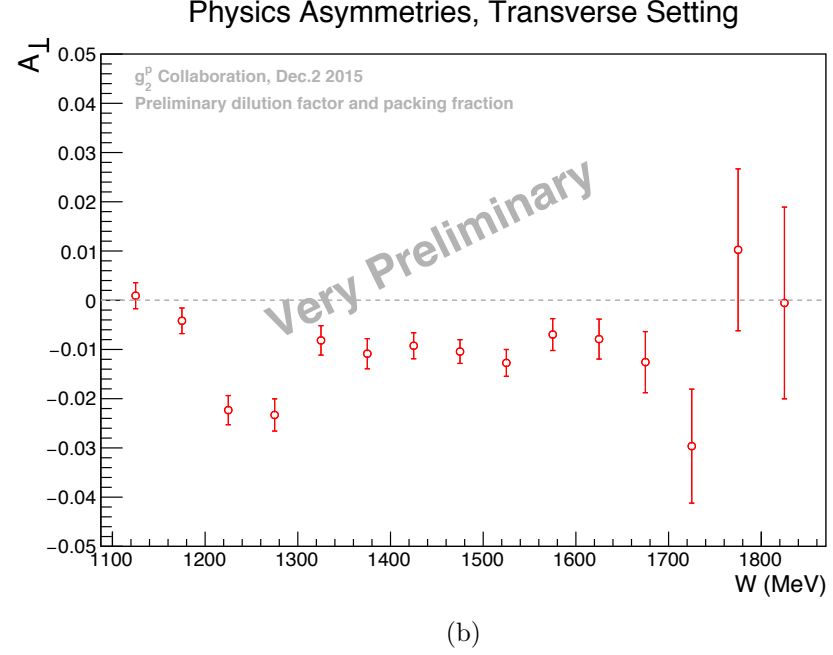
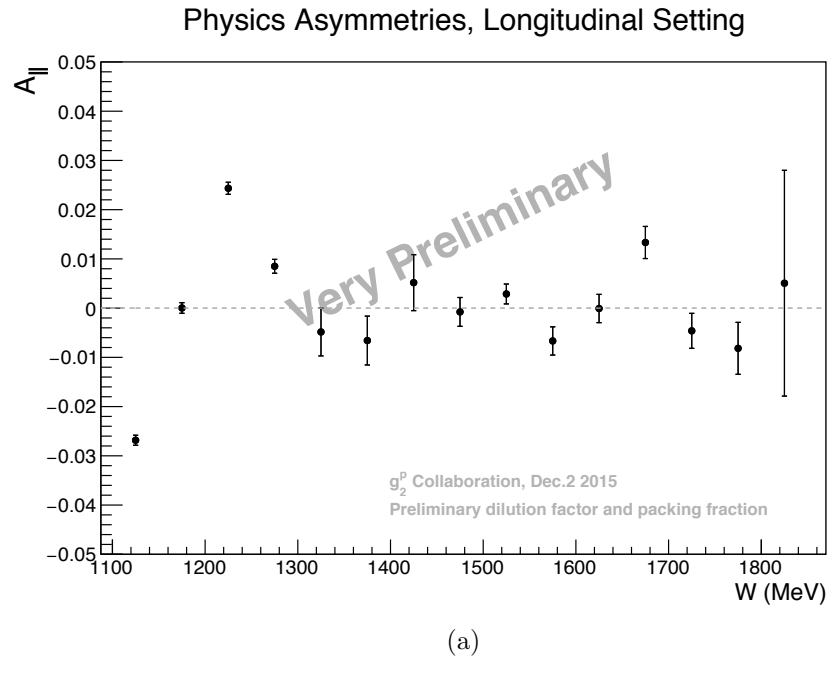


FIG. 6.1: Physics asymmetries vs. W for the longitudinal (a) and transverse (b) configuration, before any radiative corrections have been applied. The uncertainties shown are only statistical.

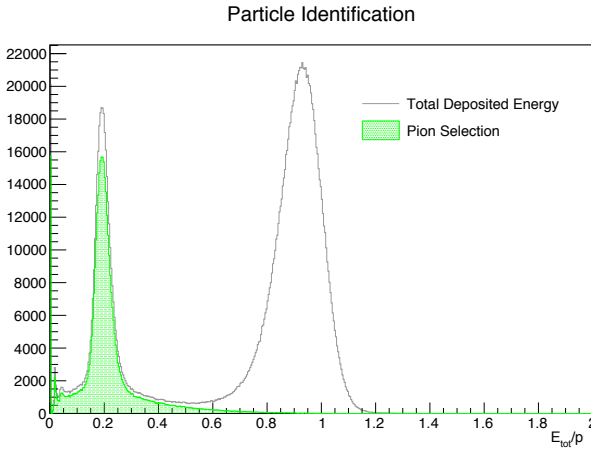


FIG. 6.2: Event selection for calculating the pion asymmetry. The blue line shows the total energy deposited in the calorimeter, divided by the particle's momentum. The peak centered around 1 contains electron events, while the peak to the left contains pion events. The shaded region represents the selection of events used to calculate the pion asymmetry.

The fraction of events f_π and f_{e^-} are determined by calculating the yield from pions and electrons. To distinguish between electrons and hadrons, the gas Cherenkov and lead glass calorimeters are used. To determine the size of the pion asymmetry, a very clean sample must be selected for each of these particles. To calculate the pion asymmetry, a cut was placed on events that did not produce a signal in the gas Cherenkov, as shown in Fig. 6.2.

Similarly, to identify a clean electron sample for physics analysis, a cut is placed on the gas Cherenkov above the single photoelectron peak (the location of this cut is described in detail in Sec. 5.3). Events to the right of this cut are counted as good electron events, while events below this cut are considered to be pion contamination. Fig. 6.3 shows the event selection as a result of this cut. Using these selections, the resulting electron and pion asymmetries can be calculated and are shown in Figs. 6.4 and 6.5. It should be noted that the pion asymmetry is significantly larger in magnitude than the electron asymmetry. If we compare the statistical uncertainties

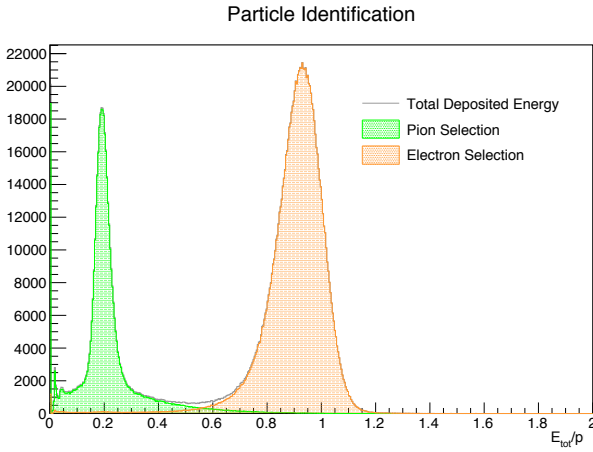
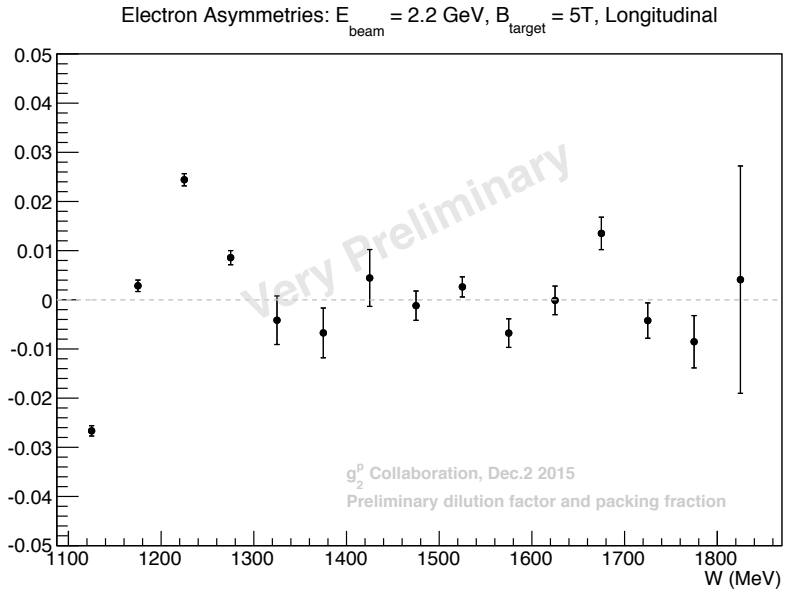


FIG. 6.3: Event selection for calculating the pion and electron yields. The blue line shows the total energy deposited in the calorimeter, divided by the particle's momentum. The orange shaded region shows the selection of electron events, while the green shaded region shows the selection of pion events.

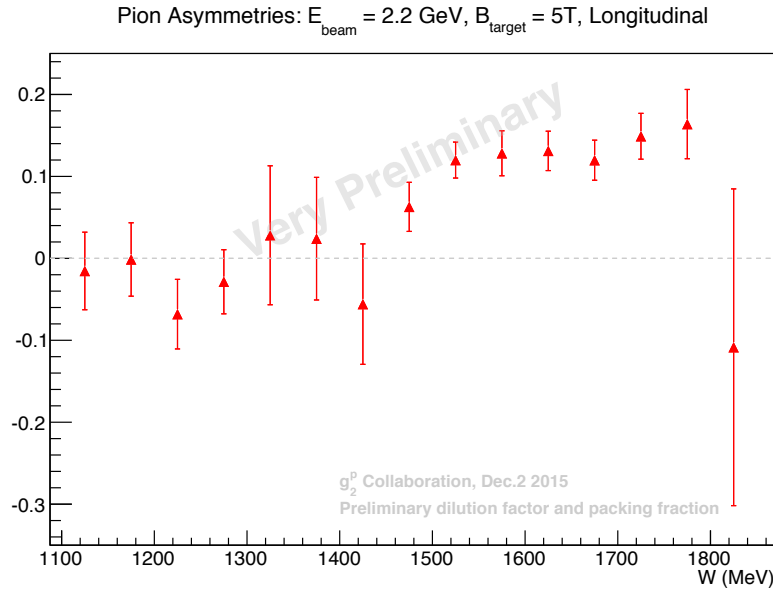
for the longitudinal and transverse settings, it is clear that more pions are produced in the transverse configuration.

Next we can use Eqn. 5.43 to calculate the normalized yield of pions and electrons, which is necessary for evaluating Eqn. 6.7. The electron yield, with PID cuts applied, is shown in Fig. 6.6. In comparison, the pion yield, before the lead glass cuts are applied is shown in Fig. 6.7. The y-axis of both plots have arbitrary units, but can be directly compared to each other. Since acceptance studies have not been completed yet, the data taken for different momentum settings cannot be combined into a smooth, continuous distribution. Each color represents the yield for one central momentum setting of the spectrometer. The pion contamination is significant, particularly at large W . Considering the relative size of the pion asymmetry, the electron asymmetry would be diluted if the pion contamination were not minimized.

After PID cuts are applied, the level of pion contamination is minimal. Since the method to distinguish between electrons and pions is to use events above and

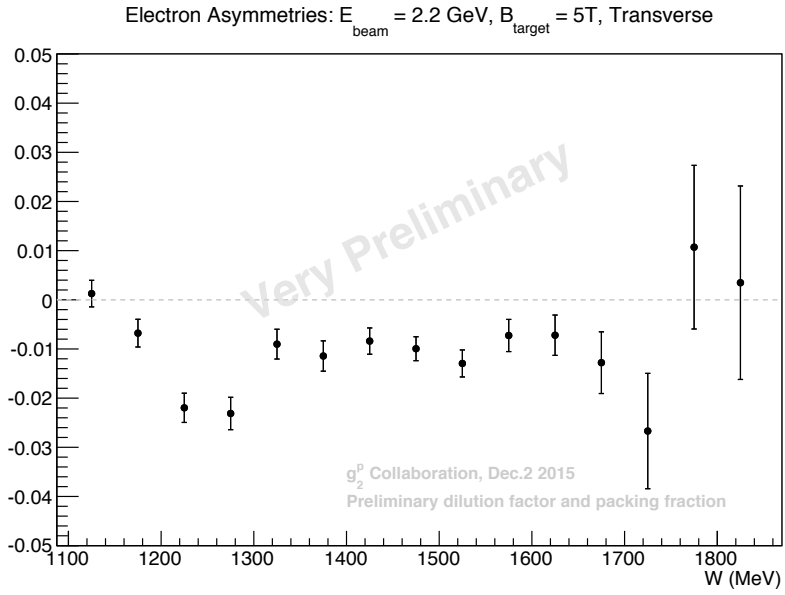


(a)

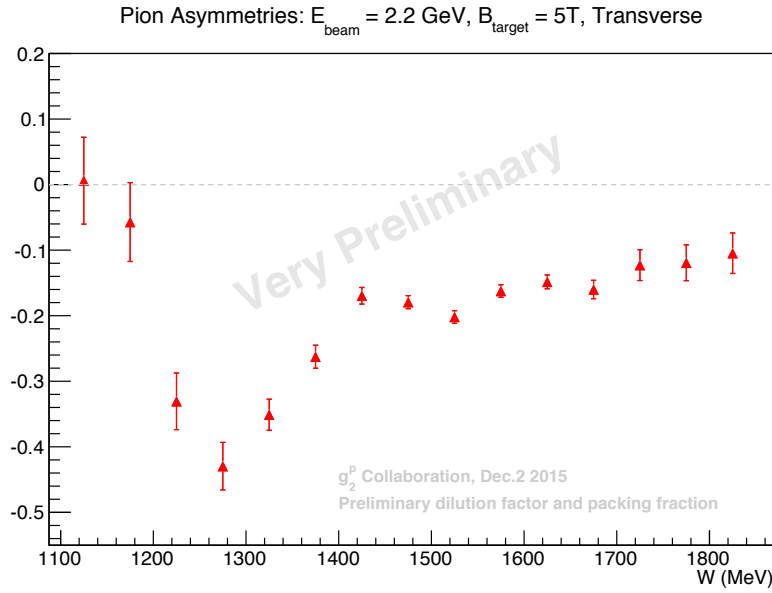


(b)

FIG. 6.4: Electron and pion asymmetries vs. W for the $E_{beam} = 2.2$ GeV, $B_{target} = 5$ T, longitudinal setting. The error bars shown are only statistical.



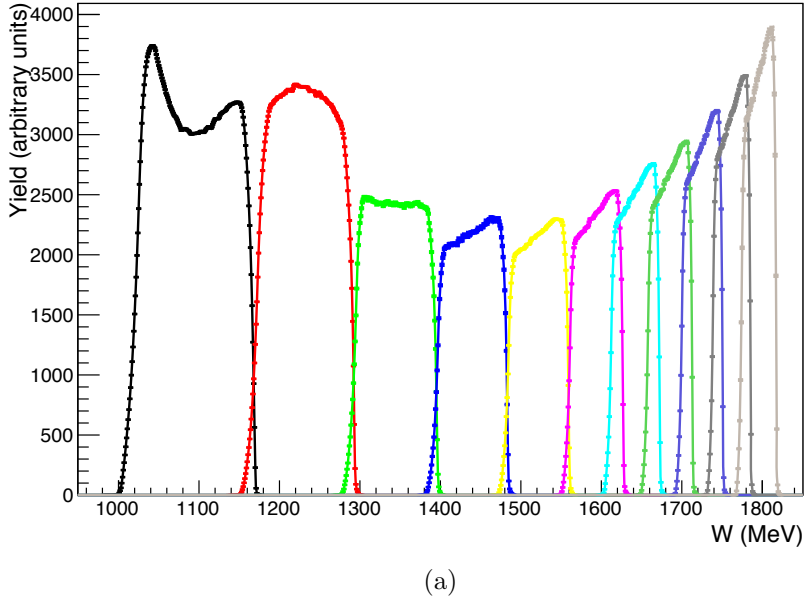
(a)



(b)

FIG. 6.5: Electron and pion asymmetries vs. W for the $E_{beam} = 2.2$ GeV, $B_{target} = 5$ T, transverse setting.

Electron Yield (Longitudinal Configuration)



Electron Yield (Transverse Configuration)

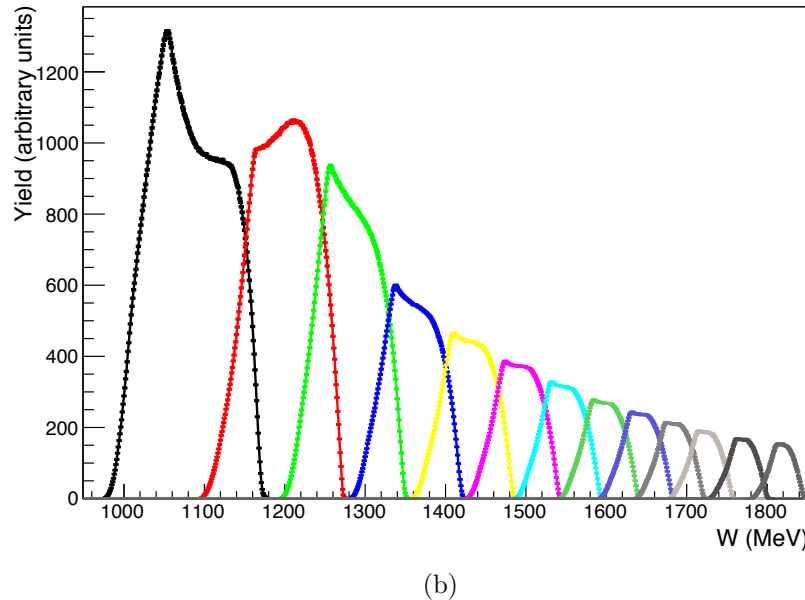
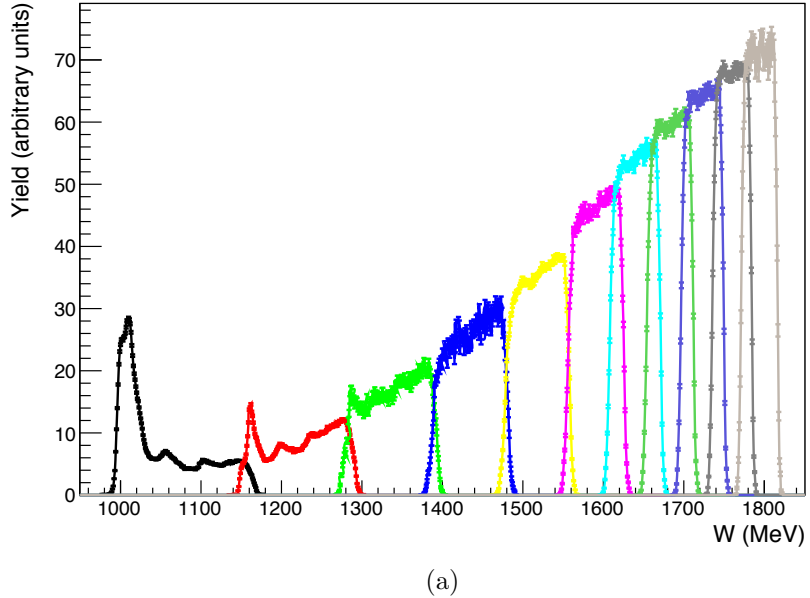


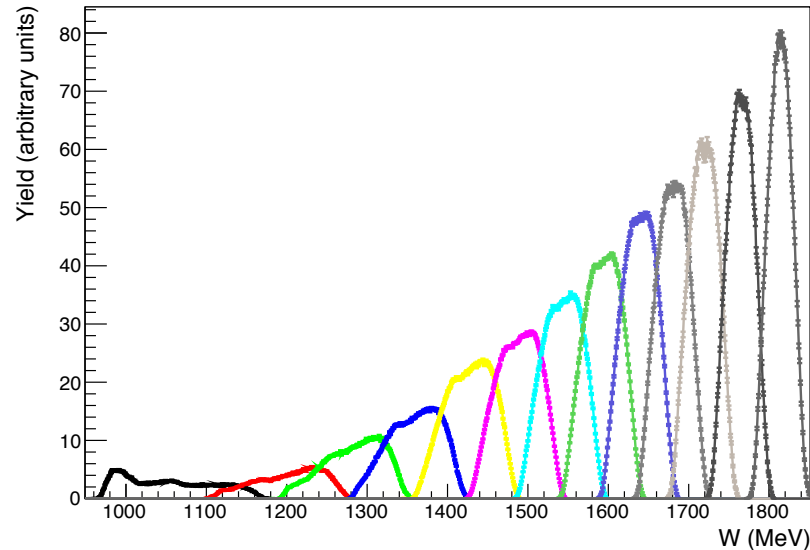
FIG. 6.6: Electron yield vs. W for a series of different momentum settings. The longitudinal configuration is shown on the top and the transverse setting is shown on the bottom. Each color represents a different central momentum setting of the spectrometer.

Pion Yield (Longitudinal Configuration)



(a)

Pion Yield (Transverse Configuration)



(b)

FIG. 6.7: Pion yields vs. W for a series of different momentum settings, before PID cuts have been applied. The longitudinal configuration is shown on the top and the transverse setting is shown on the bottom. Each color represents a different central momentum setting of the spectrometer.

below the gas Cherenkov single photoelectron peak, and in the final analysis, events below the single photoelectron peak are removed, the pion yields shown in Fig. 6.8 represent the upper limit of the correction.

For all settings, the size of the additive correction is very small; for the longitudinal configuration the largest correction is on the order of 10^{-5} (compared to an asymmetry of magnitude 10^{-3}) and for the transverse configuration the largest correction is on the order of 10^{-4} (compared to an asymmetry of magnitude 10^{-2}). The magnitude of the correction is small enough that it isn't necessary to apply the result as a correction; instead it can be included as a (small) contribution to the systematic uncertainty.

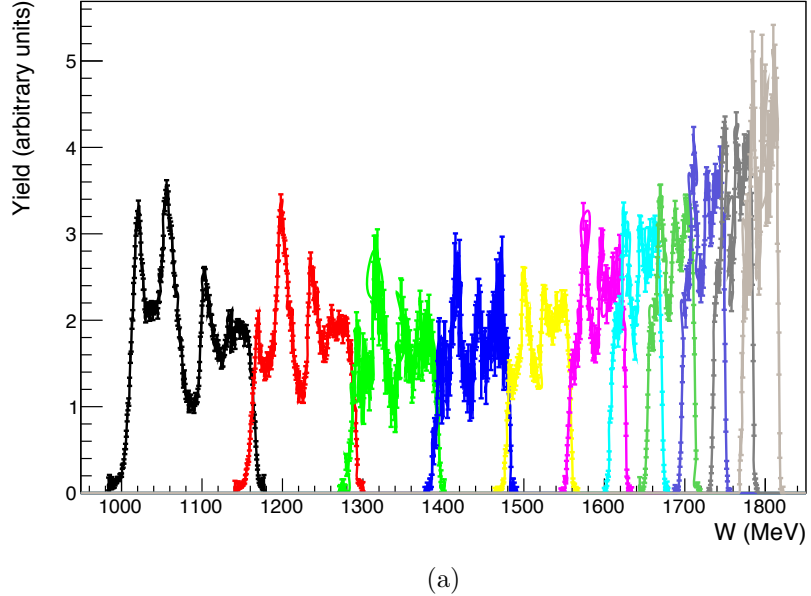
6.2 Radiative Corrections

Before, after, and during the electron interaction with the target, it is subject to energy loss due to the materials in its path and higher order effects, such as two photon exchange loops. The purpose of the radiative corrections (RC) is to account for this energy loss and correct the data accordingly. An overview of the theory behind the RC will be given in this section, along with the method used for preliminary radiative corrections to the asymmetry. Details of the unpolarized radiative corrections are given in Ref. [102].

6.2.1 Unpolarized Radiative Corrections

The first-order Feynman diagram for electron-proton scattering is shown in Fig. 6.9.

Pion Yield, After Cuts (Longitudinal Configuration)



Pion Yield, After Cuts (Transverse Configuration)

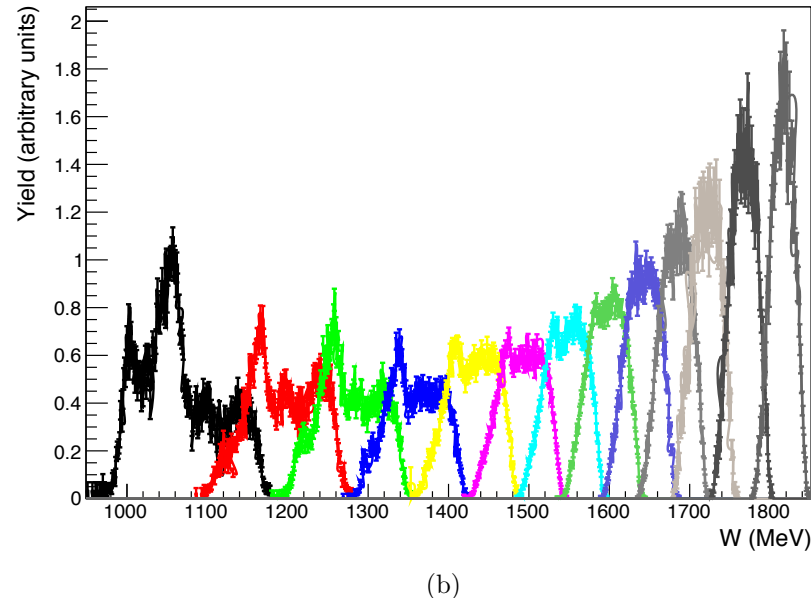


FIG. 6.8: Pion yields vs. W for a series of different momentum settings, after lead glass cuts have been applied. The longitudinal configuration is shown on the top and the transverse setting is shown on the bottom. Each color represents a different central momentum setting of the spectrometer.

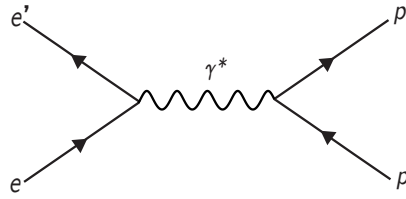


FIG. 6.9: Leading order diagram for electron-proton scattering. Reproduced from [102].

The next-to-leading-order corrections to this process are described below, and are shown in Fig. 6.10.

- Fig. 6.10 (a) shows the vacuum polarization correction, where the virtual photon splits into an e^-/e^+ pair and acts as an electric dipole [103].
- Fig. 6.10 (b) shows the vertex correction, which represents the first order deviation from the Dirac prediction for the electron magnetic moment.
- Figs. 6.10 (c) and (d) describe the electron self-energy Feynman graphs, which contribute to the renormalization of the electron mass [103].
- Figs. 6.10 (e) and (f) account for Bremsstrahlung radiation, which occurs during the electron-proton interaction as well as when the electron passes through material.

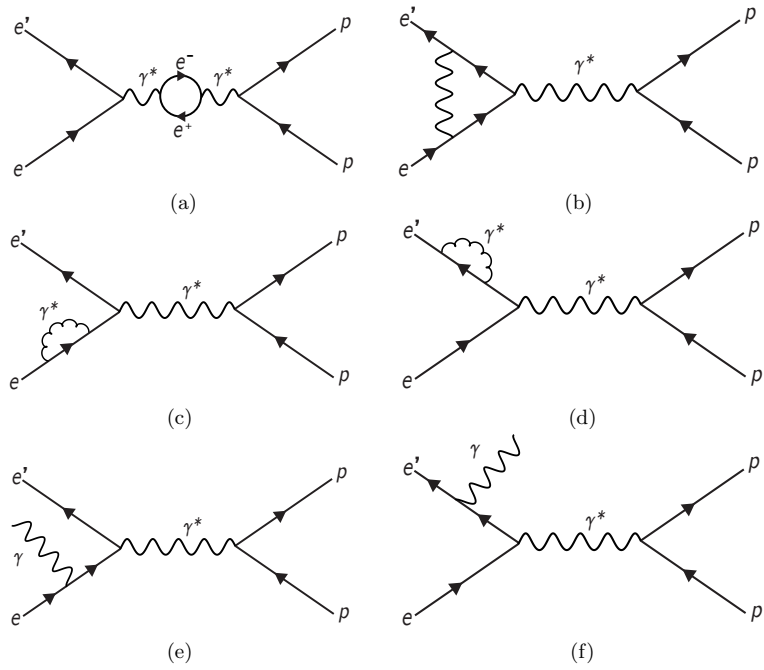


FIG. 6.10: Diagrams for higher order corrections to Fig. 6.9. Reproduced from [102].

Corrections due to two-photon exchange are expected to be of the same order as the one-loop corrections. Diagrams (a), (b), (c), and (d), as well as the two-photon exchange corrections, contribute to the cross section on the order of α^4 , which is relatively small compared to the Bremsstrahlung contribution. The correction due to Bremsstrahlung radiation is usually described in two pieces, *internal* and *external*. Fig. 6.11 shows this differentiation. In addition to Bremsstrahlung, energy can also be lost by an electron elastically scattering from an atomic electron within material in the beam path; this typically results in an energy loss of a few MeV.

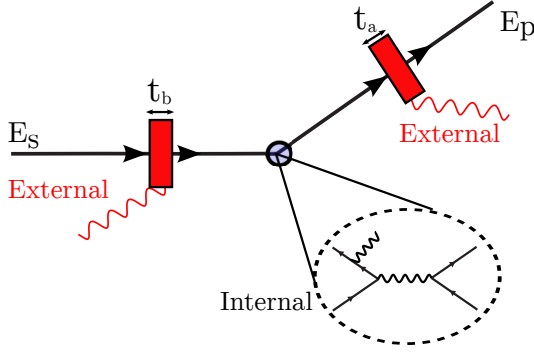


FIG. 6.11: Description of internal and external Bremsstrahlung radiation, reproduced from [102].

The amount of energy lost is dependent on the radiation thickness of the material the electron passes through. A material's radiation length is defined as the thickness of material required for the particle to lose $1 - 1/e$ of its energy. The contribution from each material is weighted by the density and thickness and then summed; the unitless weighted sum is known as the radiation thickness [104, 105]. In general, it is assumed that the electron scattering occurs in the center of the target. The uncertainty on this assumption is $< 1\%$ if the radiation thicknesses before and after scattering is less than 0.10. For the preliminary radiative corrections described in the next section, the radiation thickness before (t_b) and after (t_a) scattering is given by $t_b = 0.02249$ and $t_a = 0.02511$.

6.2.2 Preliminary Radiative Corrections

Final radiative corrections will be adjusted based on the final cross sections extracted from our data. For the preliminary results presented here, the radiative corrections to the asymmetry will be based on model predictions. Two asymmetry predictions were produced using the MAID [24] and Bosted [25] models, one with,

and one without, radiative effects included. The prediction without radiative effects included will be referred to as “unradiated” and the prediction with radiative effects included will be referred to as “radiated”.

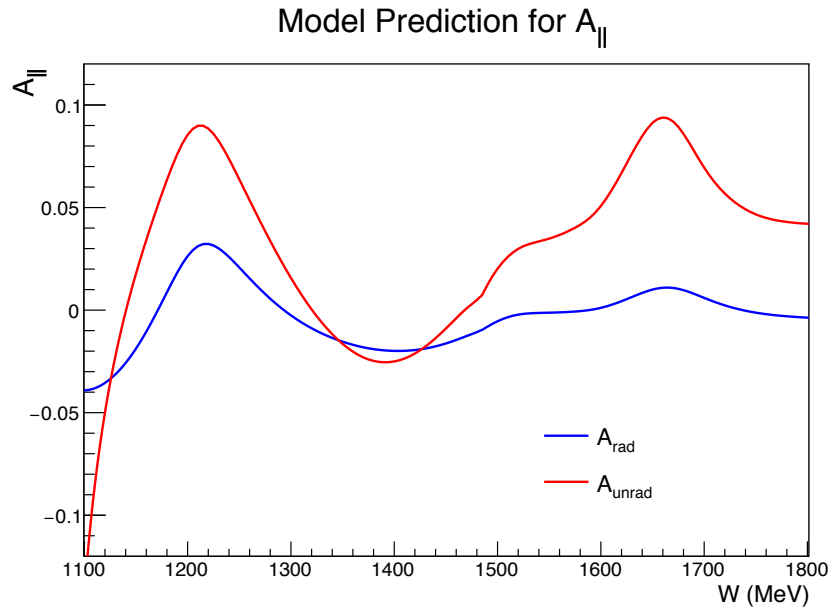
The MAID model is used to generate the polarized cross section difference. For the radiated model, the inelastic radiative effects can be broken down into two parts: internal and external. The internal radiative effects are determined using the POLRAD formalism [106]. The external RC are independent of the polarization, and are performed using the methods laid out by Mo and Tsai [107]. The elastic tail contributions can be considered in much the same way; only the internal piece is polarized. The polarized elastic cross section is calculated by first using the MASCARD code [108], and combining it with the corresponding elastic cross section. Internal polarized radiative effects are calculated using the Mo and Tsai form factors.

To produce the unpolarized cross section, the Bosted model is used. The inelastic radiative effects are calculated using the Bosted model [25] as input for both the internal and external corrections. The Mo and Tsai formalism is again used for the elastic tail contribution. Figs. 6.12 and 6.13 show the radiated and unradiated asymmetry models for the longitudinal and transverse kinematic settings. The input for the scattering angle represents the average scattering angle determined from the data.

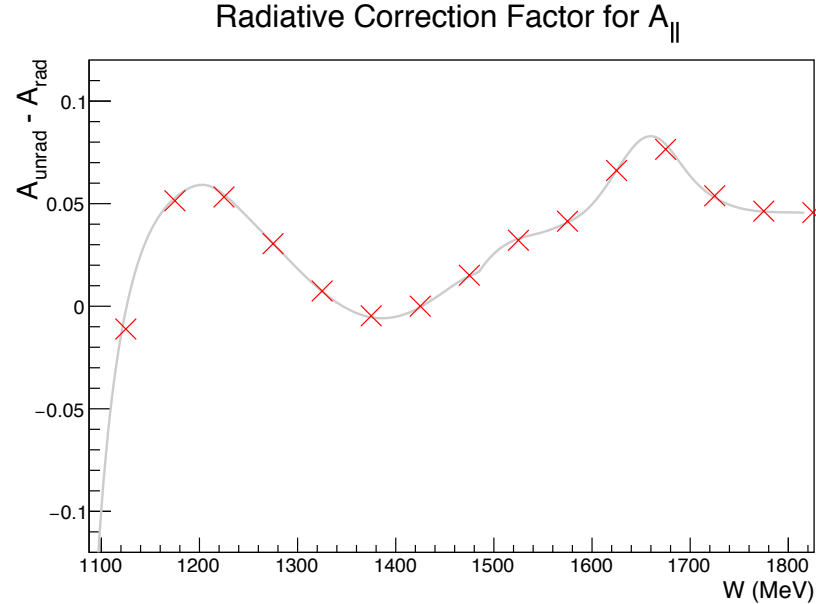
The correction for radiative effects is applied as such, where $\Delta RC = A_{unrad} - A_{rad}$, the difference between the unradiated and radiated models:

$$A_{corrected} = A_{measured} + \Delta RC. \quad (6.8)$$

The effect of applying the correction is shown in Fig. 6.14. There is reasonable

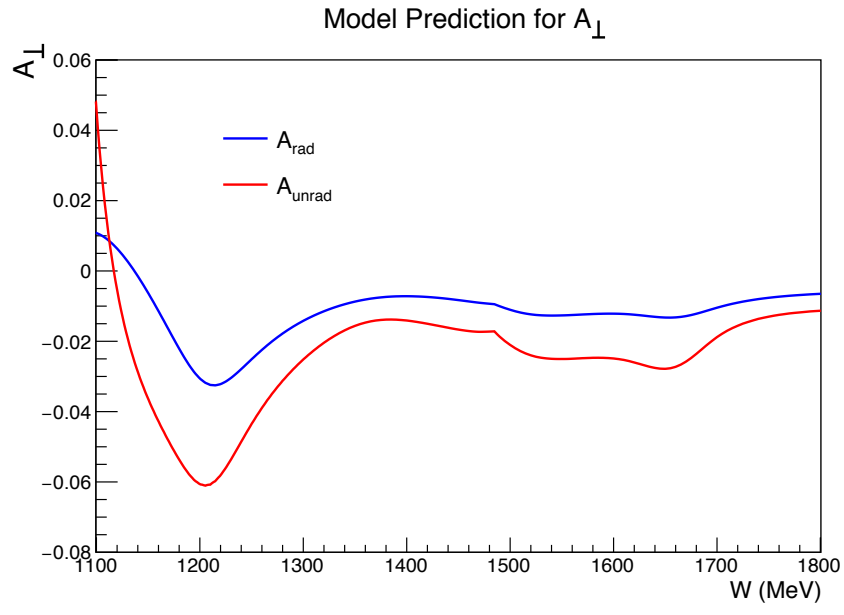


(a)

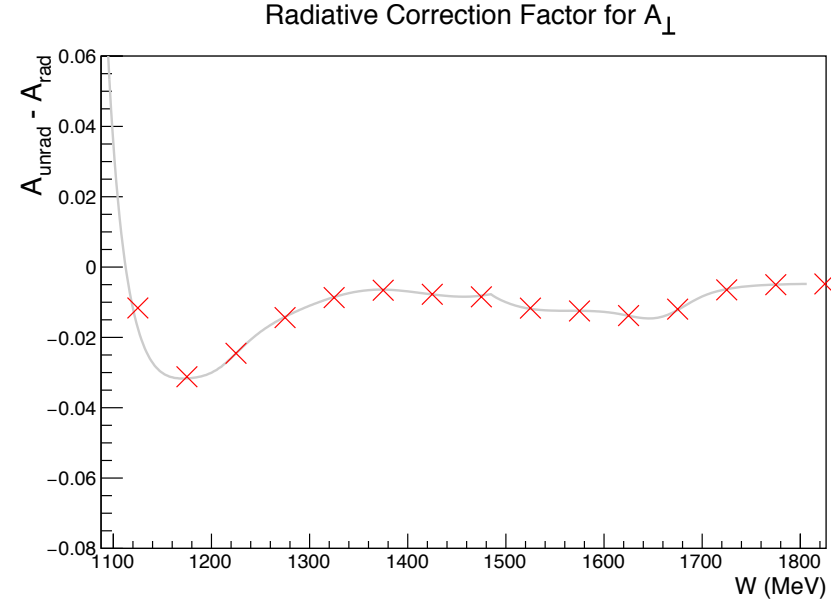


(b)

FIG. 6.12: Model predictions for the radiated and unradiated longitudinal asymmetry (a) and the additive radiative correction factor (b). The red markers in the bottom plot represent the average for each 50 MeV bin.



(a)



(b)

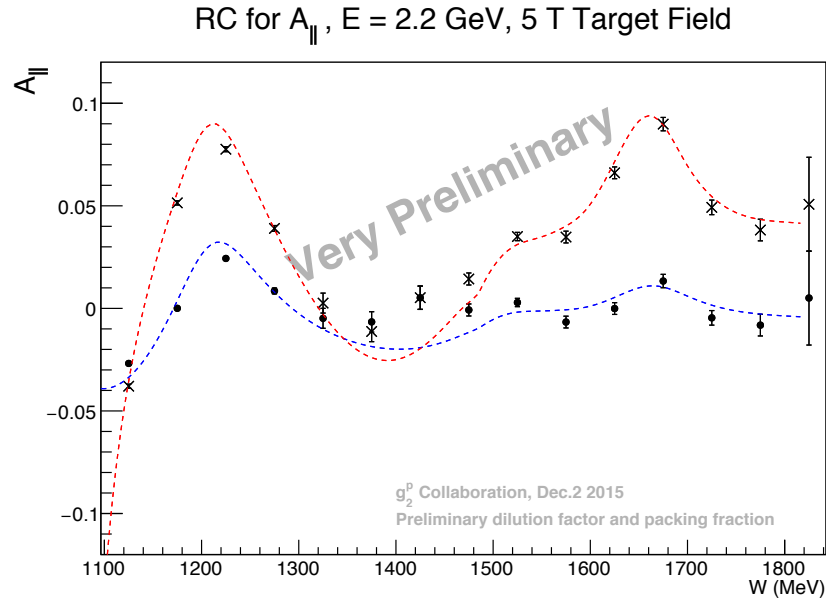
FIG. 6.13: Model predictions for the radiated and unradiated transverse asymmetry (a) and the additive radiative correction factor (b). The red markers in the bottom plot represent the average for each 50 MeV bin.

agreement between the uncorrected data points and the radiated asymmetry prediction. The largest deviation is for the region of W from 1300-1500 MeV in the longitudinal setting. The model suggests a resonance that is not mirrored in the data. This may suggest that the MAID model does not accurately predict the asymmetry, since little data is available to constrain the fit in this region. It should also be noted that the radiative corrections have a significant effect on the asymmetry, particularly at large W for the longitudinal setting. For these preliminary radiative corrections, the model was not tuned to match the data. Careful consideration will need to be taken in the final version of the radiative corrections.

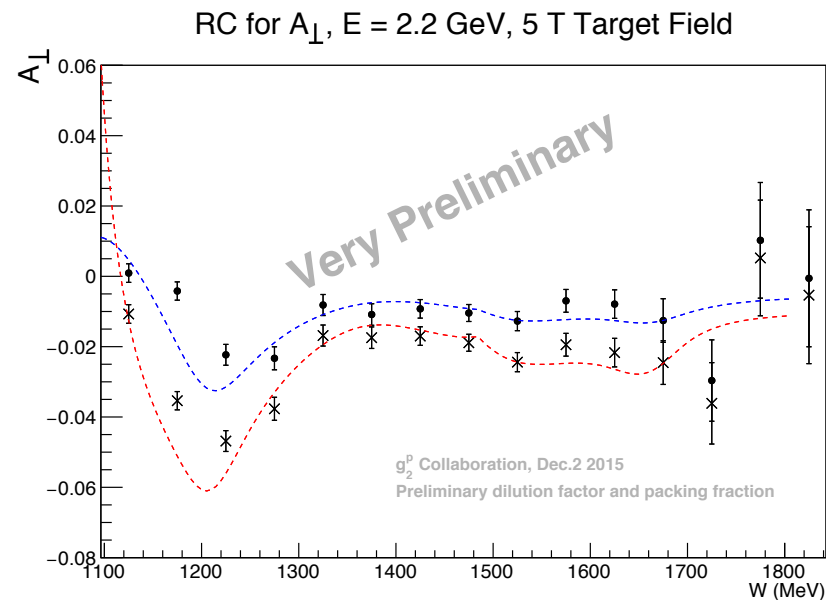
6.2.3 Contribution to Systematic Uncertainty

The contributions to the radiative correction uncertainty are summarized below. The main uncertainty in the correction comes from the MAID model prediction.

- The Bosted model [25] contributes a relative uncertainty of 5%.
- The Mo and Tsai formalism [107] assumes a 4% uncertainty for neglected higher order terms.
- Since optics studies are still being finalized, there is an additional uncertainty associated with variation in the scattering angle θ_0 . The effect of varying the scattering angle on the model prediction for the asymmetry is shown in Figs. 6.15 and 6.16. The contribution to the uncertainty varies bin to bin by $\sim 0.4 - 27\%$.
- The largest contribution to the uncertainty comes from the MAID model prediction, which is detailed in the following paragraph.

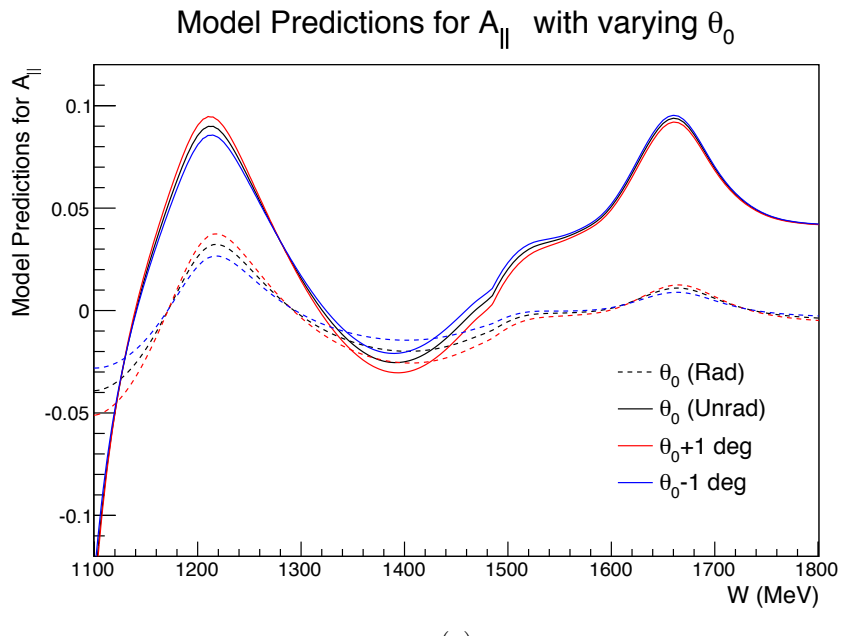


(a)

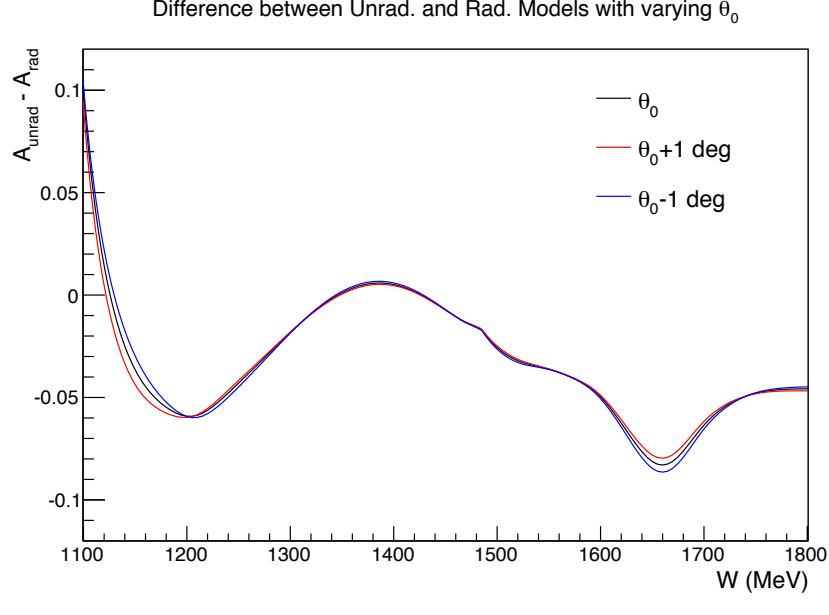


(b)

FIG. 6.14: Effect of applying the radiative corrections (Eqn. 6.8) for the longitudinal asymmetry (a) and the transverse asymmetry (b).

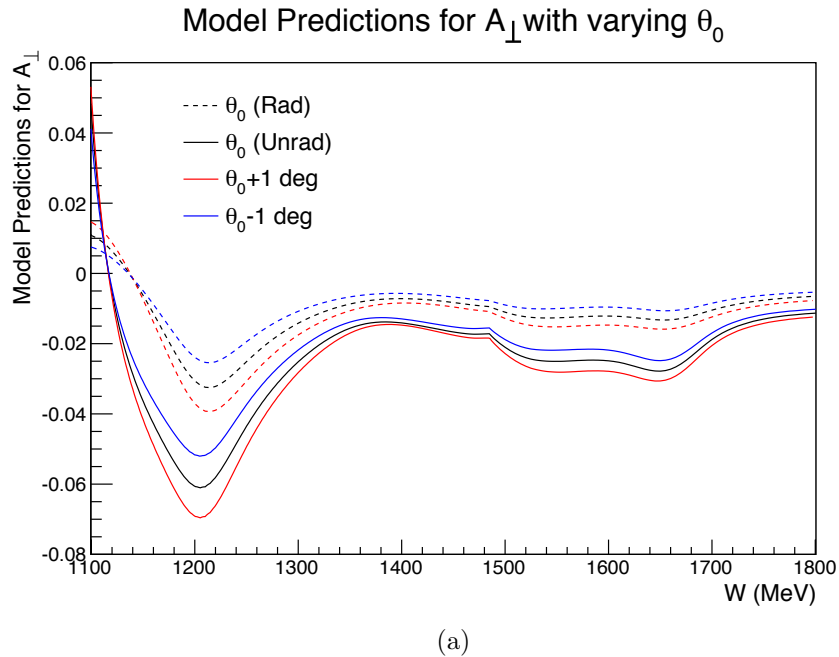


(a)

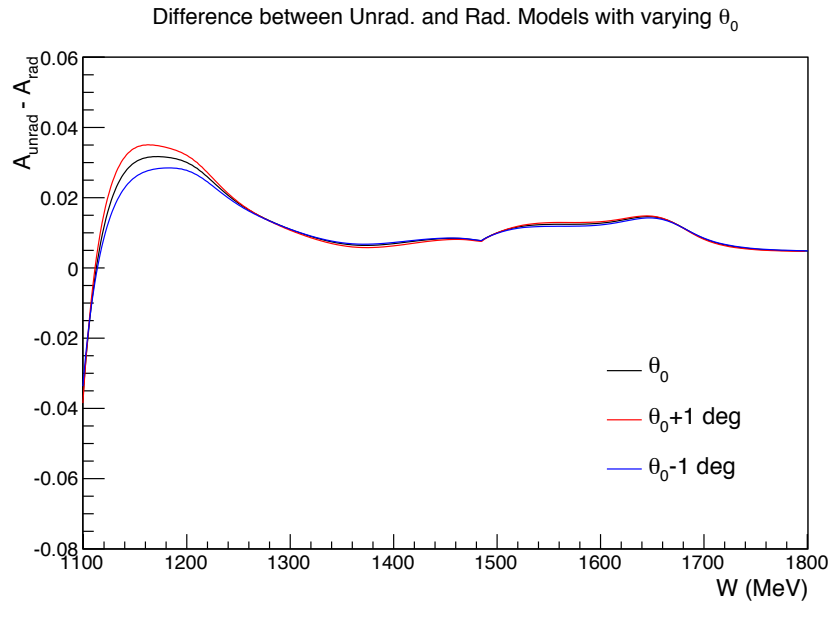


(b)

FIG. 6.15: Effect of varying θ on the radiative corrections for the longitudinal setting. The model predictions are shown in (a) with the difference between unradiated and radiated models in (b).



(a)



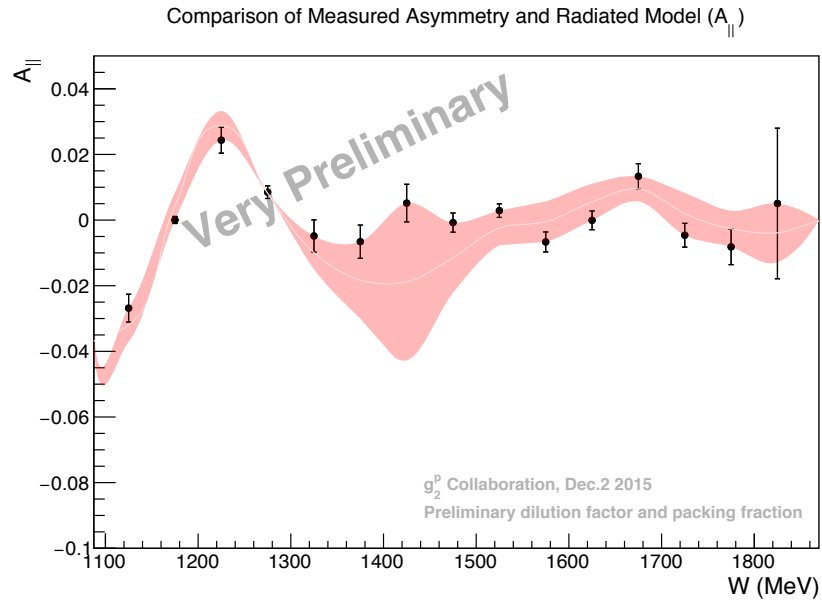
(b)

FIG. 6.16: Effect of varying θ on the radiative corrections for the transverse setting. The model predictions are shown in (a) with the difference between unradiated and radiated models in (b).

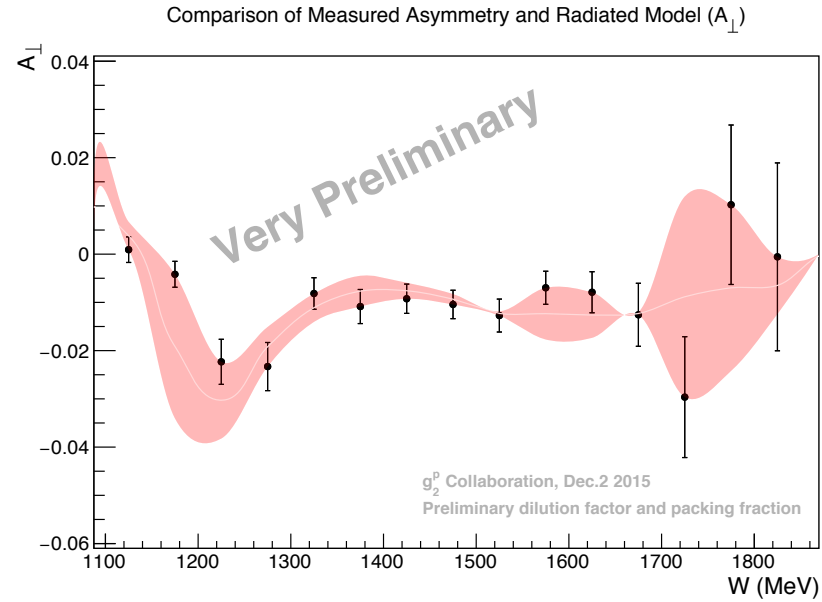
The MAID group does not list their fit errors, as they only reflect the statistical uncertainty and suggest an unrealistically small fit uncertainty due to the large number of data points included in the fit [24]. Instead, they suggest the best estimate of the uncertainty is done by comparison with different analyses. To determine the uncertainty on the model itself, the measured asymmetry, before radiative corrections have been applied, is compared to the radiated version of the MAID model. The difference between the model and our data is taken as the uncertainty. The comparison is shown in Fig. 6.17, with the red band giving the model uncertainty for each bin.

6.3 Kinematics

Due to the large target magnetic field, in the transverse configuration the scattering angle is not constant for each momentum setting. The variation in the scattering angle is shown for the longitudinal and transverse settings in Fig. 6.18. From here on, the two configurations will be referred to as kinematic set L (longitudinal configuration) and kinematic set T (transverse configuration).



(a)



(b)

FIG. 6.17: Comparison of the radiated MAID model with measured asymmetries to estimate the uncertainty on the MAID model for the longitudinal (a) and transverse (b) settings.

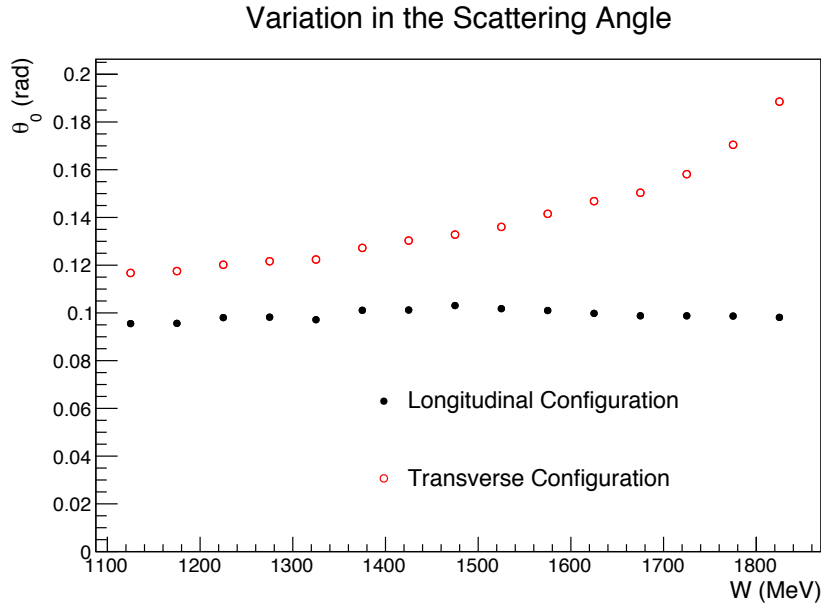


FIG. 6.18: Variation in scattering angle for the longitudinal and transverse configurations, calculated from data. The scattering angle is a constant ~ 6 degrees for the longitudinal setting, but, due to the large magnetic field, varies for the transverse setting.

6.4 Polarized Cross Section Differences

The polarized cross section differences are calculated using Eqn. 6.9 by combining the asymmetry with the unpolarized cross section,

$$\Delta\sigma_{\parallel,\perp} = 2A_{\parallel,\perp}\sigma_{unpol}. \quad (6.9)$$

In order to extract the polarized structure functions, we will need both $\Delta\sigma_{\parallel}$ and $\Delta\sigma_{\perp}$. Since the kinematics of the longitudinal and transverse settings are not the same, the asymmetries cannot simply be combined to extract the structure functions. Instead a model prediction will be used for the missing asymmetry information for

each kinematic setting. The Bosted model [25] is used as the unpolarized cross section to extract $\Delta\sigma_{\parallel,\perp}$ (see Fig. 6.19).

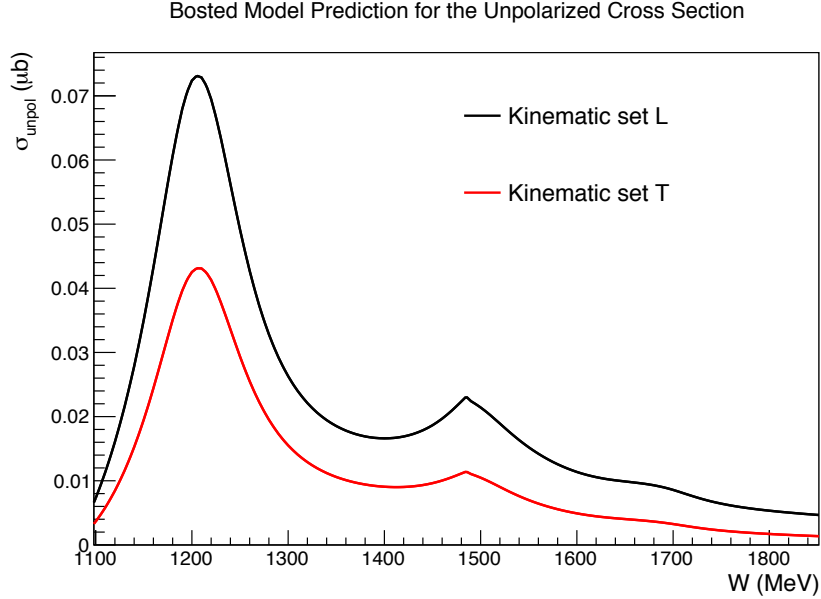


FIG. 6.19: Bosted model prediction for the unpolarized cross section, extracted at the kinematics for the longitudinal and transverse configurations.

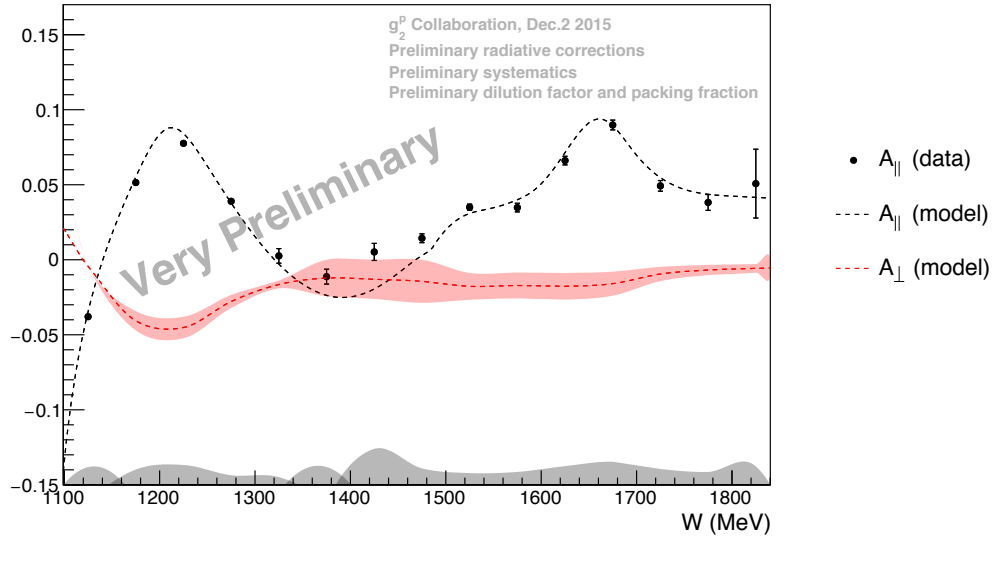
The cross section differences for the longitudinal configuration are shown in Fig. 6.20. The longitudinal asymmetry (A_{\parallel}) is extracted from data, while the transverse asymmetry (A_{\perp}) is a model prediction.

The results for the transverse configuration are shown in Fig. 6.21. This time A_{\perp} is extracted from the data while A_{\parallel} is a model prediction.

6.5 Systematic Uncertainties

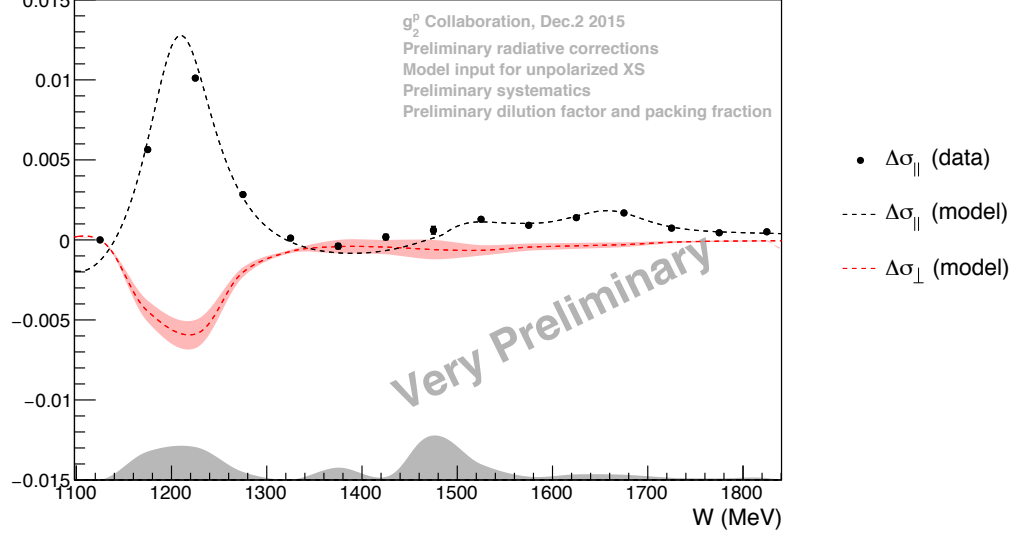
Recall that the asymmetry can be expressed as

Physics Asymmetries, Kinematic Set L



(a)

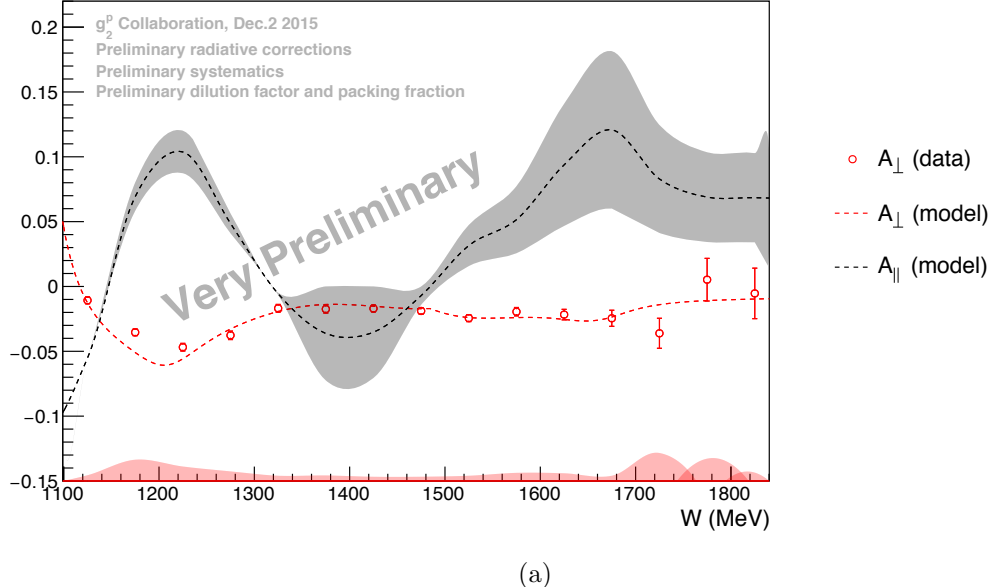
Cross Section Differences, Kinematic Set L



(b)

FIG. 6.20: Asymmetries (a) and cross section differences (b) for the longitudinal configuration. The red band shows the uncertainty on the MAID prediction (discussed in Sec. 6.2.3), and the grey band shows the systematic uncertainty on the calculated quantity.

Physics Asymmetries, Kinematic Set T



Cross Section Differences, Kinematic Set T

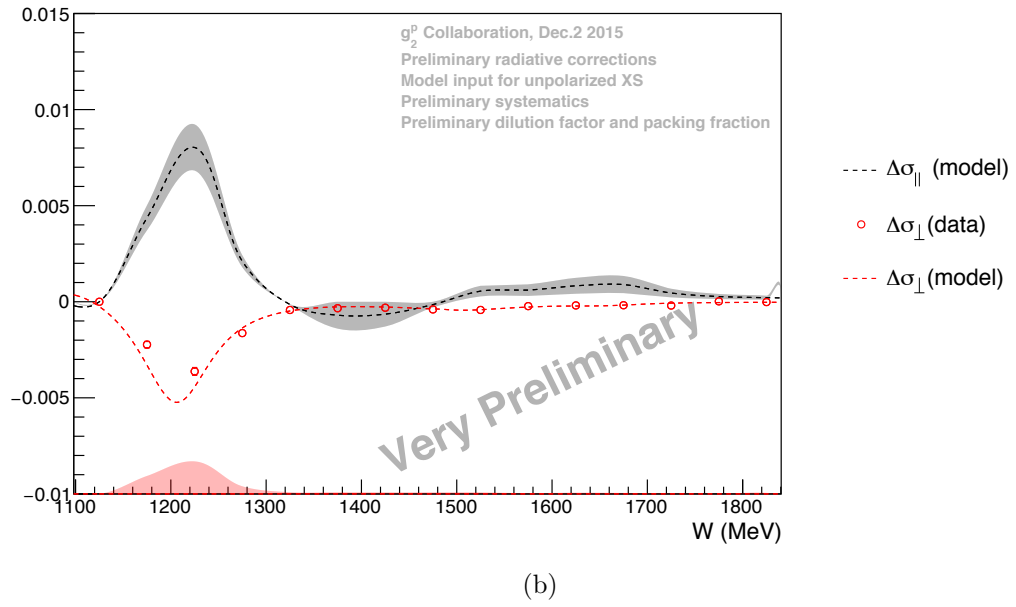


FIG. 6.21: Asymmetries (a) and cross section differences (b) for the transverse configuration. The grey band shows the uncertainty on the MAID prediction (discussed in Sec. 6.2.3), and the red band shows the systematic uncertainty on the calculated quantity.

$$A_{phys} = \left(\frac{1}{f P_b P_t} \right) A_{meas} + \Delta RC. \quad (6.10)$$

The systematic uncertainty can be expanded using standard propagation of uncertainty, with the final expression given by Eqn. 6.11, with the various contributions described below.

$$\begin{aligned} (\delta A_{phys}^{sys})^2 &= \left(\frac{\partial A}{\partial f} \right)^2 (\delta f)^2 + \left(\frac{\partial A}{\partial P_b} \right)^2 (\delta P_b)^2 + \left(\frac{\partial A}{\partial P_t} \right)^2 (\delta P_t)^2 + \delta A_Q^2 + \\ &\quad \delta A_{LT}^2 + \delta A_\pi^2 + \delta \Delta RC^2, \end{aligned} \quad (6.11)$$

- **Dilution Factor (f):** The systematic uncertainty stems mostly from the packing fraction extraction, described in Sec. 5.9.2. Since the dilution factor is extracted from the Bosted model, there is an additional 5% uncertainty.
- **Beam Polarization (P_b):** The uncertainty on the Moller measurement is given as 1.7% [100].
- **Target Polarization (P_t):** The target polarization uncertainty is still being finalized, but the current result is $\sim 1.2\%$ for the different target configurations [91].
- **Livetime Asymmetry (δA_{LT}):** Is given as the value of the livetime asymmetry described in Sec. 5.5 and is $< 1\%$.
- **Charge Asymmetry (δA_Q):** Given as the value of the charge asymmetry described in Sec. 5.4 and is $< 1\%$.
- **Pion Contamination (δA_π):** Described above in Sec. 6.1.1, this represents the upper limit of the correction due to residual pion contamination, and is $< 1\%$.

Contributions to Uncertainty (δA_{phys}^{sys}), Longitudinal Configuration

Source	Total for Run or Bin by Bin	Uncertainty	Relative/Absolute	Contribution to δA
Target Polarization	Total	1.2%	Relative to P_t	3.1E-05 - 1.1E-03
Beam Polarization	Total	1.7%	Relative to P_b	4.4E-05 - 1.5E-03
Livetime Asymmetry	Total	6.6E-06	Absolute	6.6E-06
Charge Asymmetry	Total	1.1E-04	Absolute	1.1E-04
Dilution Factor	Total	15.2%	Relative to f	3.9E-04 - 1.4E-02
Pion Contamination	Total	4.5E-05	Absolute	4.5E-05
Radiative Corrections	Bin by Bin	2.2E-03 - 2.4E-02	Absolute	2.2E-03 - 2.4E-02

TABLE 6.1: Contributions to the systematic uncertainty for the longitudinal configuration.

 Contributions to Uncertainty (δA_{phys}^{sys}), Transverse Configuration

Source	Total for Run or Bin by Bin	Uncertainty	Relative/Absolute	Contribution to δA
Target Polarization	Total	1.2%	Relative to P_t	6.3E-05 - 5.6E-04
Beam Polarization	Total	1.7%	Relative to P_b	8.9E-05 - 8.0E-04
Livetime Asymmetry	Total	6.6E-06	Absolute	5.4E-05
Charge Asymmetry	Total	1.1E-04	Absolute	1.2E-04
Dilution Factor	Total	15.2%	Relative to f	8.4E-04 - 7.5E-03
Pion Contamination	Total	4.5E-05	Absolute	2.7E-04
Radiative Corrections	Bin by Bin	8.2E-04 - 2.1E-02	Absolute	8.2E-04 - 2.1E-02

TABLE 6.2: Contributions to the systematic uncertainty for the transverse configuration.

- **Radiative Corrections (δRC):** The uncertainty due to radiative corrections, which is discussed in (Sec. 6.2.3).

To calculate the cross section difference, there is an additional relative uncertainty of 5% due to the Bosted model, which is used as the unpolarized cross section. The tables below summarize the systematic uncertainty on the cross section differences shown in Sec. 6.4.

Contributions to Uncertainty ($\delta\Delta\sigma_{\parallel,\perp}^{sys}$), Kinematic Set L		
Quantity	Contribution	Uncertainty
$\Delta\sigma_{\parallel}$	A_{\parallel} (Data)	5.1E-03 - 2.4E-02
	σ_{unpol} (Bosted Model)	2.5E-04 - 3.3E-03
$\Delta\sigma_{\perp}$	MAID Model	2.9E-05 - 8.8E-04

TABLE 6.3: Contributions to the systematic uncertainty for $\Delta\sigma_{\parallel,\perp}$ for kinematic setting L.

Contributions to Uncertainty ($\delta\Delta\sigma_{\parallel,\perp}^{sys}$), Kinematic Set T		
Quantity	Contribution	Uncertainty
$\Delta\sigma_{\parallel}$	MAID Model	2.2E-05 - 1.2E-03
	A_{\parallel} (Data)	3.3E-03 - 2.2E-02
$\Delta\sigma_{\perp}$	σ_{unpol} (Bosted Model)	7.7E-05 - 1.9E-03

TABLE 6.4: Contributions to the systematic uncertainty for $\Delta\sigma_{\parallel,\perp}$ for kinematic setting T.

6.6 Spin Structure Functions g_1^p and g_2^p

The polarized structure functions g_1 and g_2 can be written in terms of the cross section differences as:

$$g_1 = \frac{MQ^2}{4\alpha^2} \frac{y}{(1-y)(2-y)} \left[\Delta\sigma_{\parallel} + \tan \frac{\theta}{2} \Delta\sigma_{\perp} \right], \quad (6.12)$$

$$g_2 = \frac{MQ^2}{4\alpha^2} \frac{y^2}{2(1-y)(2-y)} \left[-\Delta\sigma_{\parallel} + \frac{1 + (1-y) \cos \theta}{(1-y) \sin \theta} \Delta\sigma_{\perp} \right], \quad (6.13)$$

where $y = \frac{\nu}{E}$. The results for g_1 and g_2 for the two different sets of kinematics are shown vs. W in Figs. 6.22 and 6.23. For cases where a model prediction is used as input for the asymmetry (i.e. $\Delta\sigma_{\perp}$ in the longitudinal configuration), the systematic uncertainty is assumed to be the uncertainty in the MAID prediction, discussed in

Sec. 6.2.3.

Polarized Structure Functions, Kinematic Set L

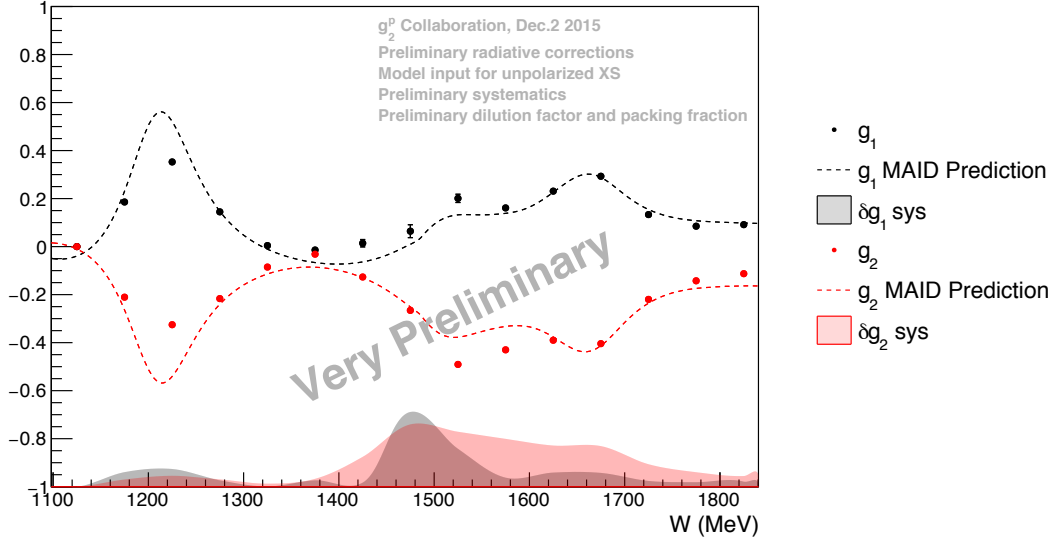


FIG. 6.22: Results for g_1^p and g_2^p for kinematic setting L. The error bars on each data point are the statistical uncertainty.

Polarized Structure Functions, Kinematic Set T

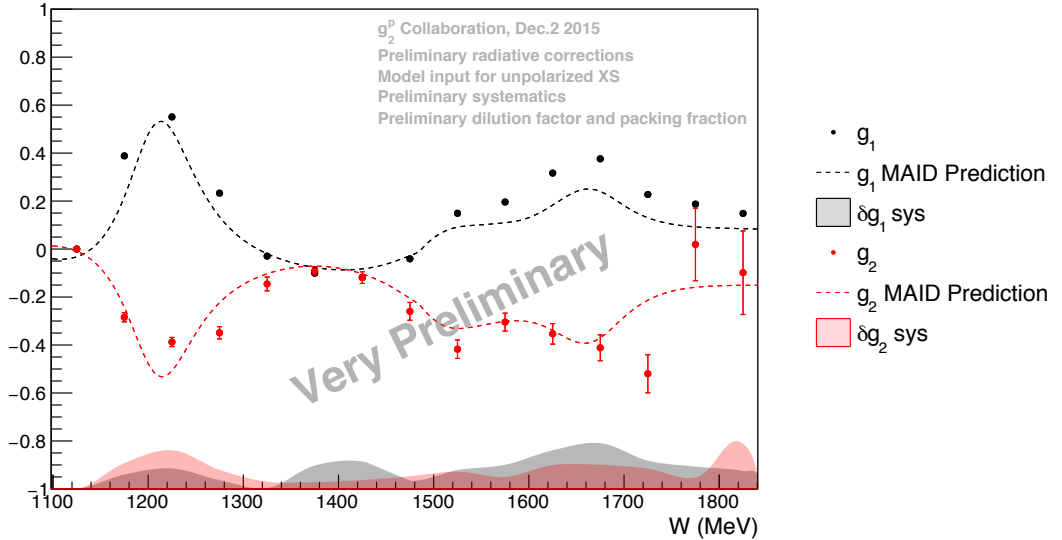


FIG. 6.23: Results for g_1^p and g_2^p for kinematic setting T. The error bars on each data point are the statistical uncertainty.

6.7 Contribution to Burkhardt-Cottingham Sum Rule

With a preliminary result for g_2 , we can begin to look at the contribution to the Burkhardt-Cottingham sum rule (discussed in Sec. 3.7.1). Since kinematic set A uses a model prediction for $\delta\sigma_{perp}$, which is the dominant contribution to g_2 , it will not be included in this section. Fig. 6.24 shows the structure function g_2^p versus Bjorken x for kinematic set B.

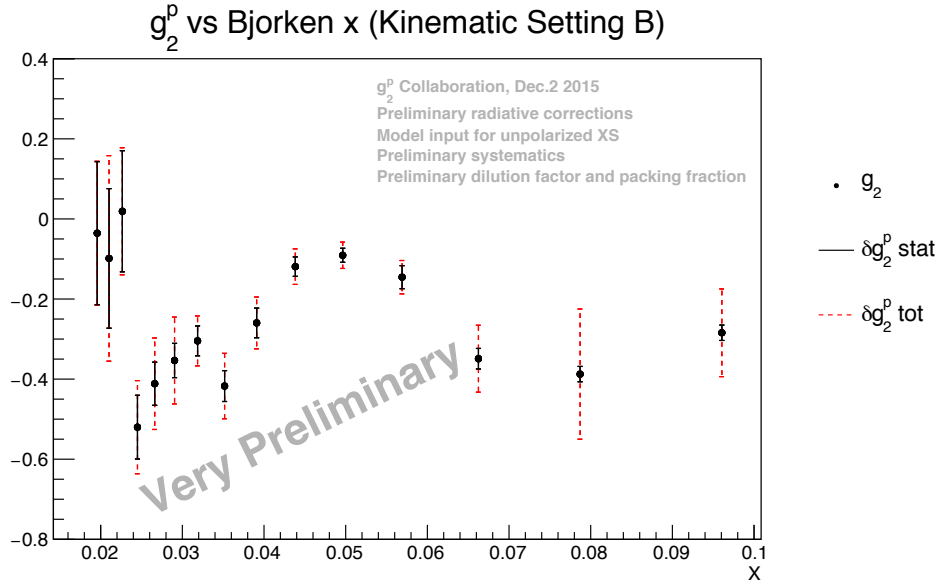


FIG. 6.24: Results for g_2^p plotted vs. Bjorken x .

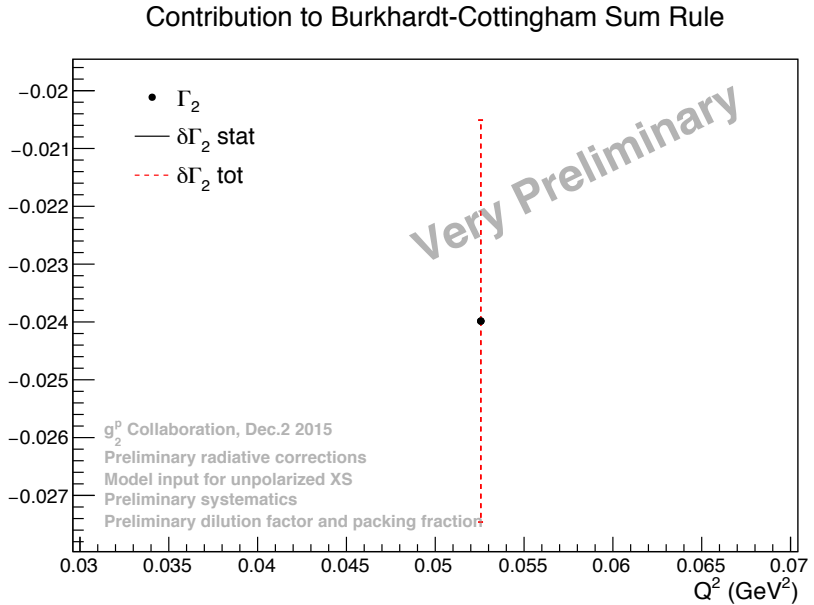


FIG. 6.25: Contribution to the BC sum integral from the resonance region.

Fig. 6.25 shows the contribution to the total integral Γ_2 from the resonance region. The statistical and systematic uncertainties are shown on the data point. As can be seen in Fig. 6.24, the range of x covered by our data is small; to perform a full test of the BC sum rule, it is necessary to understand the extrapolation to low and high x . The RSS experiment measured g_2^p in the resonance region at an average momentum transfer of $Q^2 = 1.3 \text{ GeV}^2$ [44]. Fig. 6.26 shows the RSS results for g_2^p versus Bjorken x . Our result is consistent with theirs in that the contribution to Γ_2 from the measured resonance region is overall negative. The RSS result suggests that the function g_2 begins to rise as you move to higher x , which may compensate for the negative contribution from the resonance region.

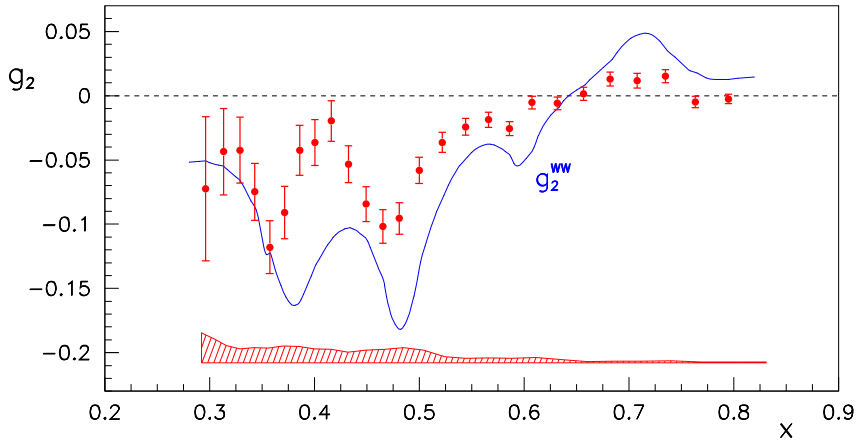


FIG. 6.26: RSS results for g_2^p at an average $Q^2 = 1.3 \text{ GeV}^2$ [44]. The statistical uncertainties are shown on the data points, and the systematic uncertainties are shown in the red band. The blue curve shows the prediction for g_2^{WW} .

Fig. 6.27 shows the previous results for tests of this sum rule [109]. The open circles represent the value of Γ_2 over the measured region of x , the black line represents the elastic contribution, determined from elastic form factors, and the band shows the assumed contribution from the DIS region, assuming the validity of the sum rule. For our low Q^2 data point, the expected contribution from the elastic region is negative, meaning the extrapolation to $x \rightarrow 0$ must be positive to compensate. Looking back at Fig. 3.3 shows the full integral of Γ_2 . Although the SLAC results for the neutron are in agreement with the expected result of zero, there is a violation of the BC sum rule suggested for the proton, which was measured over the region $0.02 \leq x \leq 0.8$. In this case, there is an uncertainty associated with the low x extrapolation that is difficult to quantify. If this violation is confirmed, the principles applied in the derivation of the BC sum rule, which were discussed in Sec. 3.7.1, will need to be re-considered. In contrast, the precision data from JLab for the neutron and proton are in agreement with the sum rule, which suggests that g_2 is a well-behaved function.

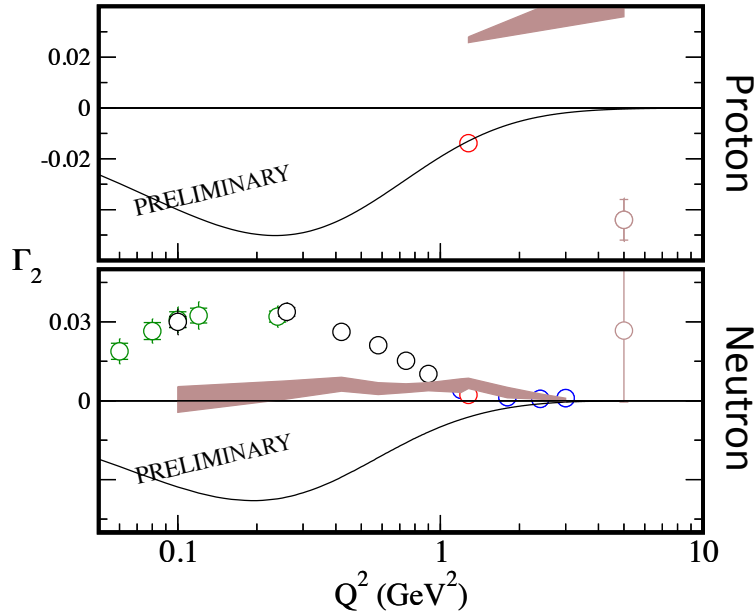


FIG. 6.27: Results for the BC sum rule for the proton (top), neutron (middle) and ${}^3\text{He}$ (bottom). Reproduced from [109]. Open circles represent the measured region. The inner (outer) error bars represent the statistical (total) uncertainties. The black curve shows the elastic contribution from nucleon form factors [110, 111] and nuclear form factors [112]. The full band represents the contribution to Γ_2 as $x \rightarrow 0$, assuming the validity of the BC sum rule. The data are from the following experiments: Brown: E155 collaboration [45], Red: RSS experiment [42, 44], Black: E94-010 [41, 42], Green: E97-110 (preliminary) [40], Blue: E01-012 (preliminary) [43].

6.8 Spin Polarizabilities γ_0 and δ_{LT}

Similar to the BC sum rule, we can look at the contribution to the second moment of g_1 and g_2 , the generalized polarizabilities γ_0 and δ_{LT} (Sec. 3.7.2). Starting with γ_0 , the value of the integrand versus x is shown in Fig. 6.28. In comparison, the value of the δ_{LT} integrand is shown versus x is shown in Fig. 6.29.

The contribution to the γ_0 integral from the resonance region is shown in

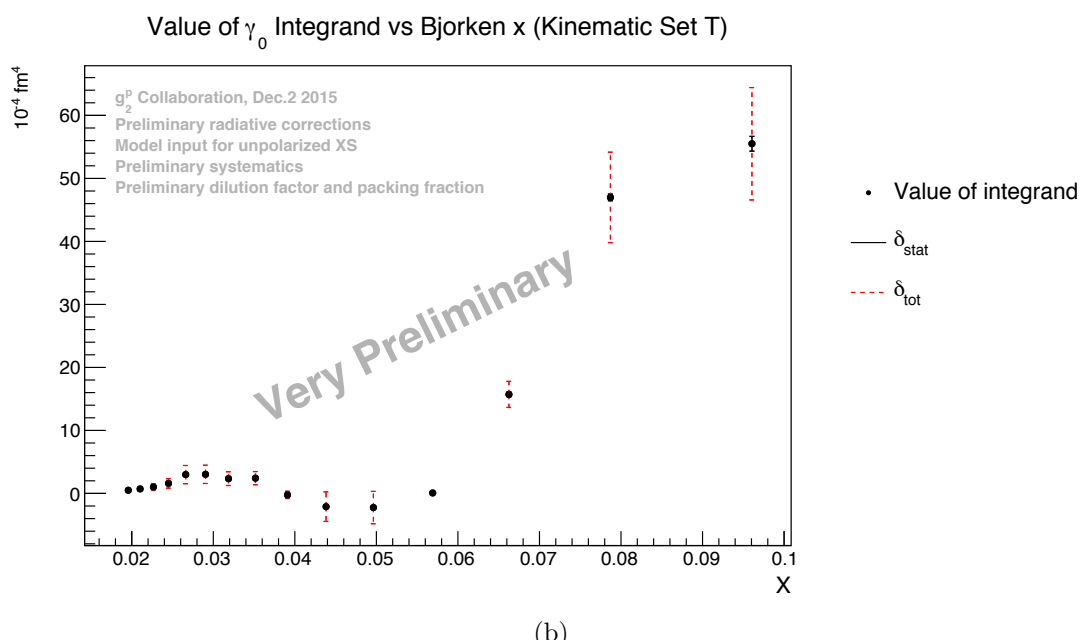
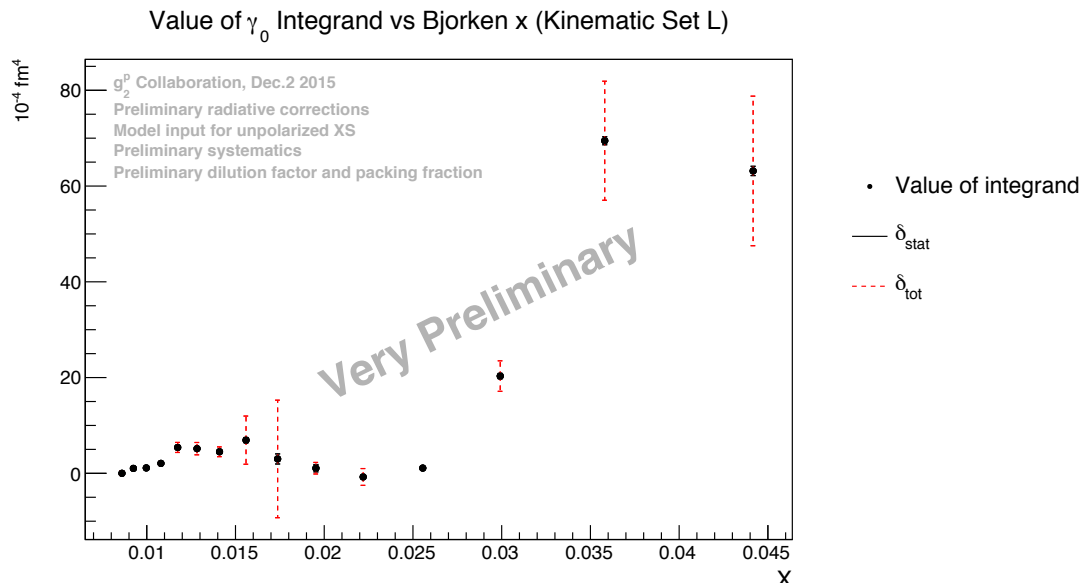


FIG. 6.28: Value of the γ_0 integral, plotted vs. Bjorken x .

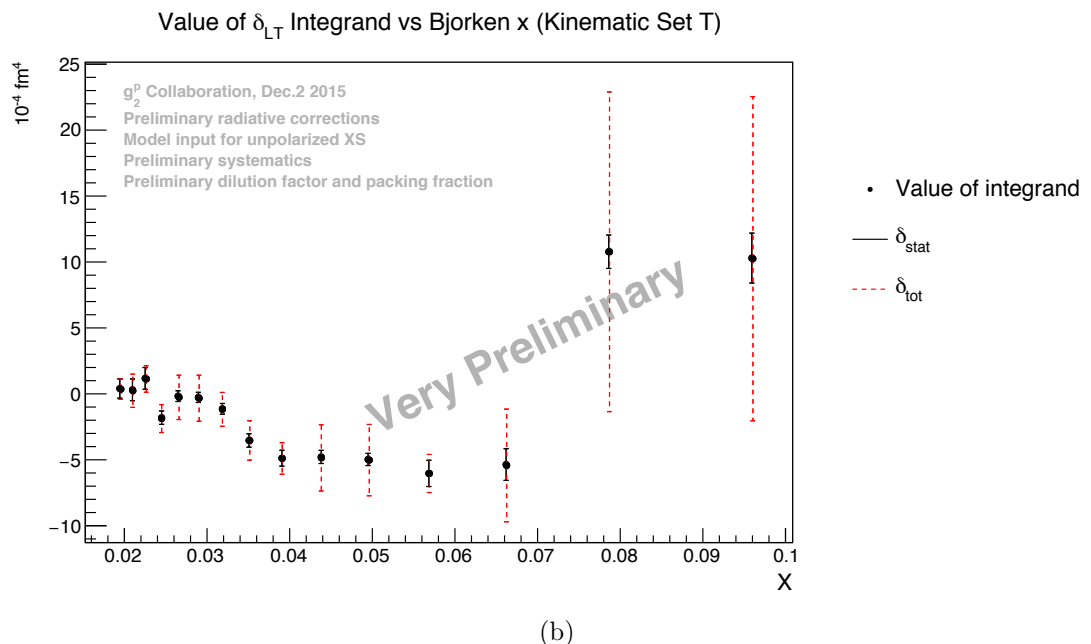
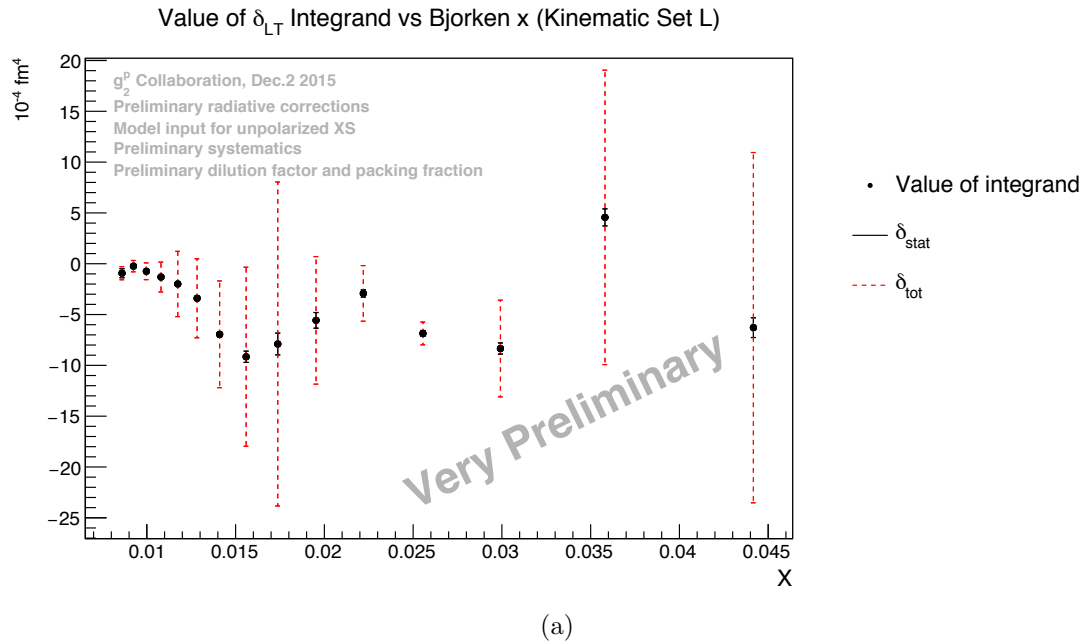
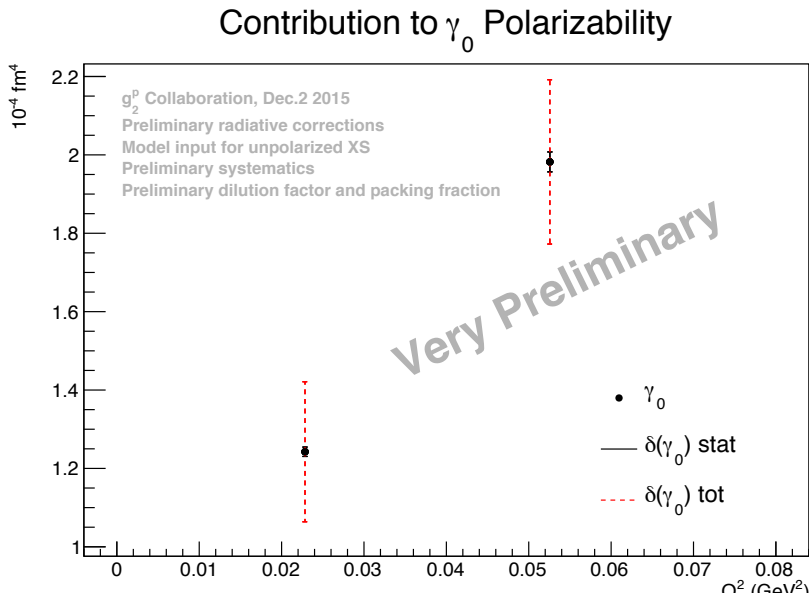


FIG. 6.29: Value of the δ_{LT} integrand, plotted vs. Bjorken x .

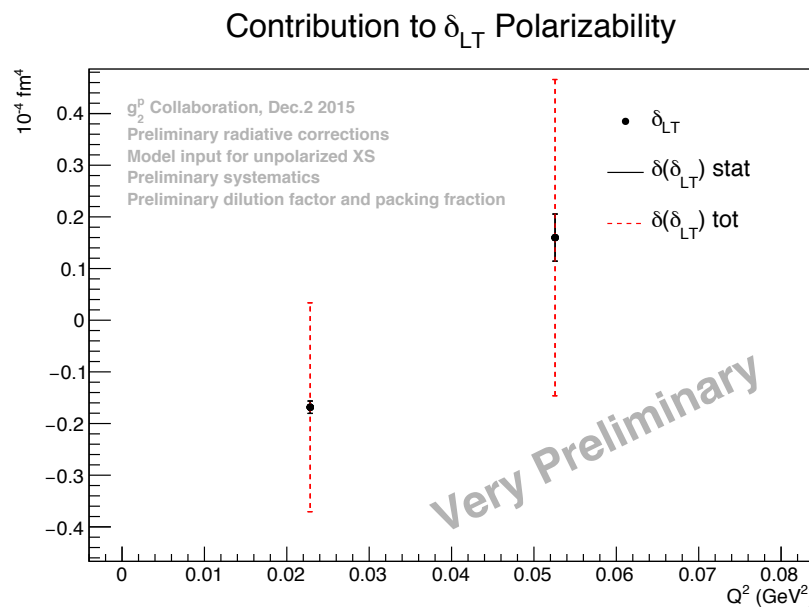
Fig. 6.30, with the statistical and systematic uncertainties given with the points.

Predictions for the neutron polarizabilities were shown in Sec. 3.7.2. There have been recent developments in the χ PT calculations that find better agreement with neutron experimental results [113], which are shown in Fig. 6.31. The previous Heavy Baryon (HB) χ PT result included in the inverse nucleon mass an additional semi-relativistic expansion, which worked poorly for the determination of the spin polarizability quantities. There are two Baryon (B) χ PT predictions included, shown by the grey and blue bands. The grey band seems to resolve the discrepancy seen for δ_{LT} for the neutron, however, if we assume the proton result will agree with the MAID prediction, this calculation suggests a discrepancy for δ_{LT} for the proton. The blue bands show agreement for both the neutron and proton. The difference between these two calculations lies in the inclusion of the Δ -resonance. For the blue curves, additional higher order terms are included in the calculation, particularly those with photons coupling to the Δ in the loops.

The contribution from our data to the spin polarizabilities does not show strong agreement with any of the χ PT predictions. The prediction for δ_{LT}^p suggests a positive value, which, based on Eqn. 3.35, says the integral over g_1^p must be greater than the integral over g_2^p . In this extraction of g_1 and g_2 , there is input from the MAID model for both kinematic set A and B. A negative result for δ_{LT} suggests that the MAID model under-estimates the value of A_{\parallel} , or, conversely, over-estimates the value of A_{\perp} . Since there is little data available at low Q^2 , the final results of this experiment will provide a test of the χ PT predictions.



(a)



(b)

FIG. 6.30: Contribution to the generalized spin polarizabilities from the resonance region. The contribution to γ_0 is shown in (a) and the contribution to δ_{LT} is shown in (b). The units on the y -axis are 10^{-4} fm^4 .

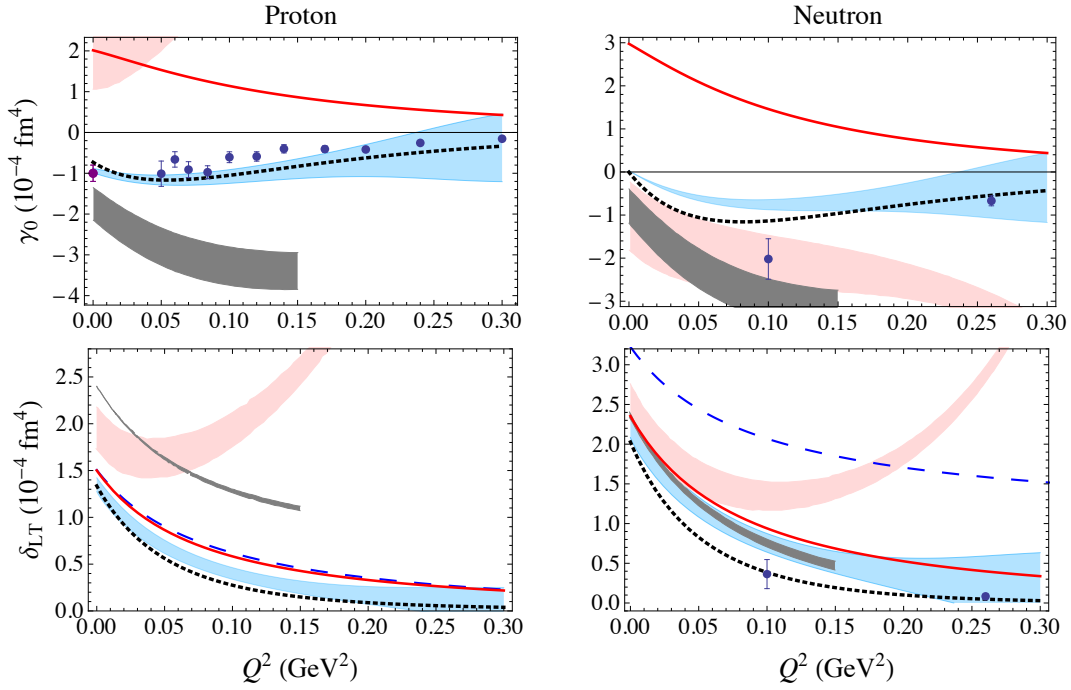


FIG. 6.31: Current χ PT predictions for the generalized spin polarizabilities. Reproduced from [113]. The red solid lines and blue bands represent the LO and NLO results of [113]. The black dotted lines are the fit from MAID2007 [24]. The grey bands are the covariant $B\chi$ PT calculation from [114]. The blue dotted line (off the scale in the γ_0 prediction) is the $\mathcal{O}(p^4)$ calculation [115]. The red band is the IRB χ PT calculation [49]. The data for γ_0^p at finite Q^2 (blue dots) are from [116], and at $Q^2 = 0$ (purple dot) from [117]. All of the neutron data are from [55].

6.9 Conclusions and Future Work

The goal of the g_2^p experiment was to extract the spin structure function g_2 for the proton in the scarcely explored low Q^2 region. For the final extraction of g_2 , a cross section obtained from our experimental data will be used in place of the Bosted model prediction used here. In addition, the preliminary method for radiative corrections will be updated with a proper tune to our data. Before a cross section can be extracted from the data, the spectrometer acceptance must be

fully understood and acceptance cuts applied. For this preliminary extraction of the spin structure functions, it was assumed that the data agrees with the MAID and Bosted predictions. While the MAID prediction agrees well in the region of the Δ -resonance, the prediction for the resonances at higher W may not be as accurate. Particularly in the longitudinal configuration at high W , the radiative effects are a large correction to the asymmetry, if we assume that the prediction using the MAID/Bosted combination is correct. This represents a strong case for the use of a cross section extracted from our own data, rather than relying on a model prediction.

Previous tests of the BC sum rule with JLab data for the proton and neutron show agreement with the expected result of zero, suggesting that g_2 is a well behaved function. These data will provide the first test of this sum rule at low Q^2 , which has remained largely untested until now. The contribution to the BC sum integral from these data suggests a negative contribution from the resonance region. A proper test of this sum rule can be performed when the final value of g_2^p has been extracted and the contributions from low x and the elastic region have been included.

These data are eagerly awaited to provide a benchmark test of χ PT predictions for the generalized spin polarizabilities δ_{LT} and γ_0 . Recent developments [113] have removed the discrepancy previously seen between the neutron data and theoretical predictions for δ_{LT} . The current prediction for δ_{LT}^p shows agreement with the MAID prediction. However, the MAID model is not well constrained for our kinematics, so a comparison with these data will be a more revealing test of the χ PT predictions.

APPENDIX A

Particle ID Cuts

The PID cuts used for data analysis are detailed in the following tables. One representative run is shown for each momentum setting; the results are available run by run in the g_2^p mysql database. The table entries are described as follows:

- Det Eff: detector efficiency of the gas Cherenkov (Cer) or lead glass calorimeter (PR)
- $(\pi/e)_{raw}$: the initial (π/e) ratio (without cuts)
- Cut on E_1/p : location of cut on the first layer of lead glass
- Cut on E_{tot}/p : location of cut on the total energy deposited in the lead glass
- Cut Eff: cut efficiency of the gas Cherenkov (Cer) or lead glass calorimeter (PR) cuts
- $(\pi/e)_{final}$: the final π/e ratio (with all cuts)

A.0.1 Right HRS Results

Note that for all kinematic settings, the cut on the gas Cherenkov is at channel 150.

Table 1: RHRSS, $E = 2.2$ GeV, 2.5 T Tranverse Target Field

p_0 (GeV)	Run #	Det Eff (Cer)	Det Eff (PR)	$(\pi/e)_{raw}$	Cut on E_1/p	Cut on E_{tot}/p	Cut Eff (Cer)	Cut Eff (PR)	$(\pi/e)_{final}$
0.541	22969	0.99940	0.98836	0.03200	0.0924	0.665	0.99076	0.99755	0.00371
0.582	22962	0.99946	0.99254	0.03442	0.0893	0.685	0.99074	0.99771	0.00397
0.626	22955	0.99949	0.99512	0.03727	0.0863	0.695	0.99075	0.99769	0.00415
0.673	22947	0.99953	0.99660	0.03925	0.0832	0.700	0.99068	0.99773	0.00413
0.724	22941	0.99955	0.99735	0.03965	0.0829	0.710	0.99060	0.99774	0.00423
0.778	22932	0.99959	0.99775	0.03849	0.0797	0.725	0.99054	0.99778	0.00443
0.837	22925	0.99962	0.99802	0.03639	0.0812	0.715	0.99054	0.99778	0.00421
0.900	22919	0.99964	0.99809	0.03500	0.0800	0.720	0.99042	0.99775	0.00417
0.968	22913	0.99965	0.99825	0.03482	0.0764	0.735	0.99045	0.99780	0.00440
1.041	22904	0.99969	0.99828	0.03357	0.0749	0.710	0.99103	0.99768	0.00395
1.078	22653	0.99967	0.99846	0.03289	0.0761	0.725	0.99050	0.99748	0.00426
1.119	22893	0.99970	0.99830	0.03352	0.0751	0.730	0.99051	0.99765	0.00435
1.159	22641	0.99969	0.99844	0.03167	0.0725	0.735	0.99038	0.99724	0.00448
1.203	22875	0.99972	0.99845	0.03147	0.0715	0.735	0.99065	0.99767	0.00428
1.247	22625	0.99972	0.99847	0.02999	0.0722	0.735	0.99059	0.99740	0.00430
1.294	22862	0.99973	0.99845	0.02937	0.0711	0.745	0.99047	0.99760	0.00442
1.341	22607	0.99974	0.99855	0.02724	0.0746	0.735	0.99036	0.99742	0.00406
1.441	22585	0.99974	0.99865	0.02326	0.0694	0.745	0.99059	0.99741	0.00424
1.496	22831	0.99975	0.99851	0.02178	0.0668	0.755	0.99057	0.99752	0.00440
1.550	22564	0.99976	0.99873	0.01951	0.0658	0.750	0.99057	0.99733	0.00422
1.608	22816	0.99975	0.99855	0.01755	0.0634	0.760	0.99053	0.99738	0.00441
1.667	22551	0.99979	0.99870	0.01506	0.0636	0.760	0.99051	0.99729	0.00439
1.729	22798	0.99978	0.99854	0.01249	0.0648	0.765	0.99026	0.99736	0.00441
1.792	22529	0.99979	0.99870	0.00979	0.0625	0.765	0.99045	0.99729	0.00435
1.859	22786	0.99976	0.99865	0.00940	0.0613	0.795	0.98974	0.99681	0.00531
1.927	22513	0.99981	0.99868	0.00664	0.0592	0.770	0.99062	0.99737	0.00432
1.940	22977	0.99979	0.99860	0.00655	0.0619	0.775	0.99055	0.99751	0.00429
2.072	22493	0.99980	0.99826	0.00715	0.049	0.755	0.99140	0.99727	0.00441
2.228	22363	0.99982	0.99838	0.00436	0.045	0.760	0.99008	0.99747	0.00406

Table 2: RHR_S, $E = 1.7$ GeV, 2.5 T Transverse Target Field

p_0 (GeV)	Run #	Det Eff (Cer)	Det Eff (PR)	$(\pi/e)_{raw}$	Cut on E_1/p	Cut on E_{tot}/p	Cut Eff (Cer)	Cut Eff (PR)	$(\pi/e)_{final}$
0.572	23500	0.99951	0.99220	0.01416	0.0909	0.680	0.99076	0.99771	0.00392
0.622	23492	0.99954	0.99517	0.01414	0.0868	0.690	0.99061	0.99769	0.00406
0.676	23480	0.99960	0.99669	0.01467	0.0828	0.705	0.99052	0.99776	0.00428
0.735	23463	0.99961	0.99749	0.01411	0.0844	0.715	0.99048	0.99768	0.00437
0.798	23449	0.99962	0.99789	0.01299	0.0827	0.715	0.99039	0.99765	0.00421
0.856	23431	0.99967	0.99805	0.01214	0.0794	0.700	0.99077	0.99766	0.00409
0.911	23415	0.99967	0.99816	0.01191	0.0790	0.715	0.99046	0.99759	0.00434
0.969	23398	0.99972	0.99825	0.01106	0.0784	0.715	0.99058	0.99758	0.00419
1.031	23381	0.99972	0.99831	0.01084	0.0776	0.725	0.99040	0.99752	0.00438
1.097	23362	0.99971	0.99833	0.01028	0.0747	0.730	0.99044	0.99745	0.00440
1.167	23339	0.99973	0.99843	0.00935	0.0737	0.735	0.99044	0.99742	0.00442
1.241	23318	0.99974	0.99842	0.00826	0.0725	0.735	0.99043	0.99734	0.00424
1.32	23299	0.99974	0.99846	0.00715	0.0697	0.740	0.99054	0.99731	0.00431
1.405	23270	0.99977	0.99850	0.00628	0.0683	0.740	0.99046	0.99743	0.00436
1.494	23506	0.99976	0.99828	0.00613	0.0656	0.735	0.99065	0.89860	0.00428
1.589	23201	0.99979	0.99779	0.00781	0.0529	0.720	0.99120	0.99722	0.00468
1.691	23509	0.99967	0.99817	0.00491	0.0568	0.715	0.99016	0.38636	0.00434

 Table 3: RHR_S, E = 1.2 GeV, 2.5 T Transverse Target Field (Normal Ammonia Cell)

p_0 (GeV)	Run #	Det Eff (Cer)	Det Eff (PR)	$(\pi/e)_{raw}$	Cut on E_1/p	Cut on E_{tot}/p	Cut Eff (Cer)	Cut Eff (PR)	$(\pi/e)_{final}$
0.548	23886	0.99952	0.98976	0.00664	0.0876	0.675	0.99083	0.99740	0.00403
0.583	23868	0.99955	0.99291	0.00661	0.0858	0.680	0.99070	0.99731	0.00413
0.620	23858	0.99957	0.99500	0.00624	0.0871	0.675	0.99073	0.99730	0.00402
0.660	23840	0.99958	0.99619	0.00658	0.0848	0.695	0.99060	0.99723	0.00438
0.702	23826	0.99961	0.99710	0.00620	0.0855	0.680	0.99050	0.99718	0.00411
0.746	23813	0.99959	0.99739	0.00638	0.0858	0.695	0.99035	0.99717	0.00442
0.794	23792	0.99961	0.99777	0.00596	0.0831	0.685	0.99041	0.99678	0.00422
0.845	23774	0.99964	0.99785	0.00565	0.0805	0.685	0.99056	0.99666	0.00408
0.870	23946	0.99964	0.99792	0.00569	0.0805	0.685	0.99046	0.99701	0.00417
0.899	23756	0.99965	0.99792	0.00567	0.0801	0.690	0.99051	0.99664	0.00416
0.936	23934	0.99966	0.99793	0.00585	0.0791	0.685	0.99049	0.99687	0.00424
0.956	23734	0.99964	0.99795	0.00592	0.0774	0.695	0.99042	0.99671	0.00428
1.006	23906	0.99968	0.99784	0.00641	0.0736	0.690	0.99060	0.99673	0.00440
1.017	23698	0.99966	0.99763	0.00668	0.0728	0.695	0.99055	0.99682	0.00450
1.082	23895	0.99961	0.99634	0.01045	0.0665	0.615	0.99002	0.99579	0.00469

1.15	23893	0.99868	0.99509	0.00556	0.0226	0.610	0.98996	0.98845	0.00455
------	-------	---------	---------	---------	--------	-------	---------	---------	---------

Table 4: RHRS, E = 1.2 GeV, 2.5 T Transverse Target Field (Short Ammonia Cell)

p_0 (GeV)	Run #	Det Eff (Cer)	Det Eff (PR)	$(\pi/e)_{raw}$	Cut on E_1/p	Cut on E_{tot}/p	Cut Eff (Cer)	Cut Eff (PR)	$(\pi/e)_{final}$
0.651	24095	0.99961	0.99603	0.00669	0.0860	0.690	0.99061	0.99745	0.00421
0.700	24060	0.99963	0.99687	0.00643	0.0866	0.685	0.99028	0.99736	0.00434
0.753	24025	0.99963	0.99750	0.00602	0.0850	0.675	0.99056	0.99736	0.00403
0.809	23995	0.99965	0.99773	0.00583	0.0816	0.685	0.99060	0.99719	0.00417
0.870	23974	0.99964	0.99739	0.00688	0.0805	0.685	0.98958	0.99709	0.00480

Table 5: RHRS, E = 2.2 GeV, 5 T Longitudinal Target Field

p_0 (GeV)	Run #	Det Eff (Cer)	Det Eff (PR)	$(\pi/e)_{raw}$	Cut on E_1/p	Cut on E_{tot}/p	Cut Eff (Cer)	Cut Eff (PR)	$(\pi/e)_{final}$
0.991	24591	0.99967	0.99815	0.02719	0.0767	0.720	0.99043	0.99725	0.00434
1.055	24585	0.99970	0.99825	0.02872	0.0758	0.725	0.99042	0.99744	0.00431
1.122	24561	0.99969	0.99824	0.02961	0.0749	0.730	0.99043	0.99737	0.00425
1.194	24550	0.99971	0.99827	0.03020	0.0737	0.740	0.99022	0.99738	0.00438
1.27	24532	0.99972	0.99837	0.02927	0.0709	0.745	0.99048	0.99737	0.00438
1.351	24514	0.99976	0.99832	0.02721	0.0696	0.745	0.99042	0.99745	0.00428
1.468	24486	0.99975	0.99847	0.02308	0.0695	0.750	0.99033	0.99750	0.00425
1.596	24447	0.99985	0.99849	0.01813	0.0702	0.760	0.99002	0.99766	0.00429
1.735	24350	0.99978	0.99840	0.01252	0.0611	0.765	0.99055	0.99770	0.00436
2.05	24630	0.99984	0.99824	0.00742	0.0615	0.760	0.98998	0.99802	0.00445

Table 6: RHRS, E = 2.2 GeV, 5 T Transverse Target Field

p_0 (GeV)	Run #	Det Eff (Cer)	Det Eff (PR)	$(\pi/e)_{raw}$	Cut on E_1/p	Cut on E_{tot}/p	Cut Eff (Cer)	Cut Eff (PR)	$(\pi/e)_{final}$
1.016	24726	0.99916	0.99759	0.35403	0.0807	0.700	0.99017	0.99753	0.00494
1.104	24723	0.99934	0.99773	0.29034	0.0725	0.710	0.99050	0.99755	0.00498
1.175	24720	0.99945	0.99785	0.23695	0.0698	0.720	0.99069	0.99769	0.00482
1.249	24714	0.99955	0.99802	0.18569	0.0689	0.730	0.99049	0.99790	0.00485
1.329	24708	0.99964	0.99815	0.14066	0.0662	0.735	0.99059	0.99797	0.00478
1.414	24698	0.99970	0.99828	0.10316	0.0665	0.740	0.99051	0.99811	0.00445

1.504	24691	0.99974	0.99828	0.07206	0.0638	0.755	0.99053	0.99811	0.00480
1.6	24684	0.99974	0.99835	0.05237	0.0625	0.750	0.99058	0.99798	0.00445
1.703	24677	0.99978	0.99840	0.02807	0.0599	0.760	0.99068	0.99809	0.00456
1.811	24662	0.99981	0.99845	0.01460	0.0585	0.765	0.99062	0.99815	0.00449
1.926	24648	0.99983	0.99849	0.00814	0.0571	0.770	0.99089	0.99815	0.00428
2.05	24631	0.99984	0.99827	0.00744	0.0615	0.760	0.99003	0.99808	0.00439

Table 7: RHRS, E = 3.3 GeV, 5 T Transverse Target Field

p_0 (GeV)	Run #	Det Eff (Cer)	Det Eff (PR)	$(\pi/e)_{raw}$	Cut on E_1/p	Cut on E_{tot}/p	Cut Eff (Cer)	Cut Eff (PR)	$(\pi/e)_{final}$
1.945	24770	0.99950	0.99820	0.28367	0.0566	0.745	0.99056	0.99776	0.00515
2.070	24754	0.99962	0.99834	0.19549	0.0541	0.755	0.99070	0.99788	0.00512
2.202	24736	0.99971	0.99835	0.13156	0.0563	0.760	0.99078	0.99805	0.00453

A.0.2 Left HRS Results

Note that for all kinematic settings, the cut on the gas Cherenkov is at channel 200.

Table 8: LHRs, $E = 2.2$ GeV, 2.5 T Transverse Target Field

p_0 (GeV)	Run #	Det Eff (Cer)	Det Eff (PR)	$(\pi/e)_{raw}$	Cut on E_1/p	Cut on E_{tot}/p	Cut Eff (Cer)	Cut Eff (PR)	$(\pi/e)_{final}$
0.541	3935	0.99968	0.98105	0.05227	0.255	0.580	0.98976	0.99914	0.00442
0.582	3929	0.99970	0.98746	0.04898	0.254	0.580	0.98976	0.99911	0.00431
0.626	3922	0.99974	0.99171	0.04589	0.252	0.585	0.98973	0.99920	0.00445
0.673	3915	0.99973	0.99445	0.04272	0.253	0.585	0.98972	0.99923	0.00435
0.724	3907	0.99978	0.99322	0.04049	0.251	0.590	0.98970	0.99932	0.00445
0.778	3901	0.99978	0.99593	0.03760	0.244	0.590	0.98970	0.99935	0.00443
0.837	3893	0.99984	0.99757	0.03564	0.246	0.590	0.98971	0.99940	0.00430
0.900	3885	0.99981	0.99841	0.03474	0.244	0.595	0.98967	0.99935	0.00450
0.968	3882	0.99988	0.99888	0.03381	0.240	0.595	0.98961	0.99943	0.00446
1.003	3643	0.99992	0.99901	0.03434	0.237	0.595	0.98961	0.99938	0.00448
1.041	3872	0.99986	0.99915	0.03314	0.238	0.595	0.98981	0.99943	0.00436
1.078	3628	0.99995	0.99928	0.03371	0.239	0.595	0.98971	0.99945	0.00429
1.119	3866	0.99989	0.99931	0.03217	0.238	0.595	0.98978	0.99946	0.00424
1.159	3616	0.99994	0.99938	0.03302	0.236	0.600	0.98962	0.99941	0.00447
1.203	3845	0.99989	0.99940	0.03142	0.233	0.595	0.98975	0.99948	0.00436
1.247	3596	0.99994	0.99943	0.03085	0.231	0.595	0.98971	0.99946	0.00431
1.294	3834	0.99991	0.99947	0.02941	0.229	0.595	0.98987	0.99946	0.00434
1.340	3585	0.99995	0.99952	0.02811	0.227	0.590	0.99019	0.99941	0.00398
1.391	3823	0.99990	0.99948	0.02700	0.226	0.595	0.98960	0.99943	0.00445
1.441	3554	0.99995	0.99957	0.02576	0.226	0.595	0.98970	0.99946	0.00434
1.496	3817	0.99993	0.99951	0.02333	0.221	0.590	0.99001	0.99948	0.00428
1.550	3531	0.99996	0.99959	0.02176	0.223	0.595	0.98978	0.99940	0.00442
1.608	3787	0.99992	0.99957	0.01957	0.219	0.590	0.98989	0.99945	0.00422
1.667	3520	0.99997	0.99956	0.01764	0.218	0.590	0.98986	0.99946	0.00425
1.729	3774	0.99992	0.99954	0.01550	0.219	0.590	0.98977	0.99945	0.00427
1.792	3497	0.99996	0.99959	0.01365	0.218	0.590	0.98979	0.99951	0.00428
1.859	3772	0.99992	0.99960	0.01175	0.216	0.590	0.98977	0.99934	0.00436
1.927	3477	0.99996	0.99969	0.01005	0.215	0.585	0.99015	0.99948	0.00397
1.940	3941	0.99993	0.99962	0.01018	0.212	0.585	0.98985	0.99946	0.00423
2.072	3457	0.99997	0.99902	0.01118	0.197	0.575	0.98989	0.99937	0.00418
2.228	3444	0.99996	0.99980	0.00871	0.212	0.590	0.99002	0.99941	0.00413

Table 9: LHRs, E = 1.7 GeV, 2.5 T Transverse Target Field

p_0 (GeV)	Run #	Det Eff (Cer)	Det Eff (PR)	$(\pi/e)_{raw}$	Cut on E_1/p	Cut on E_{tot}/p	Cut Eff (Cer)	Cut Eff (PR)	$(\pi/e)_{final}$
0.572	4551	0.99976	0.98683	0.02347	0.255	0.585	0.98965	0.99926	0.00447
0.622	4539	0.99976	0.99159	0.02125	0.254	0.585	0.98949	0.99928	0.00448
0.676	4528	0.99982	0.99472	0.01964	0.254	0.590	0.98957	0.99929	0.00451
0.735	4513	0.99984	0.99402	0.01796	0.250	0.590	0.98973	0.99936	0.00447
0.798	4496	0.99983	0.99667	0.01664	0.251	0.590	0.98974	0.99938	0.00425
0.856	4482	0.99987	0.99785	0.01574	0.255	0.590	0.98960	0.99937	0.00404
0.911	4465	0.99987	0.99848	0.01553	0.244	0.595	0.98964	0.99940	0.00437
0.969	4445	0.99987	0.99894	0.01448	0.244	0.590	0.99006	0.99944	0.00401
1.031	4428	0.99989	0.99910	0.01446	0.241	0.595	0.98971	0.99945	0.00427
1.097	4409	0.99990	0.99925	0.01374	0.239	0.595	0.98981	0.99944	0.00425
1.167	4384	0.99989	0.99932	0.01368	0.233	0.600	0.98960	0.99942	0.00456
1.241	4358	0.99990	0.99938	0.01219	0.234	0.595	0.98970	0.99945	0.00421
1.32	4341	0.99989	0.99939	0.01100	0.230	0.595	0.98964	0.99941	0.00429
1.405	4292	0.99989	0.99948	0.00978	0.229	0.595	0.98997	0.99941	0.00414
1.494	4332	0.99991	0.99943	0.01002	0.220	0.605	0.98922	0.99940	0.00433
1.589	4220	0.99992	0.99892	0.01139	0.214	0.590	0.98934	0.99929	0.00446
1.691	4574	0.99990	0.99979	0.00867	0.231	0.605	0.98997	0.99915	0.00403

Table 10: LHRs, E = 1.2 GeV, 2.5 T Transverse Target Field (Normal Ammonia Cell)

p_0 (GeV)	Run #	Det Eff (Cer)	Det Eff (PR)	$(\pi/e)_{raw}$	Cut on E_1/p	Cut on E_{tot}/p	Cut Eff (Cer)	Cut Eff (PR)	$(\pi/e)_{final}$
0.548	5007	0.99975	0.98134	0.01099	0.252	0.575	0.98997	0.99917	0.00438
0.583	4987	0.99979	0.98667	0.01075	0.257	0.580	0.98982	0.99916	0.00446
0.620	4980	0.99981	0.99060	0.01035	0.255	0.580	0.98973	0.99922	0.00439
0.660	4963	0.99983	0.99377	0.00974	0.252	0.580	0.98974	0.99922	0.00423
0.702	4949	0.99984	0.99146	0.00985	0.254	0.585	0.98967	0.99923	0.00433
0.746	4931	0.99986	0.99464	0.00961	0.247	0.585	0.98952	0.99922	0.00432
0.794	4905	0.99986	0.99641	0.00993	0.247	0.595	0.98937	0.99918	0.00469
0.845	4886	0.99986	0.99741	0.00943	0.246	0.590	0.98961	0.99920	0.00434
0.870	5089	0.99986	0.99781	0.00858	0.237	0.575	0.99017	0.99921	0.00392
0.896	4861	0.99986	0.99814	0.00968	0.245	0.595	0.98933	0.99910	0.00445
0.936	5070	0.99986	0.99842	0.00968	0.239	0.590	0.98946	0.99920	0.00443
0.956	4841	0.99986	0.99860	0.00988	0.241	0.595	0.98941	0.99918	0.00453
1.006	5047	0.99986	0.99875	0.01019	0.233	0.590	0.98951	0.99916	0.00446
1.017	4788	0.99988	0.99787	0.01261	0.222	0.585	0.98830	0.99892	0.00487
1.082	5034	0.99976	0.99762	0.01580	0.207	0.580	0.98864	0.99843	0.00500

1.113	5030	0.99934	0.99903	0.00945	0.228	0.575	0.98998	0.99467	0.00415
1.150	5029	0.99983	0.99855	0.00952	0.216	0.570	0.98612	0.98624	0.00404
1.168	5025	0.99870	0.99834	0.00944	0.214	0.590	0.98997	0.99236	0.00395

Table 11: LHRS, E = 1.2 GeV, 2.5 T Transverse Target Field (Short Ammonia Cell)

p_0 (GeV)	Run #	Det Eff (Cer)	Det Eff (PR)	$(\pi/e)_{raw}$	Cut on E_1/p	Cut on E_{tot}/p	Cut Eff (Cer)	Cut Eff (PR)	$(\pi/e)_{final}$
0.523	5290	0.99980	0.97312	0.01211	0.252	0.565	0.98971	0.99924	0.00423
0.563	5288	0.99980	0.98199	0.01097	0.249	0.565	0.98989	0.99927	0.00422
0.651	5265	0.99985	0.99231	0.01033	0.249	0.575	0.98965	0.99937	0.00437
0.700	5238	0.99985	0.99474	0.01011	0.249	0.580	0.98941	0.99930	0.00451
0.746	5322	0.99988	0.99398	0.00942	0.244	0.575	0.98998	0.99935	0.00418
0.753	5200	0.99985	0.99442	0.00973	0.244	0.580	0.98980	0.99936	0.00444
0.794	5320	0.99984	0.99620	0.00910	0.242	0.575	0.99004	0.99926	0.00416
0.845	5318	0.99983	0.99733	0.00881	0.241	0.575	0.99010	0.99934	0.00404
0.870	5138	0.99987	0.99689	0.01120	0.228	0.575	0.98883	0.99924	0.00469
0.896	5316	0.99982	0.99821	0.00909	0.240	0.580	0.99009	0.99932	0.00426
0.956	5276	0.99985	0.99867	0.00911	0.234	0.585	0.98983	0.99932	0.00426
1.017	5274	0.99990	0.99847	0.00986	0.212	0.570	0.99008	0.99927	0.00415
1.082	5272	0.99985	0.99698	0.01435	0.170	0.540	0.99001	0.99895	0.00453

Table 12: LHRS, E = 2.2 GeV, 5 T Longitudinal Target Field

p_0 (GeV)	Run #	Det Eff (Cer)	Det Eff (PR)	$(\pi/e)_{raw}$	Cut on E_1/p	Cut on E_{tot}/p	Cut Eff (Cer)	Cut Eff (PR)	$(\pi/e)_{final}$
0.991	5902	0.99989	0.99890	0.02800	0.244	0.595	0.98963	0.99938	0.00436
1.055	5890	0.99987	0.99915	0.02914	0.241	0.595	0.98987	0.99933	0.00430
1.122	5885	0.99987	0.99929	0.02926	0.239	0.590	0.98992	0.99938	0.00403
1.194	5872	0.99989	0.99933	0.02996	0.236	0.595	0.98982	0.99941	0.00435
1.27	5866	0.99988	0.99939	0.02907	0.233	0.590	0.98990	0.99938	0.00421
1.351	5855	0.99990	0.99943	0.02766	0.231	0.590	0.98975	0.99944	0.00420
1.468	5838	0.99991	0.99950	0.02453	0.228	0.590	0.98972	0.99946	0.00431
1.596	5829	0.99992	0.99951	0.01999	0.223	0.585	0.98991	0.99948	0.00419
1.735	5827	0.99993	0.99953	0.01499	0.219	0.580	0.99003	0.99949	0.00402
1.886	5781	0.99996	0.99964	0.01079	0.213	0.580	0.99010	0.99954	0.00416
2.05	5706	0.99992	0.99924	0.01046	0.205	0.575	0.98989	0.99942	0.00417
2.228	5630	0.99992	0.99986	0.00836	0.215	0.585	0.99014	0.99934	0.00397

Table 13: LHRs, E = 2.2 GeV, 5 T Transverse Target Field

p_0 (GeV)	Run #	Det Eff (Cer)	Det Eff (PR)	$(\pi/e)_{raw}$	Cut on E_1/p	Cut on E_{tot}/p	Cut Eff (Cer)	Cut Eff (PR)	$(\pi/e)_{final}$
0.919	6085	0.99921	0.99822	0.46241	0.239	0.600	0.98972	0.99875	0.00454
1.016	6084	0.99943	0.99865	0.37722	0.230	0.600	0.98960	0.99899	0.00458
1.104	6083	0.99966	0.99891	0.30164	0.230	0.605	0.98962	0.99927	0.00475
1.175	6059	0.99968	0.99909	0.24180	0.231	0.600	0.98964	0.99933	0.00444
1.249	6053	0.99976	0.99917	0.19667	0.227	0.605	0.98951	0.99938	0.00470
1.329	6044	0.99978	0.99925	0.15003	0.227	0.605	0.98941	0.99941	0.00465
1.414	6031	0.99984	0.99934	0.11008	0.228	0.605	0.98945	0.99949	0.00468
1.504	6021	0.99990	0.99941	0.07824	0.222	0.605	0.98928	0.99955	0.00479
1.6	6011	0.99988	0.99940	0.05755	0.219	0.590	0.98999	0.99952	0.00405
1.703	6002	0.99990	0.99947	0.03308	0.216	0.600	0.98949	0.99953	0.00459
1.811	5978	0.99992	0.99958	0.01885	0.216	0.600	0.98948	0.99957	0.00451
1.926	5962	0.99994	0.99961	0.01181	0.213	0.595	0.98988	0.99958	0.00419
2.05	5954	0.99994	0.99925	0.01052	0.199	0.585	0.99003	0.99954	0.00417
2.228	6065	0.99994	0.99988	0.00804	0.208	0.595	0.99017	0.99966	0.00401

Table 14: LHRs, E = 3.3 GeV, 5 T Transverse Target Field

p_0 (GeV)	Run #	Det Eff (Cer)	Det Eff (PR)	$(\pi/e)_{raw}$	Cut on E_1/p	Cut on E_{tot}/p	Cut Eff (Cer)	Cut Eff (PR)	$(\pi/e)_{final}$
2.342	6148	0.99990	0.99952	0.08573	0.200	0.585	0.98980	0.99952	0.00427
2.492	6157	0.99991	0.99959	0.05089	0.197	0.585	0.98975	0.99955	0.00438
2.651	6170	0.99993	0.99960	0.02928	0.195	0.580	0.98995	0.99604	0.00408
2.800	6183	0.99995	0.99960	0.01720	0.191	0.580	0.98972	0.99955	0.00433
2.820	6129	0.99996	0.99960	0.01589	0.189	0.580	0.98978	0.99951	0.00433
3.000	6207	0.99996	0.99961	0.01068	0.185	0.575	0.98998	0.99962	0.00420

BIBLIOGRAPHY

- [1] D. P. Zeeman, Philosophical Magazine Series 5 **43**, 226 (1897).
- [2] <https://www.cfa.harvard.edu/~woolsey/zeeman.html>.
- [3] <http://hyperphysics.phy-astr.gsu.edu/hbase/quantum/sodzee.htmlc1>.
- [4] W. Gerlach and O. Stern, Zeitschrift für Physik **9**, 349 (1922).
- [5] B. Friedrich and D. Herschbach, Physics Today **56** (2003).
- [6] W. Pauli, Z. Phys. **31**, 373 (1925).
- [7] E. C. Stoner, Philosophical Magazine **48**, 719 (1924).
- [8] V. Sulkosky, Ph.D. thesis, The College of William and Mary (2007).
- [9] A. Thomas and W. Weise, *The Structure of the Nucleon* (Wiley, 2001).
- [10] J. D. Bjorken and E. A. Paschos, Phys. Rev. **185**, 1975 (1969).
- [11] R. P. Feynman, Phys. Rev. Lett. **23**, 1415 (1969).
- [12] D. Drechsel and L. Tiator, Journal of Physics G: Nuclear and Particle Physics **18**, 449 (1992).
- [13] D. Drechsel, S. S. Kamalov, and L. Tiator, Phys. Rev. D **63**, 114010 (2001).
- [14] K. Slifer, Ph.D. thesis, Temple University (2004).
- [15] F. J. Gilman, Phys. Rev. **167**, 1365 (1968).
- [16] L. N. Hand, Phys. Rev. **129**, 1834 (1963).
- [17] R. Roberts, *The Structure of the Proton: Deep Inelastic Scattering*, Cambridge Monographs on Mathematical Physics (Cambridge University Press, 1993).
- [18] C. G. Callan and D. J. Gross, Phys. Rev. Lett. **22**, 156 (1969).
- [19] R. L. Jaffe and X. Ji, Phys. Rev. D **43**, 724 (1991).
- [20] S. Wandzura and F. Wilczek, Physics Letters B **72**, 195 (1977).

- [21] K. G. Wilson, Phys. Rev. **179**, 1499 (1969).
- [22] S. Scherer, Adv. Nucl. Phys. **27**, 277 (2003).
- [23] V. Bernard, N. Kaiser, and U.-G. Meiner, International Journal of Modern Physics E **04**, 193 (1995).
- [24] D. Drechsel, S. S. Kamalov, and L. Tiator, Eur. Phys. J. **A34**, 69 (2007).
- [25] P. E. Bosted and M. E. Christy, Phys. Rev. C **77**, 065206 (2008).
- [26] T. Armstrong, W. Hogg, G. Lewis, A. Robertson, G. Brookes, A. Clough, J. Freeland, W. Galbraith, A. King, W. Rawlinson, et al., Nuclear Physics B **41**, 445 (1972).
- [27] S. Michalowski, D. Andrews, J. Eickmeyer, T. Gentile, N. Mistry, R. Talman, and K. Ueno, Phys. Rev. Lett. **39**, 737 (1977).
- [28] D. O. Caldwell, V. B. Elings, W. P. Hesse, R. J. Morrison, F. V. Murphy, and D. E. Yount, Phys. Rev. **D7**, 1362 (1973).
- [29] M. MacCormick, G. Audit, N. d'Hose, L. Ghedira, V. Isbert, S. Kerhoas, L. Y. Murphy, G. Tamas, P. A. Wallace, S. Altieri, et al., Phys. Rev. C **53**, 41 (1996).
- [30] M. Osipenko, G. Ricco, S. Simula, M. Battaglieri, M. Ripani, G. Adams, P. Ambrozewicz, M. Anghinolfi, B. Asavapibhop, G. Asryan, et al. (CLAS Collaboration), Phys. Rev. C **73**, 045205 (2006).
- [31] I. Niculescu, Ph.D. thesis, Hampton University (1999).
- [32] S. Malace, Ph.D. thesis, Hampton University (2006).
- [33] S. Rock, R. G. Arnold, P. Bosted, B. T. Chertok, B. A. Mecking, I. Schmidt, Z. M. Szalata, R. C. York, and R. Zdarko, Phys. Rev. Lett. **49**, 1139 (1982).
- [34] V. Tvaskis, J. Steinman, and R. Bradford, Nuclear Physics B - Proceedings Supplements **159**, 163 (2006), proceedings of the 4th International Workshop on Neutrino-Nucleus Interactions in the Few-GeV RegionProceedings of the 4th International Workshop on Neutrino-Nucleus Interactions in the Few-GeV Region.
- [35] C. Keppel, M. Niculescu, and spokespersons., very Preliminary Results from JLab E00-002.
- [36] S. Dasu, P. de Barbaro, A. Bodek, H. Harada, M. W. Krasny, K. Lang, E. M. Riordan, L. Andivahis, R. Arnold, D. Benton, et al., Phys. Rev. D **49**, 5641 (1994).

- [37] H. Burkhardt and W. Cottingham, Annals of Physics **56**, 453 (1970).
- [38] R. L. Jaffe, in *Internal spin structure of the nucleon. Proceedings, Symposium, SMC Meeting, New Haven, USA, January 5-6, 1994* (1994).
- [39] M. Ahmed and G. Ross, Physics Letters B **56**, 385 (1975).
- [40] F. G. J.-P. Chen, A. Deur (1997), experimental Proposal.
- [41] M. Amarian, L. Auerbach, T. Averett, J. Berthot, P. Bertin, B. Bertozzi, T. Black, E. Brash, D. Brown, E. Burtin, et al. (Jefferson Lab E94010 Collaboration), Phys. Rev. Lett. **92**, 022301 (2004).
- [42] K. Slifer, M. Amarian, L. Auerbach, T. Averett, J. Berthot, P. Bertin, B. Bertozzi, T. Black, E. Brash, D. Brown, et al. (Jefferson Lab E94010 Collaboration), Phys. Rev. Lett. **101**, 022303 (2008).
- [43] P. Solvignon, N. Liyanage, J.-P. Chen, S. Choi, K. Aniol, T. Averett, W. Boeglin, A. Camsonne, G. D. Cates, C. C. Chang, et al. (Jefferson Lab E01-012 Collaboration), Phys. Rev. Lett. **101**, 182502 (2008).
- [44] F. R. Wesselmann, K. Slifer, S. Tajima, A. Aghalaryan, A. Ahmidouch, R. Asaturyan, F. Bloch, W. Boeglin, P. Bosted, C. Carasco, et al. (Resonance Spin Structure Collaboration), Phys. Rev. Lett. **98**, 132003 (2007).
- [45] P. Anthony, R. Arnold, T. Averett, H. Band, N. Benmouna, W. Boeglin, H. Borel, P. Bosted, S. Bltmann, G. Court, et al., Physics Letters B **553**, 18 (2003).
- [46] J.-P. CHEN, International Journal of Modern Physics E **19**, 1893 (2010).
- [47] J.-P. CHEN, A. DEUR, and Z.-E. MEZIANI, Modern Physics Letters A **20**, 2745 (2005).
- [48] F. E. Low, Phys. Rev. **96**, 1428 (1954).
- [49] V. Bernard, T. R. Hemmert, and U.-G. Meißner, Phys. Rev. D **67**, 076008 (2003).
- [50] X. Ji, C.-W. Kao, and J. Osborne, Phys. Rev. D **61**, 074003 (2000).
- [51] V. Sulkosky, PoS **CD12**, 023 (2013).
- [52] S. G. Karshenboim, Canadian Journal of Physics **77**, 241 (1999).
- [53] V. Nazaryan, C. E. Carlson, and K. A. Griffioen, Phys. Rev. Lett. **96**, 163001 (2006).
- [54] A. C. Zemach, Phys. Rev. **104**, 1771 (1956).

- [55] M. Amarian, L. Auerbach, T. Averett, J. Berthot, P. Bertin, W. Bertozzi, T. Black, E. Brash, D. Brown, E. Burton, et al. (Jefferson Lab E94010 Collaboration), *Phys. Rev. Lett.* **93**, 152301 (2004).
- [56] A. Camsonne, J. Chen, D. Crabb, and K. S. spokespersons, Jefferson Lab Experimental Proposal E08-027.
- [57] I. Sick, *Physics Letters B* **576**, 62 (2003).
- [58] P. G. Blunden and I. Sick, *Phys. Rev. C* **72**, 057601 (2005).
- [59] P. J. Mohr, B. N. Taylor, and D. B. Newell, *Rev. Mod. Phys.* **84**, 1527 (2012).
- [60] M. Niering, R. Holzwarth, J. Reichert, P. Pokasov, T. Udem, M. Weitz, T. W. Hänsch, P. Lemonde, G. Santarelli, M. Abgrall, et al., *Phys. Rev. Lett.* **84**, 5496 (2000).
- [61] M. Fischer, N. Kolachevsky, M. Zimmermann, R. Holzwarth, T. Udem, T. W. Hänsch, M. Abgrall, J. Grünert, I. Maksimovic, S. Bize, et al., *Phys. Rev. Lett.* **92**, 230802 (2004).
- [62] B. de Beauvoir, C. Schwob, O. Acef, L. Jozefowski, L. Hilico, F. Nez, L. Julien, A. Clairon, and F. Biraben, *The European Physical Journal D - Atomic, Molecular, Optical and Plasma Physics* **12**, 61 (2000).
- [63] C. Schwob, L. Jozefowski, B. de Beauvoir, L. Hilico, F. Nez, L. Julien, F. Biraben, O. Acef, J.-J. Zondy, and A. Clairon, *Phys. Rev. Lett.* **82**, 4960 (1999).
- [64] M. I. Eides, H. Grotch, and V. A. Shelyuto, *Physics Reports* **342**, 63 (2001).
- [65] S. G. Karshenboim, *Physics Reports* **422**, 1 (2005).
- [66] W. E. Lamb and R. C. Rutherford, *Phys. Rev.* **72**, 241 (1947).
- [67] R. Pohl, A. Antognini, F. Nez, F. D. Amaro, F. Biraben, J. M. R. Cardoso, D. S. Covita, A. Dax, S. Dhawan, L. M. P. Fernandes, et al., *Nature* **466**, 213 (2010).
- [68] C. E. Carlson, V. Nazaryan, and K. Griffioen, *Phys. Rev. A* **83**, 042509 (2011).
- [69] J. Alcorn, B. Anderson, K. Aniol, J. Annand, L. Auerbach, J. Arrington, T. Averett, F. Baker, M. Baylac, E. Beise, et al., *Nuclear Instruments and Methods in Physics Research Section A: Accelerators, Spectrometers, Detectors and Associated Equipment* **522**, 294 (2004).
- [70] T. Maruyama, A. Brachmann, J. Clendenin, T. Desikan, E. Garwin, R. Kirby, D.-A. Luh, J. Turner, and R. Prepost, *Nuclear Instruments and Methods in Physics Research Section A: Accelerators, Spectrometers, Detectors and Associated Equipment* **492**, 199 (2002).

- [71] M. B. et. al., in *Proc. of 2005 Particle Accelerator Conference* (2005).
- [72] C. Yan, J. Beaufait, P. Brindza, R. Carlini, W. Vulcan, and R. Wines, Tech. Rep., CEBAF (1993).
- [73] A. W. Overhauser, Phys. Rev. **92**, 411 (1953).
- [74] C. D. Jeffries, Phys. Rev. **106**, 164 (1957).
- [75] A. Abragam and W. G. Proctor, Phys. Rev. **109**, 1441 (1958).
- [76] J. Pierce, J. Maxwell, and C. Keith, Physics of Particles and Nuclei **45**, 303 (2014).
- [77] K. Fissum, W. Bertozzi, J. Chen, D. Dale, H. Fenker, J. Gao, A. Gavalya, S. Gilad, C. Leathers, N. Liyanage, et al., Nuclear Instruments and Methods in Physics Research Section A: Accelerators, Spectrometers, Detectors and Associated Equipment **474**, 108 (2001).
- [78] M. Iodice, E. Cisbani, S. Colilli, R. Crateri, S. Frullani, F. Garibaldi, F. Giuliani, M. Gricia, M. Lucentini, A. Mostarda, et al., Nuclear Instruments and Methods in Physics Research Section A: Accelerators, Spectrometers, Detectors and Associated Equipment **411**, 223 (1998).
- [79] W. Leo, *Techniques for Nuclear and Particle Physics Experiments: A How-to Approach* (Springer, 1994).
- [80] <https://userweb.jlab.org/~kalyan/g2p/thirdarm/thirdarm.pdf> (2012).
- [81] H.-J. Lu, Y.-X. Ye, Y. Jiang, X.-H. Yan, and P. Zhang, Tech. Rep., University of Science and Technology of China (2005).
- [82] R. Zielinski, Tech. Rep., University of New Hampshire (2012), https://hallaweb.jlab.org/wiki/index.php/G2p_technotes.
- [83] J. Liu, Tech. Rep., University of Virginia (2013), https://hallaweb.jlab.org/wiki/index.php/G2p_technotes.
- [84] S. J. A. Deur, Tech. Rep., Jefferson Lab LPC/Unviersite Blaise Pascal, California Institute of Technology (2000).
- [85] C. Gu, Tech. Rep., University of Virginia (2016), https://hallaweb.jlab.org/wiki/index.php/G2p_technotes.
- [86] M. Huang, Tech. Rep., Duke University (2014), https://hallaweb.jlab.org/wiki/index.php/G2p_technotes.
- [87] <http://hallaweb.jlab.org/experiment/g2p/survey/>.

- [88] T. Badman, Tech. Rep., University of New Hampshire (2012), https://hallaweb.jlab.org/wiki/index.php/G2p_technotes.
- [89] J. Liu, Tech. Rep., University of Virginia (2013), https://hallaweb.jlab.org/wiki/index.php/G2p_technotes.
- [90] C. Gu, Tech. Rep., University of Virginia (2015), https://hallaweb.jlab.org/wiki/index.php/G2p_technotes.
- [91] T. Badman, Tech. Rep., University of New Hampshire (2013), https://hallaweb.jlab.org/wiki/index.php/G2p_technotes.
- [92] P. Zhu, Tech. Rep., University of Science and Technology of China (2014), https://hallaweb.jlab.org/wiki/index.php/G2p_technotes.
- [93] C. R. Carman and J. L. Pellegrin, Nucl. Instrum. Meth. **113**, 423 (1973).
- [94] T. Badman, Tech. Rep., University of New Hampshire (2015), https://hallaweb.jlab.org/wiki/index.php/G2p_technotes.
- [95] M. Cummings, Tech. Rep., The College of William and Mary (2015), https://hallaweb.jlab.org/wiki/index.php/G2p_technotes.
- [96] M. Cummings, Tech. Rep., College of William and Mary (2013), https://hallaweb.jlab.org/wiki/index.php/G2p_technotes.
- [97] J. W. Lightbody and J. S. OConnell, Computers in Physics **2** (1988).
- [98] S. Venkat, J. Arrington, G. A. Miller, and X. Zhan, Phys. Rev. C **83**, 015203 (2011).
- [99] C. D. Jager, H. D. Vries, and C. D. Vries, Atomic Data and Nuclear Data Tables **14**, 479 (1974), nuclear Charge and Moment Distributions.
- [100] <http://hallaweb.jlab.org/equipment/moller/e08-027.html> (2012).
- [101] Y. Qiang, *Statistical fluctuation of prescaled events*, ELOG entry, <https://hallaweb.jlab.org/dvcslog/g2p/170>.
- [102] R. Zielinski, Tech. Rep., University of New Hampshire (2014), https://hallaweb.jlab.org/wiki/index.php/G2p_technotes.
- [103] J. Schwinger, Phys. Rev. **75**, 1912 (1949).
- [104] J. Singh and V. Sulkosky, Tech. Rep., University of Virginia, College of William and Mary (2007).
- [105] K. A. Olive et al. (Particle Data Group), Chin. Phys. **C38**, 090001 (2014).

- [106] I. Akushevich, A. Ilyichev, N. Shumeiko, A. Soroko, and A. Tolkachev, Computer Physics Communications **104**, 201 (1997).
- [107] L. W. MO and Y. S. TSAI, Rev. Mod. Phys. **41**, 205 (1969).
- [108] A. Afanasev, I. Akushevich, and N. Merenkov, Phys. Rev. D **64**, 113009 (2001).
- [109] K. Slifer, AIP Conference Proceedings **1149**, 130 (2009).
- [110] E. L. Lomon, Phys. Rev. C **66**, 045501 (2002).
- [111] P. Mergell, U.-G. Meiner, and D. Drechsel, Nuclear Physics A **596**, 367 (1996).
- [112] A. Amroun, V. Breton, J.-M. Cavedon, B. Frois, D. Goutte, F. Juster, P. Leconte, J. Martino, Y. Mizuno, X.-H. Phan, et al., Nuclear Physics A **579**, 596 (1994).
- [113] V. Lensky, J. M. Alarcón, and V. Pascalutsa, Phys. Rev. C **90**, 055202 (2014).
- [114] V. Bernard, E. Epelbaum, H. Krebs, and U.-G. Meiñner, Phys. Rev. D **87**, 054032 (2013).
- [115] C. W. Kao, T. Spitzenberg, and M. Vanderhaeghen, Phys. Rev. D **67**, 016001 (2003).
- [116] Y. Prok, P. Bosted, V. Burkert, A. Deur, K. Dharmawardane, G. Dodge, K. Griffioen, S. Kuhn, R. Minehart, G. Adams, et al., Physics Letters B **672**, 12 (2009).
- [117] H. Dutz, K. Helbing, J. Krimmer, T. Speckner, G. Zeitler, J. Ahrens, S. Altieri, J. R. M. Annand, G. Anton, H.-J. Arends, et al. (GDH Collaboration), Phys. Rev. Lett. **91**, 192001 (2003).

VITA

Melissa Ann Cummings

Melissa Cummings was born on April 22, 1987 in Rochester, New York. She graduated from Marion High School in the spring of 2005. She went on to major in physics and minor in mathematics at the State University of New York at Geneseo, and obtained a Bachelor of Arts degree in May of 2009. During the following fall she began her graduate studies at the College of William and Mary, where she obtained a Master of Science degree in physics in January 2011. She began working with Dr. Todd Averett in the Hadronic Physics Group, studying the spin structure of the proton. Her research was focused at Jefferson Lab in Newport News, Virginia. She defended her dissertation on December 18, 2015 at the College of William and Mary. In February 2016, she began working at the Institute for Defense Analyses in Alexandria, Virginia.